

Magnetic Anisotropy of Molecular Nanomagnets

Von der Fakultät Mathematik und Physik der Universität Stuttgart
zur Erlangung der Würde eines Doktors der Naturwissenschaften (Dr. rer. nat.)
genehmigte Abhandlung

vorgelegt von

Fadi El Hallak
aus Tripoli (Libanon)

Hauptberichter: Prof. Dr. Martin Dressel

Mitberichter: Prof. Dr. Jörg Wrachtrup

Mitberichter: Dr. habil. Joris van Slageren

Tag der mündlichen Prüfung: 25. August 2009

1. Physikalisches Institut der Universität Stuttgart
Stuttgart 2009

Contents

List of Abbreviations	7
Zusammenfassung	9
1 Molecular Nanomagnets	17
1.1 Introduction	17
1.2 Magnetic anisotropy	18
1.2.1 The origin of magnetic anisotropy	19
1.2.2 Spin Hamiltonian approach	21
1.3 Slow relaxation of the magnetization	24
1.4 Quantum tunneling in molecular clusters	24
1.5 Experimental techniques	27
1.5.1 Standard magnetometry	27
1.5.2 Frequency domain magnetic resonance spectroscopy	28
1.5.3 Inelastic neutron scattering	29
1.6 Modeling Methods	30
1.6.1 Spin angular momentum	31
1.6.2 Hilbert space representation	32
1.6.3 Choice of the quantization axis	33
1.6.4 Calculating thermodynamic observables	37
1.7 Motivation and outline of the Thesis	38
2 Cantilever Torque Magnetometry	41
2.1 Introduction	41
2.2 Theoretical background	42
2.2.1 Torque and Faraday forces	42
2.2.2 Magnetically anisotropic clusters	46
2.2.3 Antiferromagnetic clusters	55
2.2.4 Avoided level crossings	56
2.3 The torque magnetometer	57
2.3.1 Capacitive detection	57
2.3.2 Non-linear response	60
2.3.3 Calibration	62
2.3.4 Cantilever design	65
2.4 Insert	68
2.5 Exploiting the experimental setup	73

2.5.1	Crystal orientation	73
2.5.2	Temperature calibration	73
2.5.3	Remnant field	75
3	Breakdown of the Giant Spin Model in Mn₆ SMM	77
3.1	Introduction	77
3.2	Results and discussion	79
3.2.1	FDMRS	79
3.2.2	Inelastic neutron scattering	82
3.3	Conclusions	86
4	Magnetic Anisotropy of a Photomagnetic Iron Dimer	89
4.1	Introduction	89
4.2	Experimental	90
4.3	Results and discussion	91
4.3.1	Crystal structure and photomagnetic measurements	91
4.3.2	FDMRS	92
4.3.3	Susceptibility and angle resolved magnetization measurements	94
4.3.4	Cantilever torque magnetometry	97
4.4	Conclusions	101
5	A Weakly Coupled Fe(II) Dimer	103
5.1	Introduction	103
5.2	Experimental	104
5.3	Results	104
5.3.1	Crystal structure	104
5.3.2	Magnetization and low field torque studies	105
5.3.3	High field torque magnetometry	108
5.4	Analysis and discussion	110
5.5	Properties of low lying energy states	115
5.6	Conclusions	117
5.7	Supplementary Information	119
6	High Field TM on a Molecular Dysprosium Triangle	123
6.1	Introduction	123
6.2	Experimental	126
6.3	Results and discussion	126
6.3.1	Spin Hamiltonian model	126
6.3.2	Low field torque magnetometry	128
6.3.3	High field torque magnetometry	129
6.4	Conclusions	138
7	Torque Detected Electron Spin Resonance	141
7.1	Introduction	141
7.2	Basic principle	142
7.3	Experimental setup	144
7.4	Results and discussion	145

7.4.1	Cantilever torque magnetometric measurements	146
7.4.2	Torque detected electron spin resonance	148
7.5	Conclusions	158
8	Summary	161
	Bibliography	167
	Acknowledgements	171

List of Abbreviations

AF	Antiferromagnetic
BWO	Backward Wave Oscillator
CTM	Cantilever Torque Magnetometry
ESR	Electron Spin Resonance
FDMRS	Frequency Domain Magnetic Resonance Spectroscopy
HS	High Spin
INS	Inelastic Neutron Scattering
LS	Low Spin
MW	Microwave
NVT	Néel Vector Tunneling
SMM	Single Molecule Magnet
SQUID	Superconducting QUantum Interference Device
SHPs	Spin Hamiltonian Parameters
TM	Torque Magnetometry
TDESR	Torque Detected Electron Spin Resonance
QTM	Quantum Tunneling of the Magnetization
VSM	Vibrating Sample Magnetometer
ZFS	Zero Field Splitting

Zusammenfassung

Magnetische Anisotropie liegt im Fokus der Forschung über molekularen Magnetismus. Es ist die magnetische Anisotropie, die zu langsam relaxierenden magnetischen Momenten in Einzelmolekülmagneten (SMM) führt. Die Anisotropie spielt auch für das makroskopische Quantentunneln der Magnetisierung (QTM) eine entscheidende Rolle. Der Axiale Teil des Spin-Hamiltonians definiert zusammen mit dem Spingrundzustand die Höhe der Energiebarriere ($U = DS^2 + B_4^0 S^4$), die der Inversion der Magnetisierung entgegensteht. Andererseits führt die transversale Komponente des Spin-Hamiltonians zu einer Überlagerung der Quantenspinzustände, die das Tunneln des Spins durch die Barriere ermöglicht. Als Folge erhöhen sich die Relaxationsraten der Magnetisierung, und die Energiebarriere U wird durch die effektive Energiebarriere (U_{eff}) ersetzt, die neben der thermischen auch die durch Tunneln erzeugte Relaxation berücksichtigt. In solchen Systemen ist es deshalb äußerst wichtig, die Anisotropieparameter mit großer Genauigkeit zu bestimmen. Infolgedessen kann das Verständnis der magnetischen Anisotropie in molekularen magnetischen Clustern zu einem besseren Verständnis der grundlegenden Physik des magnetischen und Quantenverhaltens der SMMs führen.

Das Ziel dieser Arbeit ist es, die magnetische Anisotropie unterschiedlicher molekularer magnetischer Systeme zu studieren. Dafür wurden unterschiedliche resonante und nicht-resonante experimentelle Methoden benutzt. Spektroskopie ist immer noch die beste Methode, um die Anisotropie in solchen Systemen zu beobachten. Wir haben magnetische Resonanz in der Frequenzdomäne benutzt, um die Spin-Feinstruktur des Grundzustandes in Nanomagneten spektroskopisch zu untersuchen. Es sind aber nicht alle Systeme spektroskopisch aktiv und diese Methode könnte in Systemen mit ungünstigen Spin-Gitter-Relaxationszeiten, großer Null-Feld-Aufspaltung (ZFS) oder übermäßiger Dipol-Verbreiterung fehlschlagen. Wir benutzten deshalb in manchen Systemen auch Magnetometriemessungen komplementär oder als Ersatz für die spektroskopischen Messungen. Letztendlich wurden beide Methoden zu einer Drehmoment detektierten ESR Technik kombiniert.

Die in dieser Arbeit vorwiegend verwendete Methode ist die Blattfeder-Drehmoment-Magnetometrie (CTM). Wir haben eine auf Kapazität basierende CTM Methode entwickelt, um Experimente an Einkristallen molekulare Magneten durchzuführen. In einer SMM sind die Spins der einzelnen Moleküle vorwiegend entlang der leichten Magnetisierungsachse (Easy Axis) des Moleküls orientiert. Die Nichtkollinearität zwischen der Easy Axis und des äußeren angelegten magnetischen Feldes induzieren ein magnetisches Moment, das die Easy Axis zum äußeren Feld ausrichtet. Zusammen mit einer Kupferplatte, welche 30-100 μm unterhalb der Blattfeder plaziert ist, erzeugt

dieses einen Plattenkondensator. Wir haben die kapazitive Methode benutzt, um den Biegeungsgrad der Blattfeder durch ein externes Drehmoment zu bestimmen. Die Biegung der Blattfeder führt zu einer Abstandsänderung gegenüber der unteren Platte und dadurch zu einer Änderung der Kapazität, die durch eine externe Kondensatorbrücke detektiert wird. Wir haben nicht-magnetische CuBe Blattfedern mit einer Dicke von 25 und 80 μm benutzt, um eine Reihe von Drehmoment-Messgeräten, die eine Empfindlichkeit von 10^{-6} bis 10^{-11} Nm haben, aufzubauen. Dazu wurde ein Probenhalter auf einer horizontal rotierenden Bühne entwickelt, und die Messmethode wurde mithilfe mehrerer Labview-Programme automatisiert. In magnetisch anisotropischen Paramagneten ist das Drehmoment, das durch ein magnetisches Feld erzeugt wird, das in der (xz) Ebene unter einem Winkel θ zur Easy Axis angelegt ist, gegeben durch,

$$\tau_y = B^2 \left(\frac{M_z}{B_z} - \frac{M_x}{B_x} \right) \cos \theta \sin \theta \quad (1)$$

Der Ausdruck in den Klammern beschreibt die magnetische Anisotropie des Systems, sodass das Drehmoment ein direktes Maß dafür darstellt. Winkelaufgelöste Drehmomentmessungen sind besonders wichtig, um das Vorzeichen der Anisotropie des Systems zu bestimmen. Magnetische Biegemessungen sind nicht nur für die Charakterisierung der Anisotropie der paramagnetischen Zentren nützlich, sondern können auch Informationen über die Austauschwechselwirkung in den Systemen liefern, speziell in antiferromagnetischen Clustern. Wir haben erfolgreich CTM eingesetzt, um sowohl die magnetische Anisotropie als auch die Austauschwechselwirkung in unterschiedlichen Systemen zu untersuchen.

Die Erhöhung der Energiebarriere gegen die inverse Magnetisierung in SMMs lag im Fokus mehrerer Studien über molekularen Magnetismus. Trotz der gemeinsamen Anstrengungen von Chemikern und Physikern, geeignete Systeme zu finden, die die Magnetisierung bei hohen Temperaturen über eine längere Zeit aufrechterhalten können, war Mn_{12} -azetat bis kürzlich das System mit der höchsten Blockierungstemperatur und Anisotropiebarriere von 3.5 K bzw. 74.4 K. Wir haben zwei unterschiedliche Varianten von Mn_6 mit dem Grundzustand $S = 12$ untersucht, wobei eine davon eine Rekordbarriere von 86 K aufweist (Verbindung 1). Überraschenderweise weist die zweite Verbindung trotz der ähnlichen Struktur eine kleinere Barriere von 53 K (Verbindung 2). FDMRS und inelastische Neutronenstreuung (INS) Messungen wurden an beiden Systemen durchgeführt, um den Grund für die unterschiedlichen Anisotropiebarrieren zu finden. Dies erlaubte uns, die tiefliegenden Spin-Anregungen zu beobachten und folglich das Energiespektrum des Systems zu entschlüsseln. Die FDMR Spektren zeigen sechs scharfe Resonanzlinien zwischen 5 und 9 cm^{-1} , die für beide Verbindungen sehr ähnlich sind. Interessanterweise werden die Resonanzfrequenzen nicht durch das Giant-Spin-Model (GSM) wiedergegeben. Trotzdem eignet sich das Model besser für die Verbindung (1) als für Verbindung (2). Inelastische Neutronenstreuung (INS) wurde benutzt, um einen besseren Einblick in die Energiespektren der zwei Verbindungen zu gewinnen. Im Gegensatz zu FDMRS ist INS sowohl für interwie für intra-multiplett Übergänge empfindlich. Das erlaubte uns, die Übergänge von $S = 12$ zu $S = 11$ zu untersuchen. Die INS Spektren zeigen, dass in der Verbindung (2) der $S = 11$ Spinzustand näher am $S = 12$ Zustand liegt. Demzufolge sind die Spinzustände stark gemischt und ermöglichen neue Tunnelpfade, die die

Magnetisierungsrelaxation stark beeinflussen und die effektive Anisotropiebarriere reduzieren. Außerdem bewies diese Studie, dass das GSM ungeeignet für solche Systeme ist und dass die Implementierung eines mikroskopischen Hamiltonians notwendig ist. Weiter wurde beobachtet, wie kleine strukturelle Verzerrungen enorme Auswirkungen auf die Anisotropiebarriere haben.

Ein besonders interessantes Teilgebiet des molekularen Magnetismus ist das der photomagnetischen Cluster. Diese Systeme, oft mononukleare Fe(II) Komplexe, können einen Spinübergang durchführen von einem Zustand mit niedrigem Spin (low spin LS) zu einem Zustand mit großem Spin (high spin HS), unter Einfluss von Temperatur, Druck oder Bestrahlung. In diesen Untersuchungen beabsichtigten wir die Kombination einer starken magnetischen Anisotropie mit dem simultanen Schalten der Spinzustände in einem System durch Licht zu ermöglichen. Das Ziel ist die Erzeugung eines photo-schaltbaren einzelmolekularen Magneten. Das System, das wir dafür gewählt haben, ist $[\text{Fe}(\text{bpp})(\text{NCS})_2]_2(4,4'\text{-bpy})$ (von nun an $\text{Fe}_2\text{-NCS}$). Wir zeigen, wie sich unterschiedliche experimentelle Techniken gegenseitig ergänzen können, um den Magnetismus eines Systems komplett zu charakterisieren. Die photomagnetischen Studien wurden an der Universität de Bordeaux mit Dr. Patrick Rosa und seinen Mitarbeitern durchgeführt. Bei höheren Temperaturen zeigt die Suszeptibilität ein paramagnetisches Verhalten. Während der Abkühlung gibt es einen plötzlichen Abfall in χT bei ca. 115 K. Die Suszeptibilität zeigt eine leichte thermische Hysterese bei diesem Übergang. Diese Hysterese wurde auch in Studien zur Kristallstruktur beobachtet. Dieser Abfall des χT Wertes bestätigt die Tatsache, dass eines der Fe(II) Ionen im Molekül in seiner LS Konfiguration ($S = 0$) vorliegt. Lichtbestrahlung erzeugt einen Zuwachs der Suszeptibilität bis zur Sättigung nach 10 Minuten. Dieser LIESST Effekt ändert die Elektronenkonfiguration der LS Zentren in HS metastabile Zustände. Wir haben die magnetische Anisotropie des LS-HS Zustandes, der bei tiefen Temperaturen ein $S = 2$ Grundzustand besitzt, mit FDMRS, winkelaufgelöste Magnetisierungsmessungen und CTM untersucht. Die FDMR Spektren zeigen einen einzigen magnetischen Resonanzübergang bei ungefähr 9 cm^{-1} . Die Temperaturabhängigkeit zeigt, dass der beobachtete Übergang ein Grundzustandsübergang ist. Das Fehlen des Übergangs in den angeregten Zustand lässt die Frage über den Typ der Anisotropie des Systems offen. Für eine Easy Axis Anisotropie würde der beobachtete Übergang einen D Wert von -3 cm^{-1} ergeben, während ein D von $+9 \text{ cm}^{-1}$ eher für den Fall einer Hard Axis Anisotropie zu erwarten ist. Um diese Unklarheit zu lösen, wurden winkelaufgelöste Magnetisierungsmessungen in zwei unterschiedlichen kristallographischen Ebenen durchgeführt. Die Absolutwerte der Magnetisierungs-Maxima und -Minima in beiden Ebenen waren sehr ähnlich, was die Zuweisung der Easy (oder Hard) Axis auf einer kristallographischen Achse unmöglich machte. Da die Einheitszelle zwei Moleküle enthält, wurde eine Verbindung zwischen der molekularen Achsen und den kristallographischen Achsen gesucht, um die winkelaufgelöste Magnetisierungsmessungen verstehen zu können. Dies beschränkte die Anisotropie-Axis auf entweder die Hard Axis neben der (Fe-Pyrazole-Fe) Hauptachse oder die Easy Axis neben der (Fe-Pyridine-Fe) Hauptachse. Winkelaufgelöste wie auch feldabhängige Drehmomentmessungen beweisen, dass das System eine Hard Axis Anisotropie entlang der (Fe-Pyrazole-Fe) Hauptachse besitzt, mit einem D Wert von 9 cm^{-1} . Diese Studien führen zu einem besseren Verständnis der magnetischen Anisotropie in Spin-Crossover-Systemen. Für

das Studium der magnetischen Anisotropie molekularer Magneten haben wir hiermit die Notwendigkeit der Anwendung mehrerer komplementären Techniken bewiesen, da die durch eine einzige Technik gewonnenen Informationen in manchen Fällen nicht nur zu unvollständigen, sondern auch zu falschen Annahmen führen können. Unser oberstes Ziel ist es, ein photoschaltbares System mit starker Easy Axis-Anisotropie zu finden, was letztlich zu photoschaltbaren SMMs führen könnte.

Molekulare Cluster mit antiferromagnetischen (AF) Austauschwechselwirkungen haben durch ihre vielfältigen quantenmagnetischen Eigenschaften ein großes Interesse geweckt. Insbesondere sind sie vielversprechende Kandidaten, um die makroskopische Quantenkohärenz zu beobachten, wie sie im kohärenten Tunneln des Néel Vektors reflektiert wird. Die meisten beschriebenen Systeme haben relativ starke Austauschkopplungskonstanten ($J > D$), was zu dem typischen Bild des Energiespektrums solcher AF Systeme führt; ein System mit unmagnetischem Grundzustand ($S = 0$ für eine gerade Zahl gleicher Spins), das sukzessiv seinen Spin Grundzustand ändert in $S = 1$, $S = 2$, etc... unter dem Einfluss eines äußeren magnetischen Feldes, welches entlang der Easy oder Hard Axis angelegt wird. Wir haben ein einzigartiges antiferromagnetisches Fe(II) Dimer studiert. Im Gegensatz zu anderen, üblicherweise beobachteten stark gekoppelten Systemen zeigt hier die Magnetisierung nur eine Niveaufkreuzung bei etwa 4.2 Tesla und steigt danach sanft weiter bis 12 Tesla. Das Modell, das wir basierend auf der vollständigen Charakterisierung des Systems vorschlagen, nimmt an, dass die Austauschkopplung viel schwächer ist als die starke Einzelkern-Anisotropie der Fe(II). Die Größe der Austauschwechselwirkung und der g -Faktor werden aus der Suszeptibilität und den Magnetisierungsmessungen bestimmt. Andererseits wird das Vorzeichen und die Größe der Einzel-Ion Anisotropie D aus den Niedrig- und Hochfeld-Drehmoment-Magnetometrie-Messungen bestimmt. Die Kombination dieser Daten erlaubte eine genaue Bestimmung der Spin-Hamiltonian-Parameter zu $g = 2.23(5)$, $J = -1.74(6) \text{ cm}^{-1}$, und $D = -8.5(4) \text{ cm}^{-1}$. Die Folgen einer schwachen Wechselwirkung auf die magnetischen und Quanteneigenschaften des Systems sind sehr wichtig. Für $D = 0$ (oder $D \ll J$), ist $[\hat{S}, \hat{H}] = 0$, d.h. der Gesamtspin S bleibt erhalten. Falls $D \gg J$ sind die Spinzustände stark gemischt, und S ist keine gute Quantenzahl mehr; jedoch bleibt M_S eine gute Quantenzahl in Abwesenheit eines transversalen Feldes. Die Energien der unterschiedlichen Spins werden in der schwachen Kopplung neu geordnet; und in unserem Fall beobachten wir, dass der $M_S = -4$ Zustand am nächsten zu dem unmagnetischen Dublett-Grundzustand liegt. Als Folge beobachtet man anstelle eines sukzessiven Ansteigens der Magnetisierung eine große magnetische Stufe direkt beim ersten Kreuzungspunkt der Niveaus, was magnetisch einem Übergang vom Spin $M_S = 0$ zu einem Spin $M_S = -4$ entspricht. Diese Stufe ist ein Analogon zu dem Spin-Flip, der in Antiferromagneten mit langreichweitiger Ordnung beobachtet wurde. Auf der anderen Seite sind die Energie und Aufbau des Grundzustands Dubletts, welches den zwei Zuständen mit unterschiedlichen Orientierungen des Néel Vektors entspricht, stark von dem J/D Verhältnis abhängig. Die Tunnelaufspaltung, die die Energie dieser zwei Dubletts trennt, wurde aus dem Hamiltonian auf ungefähr 83 MHz geschätzt. Weiter wurde der "Tunneling action" S_0/\hbar , die ein Maß darstellt für die Wahrscheinlichkeit, dass der Néel Vektor tunnelt, auf 12.5 geschätzt, was zweimal größer ist als der veröffentlichte Wert für den Fe₁₈ antiferromagnetischen Ring. Aufgrund dieser Werte für Δ und S_0/\hbar schlagen wir dieses System als potenziellen Kandidaten vor, um das

kohärente Tunneln des Néel Vektors zu beobachten.

Lanthaniden unterscheiden sich grundsätzlich von den anderen Übergangsmetallen, da ihre Valenzelektronen nicht in den 3d, sondern in den 4f Orbitalen sind. Dadurch haben Lanthanide schwächere Ligandenfelder als die Ionen der Übergangsmetalle. Dennoch besitzen sie große magnetische Drehmomente und sehr oft eine hohe magnetische Anisotropie aufgrund der starken Spin-Bahn-Kopplung, wodurch sie zu interessanten Bausteinen für SMMs werden. Mononukleare 4f Komplexe haben eine langsame Relaxation der Magnetisierung bei sehr hohen Temperaturen gezeigt im Vergleich zu solchen, die in Übergangsmetallen beobachtet wurden. Trotz dem phasenverschobenen Wechselstrom Signal, das oberhalb 40 K auftrat, wurden Hysterese-Kurven nur bei sehr niedrigen Temperaturen beobachtet (mK Bereich). Weitgehend besteht Einigkeit in der Annahme, dass schnelles Tunneln in diesen Systemen der Grund für die Abwesenheit von Hysterese-Kurven ist. Daher ist es von großer Bedeutung, Informationen über die tiefliegenden Unterniveaus des elektronischen Systems 4f zu erhalten, um den Magnetismus zu verstehen, insbesondere die Relaxationsmechanismen in diesen Verbindungen. Wir haben ein Dy₃ Dreieck ausgewählt mit besonderen magnetischen Eigenschaften; das System zeigt nämlich eine langsame Relaxation der Magnetisierung, obwohl es einen nichtmagnetischen Grundzustand besitzt. Mit Hilfe des effektiven Spin-Modells zur Beschreibung des Systems, haben wir ein Spin-Hamiltonian entwickelt, der berücksichtigt, dass für jedes Dy³⁺ das Grundzustandsdublett $|15/2, \pm 15/2\rangle$ ist und die angeregten Dublettzustände $|15/2, \pm 5/2\rangle$ auf einem Energieniveau δ , vom Grundzustand aus, sitzen. Da wir wissen, dass das Drehmomentsignal stark von der Anisotropie abhängt, haben wir Drehmomentsignale für transversale Felder berechnet, die Peaks bei hohen magnetischen Feldern vorhersagen. Letztendlich haben wir Drehmoment-Magnetometriemessungen an Hochfeldlaboratorien in Grenoble und Tallahassee durchgeführt. Die Ergebnisse haben unsere Vorhersagen bestätigt, indem sie ein Drehmomentsignal bei etwa 28 Tesla ergaben, was uns erlaubte die Anisotropie zu quantifizieren $\delta = 250 \pm 10 \text{ cm}^{-1}$. Zusätzlich weisen die temperaturabhängigen Untersuchungen der Stufe, die in dem Drehmomentsignal bei der Niveaureuzung in mK Bereich beobachtet wird, auf eine Mischung der Niveaus im Bereich 100-200 mK. Dieser Wert, der im einfachen Effektivspinmodell berücksichtigt wird, kann eine plausible Erklärung für die Erhöhung der magnetischen Relaxationsrate abgeben, die bei der Niveaureuzung in früheren Studien beobachtet wurde. Weiterhin wurden im Drehmomentsignal zwei unterschiedliche Wendepunkte beobachtet, welche dem Grundzustand bzw. angeregten Zustand Kreuzung im Energiediagramm zugeordnet werden können. Aus den Positionen dieser Wendepunkte kann eine Abschätzung von $\phi = 20^\circ$ gewonnen werden, welche die Spinstruktur in dem Dy₃ Dreieck klärt. Mehr Untersuchungen sind notwendig, um ein neues Modell zu entwickeln, das eine genauere Erklärung der Magnetisierung dieser Systeme liefert. Diese Studie wurde an einem System mit komplizierter Kristallstruktur durchgeführt. Im Großen und Ganzen hat diese Studie zum besseren Verständnis der Lanthanide basierten Systeme geführt. Vor allem haben wir gezeigt, dass Hochfeld-Drehmoment-Magnetometrie eine geeignete Methode für die Untersuchung der Anisotropie dieser Systeme, vor allen mononuklearer Lanthanid SMMs sein kann.

Nachdem wir die Spektroskopie und CTM erfolgreich verwendet haben, um die

magnetische Anisotropie in unterschiedlichen SMMs zu untersuchen, haben wir unsere Erfahrungen benutzt, um sie zu kombinieren und eine neuartige Drehmoment detektierte ESR (TDESR) Methode zu entwickeln, um sehr kleine SMMs Einkristalle in einem Breitband Frequenzbereich untersuchen zu können. Übliche ESR Spektrometer sind sehr empfindlich, haben aber begrenzte diskrete Frequenzen, während Breitbandtechniken wie FDMRS oder INS eine schwache Empfindlichkeit haben. TDESR kombiniert beide Eigenschaften, hohe Empfindlichkeit und Breitbandspektroskopie. TDESR misst die Wirkung, die ein magnetischer Resonanzübergang auf das magnetische Drehmoment der Probe ausübt. Bei Resonanz induziert die Mikrowelle eine Spin-Rotation und folglich ändert sich das Drehmoment für ein Ensemble von Spins. Diese Änderung des Drehmoments wird durch das höchstempfindliche Drehmoment-Magnetometer detektiert. Der experimentelle Aufbau für die TDESR Messungen besteht aus zwei Teilen. Der erste ist der optische Teil, der die Erzeugung und die Fokussierung der Mikrowelle auf den Kristall übernimmt. Der zweite ist das Drehmoment-Magnetometer, das das Drehmomentsignal unter einem äußeren magnetischen Feld misst. Ein spezieller Probenhalter wurde entwickelt, um Drehmoment-Magnetometrie-Messungen unter Mikrowellen einstrahlung durchzuführen. Die Messungen können in der Frequenzdomäne ausgeführt werden, wo ein Frequenzbereich von 30 GHz - 1.5 THz umfasst werden kann bei konstantem magnetischen Feld, oder in der Feld-Domäne (0-8 Tesla) bei konstanter Mikrowellen-Frequenz. Dazu können auch winkelabhängige ESR-Messungen durchgeführt werden, mit einer Rotationsmöglichkeit zwischen 0 und 180°. Um das Konzept zu testen, wurde eine Fe₄-rac Verbindung mit einem $S = 5$ Spin-Grundzustand ausgewählt. Die Dualität unserer Technik erlaubt es uns, das System zunächst mit dem Drehmoment-Magnetometer zu untersuchen und danach TDESR durchzuführen. Beide Messungen werden an der gleichen Probe "in situ" durchgeführt. Übliche Drehmoment Messungen ergaben eine Abschätzung für die axiale Anisotropie des Systems ($D = -0.4 \text{ cm}^{-1}$) und ermöglichten uns, die genaue Orientierung der Easy Axis zu bestimmen. TDESR Messungen wurden in Frequenz- und in der Feld-Domäne bei unterschiedlichen Temperaturen und Winkeln durchgeführt. Die ermittelten Spin-Hamiltonian-Parameter [$D = -0.448(2) \text{ cm}^{-1}$, $E = 0.03(1) \text{ cm}^{-1}$, $B_4^0 = 1.8(3) \times 10^{-5} \text{ cm}^{-1}$, und $g = 1.985(4)$] stimmen mit denen überein, die durch Hochfrequenz-ESR-Messungen am Pulver bestimmt wurden. Die gewonnenen Spektren beweisen die hohe Empfindlichkeit der Technik. Der Nachteil des jetzigen Aufbaus liegt in dem Effekt der nichtlinearen Antwort des Drehmomentmeters auf die beobachteten Intensitäten. Um dieses Problem zu umgehen, schlagen wir den Einbau einer Feedback Schleife vor, welche den Betrieb des Drehmomentmagnometers im konstanten Kapazitätsmodus erlaubt. Weiterhin wurde gezeigt, dass die Vielfältigkeit der experimentellen Parameter, die variiert werden können (magnetisches Feld, Mikrowelle-Frequenz, Winkel, Polarisation und Temperatur) uns die Möglichkeit gibt, das ganze Energiediagramm vieler Systeme zu beobachten.

In der vorliegenden Arbeit haben wir die magnetische Anisotropie mehrerer molekularer Magneten mit unterschiedlichen magnetischen Eigenschaften untersucht. Im Einzelnen haben wir beobachtet, wie das Zusammenspiel, der Austausch und Einzelion-Anisotropie die Anisotropie-Barriere (wie in den Mn₆ Systemen), die Energie-Niveau-Schemata und die magnetischen Eigenschaften (Fe₂-Penta) beeinflussen kann. Weiterhin hat unsere Studie des Dy₃ zu dem Verständnis der magnetischen Anisotropie

in Lanthanide basierten molekularen Magneten beigetragen, was zur Entwicklung besserer SMMs führen könnte. Für das Studium der magnetischen Anisotropie molekularer Magneten haben wir hiermit die Notwendigkeit der Anwendung mehrerer komplementärer Techniken bewiesen, da die durch eine einzige Technik gewonnenen Informationen nicht nur zu unvollständigen, sondern auch zu falschen Schlüssen führen können. Letztendlich haben wir eine neue Drehmoment-detektierte-ESR-Methode entwickelt, eine vielversprechende Methode, um die magnetische Anisotropie molekularer Nanomagnete zu untersuchen.

Chapter 1

Molecular Nanomagnets

1.1 Introduction

Magnetism remains one of the most fascinating and intriguing phenomena observed in nature. Elementary particles, which are the basic building blocks of our universe, are mainly characterized by their mass, charge, and spin. The last, which is an intrinsic property of these particles, defines their magnetic moment. Magnetic properties of materials have therefore been, and continue to be thoroughly investigated by researchers all over the world. Magnetic materials are in our everyday's life, from simple technologies like wristwatches or earplugs, to electrical motors and generators, hard disks and computers, magnetic resonance imaging and medical applications, and the list goes on. These applications essentially rely on magnetic materials. The exploitation of new technologies ultimately drives a need for new devices and structures that exhibit superior functionality and performance. These new devices and structures, in turn, will require new materials. The global market for magnetic materials is forecast to reach \$28.5 billion by 2012 [1]. On the other hand, magnetism is interesting from a fundamental point of view, and new observations and theories arise one year after the other in this field of research. As a consequence of this continued importance of magnetic materials and magnetism in general, numerous enterprises and laboratories aim at developing and discovering new magnetic materials with improved properties and interesting physical behavior.

Molecular magnets are new class of magnetic materials which have interesting physical, magnetic, and chemical properties. A molecular magnet is a molecule comprising one or more magnetic centers which are coupled to each other via the exchange interaction leading to a net total spin for the molecule. These magnetic centers can be transition metal ions, lanthanides, or a mixture of both. The molecules can be chemically synthesized, and their chemical properties can be altered to an astonishing extent by changing the linkers which bridge the magnetic ions to each other. In addition, chemists can control the surrounding ligands which link the molecules to each other or even to metal surfaces [2] or carbon nanotubes [3] for instance. Figure 1.1 shows several examples of different molecular nanomagnets having different structures and spin ground states. This figure demonstrates the esthetic beauty of these molecules.

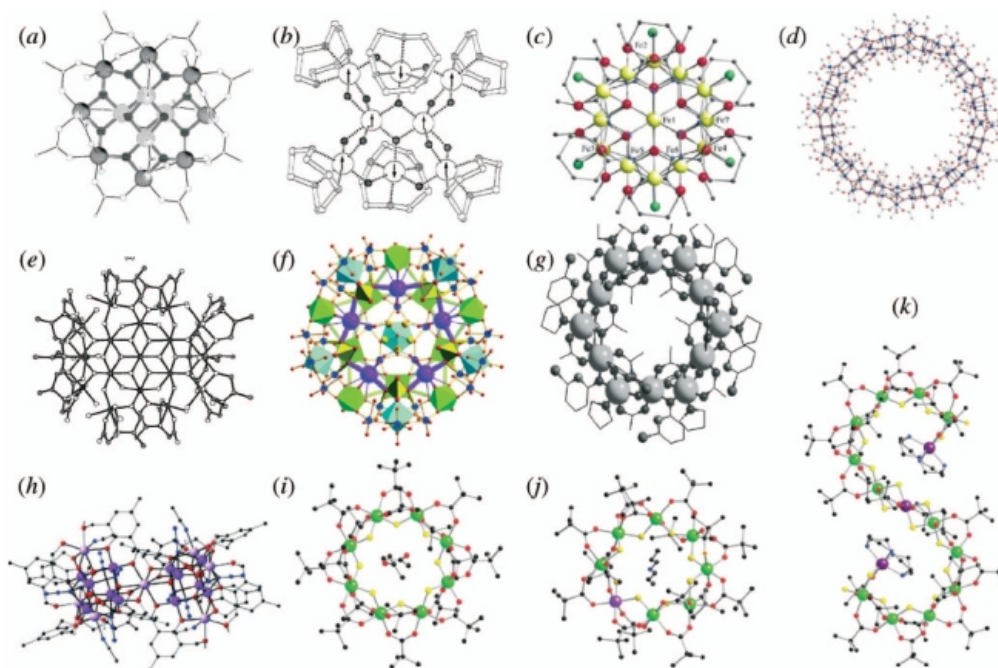


Figure 1.1: Examples of molecular nanomagnets: (a) Mn_{12} ($S = 10$) (b) Fe_8 ($S = 10$) (c) Mn_9 ($S = 17/2$) (d) Mn_{84} ($S \approx 6$) (e) Fe_{19} ($S = 33/2$) (f) keplerate containing twelve $\{\text{Mo}^{VI}\text{Mo}_5^{VI}\}$ fixed by thirty V^{IV} linkers (g) Ni_{12} ($S = 12$) (h) Mn_{19} ($S = 81/2$) (i) Cr_8 ($S = 0$), (j) Cr_7Ni ($S = 1/2$) (k) $\text{Cr}_{12}\text{Ni}_3$, a wheel which failed to close, producing an S shaped molecule (after [8]).

Besides their large spin ground states, these molecules have large uniaxial magnetic anisotropies. Single molecule magnets (SMMs) are molecular magnets with an easy axis anisotropy, i.e. their spin has a preferential molecular orientation along which it points at low temperatures. A direct consequence of this is the slow relaxation of the magnetization of purely molecular origin below certain temperatures, and the magnetization curves show hysteresis, hence the name single molecule magnet. Another reason for their presence as top research topic today is the complicated and fascinating quantum phenomena that these systems display. Despite the large number of coupled atomic spins, the macro spin of the molecule obeys the rules of quantum mechanics. The M_S states of the spin ground state S which correspond to the different rotations of the spin are quantized in energy. Spin rotations can be induced by microwave radiation of energy equal to the quantized energy difference between two different M_S states [4][5]. Furthermore, macroscopic quantum tunneling of the magnetization between two different spin rotations was also observed in SMMs [6][7].

1.2 Magnetic anisotropy

Without the effect of magnetic anisotropy, it would have been difficult to discover magnetism. Almost all applications employing magnetic materials depend in some way

or the other, on the fact that it is more favorable to magnetize a magnetic material in one direction than in the other. This different magnetic response of the material in different directions is what makes it magnetically anisotropic. A very common and simple example of the application of magnetic anisotropy is the compass. The needle of a compass is magnetized along the needle's direction and not perpendicular to it, as a consequence it responds to the magnetic field of the earth by aligning along its direction [9].

The sources of the magnetic anisotropy are numerous and can vary from one system to another. There are three main anisotropies which one usually observe in magnetic systems, the exchange anisotropy where the interaction between neighboring spins is anisotropic, the g value anisotropy which is field dependent, and the single-ion anisotropy which strictly depends on the interplay between the spin-orbit coupling and the crystal field. The latter is the origin of the anisotropy in molecular nanomagnets. In the following, we briefly give a qualitative picture of the physical origin behind the magnetic anisotropy in these systems. We shall also see the consequences of the anisotropy on the magnetic properties, which lead to slow relaxation of the magnetization, and on the quantum mechanical properties leading to macroscopic quantum tunneling.

1.2.1 The origin of magnetic anisotropy

The magnetic properties of a free single atom (or ion) are determined by the electrons which occupy the unfilled electronic shells. The spin and orbital magnetic moment of the individual electrons can couple together to give a total spin S and orbital magnetic moment L for the whole atom. There are $(2S+1)(2L+1)$ ways to combine the orbital and spin magnetic moments for the ground state of the atom. The different states resulting from these combinations are associated to different spatial and orbital paths for the electrons around the nucleus. The electrostatic interaction between the electrons varies depending on how close the electrons are together in these different paths and thus the states are not energetically equivalent. The spin and orbital angular momentum are coupled together by the spin-orbit interaction [10]. The total conserved angular momentum is given by $J = L+S$, and the states with different L and S are split into different J levels; a splitting which is known as the fine structure. J takes the values from $L-S$, to $L+S$, and the value of the splitting depends on the strength of the spin-orbit coupling designated by λ . The energies of the different J values can be given by [11],

$$\lambda L \cdot S = \frac{\lambda}{2} [J(J+1) - L(L+1) - S(S+1)] \quad (1.1)$$

where λ depends on the atomic number Z ($\lambda \propto Z^4$). There are several combinations of L and S , but only one J value is the ground state of the system. Hund's rules follow the reasoning of minimizing the energy of the electrons [11], and set some guidelines to obtain the ground state of the atom¹. The ground state of the atom is denoted

¹Note that Hund's rules implement the Russel Sanders coupling scheme; for atoms with high atomic number, the j-j coupling gives a better description of the system.

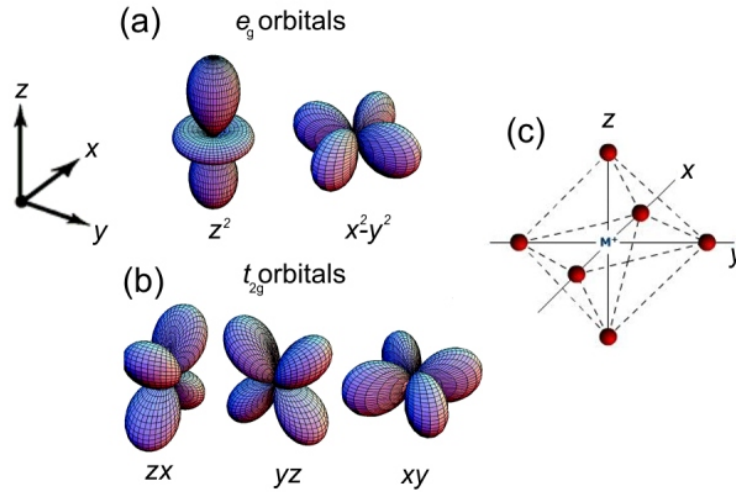


Figure 1.2: (a) The angular distribution of the d_{z^2} and $d_{x^2-y^2}$ orbitals (e_g), and (b) d_{xy} , d_{xz} , and d_{yz} orbitals (t_{2g}). (c) A metal ion M^+ in an octahedral environment.

as $^{2S+1}L_J$ where $2S+1$ describes the spin multiplicity and J gives the value of the total angular momentum value, while L is a letter that describes the orbital angular momentum and is represented by (S, P, D, F... for $L = 0, 1, 2, 3, 4...$). Each J value has the degeneracy of $2J+1$ levels which are split in an external magnetic field (Zeeman splitting). This degeneracy can be also lifted if the atom (or ion) is introduced into a lattice.

In order to understand the effect of the local environment in a lattice on the energy levels of the atom, it is necessary to recall that the different atomic orbitals can have different shapes. Only the s orbitals are spherically symmetric, while other orbitals have a pronounced angular dependence of the electron density. Figure 1.2 shows the shapes of the 5 different d orbitals. The d orbitals fall into two groups, the t_{2g} (d_{xy} , d_{xz} , and d_{yz}) which point in between the x, y, and z axes, and the e_g which consist of the d_{z^2} pointing along the z axis, and the $d_{x^2-y^2}$ having lobes along the x and y axes. In a spherically symmetric environment (a sphere of uniform negative charge), the 10 d electrons will all see the same charge independent of which orbital they occupy. On the contrary, in octahedral surroundings (Figure 1.2 (c)), the metal ion is in the center, and oxygen ions are at the corners of the octahedron in a metal oxide for instance. The electrons in the e_g orbitals have higher overlap with those from the p orbitals of the oxygen ions than the electrons from the t_{2g} orbitals. Hence, the Coulomb repulsion is less for the e_g electrons than that of t_{2g} ones and therefore, the e_g orbitals become more energetically favorable. The splitting of the d orbitals is therefore due to the electrostatic field of the neighboring ions (or ligands), which is known as the ligand field splitting. In short, the ligand field energetically favors some orbitals to the others, i.e. certain angular distributions to others. In other words, it introduces anisotropy. However, in most transition metal ions, the orbital angular momentum is quenched, and only the spin magnetic moment remains. The electron spin itself does not have a preferential direction and is therefore not isotropic. It is the coupling between the spin and orbital moments which renders the magnetic properties anisotropic. For an

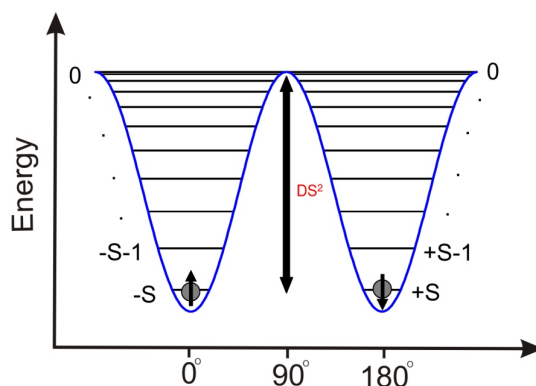


Figure 1.3: Energy levels of the different M_S states of the S spin ground state. The x axis indicates the angle between the magnetic moment and the easy axis of the molecule. The spin of an individual molecule is localized either in the left or in the right well if the molecule does not have enough thermal energy to overcome the energy barrier DS^2 .

electron in a particular orbital to have a first order orbital angular momentum about a specified axis, it must be possible, by rotation about that axis, to switch into an identical degenerate orbital which has a vacancy for an electron of the spin concerned (up or down). The orbitals comprising the t_{2g} set in an octahedral surrounding can be converted into one another by rotation about a given axis but the $d_{x^2-y^2}$ and d_{z^2} cannot. In complexes where there exists orbital degeneracy in the e_g set (such as Mn(III)), the orbital angular momentum is quenched by the octahedral crystal field. Quenching of the orbital momentum can also occur by further lowering of the symmetry from octahedral. Nevertheless, the ground state of the system still possesses some orbital character by virtue of spin-orbit coupling matrix-elements to higher lying states.

The above picture is valid for transition metal ions, where the spin-orbit coupling is much weaker than the crystal field. The electronic states are therefore perturbed by the crystal field which in turn is perturbed by the spin-orbit coupling, and eventually an external magnetic field. The situation is rather different for lanthanides. Lanthanides are heavier atoms, thus the spin-orbit coupling is stronger than in transition metals. On the other hand, the magnetic orbitals (i.e. the orbitals occupied by the unpaired electrons) are the f rather than the d orbitals. F orbitals are closer to the nucleus than the d orbitals and hence their interaction with the ligands (ligand field) is much weaker. Furthermore, the exchange interaction between lanthanides ions is rather weak, which makes the assembly of polynuclear lanthanide based SMMs difficult compared to that of transition metal ions.

1.2.2 Spin Hamiltonian approach

The spin Hamiltonian (SH) approach, is a very practical way to describe the interactions in a spin system, using only spin operators. Its convenience lies in the simplification of many-body electronic systems, by disregarding all the interactions which are not spin related, or in other words, all interactions which are irrelevant to describe

the magnetism of the system. Hence, the full Hamiltonian which takes the kinetic and potential energy of a many body problem is replaced by a spin Hamiltonian where only spin related interactions are taken into account. There are three essential interactions which contribute to the SH in molecular magnetic systems, namely, the single ion anisotropy, the exchange interaction, and the Zeeman interaction. The exchange interaction exists between different neighboring spins in a cluster. It is of electrostatic origin, and it arises due to a competition between the coulomb repulsion, and parity of the wavefunction, i.e. Pauli principle. The Zeeman interaction exists between the externally applied magnetic field, and the spin magnetic moments. Here, we concentrate on the single ion anisotropy. The inclusion of the exchange and the Zeeman terms is discussed in Section 1.6.

For a magnetic center of spin S , the anisotropy term can be expressed as,

$$\hat{H}_{\text{Anisotropy}} = \hat{S} \cdot \mathbf{D} \cdot \hat{S} \quad (1.2)$$

where \mathbf{D} is the anisotropy tensor, which is real and symmetric. It is always possible to find an orthogonal coordinate system in which the only non-vanishing elements of \mathbf{D} are along the diagonal. This condition is satisfied, when the orthogonal eigenvectors of \mathbf{D} are taken along the individual axes in an orthogonal system of coordinates

$$\mathbf{D} = \begin{pmatrix} D_{xx} & 0 & 0 \\ 0 & D_{yy} & 0 \\ 0 & 0 & D_{zz} \end{pmatrix} \quad (1.3)$$

Consequently, (1.2) can be written as,

$$\hat{H}_{\text{Anisotropy}} = D_{xx}\hat{S}_x^2 + D_{yy}\hat{S}_y^2 + D_{zz}\hat{S}_z^2 \quad (1.4)$$

Subtracting the constant $(1/2)(D_{xx}+D_{yy})(S_x^2+S_y^2+S_z^2)$, one obtains [12]

$$\hat{H}_{\text{Anisotropy}} = D\hat{S}_z^2 + E(\hat{S}_x^2 - \hat{S}_y^2) \quad (1.5)$$

where

$$D = D_{zz} - \frac{1}{2}D_{xx} - \frac{1}{2}D_{yy}; \quad E = \frac{1}{2}(D_{xx} - D_{yy}) \quad (1.6)$$

D and E are the axial and transverse anisotropy parameters, respectively. In a cubic symmetry, $D_{xx} = D_{yy} = D_{zz}$, i.e. $D = E = 0$, and the system is isotropic. In axial symmetry, $D_{xx} = D_{yy}$, thus $E = 0$, and the Hamiltonian reduces to,

$$\hat{H}_{\text{Anisotropy}} = D\hat{S}_z^2 \quad (1.7)$$

The energies of the spin multiplets are therefore given in terms of D and M_S as,

$$E(M_S) = DM_S^2 \quad (1.8)$$

The $2S + 1$ levels are readily split in the absence of an external field, and hence the term, zero field splitting (ZFS). For a negative D , the $M_S = \pm S$ are the lowest states in energy, and the spin has a preferential orientation, or an easy axis orientation

(Figure 1.3). The potential energy of a classical spin under a uniaxial anisotropy with a negative D is shown in Figure 1.4 (a). The lowest energy is obviously along the $\pm z$ direction (up or down), which quantum mechanically corresponds to the lowest M_S states $\pm S$. The x and y direction are equivalent in an axial symmetry as seen from the potential energy. Lowering the symmetry from axial, leads to a non-zero E term which describes the anisotropy in the xy plane. The x and the y direction are no longer equivalent. This is depicted in Figure 1.4 (b). Typically, the x is the called intermediate, and y is the hard axis. The inclusion of an E term therefore leads to, lifting the degeneracy between the $+M_S$ and $-M_S$ states (for integer spins). This is accompanied by the mixing of the eigenstates of the system. The E term mixes states differing in M_S by ± 2 . This mixing has a pronounced effect on the relaxation of the magnetization and the phenomenon of quantum tunneling as described below.

The above Hamiltonians are adequate for systems with axial or rhombic symmetry. In reality, systems may have lower symmetries or they can be slightly distorted, so that the energy levels are affected by these distortions, and can not be simply reproduced with the above Hamiltonians. In addition to second order spin components, one may have to add fourth, or sixth order terms to properly describe the energy diagram of the system. A commonly used approach is the extended Steven's operators system,

$$\mathbf{H}_{\text{Anisotropy}} = \sum_{N,k} B_N^k \hat{O}_N^k \quad (1.9)$$

where the sum runs over $N = 2, 4, 6, \dots, 2S$; and the integer k satisfies $-N \leq k \leq N$. B_N^k are the anisotropy parameters, and the \hat{O}_N^k are the Steven's operators (tabulated in [13]). In principle, the crystal field symmetry determines the terms which are included in the spin Hamiltonian. For orthorhombic symmetry, the fourth order terms, B_4^0 , B_4^2 , and B_4^4 have non-zero values. For tetragonal symmetry, only B_4^0 , and B_4^4 have nonzero values. Quite often, the spin Hamiltonian for the single ion anisotropy is written as,

$$\hat{H}_{\text{Anisotropy}} = D[\hat{S}_z^2 - \frac{1}{3}S(S+1)] + B_4^0 \hat{O}_4^0 + E(\hat{S}_x^2 - \hat{S}_y^2) + B_4^2 \hat{O}_4^2 + B_4^4 \hat{O}_4^4 \quad (1.10)$$

where $D = 3B_2^0$, and $E = B_2^2$. The B_4^0 is the fourth order axial term, have the same function as D . The B_4^4 , on the other hand, mixes M_S states differing by ± 4 .

The above discussion is valid for a single ion. SMMs are magnetic clusters which compromise several single ions coupled together via the exchange interaction. The dimensions of the microscopic Hamiltonian that describes the coupling between n spins s is $(2s+1)^n$. In the Fe_8 cluster for example, this is around 10^6 . In order to deal with such big systems, one exploits the fact that only the low lying states are important at low temperatures. One particular approximation is the giant spin model (GSM), which takes into account only the total spin ground state of the system, considering that the excited states are much higher in energy. This approximation is only valid in the strong exchange limit ($J \gg D$), as we demonstrate in two nice examples in Chapter 3 and 5. The giant spin Hamiltonian is expressed as (1.10), with the spin operators of the giant spin employed rather than those of the single-ion. Besides that, the spin Hamiltonian parameters, are those which describe the coupled spin, and they are given as a linear combination of the single ion parameters [14].

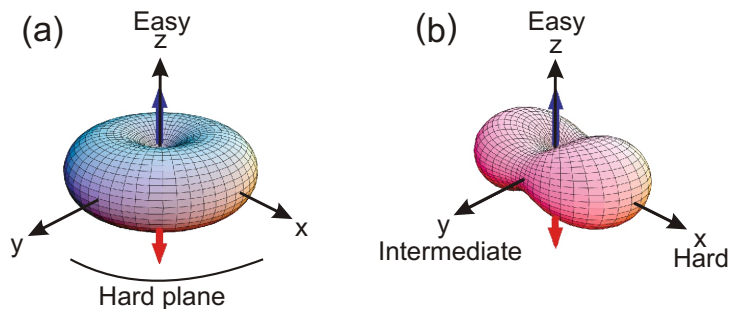


Figure 1.4: (a) The classical potential energy of a spin experiencing a uniaxial crystal field with negative D , and (b) the same in addition to a transverse second-order term E (after [15]).

1.3 Slow relaxation of the magnetization

The key for understanding the relaxation of the magnetization lies in the double-well potential describing the energy levels of the spin ground state (Figure 1.3). A molecule in the left well with spin down ($M_S = -S$) for instance, can invert its spin orientation in two ways: 1- by thermal relaxation over the barrier; 2- by tunneling through the barrier. The latter is discussed in the next section. The spin can thermally overcome the barrier, by absorbing phonons, and thus climbing the spin ladder to the other side of the well. Phonon-induced transitions are allowed for $\Delta M_S = \pm 1, \pm 2$. Consequently, a molecule can flip its spin only if it possesses enough thermal energy to overcome the barrier $U = DS^2$ (or $DS^2 + B_4^0 S^4$ for non-zero B_4^0). At low temperatures, the molecule lacks the adequate thermal energy to overcome the barrier, and therefore the spin orientation is frozen. For an ensemble of spins, the relaxation time is given by the Arrhenius law as,

$$\tau = \tau_o e^{U/k_b T} \quad (1.11)$$

where τ_o is the inverse of the attempt frequency (the transition rate between individual M_S levels). At high temperatures, the spins rapidly fluctuate. As the system is cooled down, the fluctuations slow down, i.e. the relaxation time τ gets longer. The system appears to be static, when τ becomes much longer than the time scale of the particular experiment used to measure its value. The temperature at which these fluctuations "freeze out", which is also known as the blocking temperature, depends on our definition of how much τ should be longer than the measurement time. AC susceptibility, which is frequently used to study the magnetization relaxations in SMMs, typically probes the time scale between $10^{-1} - 10^{-5}$ seconds (1 Hz - 100 kHz).

1.4 Quantum tunneling in molecular clusters

Among all successes of quantum mechanics during its infancy in the early 30's, none was more impressive than the tunneling effect. Tunneling occurs in all quantum systems.

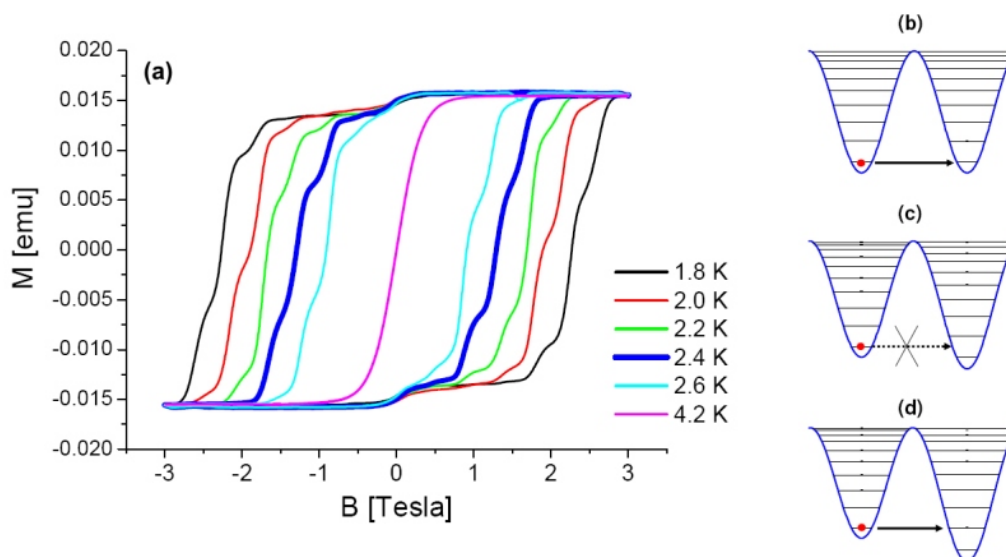


Figure 1.5: (a) Hysteresis curves of a Mn_{12} -acetate single crystal at different temperatures with an axially applied magnetic field. The steps indicate the relative change in magnetization upon tunneling. The energy levels of the different M_S states corresponding to zero field tunneling, off resonance condition, and tunneling to excited states are shown in (b), (c), and (d), respectively.

The experimental observation of tunneling revealed the beauty of quantum physics and paved the way for its practical applications after being a purely theoretical field of research for a long period. Perhaps the most renowned application of quantum tunneling is scanning tunneling microscopy (STM), where an electron can tunnel from one metal to the other through vacuum (potential barrier). This is experimentally realized by monitoring a current between a metallic tip few nm above a metallic surface under an externally applied bias voltage. Tunneling of the spins in molecular clusters obeys the same quantum mechanical principles, even though the entity that tunnels is not the same. In these systems, the coupled spin of a molecule tunnels from one spin state to another again through an energy barrier. This relatively new form of tunneling breaks some new ground as it involves macroscopic objects, considering that the tunneling spins are coupled spins, with a large number of electrons. In 1995, Jonathan Friedman and his collaborators observed steps in the hysteresis curves (as the one shown in Figure 1.5 (a)) in Mn_{12} -acetate at temperatures between 1.7 and 3 K. These steps were the first direct evidence to the quantum tunneling of the magnetization (QTM). Mn_{12} -acetate, and molecular magnets in general, have large spin ground state, which makes them on the boundary between microscopic and mesoscopic spin systems ($\mu \sim 10^3 \hbar$). The larger the spin, of course, the less restrictive is the orientational quantization of the angular momentum. In the classical limit, a spin can point in any direction. Therefore, the observation of quantum tunneling in such molecular clusters with high spins may help in elucidating the long-standing problem of how, quite generally, nature arranges the transition between the quantum and classical realms.

In general, in order for tunneling to be observed, three main conditions have to

coexist: (i) there should be an overlap between the wave functions of the initial, and the final state, between which the system tunnels; (ii) these two states must be degenerate in energy²; (iii) an observable which indicates that the system has tunneled should be experimentally monitored. To illustrate the process of quantum tunneling in single-molecule magnets, let us consider the following spin Hamiltonian,

$$\hat{H} = D\hat{S}_z^2 + E(\hat{S}_x^2 - \hat{S}_y^2) + g\mu_B(\hat{S}_x B_x + \hat{S}_y B_y + \hat{S}_z B_z) \quad (1.12)$$

In the absence of any transverse anisotropy and at zero applied magnetic field, the energies of the system are given by (1.8), where $E(M_S) = E(-M_S)$, and we have the typical double well potential picture as shown in Figure 1.3. The eigenstates of the system are given by the eigenvectors $|M_S\rangle$ of the S_z operator. At low temperatures, the spin of the molecule occupies the ground state $|M_S\rangle$ or $| -M_S\rangle$, and it is localized with zero probability to tunnel to the other side of the well. For a finite transverse anisotropy, the S_z eigenvectors are not the energy eigenstates. Rather, $E \neq 0$ gives rise to a mixing of states $|M_S\rangle$ and $|M_S \pm 2\rangle$, and it lifts the degeneracy of the M_S and $-M_S$ states. For an $S = 1$ system for instance, the transverse anisotropy lifts the degeneracy between $|+1\rangle$ and $| -1\rangle$ states. The energy eigenstates are $|0\rangle$, and $|e_{\pm}\rangle = (|+1\rangle \pm |-1\rangle)/\sqrt{2}$ of energies $E_0 = 0$ and $E_{\pm} = -D \pm 2E$, respectively. At low temperatures, the system now simultaneously occupies the two eigenstates $|e_{\pm}\rangle$, and there is an equal probability of finding the system on either side of the well (i.e. with spin up or spin down). In a dynamic picture, the system oscillates between the two states at a frequency given by Δ/\hbar , where $\Delta = E_+ - E_-$, is the separation in energy between the two states, and is also called the tunnel splitting. Note that the transverse term mixes the two states only if they are degenerate (or very close in energy $E_+ - E_- < \Delta/2$), hence the second condition to observe tunneling. For systems with $S > 1$, the transverse term does not only lead to a mixing of states $\pm|M_S\rangle$ on opposite sides of the anisotropy barrier, but rather the eigenstates are complicated superpositions of several states. An externally applied transverse field (B_x) can have a similar effect to that of E by introducing a perturbation which does not commute with S_z , thus mixing the eigenstates of the system.

The tunneling through the barrier is accompanied by a spin flip. It is therefore reflected in the magnetization curves at low temperatures. The hysteresis curve of a SMM is not smooth as that of a ferromagnet and it shows steps in the magnetization at certain external field values. Figure 1.5 (a) shows a magnetic hysteresis curve of a Mn_{12} -acetate single crystal at various temperatures under the effect of an axial field. Above 2 Tesla, the magnetization is saturated, and all the spins are on one side of the well (only the $M_S = -10$ is occupied). As the field is decreased, the magnetization remains constant until zero field, where the -10 and the $+10$ states are degenerate (Figure 1.5 (b)), and some of the spins can tunnel through the barrier from the -10 to the $+10$ state. This is accompanied by a step in the magnetization at zero field. As the field is increased further, the occupied M_S states on opposite sides of the barrier are off resonance again (Figure 1.5 (c)), and a plateau is observed in the magnetization. This steady value of the magnetization persists until the resonance condition is satisfied

²In fact we will see that they are not exactly degenerate but separated by a small energy splitting.

at a finite axial field (Figure 1.5 (d)), and once again a step in the magnetization is observed indicating that the few spins have tunneled.

QTM therefore strongly affects the relaxation process of the magnetization. In the presence of quantum tunneling, the relaxation time can still be described by the Arrhenius law (1.11) with a modified energy barrier. The barrier is replaced by an effective energy barrier U_{eff} , which accounts for under barrier relaxation induced by tunneling, thus, U_{eff} is smaller than U . In practice, a temperature independent tunneling rate (which is observed at low temperatures) is considered as a signature of ground state quantum tunneling.

1.5 Experimental techniques

Since the early 1990s, an increasing number of experimental techniques have been used to characterize molecular magnetic clusters. Many of them, have been in particular used to study the magnetic anisotropy in these classes of materials. These techniques are mainly divided into two groups, resonant or spectroscopic techniques such as ESR, FDMRS, INS; and non-resonant techniques such as magnetometry (SQUID, VSM, micro-Hall probes, etc...), torque magnetometry, and ac susceptometry. A third, less common group, is one which involves a combination of resonant and non-resonant techniques simultaneously. Chapter 2 gives a detailed description of cantilever torque magnetometry, while the Chapter 7 describes the torque detected broad band ESR method that we have developed. In this section, we briefly introduce the other experimental techniques which were used in this work.

1.5.1 Standard magnetometry

Superconducting QUantum Interferometer Device (SQUID) is the most commonly used magnetometer to characterize magnetic materials. It is not within our scope to cover the theory of operation of SQUID magnetometers and the reader is referred to a specialized text [16]. Typical experimental capabilities for commercial SQUID magnetometers are temperatures between 1.8 and 400 K, and magnetic fields up to 7 Tesla. Due to their sensitivity to the external field, commercial SQUIDs are limited by this upper field value. The other less sensitive alternative to SQUIDs, is the vibrating sample magnetometer (VSM) which can be equipped with magnets producing fields over 10 Tesla. In a VSM, the sample is moved at a frequency of 50-100 Hz up and down over a length of a few mm in a pickup coil. The induced current measured in the coil is related to the magnetization of the sample. In general, two types of magnetic measurements are performed: (i) the magnetic moment versus temperature at a fixed external field; or (ii) the magnetic moment versus field at a fixed temperature. The former can give an estimate of the isotropic exchange coupling in systems where the exchange interaction is the dominant term in the Hamiltonian (strong exchange). The ZFS become important at low temperatures where they could modify the susceptibility values. The measurement of the magnetic moment vs field yields can give the spin ground state of

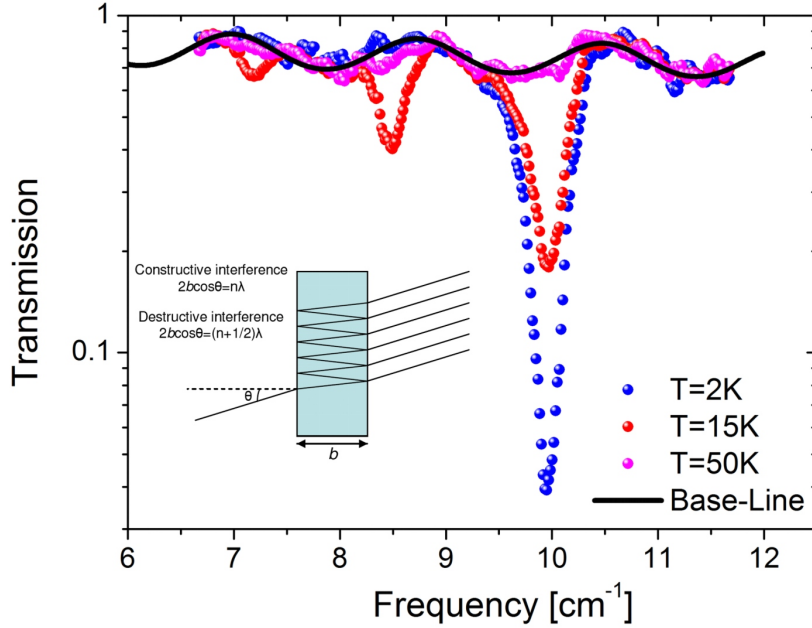


Figure 1.6: FDMRS on a Mn_{12} -Pivalate powder pellet showing 3 resonance lines between the ± 10 to ± 9 , ± 9 to ± 8 , and ± 8 to ± 7 M_S states at 9.96, 8.49, and 7.16 cm^{-1} , respectively [5]. The inset illustrates the oscillations within the plane parallel pellet leading to constructive and destructive oscillations which cause the oscillation of the baseline (see text).

the system in case it is well isolated in energy from the spin excited states, and it also yields the g value. Measurements of the magnetization of single crystals along different orientations may give good estimates for the strength and the sign of the magnetic anisotropy in the system.

1.5.2 Frequency domain magnetic resonance spectroscopy

Frequency domain magnetic resonance spectroscopy (FDMRS) is a frequency swept electron spin resonance (ESR) technique. The technique was originated by Richards and co-workers in the late 60s, who used an infrared Michelson interferometer [17] to determine ZFS parameters of systems not amenable to studies by conventional ESR. Unlike conventional ESR spectrometers, FDMRS can detect magnetic resonance transitions in the absence of an externally applied magnetic field. This is practically done by sweeping the frequency of the microwave radiation rather than the external field. An absorption of the microwave radiation is observed at the resonance condition,

$$\hbar\omega = \Delta E \quad (1.13)$$

where ω is the angular frequency of the microwave radiation, and ΔE is the energy difference between the two spin states involved in the transition. The observed transitions are governed by the selection rules, $\Delta S = 0$, and $\Delta M_S = \pm 1$. The technique

is not limited to zero external fields but one may also perform a transmission measurement at a fixed finite field (0-8 Tesla in our spectrometer). The principle of the technique is fairly simple, the microwave radiation is transmitted through a sample and the transmitted intensity is monitored. At the resonance frequency, an absorption line is observed which is reflected as a drop in the transmitted intensity. Figure 1.6 shows typical FDMRS spectra recorded on a Mn_{12} -Pivalate pellet at different temperatures [5]. The absorption lines correspond to the lowest three magnetic resonance transitions within the $S = 10$ ground state. Figure 1.7 shows a schematic drawing of the FDMRS spectrometer used. The practical importance of this method lies in the tunable frequency sources in the range ($1\text{-}48\text{ cm}^{-1}$), the Backward Wave Oscillators (BWOs). BWOs are electrovacuum devices, placed in a magnetic field and supplied with a high voltage to emit a linearly polarized monochromatic electromagnetic radiation. The radiation has high intensity ($\sim 10\text{ mW}$), high monochromaticity ($\Delta f/f \simeq 10^{-5}$), and high degree of polarization (99.9%). Leaving the BWO source, the radiation propagates through free space, where it is directed onto the sample and after that onto the detector (Golay Cell) by the aid of several polyethylene or Teflon lenses. For zero-field measurements, a homemade helium bath cryostat ($T=1.5\text{-}300\text{ K}$) was used, and for zero or in-field measurement ($T= 1.5\text{-}300\text{ K}$, $H = 0\text{-}7\text{ T}$) an Oxford Instruments Spectromag 4000 with a split-coil superconducting magnet was used. Both Voigt ($\mathbf{q} \perp \mathbf{B}_{ext}$) and Faraday ($\mathbf{q} // \mathbf{B}_{ext}$) geometries can be used (where \mathbf{q} is the wave-vector, and \mathbf{B}_{ext} is the external applied magnetic field). The propagation of the radiation through free space and the absence of a microwave cavity renders this technique much less sensitive than a conventional ESR technique. This disadvantage makes it difficult to study small single crystals and one has to usually study a polycrystalline powder sample pressed into a pellet. The fact that the sample is a slab of parallel faces with a finite thickness b results in a Fabry-Pérot like interference pattern (apparent in the baseline which results from constructive and destructive interferences of the radiation (Figure 1.6)). The interference pattern leads to oscillation in the baseline of the transmission spectrum. For normal incidence, the condition for constructive interference is satisfied whenever the wavelengths or its integer multiple is equal to $2b$, and destructive interference occurs whenever $2b$ is equal to half integer of the wavelengths. The technique is suited for the study of any type of magnetic excitations, such as the magnetic properties of paramagnetic ions, and of exchange coupled clusters in general, and single-molecule magnets in particular [18].

1.5.3 Inelastic neutron scattering

Neutrons have been found to be very useful in studying magnetism in condensed matter. The neutron is a spin $1/2$ particle and has a non-zero magnetic moment. Thermal neutrons have wavelengths which are comparable to atomic spacings, thus permitting diffraction measurements to be performed. In an elastic neutron scattering experiment, the neutrons are elastically scattered off the nuclei of the atoms to produce Bragg reflections, thus enabling structural studies. Due to their finite magnetic moment, the neutrons scatter on atomic magnetic moments as well, via the electromagnetic interactions, which makes them suitable to investigate magnetic structure and ordering. On

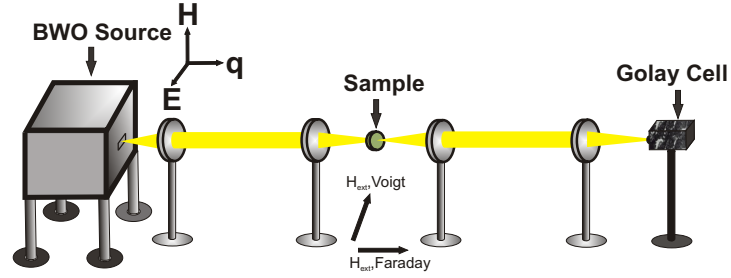


Figure 1.7: Schematic drawing of the FDMRS setup.

the other hand, in an inelastic neutron scattering experiment, the incident and the scattered neutrons have different energies corresponding to different wave-vectors. The neutron produces an excitation of energy $\hbar\omega$ and wave-vector \mathbf{q} in the sample. Conservation of energy and momentum implies that: $E_0 = E_1 + \hbar\omega$ and $\mathbf{k}_0 = \mathbf{k}_1 + \mathbf{q}$, where (E_0, \mathbf{k}_0) and (E_1, \mathbf{k}_1) are the energy and wave-vector of the incident and scattered neutron, respectively. Hence, a measurement of E_0 , E_1 , \mathbf{k}_0 , and \mathbf{k}_1 allows the determination of ω and \mathbf{q} . The neutrons are therefore used to induce magnetic resonance transitions between spin states differing in energy by $\hbar\omega$ in molecular magnets. The selection rules obeyed are different from those of ESR, and are given by, $\Delta S = 0, \pm 1$ and $\Delta M_S = 0, \pm 1$. This gives the technique the advantage of probing excitations between different spin multiplets, hence the possibility to investigate isotropic exchange interactions. Another advantage to ESR, is that the intensity is dependent on the population of the initial state only, whereas in magnetic resonance techniques it is the population difference between initial and final states which governs the intensity. Neutrons have energies which range from the meV to the eV range. Thus energy scales from μeV to eV transitions can be probed. The possibility of tuning the energy of neutrons, and the fact that the energy difference is probed, eliminate the necessity of applying an external field as in the case of FDMRS. The disadvantage of INS lies in its low sensitivity making it essential to use large amounts of powders since big enough single crystals of molecular magnets are very rare. In addition, the technique is very expensive in terms of time and money. We do not intend to give a full description of INS here, interested readers can refer to a review [19], where the technique and its application in molecular magnetism were recently reviewed.

1.6 Modeling Methods

In this section, we introduce basic quantum mechanical concepts to illustrate the procedure followed in the self-written software developed as part of this PhD project to perform most of the calculations and modeling of the magnetic data shown through out this Thesis. The software was written in Mathematica. This section is by no means to be considered as a sufficient background for quantum mechanical calculations on molecular clusters. For that we suggest the following references [20][21].

In order to evaluate the thermodynamic observables of the system which describe its magnetic properties, one has to first calculate the magnetic energy spectrum. The spin Hamiltonian of the system shall be expressed in terms of the different interactions that can influence the energy of the spin system. As discussed previously, for the majority of molecular magnetic systems, the interaction between the single-ion magnetic moments can be rather well described by the Heisenberg model with isotropic exchange interaction, an additional anisotropy term, and a Zeeman term in the presence of an external magnetic field. Other interactions, such as intermolecular dipolar interactions, antisymmetric exchange, or spin-phonon coupling terms can be also added to the Hamiltonian depending on the system under consideration.

1.6.1 Spin angular momentum

The spin angular momentum operator can be described as a vector $\hat{\mathbf{S}}(\hat{S}_x, \hat{S}_y, \hat{S}_z)$ where the three components can be expressed in terms of the Pauli spin matrices as,

$$\hat{S}_x = \frac{1}{2} \begin{pmatrix} 0 & 1 \\ 1 & 0 \end{pmatrix} \quad \hat{S}_y = \frac{1}{2} \begin{pmatrix} 0 & -i \\ i & 0 \end{pmatrix} \quad \hat{S}_z = \frac{1}{2} \begin{pmatrix} 1 & 0 \\ 0 & -1 \end{pmatrix} \quad (1.14)$$

This mathematical representation of the spins describes the intrinsic spin property where the spin angular momentum is limited to $2S + 1$ quantized values along a particular axis ($S, S - 1, \dots, -S$) (Note that we follow the convention that the angular momentum is measured in the units of \hbar). In addition, the magnitude of the total spin angular momentum is given by $\sqrt{S(S + 1)}$. The angular momentum is by convention quantized along the z-axis and its projection is defined by the parameter m_s . There is nothing particular about the z axis besides its simple representation. If the electron spin is therefore pointing along the z-axis³, the two eigenstates corresponding to the spin being parallel (up) or antiparallel (down) to the z axis are given by [10],

$$\begin{aligned} |\uparrow_z\rangle &= \begin{pmatrix} 1 \\ 0 \end{pmatrix} \\ |\downarrow_z\rangle &= \begin{pmatrix} 0 \\ 1 \end{pmatrix} \end{aligned} \quad (1.15)$$

The \hat{S}_z operator applied on the above eigenstates will therefore give us the corresponding angular momentum value m_s of $\pm\frac{1}{2}$,

$$\begin{aligned} S_z |\uparrow_z\rangle &= \frac{1}{2} |\uparrow_z\rangle \\ S_z |\downarrow_z\rangle &= -\frac{1}{2} |\downarrow_z\rangle \end{aligned} \quad (1.16)$$

³Note that we can equally take the spin to be along the x- or the y-axis but keeping in mind that the corresponding eigenstates are different [22].

1.6.2 Hilbert space representation

The spin Hamiltonian can be mathematically expressed in terms of the spin operators. Once the Hamiltonian is written, the energy spectrum can be obtained by performing exact diagonalization of the Hamiltonian. This process can be easily performed for simple systems but as soon as the dimension of the Hilbert space escalates, the problem starts to be difficult to be solved by current computers. For N coupled spins each with a spin S , the dimension of the Hilbert space is given by $(2S + 1)^N$. The dimension of the Hilbert space is equivalent to the number of eigenstates of the system or the basis. For example, for a single spin $\frac{1}{2}$ ($N = 1$; $S = \frac{1}{2}$), the dimension of the Hilbert space is 2 and it corresponds to the two eigenstates namely: spin $|\uparrow\rangle$ and spin $|\downarrow\rangle$. For more than one spin, the dimension of the Hilbert space changes and consequently the single spin operators have to be redefined in the extended Hilbert space. To elucidate this, let us take the example of a two spin system (a Cu^{2+} dimer for instance) each with $S = 1/2$. The dimension of the Hilbert space in this case is 2^2 and the basis of the system can be written as,

$$\begin{aligned} |\uparrow\downarrow\rangle &= \begin{pmatrix} 1 \\ 0 \\ 0 \\ 0 \end{pmatrix} & |\uparrow\uparrow\rangle &= \begin{pmatrix} 0 \\ 1 \\ 0 \\ 0 \end{pmatrix} \\ |\downarrow\uparrow\rangle &= \begin{pmatrix} 0 \\ 0 \\ 1 \\ 0 \end{pmatrix} & |\downarrow\downarrow\rangle &= \begin{pmatrix} 0 \\ 0 \\ 0 \\ 1 \end{pmatrix} \end{aligned} \quad (1.17)$$

where the first arrow in the bracket notation stands for spin number one and the second arrow stands for spin number two. The spin operator of the individual spin must therefore act on one spin but not the other. In other words \hat{S}_{1_i} must act only on spin 1 and likewise \hat{S}_{2_i} on spin 2. This can be achieved by constructing a new spin operator $\hat{S}_{1(2)_i}$ which is the tensor product of \hat{S}_i and the identity matrix I . The \hat{S}_{1_z} and \hat{S}_{2_z} for the two spin $\frac{1}{2}$ system are given by,

$$\begin{aligned} \hat{S}_{1_z} &= S_z \otimes I \\ \hat{S}_{2_z} &= I \otimes S_z \end{aligned} \quad (1.18)$$

substituting for \hat{S}_z from Eq. 1.14 we get,

$$\hat{S}_{1_z} = \frac{1}{2} \begin{pmatrix} 1 & 0 & 0 & 0 \\ 0 & 1 & 0 & 0 \\ 0 & 0 & -1 & 0 \\ 0 & 0 & 0 & -1 \end{pmatrix} \quad (1.19)$$

Applying \hat{S}_{1_z} on the different states of Eq. 1.17 we get,

$$\begin{aligned}
 \hat{S}_{1_z}|\uparrow\uparrow\rangle &= \frac{1}{2}|\uparrow\uparrow\rangle \\
 \hat{S}_{1_z}|\uparrow\downarrow\rangle &= \frac{1}{2}|\uparrow\downarrow\rangle \\
 \hat{S}_{1_z}|\downarrow\uparrow\rangle &= -\frac{1}{2}|\downarrow\uparrow\rangle \\
 \hat{S}_{1_z}|\downarrow\downarrow\rangle &= -\frac{1}{2}|\downarrow\downarrow\rangle
 \end{aligned}
 \tag{1.20}$$

We can directly see that \hat{S}_{1_z} acts only on the first spin with eigenvalue returned corresponding to the state of spin 1 irrespective of the state of spin 2. This can be generalized as well to other spin operators like the raising and the lowering operators. In that particular case, the \hat{S}_{j+} (\hat{S}_{j-}) operator will raise (lower) the corresponding spin j leaving the other spins unaltered.

The spin operator can be written in a more general form

$$\hat{S}_{j_z} = \underbrace{\dots I \otimes I \otimes \hat{S}_z \otimes I \otimes I \dots}_N
 \tag{1.21}$$

where \hat{S}_z is placed in the j th position.

1.6.3 Choice of the quantization axis

The orientation of the quantization axis is particularly important in the presence of more than one orientation dependent interaction. For instance, when there is a co-existence of the Zeeman and single ion anisotropy terms which is often the case in molecular magnets. The quantization axis can therefore be assigned along the magnetic field direction or along the easy axis of the molecule (c-axis). The choice of the quantization axis depends on the particular example under consideration. In the following, we discuss several possibilities of describing different spins systems and end up by concluding which case is mostly used through out this Thesis. For the sake of simplicity we consider an isotropic g and J values which will be omitted together with the μ_B in the following discussions. As defined previously, the anisotropy tensor is taken by convention to be diagonal where the z , y , and x lie along the easy, intermediate, and hard axis respectively. If the quantization axis is taken to be along the c axis (the easy axis), the eigenstates can be described by $|S, M_s\rangle$ at zero magnetic field or for the field being applied parallel to the c axis. For transverse fields, the eigenstates get admixed by the field and they are no longer described by the pure $|S, M_s\rangle$ states. In some cases where the magnetic anisotropy is weak ($D \ll J$), it may be convenient to take the quantization axis along the direction of the magnetic field. The levels can then be described by $|S, M_s\rangle$ for a finite magnetic field, irrespective of the direction of the field.

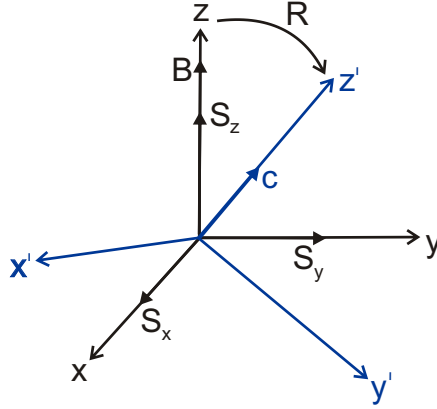


Figure 1.8: Orientation of the different spin operators, with the quantization axis taken along the external field \mathbf{B} . \mathbf{c} is the easy axis of the molecule oriented along z' , and xyz is rotated into $x'y'z'$ using \mathbf{R} .

Quantization axis along the field

Let us consider the case of a single spin \mathbf{S} with an external applied magnetic field (analogous to the giant spin model). The terms in the Hamiltonian reduce to the Zeeman and the anisotropy term.

Figure 1.8 shows a schematic drawing of the corresponding orientations of the spin vector and the external magnetic field having the quantization axis along the external field. Irrespective of the orientation of the field, the Zeeman term is always given by,

$$\mathbf{H}_{Zeeman} = \mathbf{B} \cdot \mathbf{S}_z \quad (1.22)$$

The anisotropy term is however more complicated, and it can be expressed as

$$\mathbf{H}_{Anisotropy} = \mathbf{S}' \cdot \mathbf{D} \cdot \mathbf{S}'_T \quad (1.23)$$

where \mathbf{D} is the anisotropy tensor defined in the $x'y'z'$ system of coordinates (The subscript T in \mathbf{S}'_T is used to denote the transpose of the vector \mathbf{S}'). In order to calculate the anisotropy term $\mathbf{H}_{anisotropy}$, we need to calculate the S'_x , S'_y , and S'_z which are the components of the spin vectors along x' , y' , and z' respectively as a function of S_x , S_y , and S_z . One should bear in mind that \mathbf{S}' has the same basis as \mathbf{S} and it is calculated in terms of the \mathbf{S} vector components S_x , S_y , and S_z . Let us consider \mathbf{R} as the rotation matrix that rotates the spin from the xyz to the $x'y'z'$ system of coordinates. The relation between the two spin matrices can be written as

$$\begin{aligned} \mathbf{S}' &= \mathbf{S} \cdot \mathbf{R} \\ \mathbf{S}'_T &= \mathbf{R}_T \cdot \mathbf{S}_T \end{aligned} \quad (1.24)$$

Inserting this into Eq. 1.23 we get,

$$\mathbf{H}_{Anisotropy} = \mathbf{S} \cdot \mathbf{R} \cdot \mathbf{D} \cdot \mathbf{R}_T \cdot \mathbf{S}_T \quad (1.25)$$

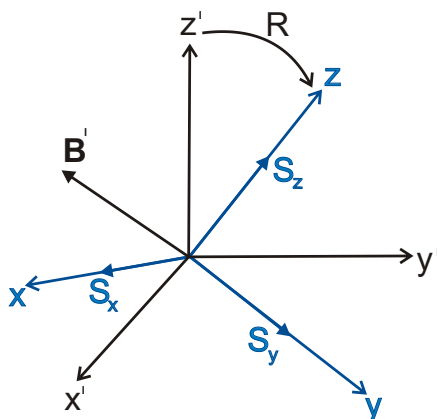


Figure 1.9: Orientation of the different spin operators, with the quantization axis taken along the easy axis of the molecule which is oriented along z -axis in the xyz frame of reference. The magnetic field B' is applied in the $x'y'z'$. R is a rotation matrix that rotates $x'y'z'$ into xyz .

This term can be easily expanded depending on \mathbf{R} , and the specific anisotropy tensor in the system. Similarly, this term can be written as $\mathbf{S} \cdot \mathbf{D}' \cdot \mathbf{S}_T$ where $\mathbf{D}' = \mathbf{R} \cdot \mathbf{D} \cdot \mathbf{R}_T$ is the anisotropy tensor defined in the (xyz) system of coordinates. \mathbf{R}_T is the inverse of the rotation matrix \mathbf{R} . However, \mathbf{D}' is not ideally the parameter of interest as it is not directly related to the molecular coordinates (or the molecular structure).

Quantization axis along the easy axis

Single Spin S

We start by taking the simple case of a single spin with the quantization axis being along the easy molecular axis (Figure 1.9). The $x'y'z'$ is the laboratory frame of reference and without loss of generality, we can take the magnetic field B' to be in the $x'z'$ plane. This is particularly important for calculating the torque as discussed later in this section. There are two equivalent approaches to describe the Hamiltonian. The first one is by rotating the magnetic field B' into B in the xyz system of coordinates ($\mathbf{B} = \mathbf{B}' \cdot \mathbf{R}$). The Zeeman term is then given by,

$$\mathbf{H}_{Zeeman} = \mathbf{B}_x \cdot \mathbf{S}_x + \mathbf{B}_y \cdot \mathbf{S}_y + \mathbf{B}_z \cdot \mathbf{S}_z \quad (1.26)$$

On the other hand, the anisotropy can be easily expressed as

$$\mathbf{H}_{Anisotropy} = \mathbf{S} \cdot \mathbf{D} \cdot \mathbf{S}_T = DS_z^2 \quad (1.27)$$

The second way of mathematically doing that is by calculating the corresponding spin angular momentum components in the $x'y'z'$ plane. The rotated spin components are given by,

$$\begin{aligned} \mathbf{S}' &= \mathbf{S} \cdot \mathbf{R}_T \\ \mathbf{S}'_T &= \mathbf{R} \cdot \mathbf{S}_T \end{aligned} \quad (1.28)$$

The anisotropy and the Zeeman terms written in the $x'y'z'$ system of coordinates as,

$$\begin{aligned}\mathbf{H}_{Zeeman} &= \mathbf{B}' \cdot \mathbf{S}' = \mathbf{B}'_x \cdot \mathbf{S}'_x + \mathbf{B}'_y \cdot \mathbf{S}'_y + \mathbf{B}'_z \cdot \mathbf{S}'_z = \mathbf{B} \cdot \mathbf{S} \\ \mathbf{H}_{Anisotropy} &= \mathbf{S}' \cdot \mathbf{D}' \cdot \mathbf{S}'_T = \mathbf{S} \cdot \mathbf{D} \cdot \mathbf{S}_T = DS_z^2\end{aligned}\quad (1.29)$$

\mathbf{D}' is the rotated anisotropy tensor in the $x'y'z'$ frame of references. Both approaches lead to the same expression of the Hamiltonian and one can use either one of them. We choose to use the former as it is more convenient to rotate the field rather than the spin matrices.

System with two spins S_1 and S_2

In case of more than one spin, the Heisenberg term is added to the Hamiltonian which describes the interaction between the spins. The anisotropy and the Zeeman term can be handled as in the case of a single spin. We take the quantization axes to be along the easy axes of the individual molecules. Again care must be taken in choosing the basis which we take as the spin matrices in the local molecular frame of reference. If the two interacting spins have their easy axes along the same direction, then the problem is relatively easy and the Heisenberg term is expressed as

$$\mathbf{H}_{Heisenberg} = \mathbf{S}_1 \cdot \mathbf{S}_{2T} = \mathbf{S}_{1x} \cdot \mathbf{S}_{2x} + \mathbf{S}_{1y} \cdot \mathbf{S}_{2y} + \mathbf{S}_{1z} \cdot \mathbf{S}_{2z} \quad (1.30)$$

If the easy axes of the two molecules are not oriented along the same direction, then the Heisenberg term has to be calculated by rotating either one of the two spins into the system of coordinates of the other. Consider the orientation of the spins shown in Figure 1.10, the Heisenberg term can be expressed as,

$$\begin{aligned}\mathbf{H}_{Heisenberg} &= \mathbf{S}_1'' \cdot \mathbf{S}_{2T} \\ &\text{or} \\ \mathbf{H}_{Heisenberg} &= \mathbf{S}_1 \cdot \mathbf{S}'_{2T}\end{aligned}\quad (1.31)$$

where S_1'' is the spin S_1 rotated in the S_2 spin system of coordinates ($x''y''z''$) and S'_2 is the spin S_2 rotated in the S_1 system of coordinates ($x'y'z'$). R is the rotation matrix which rotates $x'y'z'$ into the $x''y''z''$; the spin matrices can be written as,

$$\begin{aligned}\mathbf{S}_1'' &= \mathbf{S}_1 \cdot \mathbf{R} \\ \mathbf{S}'_2 &= \mathbf{S}_2 \cdot \mathbf{R}_T \\ \mathbf{S}'_{2T} &= \mathbf{R} \cdot \mathbf{S}_{2T}\end{aligned}\quad (1.32)$$

Substituting these terms into Eq. 1.31 we see that the two terms are equal,

$$\begin{aligned}\mathbf{S}_1'' \cdot \mathbf{S}_{2T} &= \mathbf{S}_1 \cdot \mathbf{R} \cdot \mathbf{S}_{2T} \\ \mathbf{S}_1 \cdot \mathbf{S}'_{2T} &= \mathbf{S}_1 \cdot \mathbf{R} \cdot \mathbf{S}_{2T}\end{aligned}\quad (1.33)$$

To conclude, a system with two or more spins can be treated by taking the quantization axes along the corresponding individual easy molecular axes. The anisotropy terms are calculated in the local frame of reference, the magnetic field is rotated into the local coordinates to calculate the Zeeman terms, and the Heisenberg terms are obtained by calculating the spin components of one spin in the frame of reference of the other.

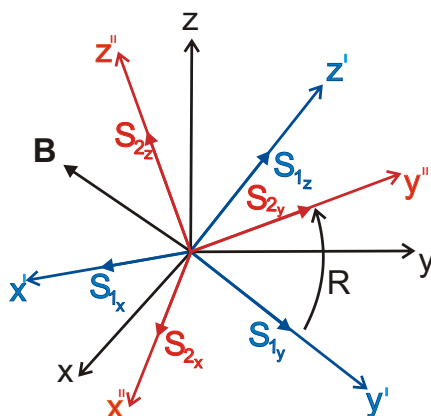


Figure 1.10: Orientation of the different spin operators of the spin 1 and 2 in the $x'y'z'$ and $x''y''z''$ frames of reference respectively. The quantization axes are taken along the easy axes of both spins in the local coordinates, and the magnetic field is applied in the xyz plane. R is a rotation matrix that rotates $x'y'z'$ into $x''y''z''$.

The spin Hamiltonian of two interacting spins in an external magnetic field with the orientations described in Figure 1.10 is,

$$\mathbf{H} = D_1 S_{z_1}^2 + D_2 S_{z_2}^2 + \mathbf{B}_1 \cdot \mathbf{S}_1 + \mathbf{B}_2 \cdot \mathbf{S}_2 + \mathbf{S}_1 \cdot \mathbf{S}_2 \quad (1.34)$$

In most torque measurements, the situation is much simpler. The reason is that a torque meter is able to measure the torque component only along one particular direction, say the y direction (the direction perpendicular to the arms of the lever; see Chapter 2). The response of the torque meter to the other two components (x and z) is relatively weak compared to that along the y direction but it is still not negligible. These components can not be measured, yet cannot be ruled out, therefore it is important to orient the crystal in such a way that τ_x and τ_z are zero. This can be done by having the magnetic field and the easy axis both lying in the xz plane (Figure 1.11). The Hamiltonian which is most frequently used reduces to,

$$\mathbf{H} = \sum_{i,j} \mathbf{S}_i \cdot \mathbf{S}_j + \sum_i [B \cos(\theta) S_{i_z} + B \sin(\theta) S_{i_x}] + \sum_i D S_{i_z}^2 \quad (1.35)$$

1.6.4 Calculating thermodynamic observables

Having evaluated the energy spectrum as a function of the magnetic field B and the angle θ between the field and the principal magnetic axis of the molecule, calculating different thermodynamic is straightforward. To that end, we define the partition function $Z(T, B, \theta)$ as

$$Z(B, \theta, T) = \sum_i e^{\frac{-E_i}{k_B T}} \quad (1.36)$$

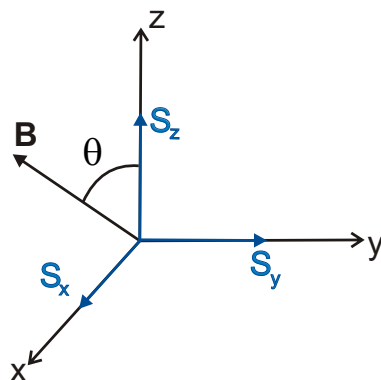


Figure 1.11: A practical orientation of the easy axis that is employed in most torque measurements. The easy axis is taken along the z direction and the magnetic field is rotated in the xz plane.

The magnetization per molecule is then given by

$$M(B, \theta, T) = - \sum_i \frac{dE_i}{dB} \frac{e^{\frac{-E_i}{k_B T}}}{Z(B, \theta, T)} \quad (1.37)$$

while the magnetic torque around along a generic axis α is

$$\tau(B, \theta, T) = \sum_i \frac{dE_i}{d\theta} \frac{e^{\frac{-E_i}{k_B T}}}{Z(B, \theta, T)} \quad (1.38)$$

which describes the rotation of the system around α at a constant magnetic field. Other observables such as the specific heat or the internal energy of the system can be evaluated as well in the same way [21]. One issue which is of importance for comparing the calculated observables, to the experimentally obtained ones, is the units to be used. Kelvin (K) and wavenumbers (cm^{-1}) are often used to parameterize the exchange constants (J) or the ZFS parameters (D, E, etc...). The units of the calculated energy values and consequently that of the magnetization or the torque depend on whether K or cm^{-1} is used. One has to be careful to use suitable units for the fundamental constants (mainly μ_B and k_B).

If Kelvin is used to express J and D then: $\mu_B = 0.671712 \text{ K}\cdot\text{T}^{-1}$, $k_B = 1$, and $[\tau]: \text{K}\cdot\text{rad}^{-1}$, $[\text{M}]: \text{emu}$, while if cm^{-1} is used then: $\mu_B = 0.466864 \text{ cm}^{-1}\cdot\text{T}^{-1}$, $k_B = 0.6950349 \text{ cm}^{-1}\text{K}^{-1}$, and $[\tau]: \text{cm}^{-1}\text{rad}^{-1}$, $[\text{M}]: \text{cm}^{-1}\text{T}^{-1}$. Usually it is convenient to express the magnetization per molecule in the unit of μ_B : $M[\mu_B]$ which is equivalent to gM_S .

1.7 Motivation and outline of the Thesis

We have seen in this chapter that the magnetic anisotropy lies at the heart of the molecular magnetism field of research. Essentially, the anisotropy is vital for the slow

relaxation of the magnetization in these systems, as well as for the observation of several quantum magnetic properties/phenomena. A high spin cluster with no magnetic anisotropy is nothing but an ordinary paramagnet which neither retains the magnetization, nor shows quantum tunneling of the magnetization. Knowing the importance of magnetic anisotropy in molecular magnets, we have aimed at explicitly investigating it in various molecular magnetic systems, in order to gain better understanding of the underlying physical phenomena. In particular, we wanted to explore the limits of the giant spin model and its application in SMMs to improve our understanding of the origin of the anisotropy in these systems. In addition, we aimed at investigating lanthanide based systems to indicate strategies for improved SMMs.

Spectroscopic and magnetometric experimental methods have been used to investigate the magnetic anisotropy in SMMs. Both classes of experiments yield related and to some extent complementary information. Spectroscopy have proved to be more effective in investigating the anisotropy, hence leading to a better description of the magnetism of most of the systems at low temperatures. We have used FDMRS and High-Frequency ESR over the years in studying SMMs. However, not all systems are spectroscopically active, spectroscopy may fail in systems with unfavorable spin-lattice relaxation times, large ZFS, or excessive dipolar broadening. In this Thesis, we have aimed at developing cantilever torque magnetometry to complement the spectroscopic capabilities that we have. Eventually, we planned to exploit our accumulative knowledge in both techniques by combining them together to create a novel torque detected ESR method to study single crystals of SMMs in a broad frequency range. Our ultimate goal, was to simultaneously use these methods to fully characterize the magnetic properties of diverse molecular magnetic systems, independent of their ZFS values, or their building blocks. In addition to the experimental considerations, we intended to develop our own modelling methods which explain and reproduce the experimental results, and aid in designing future experiments.

This Thesis is divided in the following way. After we have introduced the general properties of molecular nanomagnets in this Chapter, in Chapter 2, we introduce cantilever torque magnetometry by including the theoretical background necessary for the reader to comprehend the experimental and theoretical data presented in this Thesis. In addition, the Chapter incorporates details regarding the design, fabrication, and calibration of the experimental setup developed as a part of this PhD project. In Chapter 3, we report the results of the FDMRS and INS investigations performed on two different variants of Mn_6 compounds. Chapter 4 presents spectroscopic and magnetometric studies of the magnetic anisotropy of a photomagnetic dinuclear Fe(II) complex. Chapter 5 shows the results of a detailed magnetic study of a weakly coupled Fe(II) dimer with peculiar magnetic and quantum mechanical properties. In Chapter 6, low and high field torque magnetometric study of a unique Dy_3 triangle is presented. Chapter 7 deals with the details of the newly developed method, torque detected ESR. In addition, a proof of concept investigation is shown on an Fe_4 single crystal. Finally, the Thesis is summarized and conclusions are drawn in Chapter 8.

Chapter 2

Cantilever Torque Magnetometry

This chapter is intended as a guide for performing torque magnetometric measurements on magnetically anisotropic molecular clusters. We start by introducing the theoretical background necessary for the reader to comprehend the experimental and theoretical data presented in this work. The second section illustrates how torque magnetometric measurements should be performed and how the data can be analyzed. Some of the proposed methods to perform and interpret the experiments have not been reported in literature. The fine details that are included can have a great influence on the experiments and can tip the balance towards performing an optimized experiment. The third and the fourth sections deal with the experimental setup and they incorporate specific details regarding the design, fabrication, and calibration of its various parts. Finally, the last section shows how one can exploit an experimental setup to perform simultaneous tasks which are of great benefit for the experimentalist, albeit not directly related to the performed measurements.

2.1 Introduction

Torque magnetometry is widely used by condensed matter researchers to perform single crystal studies. The technique was extensively used to study superconductors [23][24][25], magnetic thin films, metallic multilayers, and several other magnetic systems [26] that may not be accessible by other magnetometric techniques, especially at high magnetic fields. In particular, the technique is an important tool to study the magnetic anisotropy in extremely small single crystals due to its high sensitivity. Earlier versions of torque meters were based on torque pendulums which suffered from limited sensitivity[27][28]. The implementation of cantilever devices rendered this technique more sensitive and less vulnerable to extrinsic perturbations.

A cantilever is a flexible beam which is fixed at one end and is free to deflect at the other. The sensitivity of a cantilever torque meter is determined by the stiffness of the beam, and the detection method used to probe the deflection of the beam. Besides their use in force microscopy, cantilevers have been used as magnetic torque meters, magnetic resonance detectors, temperature sensors, gas sensors, calorimeters, or spectrometers [29].

Molecular magnetic clusters, the systems which were investigated in this Thesis, quite often exhibit fairly large torque signals due to their high spin values and large magnetic anisotropy. In addition, single crystals of organic molecular clusters, often have non-uniform shapes which extend in different directions. This sets some limits on the cantilever sizes to be used in carrying out the experiments. The cantilevers used in this Thesis were designed to be robust, easy to clean, and have a large surface area to enable the mounting of single crystals with various sizes. Based on the same principle, highly sensitive torque meters were developed to study small single crystals and/or resolve weak features in the torque signals.

2.2 Theoretical background

2.2.1 Torque and Faraday forces

Magnetic anisotropy is mainly studied by two groups of experimental techniques, magnetometry and spectroscopy. The latter includes ESR and INS (Chapter 1). Magnetometry on the other hand, includes a large number of methods where either the magnetization (SQUID, VSM, Hall-bar,...etc) or the magnetic torque is measured. In order to obtain information about the magnetic anisotropy, one has to measure the magnetic response of the system along different crystallographic or molecular orientations. Magnetization measurements can serve as a first indication to characterize the magnetic anisotropy of the spin ground state of a certain system. To that end, one must perform angular dependent magnetization measurements in the different crystallographic planes. The possibility of rotating a crystal in an externally magnetic field and simultaneously measuring its magnetic response remains a difficult task [12].

Despite the fact that commercial magnetometers are able to give very precise magnetization values, yet magnetization curves are not sufficient to predict ZFS parameters in most of the cases. However, parameters like the g -value or the spin ground state S are easily extracted from the magnetization curves. On the other hand, torque measurements can give direct access to the anisotropy parameters as shown in the next sections. In a general classical picture, the magnetic torque experienced by a magnetic moment μ in an external magnetic field B is due to the non-collinearity between the field and the magnetic moment vector (Figure 2.1). The torque is therefore induced in a direction perpendicular to both the field and the magnetic moment in order to align the latter along the externally applied field. Going from a certain angle α to being parallel

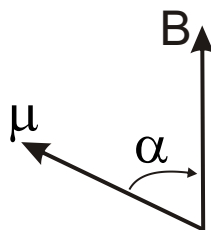


Figure 2.1: The torque is directed into the plane containing μ and B .

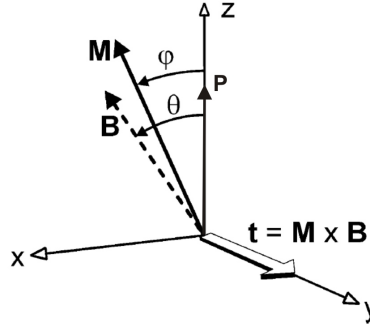


Figure 2.2: The alignment of the principal axis \mathbf{P} and the magnetic field in the laboratory frame of reference. The orientation of the magnetization vector \mathbf{M} depends on the direction of the magnetic field and that of the principal axis [30].

to the field, the system gains magnetic potential energy given by $E_M = -\mu B \cos \alpha$. The magnetic torque can be obtained by differentiating the magnetic energy with respect to α which describes the rotation of the system around an axis (y-axis) perpendicular to both the field and the magnetic moment at a constant magnetic field B ,

$$\tau_y = \frac{dE_M}{d\alpha} = \mu B \sin \alpha \quad (2.1)$$

The same expression can be obtained by taking the cross product of the magnetic moment and the magnetic field, i.e. $\tau_z = \mu \times \mathbf{B} = \mu B \sin \alpha$. In a purely isotropic paramagnet, the magnetic torque vanishes. The magnetic moments are readily aligned with the externally applied magnetic field and no torque is therefore induced. In such systems, the magnetization depends only on the magnitude of the applied field. On the other extreme, ferromagnetic systems exhibit a spontaneous magnetic moment which is oriented along a certain crystallographic axis. The torque will then cause a rotation of the crystal in order to align the magnetic moment with the external field and its expression is given by Eq. (2.1).

In magnetically anisotropic paramagnets, the situation is rather different. In this case, the magnetic moment is still field-induced but a transverse component exists which depends on the magnetic anisotropy in the system. The non-collinearity between the principal magnetic axis and the applied field results in a non-zero torque signal. If the system has an easy axis type anisotropy, the magnetic moment is pinned to this axis at temperatures below the blocking temperature in SMMs and the system thus behaves as a ferromagnet. At higher temperatures, the torque signal depends on the response of the system to the external field. In order to obtain an analytical description of the torque, let us consider the following system: a SMM with a magnetic ground state S , an isotropic g -value, and magnetic anisotropy described by an axial term D and a transverse term E . Figure 2.2 depicts the relative orientation of the magnetic field $\mathbf{B}(B_x, B_y, B_z)$ and the principal magnetic axis \mathbf{P} in the laboratory frame of reference. The magnetization is described by a vector $\mathbf{M}(M_x, M_y, M_z)$. The torque can be then expressed as

$$\tau = \mathbf{M} \times \mathbf{B} ; \quad (2.2)$$

and if we place both the principal axis \mathbf{P} and the magnetic field \mathbf{B} in the same plane

(xz), we obtain only one torque component along a direction perpendicular to both \mathbf{M} and \mathbf{B} [30],

$$\tau_y = B^2 \left(\frac{M_z}{B_z} - \frac{M_x}{B_x} \right) \cos \theta \sin \theta \quad (2.3)$$

where θ is the angle between the magnetic field and the principal axis, and B is the magnitude of the applied field. Equation 2.3 shows that the torque depends on the axial (M_z) and the transverse (M_x) components of the magnetization. The behavior of these components is different in the weak ($g\mu_B B \ll k_B T$) and strong ($g\mu_B B \gg k_B T$) field limits.

The magnetization is given by $\mathbf{M} = \chi \mathbf{B} = (\chi_{xx} B_x, \chi_{yy} B_y, \chi_{zz} B_z)$, where χ_{xx} , χ_{yy} , and χ_{zz} are the principal susceptibilities. In the weak-field limit, the magnetization changes linearly with the external field as the susceptibility χ is field independent and has a constant value. The torque will then have a quadratic dependence on the magnetic field and is expressed as,

$$\tau_y = B^2 (\chi_{zz} - \chi_{xx}) \cos \theta \sin \theta \quad (2.4)$$

The term in brackets is the difference between the magnetic susceptibilities in the x - and z - directions and therefore it is a direct measure of the magnetic anisotropy in the xz plane. For $\chi_{zz} = \chi_{xx}$, i.e. in the absence of the magnetic anisotropy, the torque is zero as expected. The torque also vanishes for $\theta = n\pi/2$ (where n is an integer), i.e. for the field being either parallel or perpendicular to the principal magnetic axis. In an intuitive picture, when the magnetic field is parallel to the easy axis for instance, all the spins point towards the direction of both the field and the easy axis, and consequently there is no torque induced. On the other hand, if the field is perpendicular to the easy axis, there are equal number of spins pointing up or down along the easy axis, thus inducing equal torques to rotate the crystal clockwise or anti-clockwise, and again the torque is zero. These two situations are hard to achieve experimentally since a perfect orientation of the crystal with the field being exactly at 0° or 90° from the quantization axis is required.

In the strong-field limit, the magnetization starts to saturate, and the susceptibility is no longer constant, but rather has a field dependence. At high magnetic fields, the spins will point towards the field independent of the direction of the easy axis, and the system is isotropic. The axial anisotropy decreases with the square of the magnetic field ($1/B^2$) to zero at high magnetic fields. Consequently, the torque tends to saturate to an asymptotic value at high fields given by [30],

$$\tau_{y_{B \rightarrow \infty}} = -2DS(S - 1/2) \cos \theta \sin \theta \quad (2.5)$$

Even though the spins point towards the field, the torque does not go to zero (For $\theta \neq n\pi/2$). This is due to the fact that the principal axis is not along the field and in this case the anisotropy axis acts as a "built-in" internal field which tries to align the spins parallel to it. In most cases, the torque signal is neither in the weak nor in the strong-field limit but it is somewhere in between. There is no analytical description for the torque signal in that region and thus the numerical value of the torque is

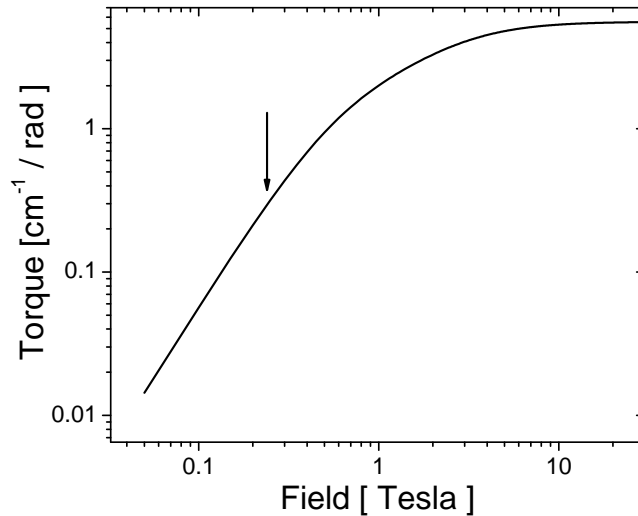


Figure 2.3: Calculated torque signal of an $S = 4$ spin ground state (see text) at 1.5 K. The arrow indicates the position of $k_B T / g \mu_B \approx 0.24$ Tesla which determines the transition from the weak to the strong field regime. A double logarithmic scale is used to demonstrate the B^2 dependence at low field.

quite often calculated by taking the derivative $dE_m/d\theta$ where E_m is the magnetic energy of the system (see Section 1.6). Figure 2.3 shows the calculated torque for an anisotropic system with an $S = 4$ spin ground state, axial anisotropy of the easy axis type $D = -0.2 \text{ cm}^{-1}$, $g = 2$, and $T = 1.5 \text{ K}$. The torque has a B^2 dependence in the low field limit ($B \ll 0.24 \text{ Tesla}$) and it saturates to $5.6 \text{ cm}^{-1}/\text{rad}$ at high field, as predicted by equations 2.4 and 2.5, respectively.

Faraday Force

In addition to the torque component, a specimen suspended in an inhomogeneous magnetic field experiences a magnetic force known as the Faraday force and is given by [31],

$$\mathbf{F} = \mathbf{M} \cdot \nabla \mathbf{B} \quad (2.6)$$

where \mathbf{M} is the magnetization of the sample and $\nabla \mathbf{B}$ the magnetic field gradient. In a homogenous magnetic field (no magnetic field gradient), this force component clearly vanishes. The samples we measured were always placed at the center of the magnetic field. Nevertheless, a small field gradient is inevitable, especially for relatively big crystals. Even though the force component is practically negligible compared to the torque component, this small contribution can become important for low torque signals (if the field is applied at very small angles to the principal magnetic axis). The force has a quadratic field dependence for regimes where the susceptibility is field independent and can thus mimic a torque signal in a certain field range. An important point to bear in mind is that the force is directed only along the magnetic field gradient. The

magnetic field is applied along the axial direction in our case, say the z direction. The gradients along x and y are negligible and consequently $F = F_z = M_z \cdot \partial B / \partial z$. If we decompose the susceptibility of the system into an isotropic χ_I and an anisotropic one χ_A , then we can write the force component as [32],

$$F_z = B \frac{\partial B}{\partial z} (\chi_I + \chi_A \cos^2 \theta) \quad (2.7)$$

where θ is the angle between the applied field and the easy magnetic axis. The angular dependence of F as well as its uniaxial direction along z turn out to be of benefit in order to eliminate the force contribution from the measured torque signal. Note that a vertical force along the z -axis will have a different effect on the cantilever depending on the orientation of the cantilever itself irrespective of the orientation of the crystal. The force will induce a maximum change in the capacitance for the cantilever being perpendicular to the force direction and will be almost negligible for the lever arms being along F_z .

2.2.2 Magnetically anisotropic clusters

In this section, we illustrate a variety of experiments that one could perform using torque magnetometry in order to obtain information on high-spin ($S > 1$) magnetically anisotropic clusters. As we have seen in the previous section, the torque signal saturates to a well defined value at high magnetic fields, which depends on the anisotropy in the system. For transverse fields, the torque signal has a distinct shape and it exhibits a characteristic peak at a certain magnetic field which again depends on the magnetic anisotropy. In the following sections we discuss the different approaches to examine anisotropy using torque magnetometry. To that end, we present data on an Fe_4 (details in chapter TDESR) compound with the SHP $\{S = 5, D = -0.449 \text{ cm}^{-1}, E = 0.03 \text{ cm}^{-1}, B_0^4 = 2.4 \times 10^{-5} \text{ cm}^{-1}, g = 1.98\}$, and simulations performed on two model systems; model system 1 with $\{S = 4, D = -0.4 \text{ cm}^{-1}, g = 2\}$ and system 2 with $\{S = 1, D = -0.4 \text{ cm}^{-1}, \text{ and } g = 2\}$ for the sake of illustration.

Asymptotic saturation value at high magnetic field

The first remarkable feature that one may think of is the saturation value of the torque at high magnetic fields, as this value is directly linked to the anisotropy parameters, and the spin ground state. However, a potential problem that rises here is the necessity to obtain a quantitative value of the torque in order to extract the anisotropy parameters. A major drawback of capacitance based torque magnetometry is that it is a semi-quantitative method where the determination of absolute values for the torque signals is rather difficult. On the one hand, this is limited by the calibration of the torque-meters which remains a difficult task, on the other hand the absolute value of the torque strongly depends on the angle θ and misorientations as small as 0.1° are very crucial. Figure 2.4 shows the torque signal calculated for the magnetic field being almost parallel ($\theta = 2^\circ$) and almost perpendicular ($\theta = 88^\circ, \theta = 87.5^\circ$) to the easy axis of system 1. In principle, the two curves at 2° and 88° should saturate to the same

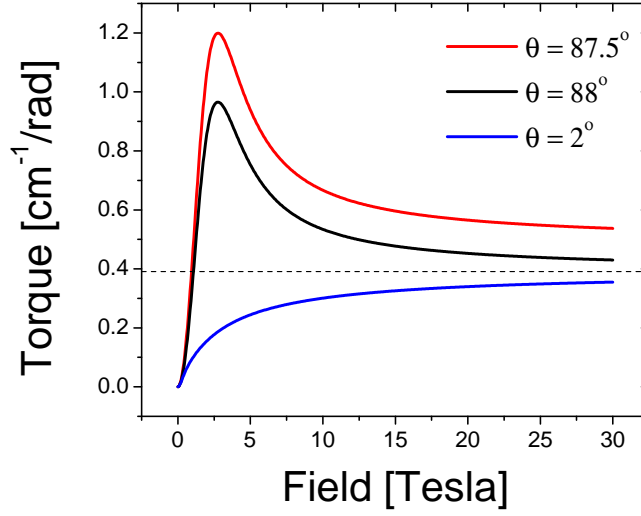


Figure 2.4: Calculated torque signals for an axial ($\theta = 2^\circ$) and a transverse ($\theta = 87.5^\circ, \theta = 88^\circ$) applied magnetic field at 1.8 K. The dashed line stands for the calculated asymptotic value of the torque for system 1 (see text) which saturates to $0.39 \text{ cm}^{-1}/\text{rad}$.

asymptotic value ($0.39 \text{ cm}^{-1}/\text{rad}$) as predicted by Eq. 2.5 but this happens only at very high fields. Note that the torque does not reach the limiting value even at 30 T. This underlines the importance of having access to high magnetic fields except for systems with very small anisotropy. Another way to extract the saturation value is by locating the asymptote (dashed line) which lies symmetrically in between the 88° and 2° curves. The simulations show a considerable difference between the 87.5° and the 88° curves. A misorientation of 0.5° is therefore sufficient to result in a certain discrepancy in the extracted anisotropy parameters. However, close to 45° the variation of the torque signal is not as significant. Figure 2.5(a) shows the variation in the torque signal with angle ($d\tau/d\theta$) versus angle; $d\tau/d\theta$ is maximum around the principal directions ($n\pi/2$) and it diminishes around 45° . Hence, it is more accurate to determine the asymptotic value of the 45° signal as the systematic error on the absolute value is less pronounced (Figure 2.5(b)).

The breaking field

Another distinct feature in the torque signal is the peak observed at a specific magnetic field value which we call the breaking field B_{Br} . This peak is evident only when the external field is close to being perpendicular to the easy axis (or close to being parallel to the hard axis). For a transverse field, the torque signal is relatively high considering that the spins are almost perpendicular to the external field. At low magnetic fields, the torque increases quadratically with B as long as the susceptibility is field independent. As the external field starts to influence the susceptibility, the torque begins to turn over in order to saturate to $-2DS(S - 1/2) \cos \theta \sin \theta$ and therefore it goes through a maxi-

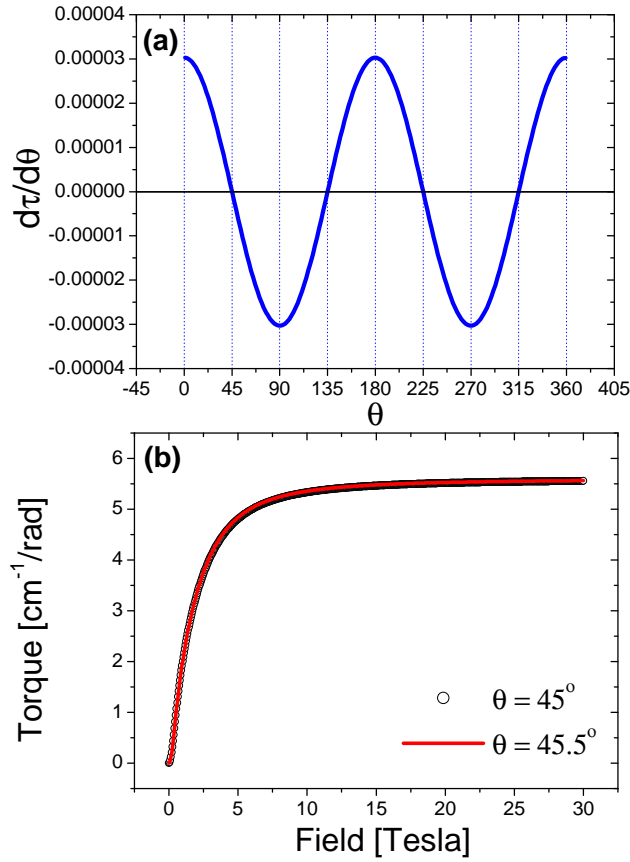


Figure 2.5: (a) The derivative of the torque versus angle at $T = 15$ K and 0.1 Tesla for system 1. (b) Torque signal at 45° and 45.5° for the same system. The difference between both signals is negligible.

imum. The stronger the anisotropy, the higher the field of this maximum will be. Therefore we can consider this field value as that which "breaks" the magnetic anisotropy of the system, and hence the name *Breaking Field* (B_{Br}). Figure 2.6 shows the torque and the corresponding magnetic anisotropy in the xz -plane for system 2 at $T = 50$ mK. The breaking field corresponds to that where the torque stops increasing with field and approaches the saturation value, while the magnetic anisotropy approaches zero. It is worth noting that there is no physical significance about the "Breaking Field". It is not linked to any particular change in the system (like a phase transition for example), but rather it is a characteristic feature which is of practical importance to determine the anisotropy in the system. This strong dependence of the breaking field on the anisotropy was exploited in high field torque magnetometry measurements where the ZFS parameters of Mn_{12} acetate were determined with high precision [30]. Besides being directly linked to the anisotropy, the breaking field is strongly dependent on the temperature. We have exploited this dependence to determine the axial anisotropy of the Fe_4 compound. Figure 2.7 shows the measured torque signal and the fit with

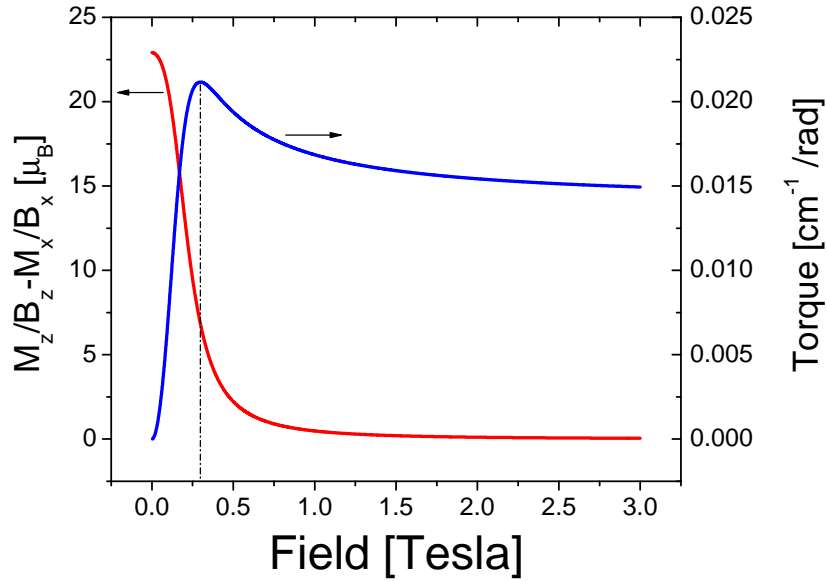


Figure 2.6: The calculated torque signal and the magnetic anisotropy of an $S = 1$ system at $\theta = 88^\circ$ and $T = 50$ mK. The black line indicates the position of the breaking field.

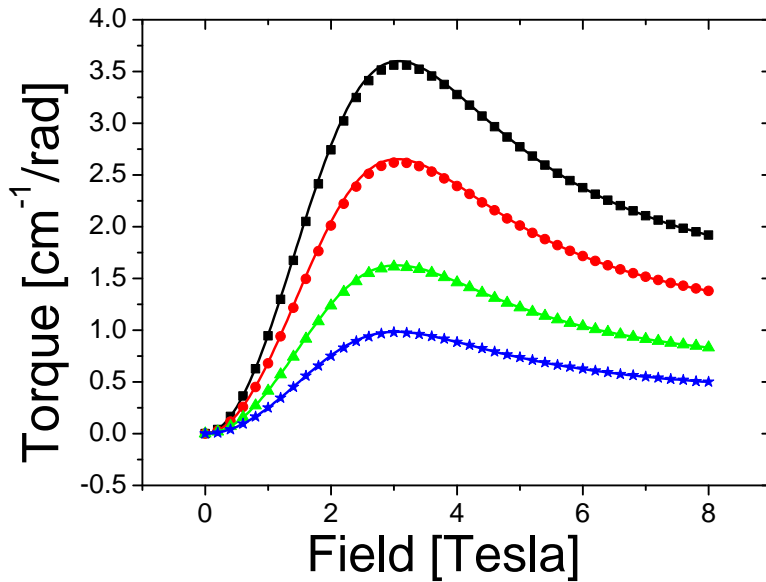


Figure 2.7: Measured torque signal at 86.5° (squares), 87.5° (bullets), 88.5° (triangles), and 89.1° (stars) at $T = 1.63$ K. The solid lines are the fits for $g = 1.98$ and $D = -0.4$ cm^{-1} (see text).

$\{D = -0.4 \text{ cm}^{-1}, E = 0 \text{ cm}^{-1}, B_4^0 = 0 \text{ cm}^{-1}, \text{ and } g = 1.98\}$. The absolute values of the torque were determined by using a scaling factor α obtained from the torque value at 8 Tesla for each curve ($\tau[\text{cm}^{-1}/\text{rad}] = \alpha \cdot \tau[\text{fF}]$ at 8 Tesla)¹. The measurements enable us to determine an approximate D value of -0.4 cm^{-1} which is close to that obtained by High-Frequency ESR. The obtained parameters well reproduce the torque signal at different temperatures (Figure 2.8(a)) and the breaking field position versus temperature(2.8(b)). However, we have found that the technique is not sensitive to transverse anisotropy parameters especially without any prior knowledge of any other spin Hamiltonian parameters. Figure 2.9 shows the calculated torque signal for two dif-

¹In principle, the absolute value should be determined from the calibration procedure See (calibration section) but in this case the mass of the crystal is not known.

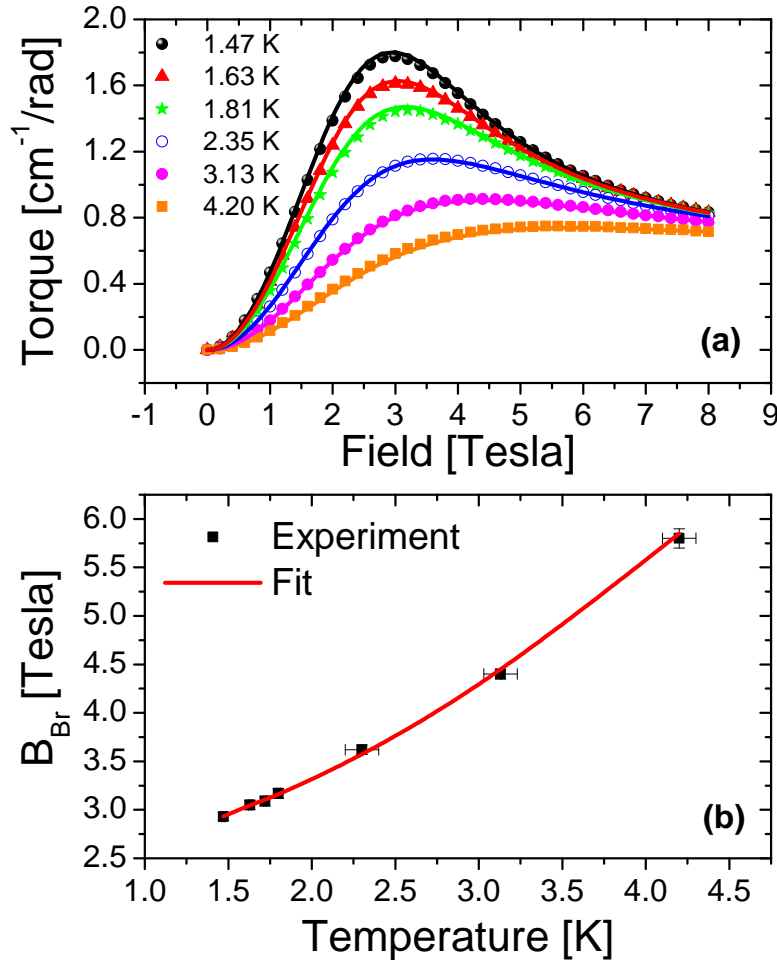


Figure 2.8: (a) The field dependence of the torque measured for an Fe₄ crystal at 88.5° for different temperatures. The solid lines are the fits for the spin Hamiltonian parameters discussed in the text. (b) Breaking field extracted from the maxima of the plots in (a) versus temperature.

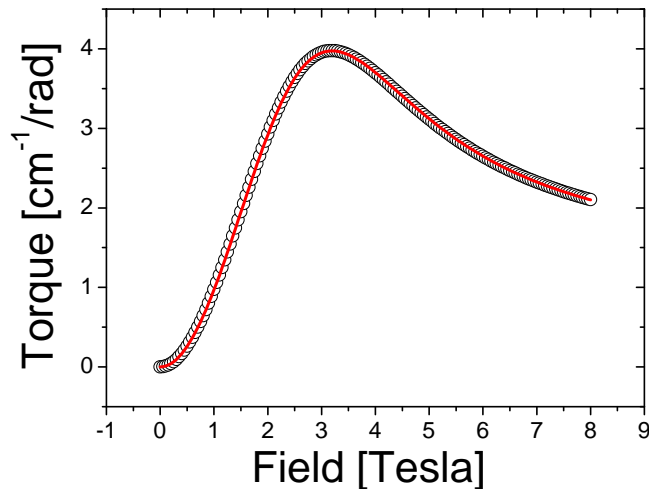


Figure 2.9: The calculated torque signals for two sets of parameters with different D and E values (see text).

ferent sets of parameters for the Fe_4 system: (1) $\{D = -0.4 \text{ cm}^{-1}, E = 0.02 \text{ cm}^{-1}, B_4^0 = 0 \text{ cm}^{-1}, g = 1.98\}$ and (2) $\{D = -0.421 \text{ cm}^{-1}, E = 0 \text{ cm}^{-1}, B_4^0 = 0 \text{ cm}^{-1}, g = 1.98\}$. One can obviously see that the two sets of parameters have different axial and transverse anisotropies but yet they give the same torque signals. This elucidates the weakness of the technique in determining transverse anisotropy parameters. Note that we have a quantitative agreement between the two sets of data in Figure 2.9 and not only a qualitative one which makes it implausible to be able to experimentally distinguish between the two situations using torque magnetometry.

Ideally, torque signals are symmetric around the principal directions (i.e. $\tau(\theta) = -\tau(\theta)$ or $\tau(90 + \theta_o) = -\tau(90 - \theta_o)$). In practice, one quite often measures asymmetric curves. Several reasons could lead to asymmetry in the measured capacitance value, amongst them is a small misorientation of the crystal, or a force component which adds up to the torque signal. As discussed earlier, the force component is expected to be very weak in all the measurements we performed since the samples were always placed at the center of the field. The contribution of the force and other extrinsic components is pronounced for small torque signals. This is nicely demonstrated in Figure 2.10 which shows torque measurements on an Fe_4 single crystal at 1.63 K. Figure 2.10 (a) shows the raw torque data corrected for the non-linear response (correction procedure explained in Section 2.3.2). The curves are clearly not symmetric around 90° and the breaking fields do not coincide, in contrast to what is expected from the calculated signals. This is shown more clearly in Figure 2.10 (b) where the $\Delta C(90 - \theta_o)$ and the $-\Delta C(90 + \theta_o)$ values do not superimpose. The extraction of the breaking field position and consequently the ZFS parameters based on these data would depend on whether the measurement is performed at $(90 - \theta_o)$ or $(90 + \theta_o)$. This leads to having a large error on the extracted ZFS parameters. The asymmetry is more pronounced for angles closer to 90° , where the absolute torque signal is smaller in magnitude. Let us assume

that the capacitance change is given by

$$\Delta C(B, \theta) = \tau_y(B, \theta) + f(B, \theta) \quad (2.8)$$

where $\tau_y(B, \theta)$ is the torque component along the y-direction and $f(B, \theta)$ is an additional component that can induce a capacitance change. $f(B, \theta)$ can be due to a Faraday force, a lateral torque component τ_x , or magnetic impurities in/on the cantilever. Assuming that the main contribution to $f(B, \theta)$ is the Faraday force component in these measurements, the change in the capacitance around (90°) can be approximated from Eq. 2.7 and Eq. 2.8 by

$$\Delta C(B, \theta) \approx \tau_y(B, \theta) + B \frac{\partial B}{\partial z} \chi_I \quad (2.9)$$

The second term on the r.h.s depends only on the magnetic field and not on the angle θ . As already noted, the direction of the force is always along the field gradient and therefore, unless ($\theta = 90^\circ$) coincides with the field being parallel to the cantilever arms (which is not the case in this measurement), the capacitance change induced by the

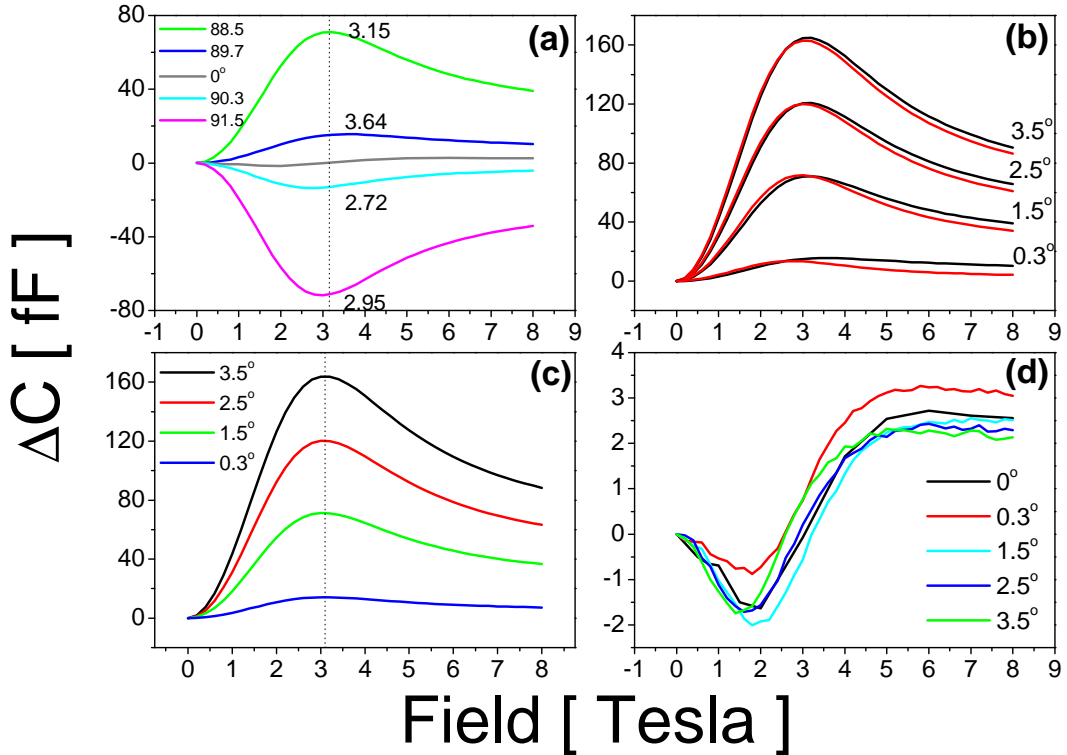


Figure 2.10: (a) Raw ΔC data corrected for non-linearity. The numbers indicate the B_{Br} value at each angle (b) $\Delta C(90 - \theta_o)$ (black lines) and $-\Delta C(90 + \theta_o)$ (red lines) at different θ_o values (c) ΔC_{diff} at different θ_o values (d) ΔC_{av} at different θ_o values, in addition, the absolute measured ΔC at 0° .

force does not change sign going from $(90 - \theta_o)$ to $(90 + \theta_o)$. Since $[\tau(90 + \theta_o) = -\tau(90 - \theta_o)]$, the difference of the capacitance change around (90°) enables us to calculate the torque component by eliminating the component induced by the force,

$$\begin{aligned}\Delta C_{diff} &= \frac{\Delta C(B, 90 - \theta_o) - \Delta C(B, 90 + \theta_o)}{2} \\ &= \frac{\tau_y(B, 90 - \theta_o) - \tau_y(B, 90 + \theta_o)}{2} \\ &= \tau_y(B, 90 - \theta_o) = -\tau_y(B, 90 + \theta_o)\end{aligned}\quad (2.10)$$

Figure 2.10 (c) shows ΔC_{diff} for different θ_o . The position of the breaking field coincides for the various angles as expected from the calculated signals. On the other hand, the average of the capacitance change around (90°) gives us access to $f(B)$,

$$\Delta C_{av} = \frac{\Delta C(B, 90 - \theta_o) + \Delta C(B, 90 + \theta_o)}{2} = f(B)\quad (2.11)$$

Figure 2.10 (d) depicts that the signals obtained by evaluating ΔC_{av} at different θ_o all superimpose, within the experimental error. Furthermore, the measured change in the capacitance $\Delta C(B, 90^\circ)$ at 90° coincides with the various ΔC_{av} . This is again expected since the torque signal vanishes at 90° ($\tau(B, 90^\circ) = 0$) and the only measured component is that of the force

$$\Delta C(B, 90^\circ) = \tau(B, 90^\circ) + f(B) = f(B)\quad (2.12)$$

Note that $f(B)$ is not solely due to the Faraday force in this case, but in addition a small contribution of the cantilever background signal is superimposed onto it. This example shows how crucial extrinsic effects are, especially for small torque signals. The effect is very small for large θ_o values, where the torque signal dominates and the effect of $f(B)$ is negligible.

Angle resolved torque

Angle resolved torque measurements can be very rich in information. Indexing the crystal and orienting it properly prior to the experiment is indispensable in order to map the magnetic data onto the molecular structure. This enables us to determine the direction and the sign of the anisotropy in the system. In other words, from a single angle dependent measurement, one is able to know whether the system has an easy or a hard axis, a quest which can be difficult and time consuming in other magnetometric techniques. Furthermore, the principal axis can be assigned to a certain crystallographic or molecular axis in some cases. Figure 2.11 shows a typical angle dependent torque signal for a system with an easy or a hard magnetic axis. Supposedly, the direction of the principal magnetic axis is known and we place the crystal such as the principal axis is parallel to the arms of the cantilever, i.e. at $\theta = 0$ the magnetic field is parallel to the principal axis and the torque is zero. For $0^\circ < \theta < 90^\circ$, a system with an easy axis anisotropy would tend to orient the easy axis along the external field

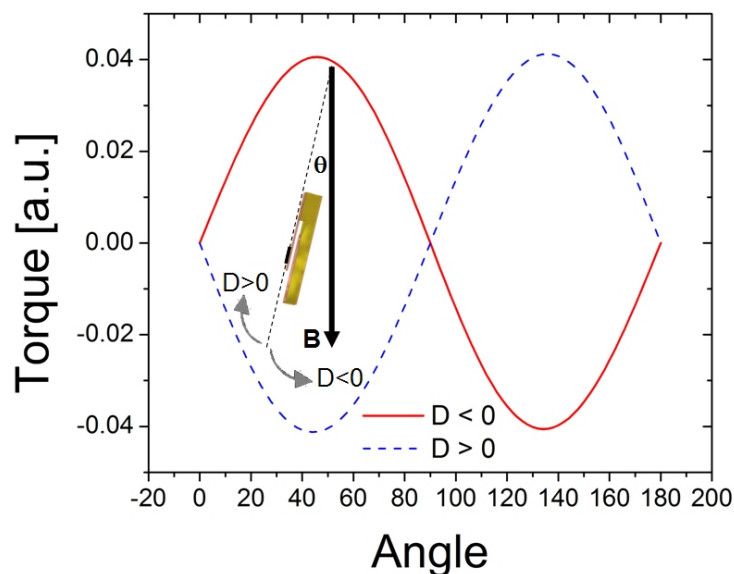


Figure 2.11: Calculated torque signal versus angle for a system with either an easy or a hard axis. The panel shows the corresponding crystal and cantilever orientation.

and thus bend the cantilever downwards, which would give a positive change in the capacitance ΔC . The situation is inverted in the case of a hard axis, where the crystal would try to move away from the external field. With this fairly simple experiment, a conclusive evidence about the nature of the magnetic anisotropy (hard or easy axis) can be directly obtained. Conventional magnetization measurements often fail to determine the sign of D , while in spectroscopy, temperature dependent measurements have to be performed to extract the same sort of information. A process which is much more time and funds consuming.

Figure 2.12 shows a polar plot of the measured torque of an Fe_4rac single crystal. The crystal was placed on its $10\bar{1}$ plane with the \mathbf{b} axis parallel to the rotation axis. The magnetic field is consequently rotated in the ac plane. The corresponding crystal structure is shown on top of the torque signal. $\theta = 0^\circ$ corresponds to the magnetic field being parallel to the cantilever arms, i.e. at 30° from \vec{n} the normal to the plane containing the 4 Fe^{3+} ions (orange balls). The principal axis \mathbf{p} is oriented along \vec{n} as imposed by the symmetry of the molecule. After a 30° rotation, the magnetic field is oriented along \mathbf{p} (dashed line) and the torque signal drops to zero. The agreement between the experimentally observed and the expected angles based on the crystal structures is evident. Rotating further by 90° , the magnetic field ends up in being in the plane of the 4 iron ions and the torque drops again to zero. The torque thus vanishes for the magnetic field being parallel or perpendicular to the easy axis. In order to distinguish the parallel from perpendicular situation, a field scan can be performed at a fixed angle close to 0° or 90° . This approach is very useful in torque magnetometric measurements; it serves as a confirmation of a correct crystal orientation, which may be complicated in some systems. If a disagreement exists between the angle resolved torque and the periodicity expected from the crystal structure, the data and/or the orientation of the crystal should be reexamined.

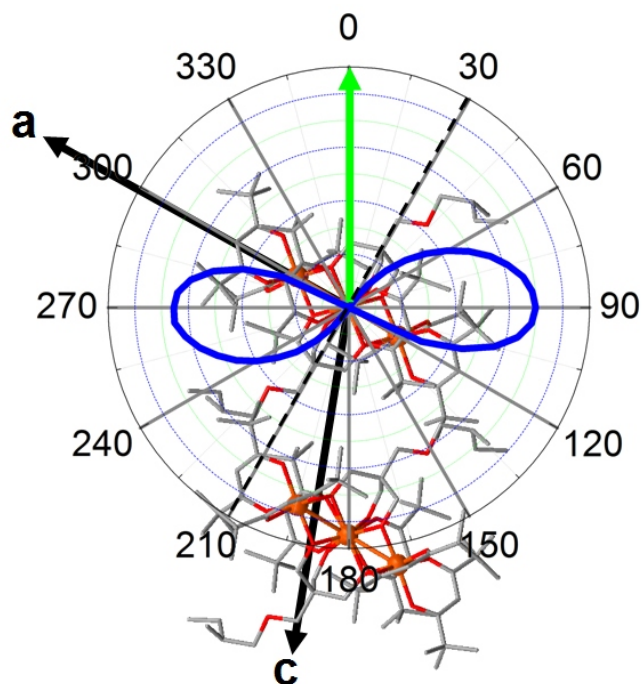


Figure 2.12: Polar plot of the torque signal (blue line) at $B = 0.5$ Tesla and $T = 1.65$ K of an Fe_4rac single crystal for the field (green arrow) being rotated in the ac crystallographic plane. The crystal structure is superimposed on the polar plot (see text). The negative part of the torque is omitted for clarity.

2.2.3 Antiferromagnetic clusters

Antiferromagnetic (AF) clusters were widely studied using torque magnetometry. These studies aim at either studying the nature of the field induced level crossings (discussed in the next section) or to investigate the electronic structure by providing information on the exchange interactions and the ZFS of the different spin states ([33][34][35][36]).

The torque signal of magnetically anisotropic AF clusters exhibits pronounced steps in association with the crossing from one spin state to the other. The steps become sharper at lower temperatures and their position depends on the exchange interaction J , the magnetic anisotropy D_S of the spin state S , and the angle at which the magnetic field is applied with respect to the anisotropy axis. In the strong exchange limit, and for high magnetic fields ($g\mu_B B \gg D_S$) Cornia et al. [34] gives an analytical expression for the crossing field as a function of θ and the different anisotropy and exchange parameters. This approach is of practical importance as it simplifies the procedure of extracting the spin Hamiltonian parameters. It should, nevertheless, be borne in mind that the crossing field can also be obtained by evaluating the energy diagram after diagonalizing the full spin Hamiltonian. Even though this procedure is more time consuming and can be more complicated in some systems, it remains a more general method and can be applied not only to systems with strong exchange but also those in the weak exchange limit, such as the Fe_2 -Penta system presented in Chapter 5.

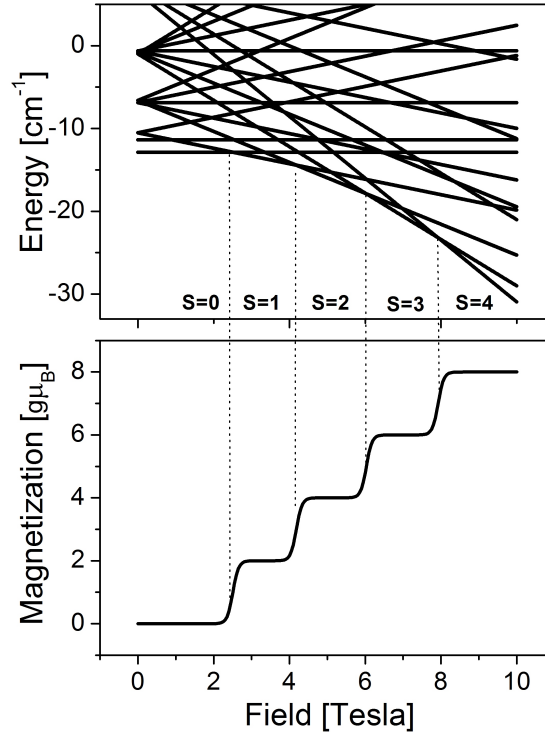


Figure 2.13: Zeeman splitting of a conventional AF dimer with an $s = 2$ spin for the single ion (Top), and its corresponding magnetization plotted vs field (bottom). The spin state crossings are reflected as steps in the magnetization curve at low temperatures.

2.2.4 Avoided level crossings

A level crossing occurs when two eigenstates of the system become degenerate in energy (they cross in energy). If one of these two levels is the ground state, the system then undergoes a transition from one ground state to another. This transition can be reflected in the properties of the system, and is therefore seen as a change in some experimental observables, which can vary depending on the nature of the transition (electronic, thermodynamic, magnetic..etc). In this Thesis, whenever a level crossing is mentioned, then we mean a magnetic level crossing that involves the ground state unless stated otherwise. A magnetic level crossing can be induced by an external magnetic field, temperature, or pressure. We will mainly discuss field induced level crossings in this section.

In addition, because we are mainly dealing with spin magnetic moments, a magnetic level crossing is correlated to either spin state crossings or crossings of the different M_S states within a certain spin ground state S . A spin state crossing can be either a pure crossing where the individual eigenstates involved in the crossing remain described by the pure eigenstates $|S, M_S\rangle$ or it can be an avoided level crossing where the two eigenstates involved in the crossing are mixed. The mixing of the different spin states depends on the symmetry of these states and the interaction that can cause a mixing. For example, interactions such as the single ion anisotropy can only mix states with

the same irreducible representation of the point group symmetry [14][37].

One way to detect avoided level crossings is specific heat measurements. At the level crossing, the magnetic specific heat vanishes indicating the absence of an energy gap between the spin states (absence of level mixing). As put forward by Oliver Waldmann [38][39], apart from specific heat, torque magnetometry can be a sensitive technique to probe level mixing. An anomaly in the torque signal is observed (peak-like feature) at the level crossing which is related to the level mixing. The anomaly is absent for $\Delta = 0$, and therefore it is a direct signature of level mixing. The key point to that is the dependence of Δ on the angle between the external field and the principal magnetic axis but not on the magnetic field itself. This intrinsic property of Δ is the reason behind the appearance of this anomaly in the torque signal but not the magnetization ². The anomaly in the torque signal is smeared out at high temperatures and therefore only systems with strong enough level mixing are considered to be good candidates to be studied with torque magnetometry. As argued above, lifting of the degeneracy at the level crossing can be induced by several interactions. In a Mn[3x3] AF grid, the origin of the level mixing ($\Delta = 0.3\text{K}$) was attributed to the single ion anisotropy which mixes the different spin states due to the slight distortion in symmetry [38]. The same system was studied in a previous work [36] at 1.75 K where the anomaly was not observed. A similar study was performed on Cr₇Zn and Cr₇Ni where the gap was estimated to be around 2 K. The gap is observed in the heterometallic rings but not in the pure Cr₈ complex [40]. The origin of the gap was therefore attributed to the breaking of the ring topology and not only distortions thus allowing S-mixing originally forbidden by symmetry. In an Fe₈Cs complex [41], the level splitting was attributed to magneto elastic coupling which appears at the level crossing due to structural instabilities induced by the magnetic anisotropy. All these systems share in common a high value of Δ which makes the observation of the anomaly in the torque possible at ³He or dilution fridge temperatures.

In our opinion, exotic features or anomalies in torque measurements can be massively misinterpreted by incorporating additional interactions in the Hamiltonian and parameterizing them to reproduce the experiments. Extrinsic effects such as misorientation, mosaicity, and/or inhomogeneity of the sample are very crucial in torque measurements and single crystal magnetic characterization in general. One piece of evidence on the importance of extrinsic effects is shown in a single crystal study to determine the easy axis orientation in SMMs by Wernsdorfer et al. [42]. We demonstrate through out this work that some of the effects that we observed in various torque measurements can equally be due to a physical origin, as well as due to extrinsic effects.

2.3 The torque magnetometer

2.3.1 Capacitive detection

The deflection of the cantilever beam under the influence of a magnetic torque can be detected in several ways among which is the optical detection [43][44], piezoresistive

²Remember that $\tau = \partial E_M / \partial \theta$ and $M = -\partial E_M / \partial B$

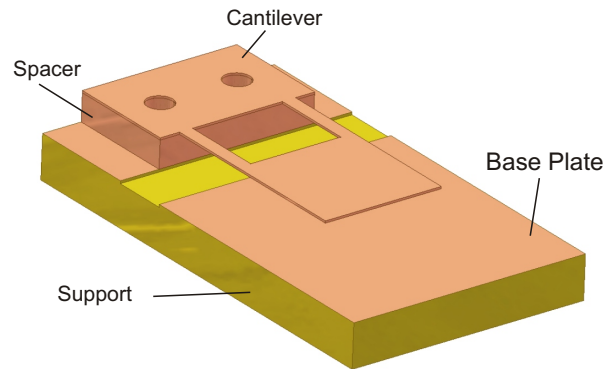


Figure 2.14: Basic parts of a capacitive torque meter.

[24][45], piezoelectric [46], or capacitive detection methods [47][48][49]. Each one of these methods has its own limitations. We have used the capacitive detection method as it is relatively simple method and its sufficiently sensitive. Figure 2.14 shows the basic parts of the capacitive torque meter that we have constructed. It consists of : (1) a cantilever, (2) a spacer, (3) a base plate, and (4) a support. The cantilever is fixed on top of the support with two screws. Two component epoxy glue was also used in some of the torque meters but proved to be intolerant for consequential cooling/heating cycles. Screwing the cantilever gave a more satisfying behavior in terms of stability versus thermal cycling. Furthermore, the screwed in levers were more straight, which is an important prerequisite for parallel plate capacitors. The degree of inclination of the beams was checked using an optical microscope and was found to be less than 10% of the separation distance.

The cantilevers, with thicknesses of 25 and 80 μm , were manufactured out of a Copper Beryllium alloy (Cu:98% Be:2%) using chemical etching. CuBe has a much higher fatigue and elastic strengths (modulus of elasticity is c.a. 100 GPa [50]) than other non-ferrous spring materials such as phosphor bronze and nickel silver [51]. It has a wide operating temperature range which enables it to retain its shape under high loads even at low temperatures. In addition, CuBe is non-magnetic. Several other materials can be used to form a cantilever and in particular Silicon is widely used. While Silicon cantilevers are highly sensitive, they are also rather expensive and fragile. Experience has proved that for single crystal measurements of magnetic molecular clusters, metallic cantilevers are superior to their rivals the silicon cantilevers because they are more robust. The spacers (2) were also chemically etched CuBe parts of dimensions ($6 \times 4 \times 0.03 \text{ mm}^3$). The spacers were placed in between the cantilever and the base plate to ensure a well defined separation distance (typically 30 - 150 μm) between the two plates.

Two different combinations of supports/base plates were used: (i) Gold or Copper on Sapphire plates and (ii) Copper on Epoxy plates. Sapphire plates of dimensions ($16 \times 9 \times 1.5 \text{ mm}^3$) were covered by 300 nm films of either Gold or Copper. Sapphire has a high thermal conductivity but the Copper/Gold layers grown on top were not stable for a long period of time. Sputtering of Copper/Gold onto the Sapphire plates

improved the adhesion onto the surface but not significantly. On the other hand, commercial Copper plated Epoxy slabs (usually used for electronic circuits) were fairly stable but Epoxy is a poor thermal conductor at low temperatures. Because most of the low temperature measurements were performed having the torque meters and consequently the samples immersed in liquid Helium, it was therefore advantageous to use the Epoxy plates as supports.

The capacitance of an ideal parallel plate capacitor is given by,

$$C = \frac{\varepsilon A}{d} \quad (2.13)$$

where ε is the permittivity of the dielectric separating the plates, A is the area of the cantilever, and d is the separation between the cantilever and the base plate. Any force F with a component that is perpendicular to the arms of the cantilever leads to a deflection of the beam by a certain value Δd . The change in the separation between the plates leads to a change in the capacitance. Using Eq. 2.13 we can calculate the change of the capacitance ΔC induced by an infinitesimal change in the separation Δd by taking the Taylor expansion of C around d_o where d_o is the separation of a free unloaded cantilever. The Taylor series of a function $F(x) = 1/(x + \delta)$ around $\delta = 0$ is given by,

$$\frac{1}{x + \delta} = \frac{1}{n!} \sum \frac{d^n f}{d\delta^n} |_{\delta=0} \delta^n \quad (2.14)$$

Similarly we can expand the capacitance as,

$$C(d_o + \delta d) = \frac{\varepsilon A}{d_o} - \frac{\varepsilon A}{d_o^2} \Delta d + \frac{\varepsilon A}{d_o^3} \Delta d^2 - \frac{\varepsilon A}{d_o^4} \Delta d^3 + \dots \quad (2.15)$$

In the absence of an applied force ($\Delta d=0$), the capacitance of the torque meter with a free beam is given by

$$C_o = \frac{\varepsilon A}{d_o} \quad (2.16)$$

Substituting for C_o in Eq. 2.17 we get,

$$C(d_o + \delta d) = C_o - \frac{C_o}{d_o} \Delta d + \frac{C_o}{d_o^2} \Delta d^2 - \frac{C_o}{d_o^3} \Delta d^3 + \dots \quad (2.17)$$

$$\Delta C = C(d_o + \delta d) - C_o = -\frac{C_o}{d_o} \Delta d + \frac{C_o}{d_o^2} \Delta d^2 - \frac{C_o}{d_o^3} \Delta d^3 + \dots$$

From the above equation, we can see that the capacitance change ΔC is related to the change in the separation Δd which in turn is directly proportional to the applied torque. Therefore, measuring the capacitance change enables us to extract quantitative values of the torque signal after performing a proper calibration. In order to measure very small changes in the capacitance, Andeen-Hagerling 2550A automatic capacitance bridge (Figure 2.15) was used to perform three terminal capacitance measurements.



Figure 2.15: Andeen Hagerling AH2550A capacitance bridge.

The resolution of the bridge is 0.8 aF and it can measure capacitances up to $1.5\mu F$. The bridge applies a 1 kHz ac voltage between 0.3 mV and 15 V (depending on the value of the capacitance measured) across the terminals of the capacitor. A very useful property of the bridge is the possibility of applying an external dc bias voltage up to 100 V. However, one has to correct for the non-linear response of the capacitance if the deflection is too strong. This will be the topic of the next two sections.

2.3.2 Non-linear response

Equation 2.17 shows that the relation between ΔC and Δd is not linear. This is depicted in Figure 2.16. The inset illustrates the linear behavior of $1/x$ for a small change δx around x_o . As δx increases, the behavior deviates from being linear and higher order terms become important. As Δd is linearly proportional to the torque, consequently the relation between ΔC and τ is also not linear for high torque values. Therefore, even if one is not interested in measuring the quantitative values of τ , one still has to correct for the non-linear terms in ΔC to obtain a 1:1 correspondence between the change in the capacitance and the change in the torque.

Without any loss of generality, we can assume that $\Delta d = K\tau$, so long we are still below the proportional elastic limit in the stress-strain relationship. This assumption is valid in all torque ranges applied in our experiments. The limit of proportionality which

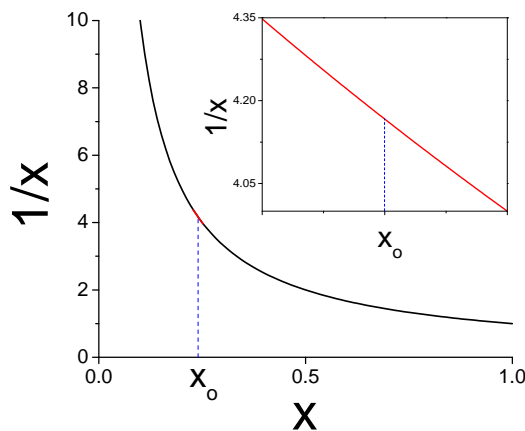


Figure 2.16: Plot of the function $1/x$. The inset shows that for a very small change of x around a value x_o , $1/x$ changes linearly with x .

is the limit beyond which the stress-strain relationship is no longer linear is around 800 MPa [51] for CuBe. While in our experiments the equivalent pressure induced due to the magnetic torque may go up to 100 Pa in an upper limit. Eq. (2.17) can then be expressed as,

$$\frac{\Delta C}{C_o} = -\frac{K\tau}{d_o} + \frac{(K\tau)^2}{d_o^2} - \frac{(K\tau)^3}{d_o^3} + \dots \quad (2.18)$$

This equation has been used in literature ([34],[52]) to correct for the non-linear response and calibrate the torque meter by taking the first two or three terms in the series and parameterizing them by the non-linearity factors. We used a similar approach to calibrate our torque meters, as explained in the next section.

A more accurate approach that we use to get the qualitative torque curves is by extracting the torque values from the capacitance and not by taking only the first two terms in the Taylor series. The absolute change of the capacitance ΔC irrespective of the relative magnitude of Δd can be expressed as,

$$\begin{aligned} \Delta C &= C(d_o + \Delta d) - C(d_o) = \frac{\varepsilon A}{d_o + \Delta d} - \frac{\varepsilon A}{d_o} \\ \frac{\Delta C}{C_o} &= \frac{\frac{1}{d_o + \Delta d} - \frac{1}{d_o}}{\frac{1}{d_o}} = \frac{-\Delta d}{d_o + \Delta d} \end{aligned} \quad (2.19)$$

where C_o and d_o are previously defined. Substituting for $\Delta d = K\tau$ we arrive at,

$$\tau = \frac{-d_o}{K} \frac{\Delta C}{C_o + \Delta C} \quad (2.20)$$

If one is only interested in the qualitative shape of the torque signal then the prefactor d_o/K can be set to 1, and the final form of the torque is given by,

$$\tau = \frac{-\frac{\Delta C}{C_o}}{1 + \frac{\Delta C}{C_o}} \quad (2.21)$$

The absolute value of C_o is crucial for this correction procedure as it determines the degree of non-linearity. This is clearly seen in Figure 2.16 where the choice of x_o (analogous to C_o) significantly changes the slope of the curve $-1/x_o^2$. It is worth noting that the relevant sign of ΔC is to be used. The non-linear terms increase the positive values of the capacitance and decrease the negative ones. Figure 2.17 shows the torque signal of the Fe₄rac compound. The uncorrected torque curves are not symmetric around 90°.

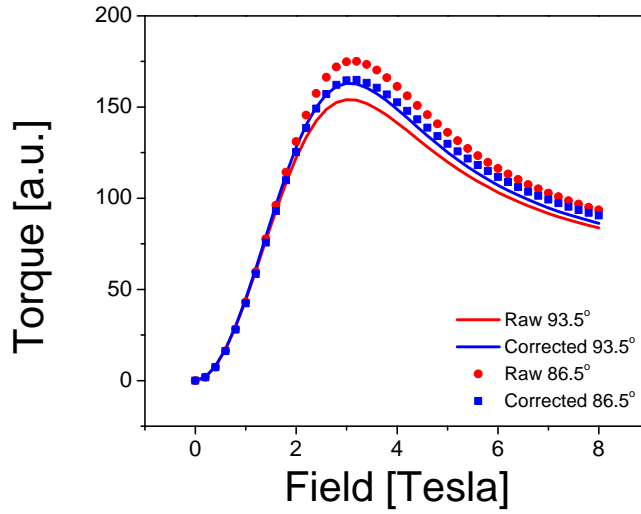


Figure 2.17: The torque signal of an Fe_4rac single crystal. Note that all the curves superimpose at low torque values. The corrected curves are symmetric around 90° . The absolute value of the 93.5° signal is plotted for clarity.

2.3.3 Calibration

In order to extract quantitative torque or magnetization values from the measurements, one has to carefully calibrate the torque meters, which can be difficult. Several calibration methods were reported in the literature which range from using samples of well known magnetic moments (magnetic tapes Fe_2O_3 [53], the Meissner effect in the superconducting state [24]) or current loops/coils which can also produce a well defined moment [48]. The drawback of these methods in general is that they strongly depend on the geometry/mass of the implemented samples and on the orientation of the samples on the cantilevers.

Following the method outlined in [54][48], we have calibrated the torque meter by applying a dc voltage between the electrodes of the capacitor and simultaneously recording the capacitance change. The dc voltage creates an electrostatic force, leading to attraction between the plates, and thus to an effective torque which causes the cantilever to bend down (Figure 2.18). This torque depends on the geometry of the torque meter rather than that of a sample like in the other methods. The geometry of the magnetometer is well defined by chemical etching and the error on its dimensions is negligible. One further advantage of this method is that the dc voltage is applied to the terminals of the electrodes by adding a dc bias to the ac voltage applied by the bridge to measure the capacitance. This facilitates the calibration procedure and eliminates the discrepancy of having a probe on top of the beam where the weight and the orientation of that probe can alter the calibrated values.

The electric field between two oppositely charged parallel plates separated by a

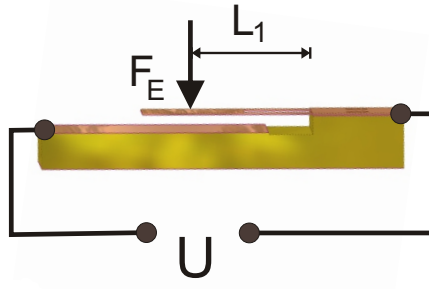


Figure 2.18: A schematic drawing of the electrostatic calibration procedure.

distance d is given by,

$$E = \frac{\sigma}{\varepsilon} \quad (2.22)$$

where σ is the charge density. For a uniform field, the electric potential difference between the plates (the dc applied voltage U in our case) can be expressed as,

$$U = Ed \quad (2.23)$$

Therefore the charge density σ is

$$\sigma = \varepsilon \frac{U}{d} \quad (2.24)$$

Assuming that the charge density is the same on the upper and the lower plate, the electrostatic force exerted on the upper plate (the cantilever) is only due to the electric field of the lower charged plate. The vertical electrostatic force can then be written as

$$F_E = Q_{upper} E_{bottom} = \sigma A \frac{U}{2d} = \frac{\varepsilon AU^2}{2d^2} \quad (2.25)$$

where A is the area of the smaller electrode which is the cantilever in our capacitor. Accordingly, the induced torque has the following form

$$\tau = F_E L_1 = 0.7L \frac{\varepsilon AU^2}{2d^2} = 0.7L \frac{C_i^2 U^2}{\varepsilon A} \quad (2.26)$$

where L is the length of the cantilever arms and C_i is the capacitance of an ideal parallel plate capacitor ($\varepsilon A/d$). The measured capacitance is equal to C_i in addition to a correction term C_f (corrected from [54]) which takes into account the finite size of the electrodes forming the capacitor. The capacitance is then expressed as

$$C = C_i + C_f = \frac{\varepsilon A}{d} + \varepsilon \frac{c_e}{\pi} \ln \frac{\sqrt{A}}{d} \quad (2.27)$$

where c_e is the circumference of the smaller electrode.

As mentioned in the previous section, the relationship between the torque and Δd is linear, and if we consider only the second order term in Eq. (2.18) then we end up with the following form of ΔC ,

$$\Delta C = K_c \tau + \alpha K_c^2 \tau^2 \quad (2.28)$$

where K_c is expressed in [F/Nm] and it is a calibration constant to be determined, while α is a parameter which corrects for the non-linear response of the torque meter. Substituting for τ from (2.26) we get

$$\Delta C = 0.7LK_c \frac{C_i^2 U^2}{\varepsilon A} \left(1 + 0.7\alpha LK_c \frac{C_i^2 U^2}{\varepsilon A}\right) \quad (2.29)$$

The calibration routine can be thus easily performed by recording the change in the capacitance versus the applied dc voltage. K_c and α are fitting parameters to be obtained from the ΔC versus U plot. C_i is calculated by subtracting C_f from the measured capacitance value at zero applied dc voltage. Figure 2.19 shows the calibration measurement for torque meter EP0105, and Table 2.1 lists the calibration parameters for three different torque meters. From the fit, we extract a $K_c = 2.24(4) \times 10^{-8}$ fF/Nm and $\alpha = 0.0018(3)$ for this particular torque meter.

In most of the studied systems in this work, the absolute value of the torque signal was of minor importance. In fact, most of the studied crystals were rather fragile and sensitive to air, thus it was advantageous to place the crystal directly on the cantilever and cover it with grease then cool it down and perform the measurements without weighing the crystal beforehand.

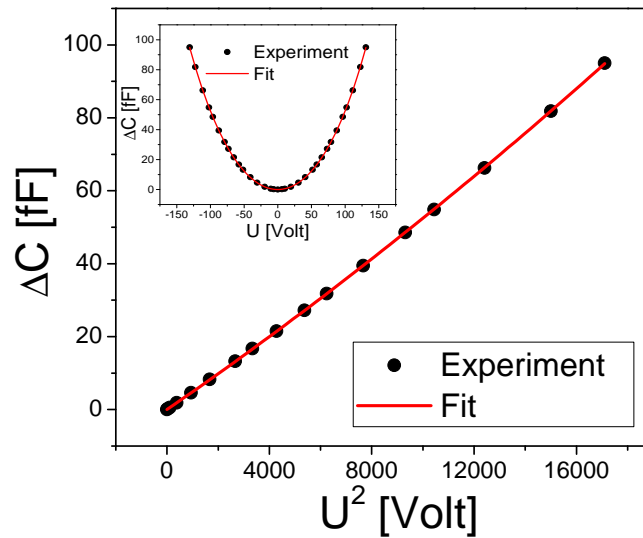


Figure 2.19: The capacitance change plotted versus the dc applied voltage for the torque meter EP8090 at 1.8 K. The inset illustrates the quadratic dependence on U .

Table 2.1: Calibration parameters of three different torque meters which cover the operation range of $10^{-11} - 10^{-6}$ Nm. The name *EP2530* for example stands for a torque meter with EPoxy base plate, with a cantilever of thickness 25 microns, and a separation distance of 30 microns.

Torque-meter	C_i [fF]	K_c [F/Nm]	α	$1/K_c$ [Nm/fF]	Range [Nm]
<i>EP2530</i>	4800	$1.00(4) \times 10^{-5}$	0.0024(3)	1×10^{-10}	$10^{-11} - 10^{-8}$
<i>EP2560</i>	1797	$8.2(2) \times 10^{-7}$	0.0059(5)	1.2×10^{-9}	$10^{-10} - 10^{-7}$
<i>EP8090</i>	2913	$2.24(4) \times 10^{-8}$	0.0018(3)	4.4×10^{-8}	$10^{-9} - 10^{-6}$

2.3.4 Cantilever design

Beam theory [55] was used to calculate the elastic curve of the cantilever beam under a certain load. This helped us in predicting the dimensions of the cantilevers to be produced to cover a wide range in sensitivity (10^{-6} - 10^{-11})Nm . Figure 2.20 (a) shows the basic design of the cantilever. The hosting area on top of which the sample is fixed (at the center O) was made large enough to contain large/long single crystals. The stiffness of the beam was then dramatically reduced by narrowing the arms of the cantilever beam. A double-armed lever was used in order to minimize the lateral force constants and thus minimize the response of the torque meter to a torque in the x or z direction. The minimum change in the capacitance value that can be detected is limited by the resolution of the bridge. This is around 0.1 fF including the effect of thermal noise and external vibrations. The sensitivity of the torque meter is determined by the

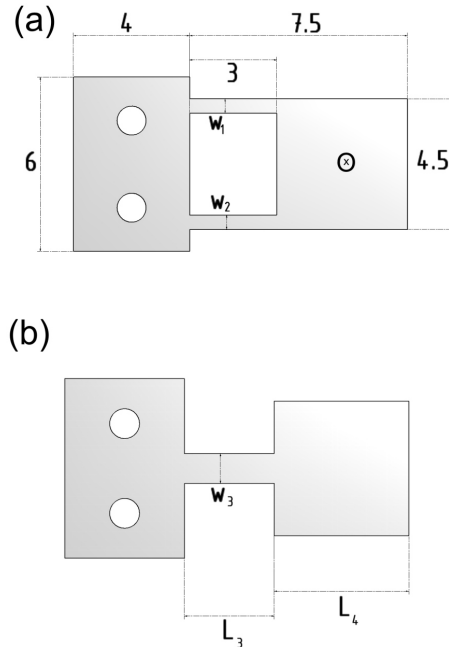


Figure 2.20: (a) Schematic drawing of the double-armed cantilever used. The dimensions are given in mm. The crossed circle is the hosting area where the sample is typically placed. (b) A single armed beam which is used to simulate the double armed beam in the beam theory calculations.

minimal torque signal that can be resolved τ_{min} . This is defined as the torque which can displace the cantilever by a distance δz_{min} , and consequently induce a capacitance change $\delta C_{min} \approx 0.1$ fF. We have therefore calculated δz_{min} as a function of the force applied (or the torque) and as a function of the dimensions and mechanical properties of the cantilever.

In order to simplify the calculations, we modeled the cantilever by a single arm lever (2.20 (b)). The width of the single arm w_3 is taken to be the sum of the widths of both arms w_1 and w_2 , and it is placed symmetrically at the center between arm 1 and arm 2. The single arm lever is considered to be a composite beam consisting of two parts having different moments of inertia about the neutral axis. Figure 2.21 shows the two parts AB (hosting area) and BC (the combined arms) and the static forces experienced by the two parts. The effect of the magnetic torque is simulated by a homogenous force placed at the center of the hosting area O. The relationship between the deflection ν and the internal moment $M(x)$ is given by [55],

$$EI \frac{d^2\nu}{dx^2} = M(x) \quad (2.30)$$

where E is the material's modulus of elasticity and I is the beam's moment of inertia coupled around a neutral axis. This is a general relationship which can be applied to any elastic beam if its material is homogenous and if it behaves in a linear-elastic manner. $\nu(x)$ can be calculated by integrating twice after evaluating the internal moment as a function of x and taking into account the corresponding boundary conditions. The maximum deflection ν_{AB} and ν_{BC} (at the points B and C) of the two individual beams AB and BC respectively is given by,

$$\nu_{AB} = \frac{FL_3^3}{3EI_{AB}} + \frac{FaL_3^2}{2EI_{AB}} \quad (2.31)$$

$$\nu_{BC} = \frac{FL_4^3}{6EI_{BC}} \left(\frac{3a}{L_4} - 1 + \left(1 - \frac{a}{L_4}\right)^3 \right)$$

where I_{AB} and I_{BC} are the moments of inertia of AB and BC respectively and they are given by,

$$I_{AB} = \frac{w_3 t^3}{12} \quad (2.32)$$

$$I_{BC} = \frac{w_4 t^3}{12}$$

where t is the thickness of the cantilever. The total deflection of the cantilever at the tip is given by,

$$\delta z_{tip} = \nu_{BC} + \nu_{AB} + \theta_3 L_4 \quad (2.33)$$

θ_3 is the maximum slope of the beam AB at the point B and it is expressed as

$$\theta_3 = \frac{FL_3^2}{2EI_{AB}} + \frac{FaL_3}{EI_{AB}} \quad (2.34)$$

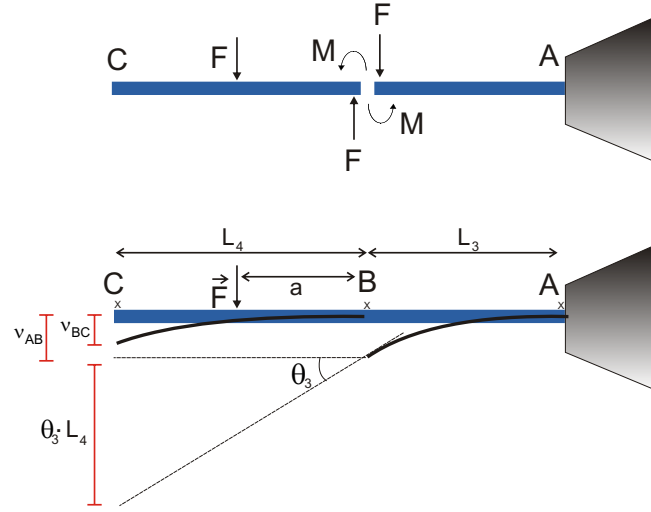


Figure 2.21: The static forces (upper picture) acting on the composite beam and the corresponding deflections (lower picture) upon the application of a force F are shown.

The average deflection of the hosting area is then taken as the average of the deflection at the point B (ν_{AB}) and that at the tip δz_{tip}

$$\delta z_{av} = \frac{\delta z_{tip} + \nu_{AB}}{2} \quad (2.35)$$

Using equation 2.19 we can rewrite the capacitance change as

$$\Delta C = C_o \frac{-\delta z_{av}}{d_o + \delta z_{av}} \quad (2.36)$$

Keeping in mind that the right sign of δz_{av} has to be used, the above expression enables us to estimate the minimum value of F (and consequently τ) which can induce a ΔC of 0.1 fF, and hence choose the suitable dimensions of the cantilever to cover the sensitivity range of interest. Several assumptions were made in calculating the deflection curve of the beam. In order to confirm the above results, we have used a finite element analysis software CATIA (Computer Aided Three Dimensional Interactive Application) to calculate the deflections of the actual beam. Figure 2.22 (a) shows the meshing of the cantilever beam with triangular finite elements of size 0.1mm (smaller element sizes lead to more accurate results at the expense of a larger computation time). A remarkable agreement between the analytically calculated elastic curve and the simulated ones using finite element theory was obtained (see below).

To demonstrate the procedure of calculation used for designing the torque meters, let us take the torque meter EP2530 in Table 2.1 as an example. This torque meter has a cantilever of thickness $25 \mu\text{m}$ and a separation distance d of $30 \mu\text{m}$. Using the dimensions of the cantilever shown in Figure 2.20 (a), the calculated average deflection for a torque of 10^{-11} Nm , according to equation 2.34, is 6.02 \AA . This change in the

separation distance leads to a change in the capacitance, given by Eq. (2.36), of 0.1271 fF, which can be easily resolved by the ac bridge. The calibration of this torque meter indeed agrees with the above predictions, within the experimental error, and shows that the sensitivity of the torque meter EP2530 goes down to 10^{-11} Nm, thus enabling us to resolve deflections of approximately 1 nm. The same cantilever was simulated with CATIA. Figure 2.22 (b) shows the analyzed beam and the deflection values of the elastic curve are shown in Figure 2.22 (c). The deflection at the center of the beam is around 5.8\AA which is in a very good agreement with the analytical value of 6.02\AA .

One additional factor was taken into account while designing the cantilevers and that is the eigenfrequency of the beam. The ac bridge applies a V_{rms} of a 1 kHz frequency, with ac voltages up to 15 Volts. If the eigenfrequency is close to 1 kHz, the bridge will drive the cantilever at a 1 kHz frequency and induce vibrational noise due to the electrostatic force between the cantilever and the lower plate. We have used the software ETBX (EngineersToolBox) to calculate the eigenfrequencies of the various beams to be between 100 and 500 Hz which is far away from the bridge operating frequency. In addition, measuring the capacitance versus different ac voltages V_{rms} did not show any dependence of either the absolute measured capacitance nor the noise level on V_{rms} .

2.4 Insert

A dedicated home made insert was developed to carry out torque measurements in an 10 Tesla Oxford Cryomag. The insert is fitted with a stepper motor, a cylindrically shaped Cernox temperature sensor, a 30 W heater, two low noise coaxial cables, and a horizontal rotating stage. Figures 2.23 and 2.24 show a schematic drawing and a picture of the developed insert, respectively.

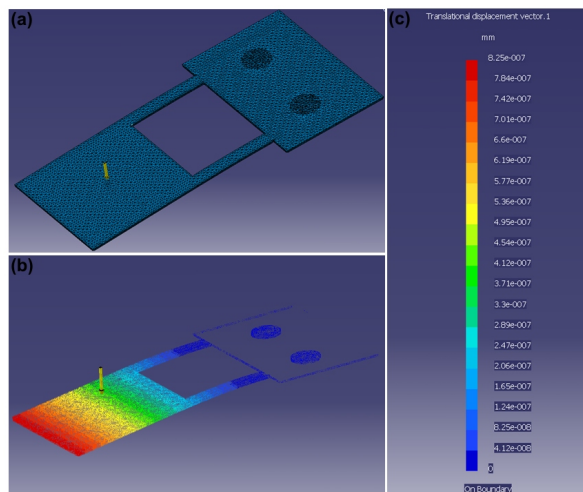


Figure 2.22: (a) The mesh describing the cantilever with the finite elements taken as triangles. (b) The deflection of the cantilever under a force F centered at the middle of the hosting area. The values of the deflection are shown in the tree in (c).

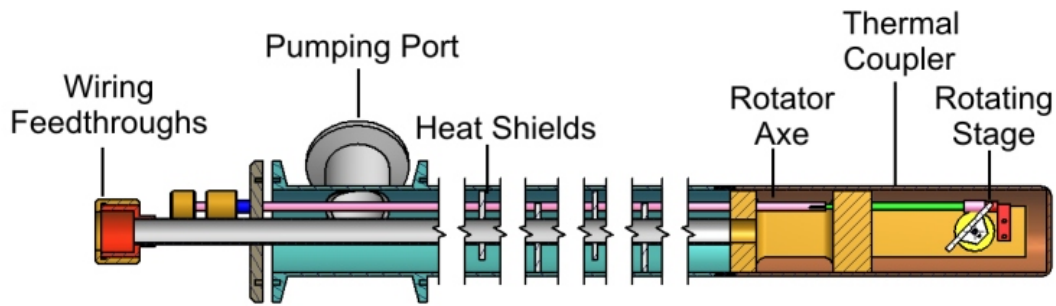


Figure 2.23: A schematic drawing of the developed insert.

The temperature sensor was calibrated between 1.3 and 300 K by measuring its dc resistivity using a four probe dc method. Low noise Axon coaxial cables (RG L 196) of nominal outer diameter of 2.03 mm and 50 ohm impedance were employed in the insert. The same coaxial cables were used in between the insert and the bridge terminals. The inner conductor of the cables is a non magnetic silver plated copper alloy, while the dielectric is extruded PTFE. A special semiconducting layer of graphite between the core and the screen is added to decrease audio noise due to oscillations, vibrations...etc. The cables were not designed to perform at liquid Helium temperatures, but several tests showed that they can be used at these temperatures. In order to measure correct absolute values of the capacitance, the low and high terminals of the capacitance bridge must "see" each other only across the terminals of the capacitor. This is particularly important in performing angle resolved measurements as the relative positions of the cables may change during rotations, thus leading to an extrinsic capacitance change if the inner conductors are not well shielded. To that end, we have assembled home made shielded wires which were wrapped around the rotating gear and connected to the terminals of the coaxial cables. The coaxial cables themselves could not be used for that purpose since they have a large diameter and could not be wrapped around the gear. In addition, the inner dielectric and external sheath of the cables easily break if continuously rotated at low temperatures. The home made cables were thus made from a 0.15 mm copper inner conductor with an insulating layer on its outer surface. The copper wire was further isolated by covering it with a thin insulating layer of diluted GE-varnish then wrapped with thin teflon wires (of diameter ca. 0.1 mm). The wrapped copper wires were inserted into hollow-like screening wires made out of silver plated copper of 1 mm diameter to have the copper wires shielded. The copper wires were connected to the inner conductors of the coaxial cables and the shields were connected to the outer screening of the coaxial cables as well. The other terminals of the wires were then connected to the electrodes of the capacitor. Meticulous care was taken in the finishing and assembly of the wires. This enabled us to perform angle resolved measurements with high precision as the capacitance was independent of any change in the cable positions. An add-on external chamber was produced into which the sample holder is inserted to perform measurements above liquid helium temperatures (Figure 2.24). The insert together with the external chamber were then

inserted into the variable temperature insert (VTI). Above 4.2 K, the sample is cooled down by helium flow. The external chamber prevents the helium gas flowing from inducing vibrations in the cantilever by encapsulating the whole insert. The sample is then cooled down by controlling the exchange gas in the chamber and the Helium flow rate in the VTI. In addition, the chamber enables a precise control of the pressure which does affect the absolute value of the capacitance. The chamber was made out of stainless steel to minimize the thermal loads into the VTI, however the lower piece was made out of copper to enhance the thermal coupling between the chamber walls and the insert.

Rotating stage

A so called Swedish rotator was designed and produced to enable the rotation of the sample around a horizontal axis in a vertical magnetic field. Figure 2.25 shows the basic design of the rotator. The principal components consist of a pin head, a spindle, a worm drive, a worm gear, an end cap, and a rotating stage. The pin head couples the spindle to the external rotating axe. The spindle is incorporated into the rotating axe over 1 cm to account for thermal contractions. The rotation of the axe, controlled by a stepper motor, causes both the spindle and consequently the worm drive to rotate

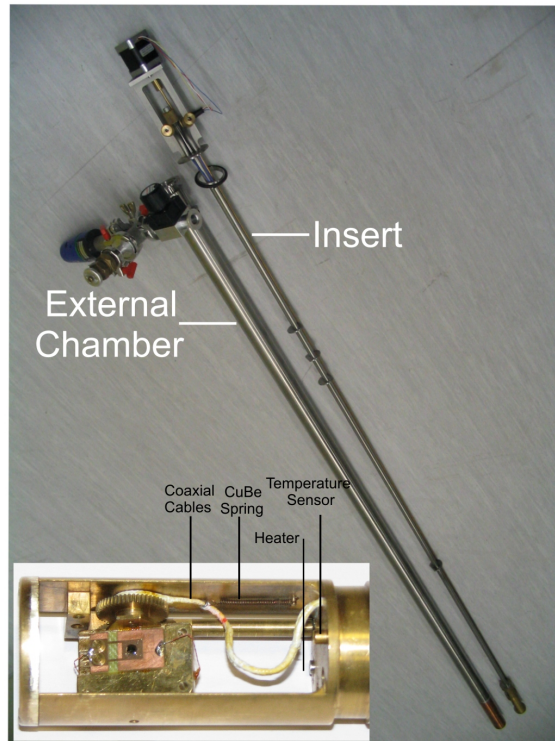


Figure 2.24: Torque magnetometry insert together with the external chamber. The inset shows the head of the insert where the temperature sensor, heater, and the rotating stage are located.

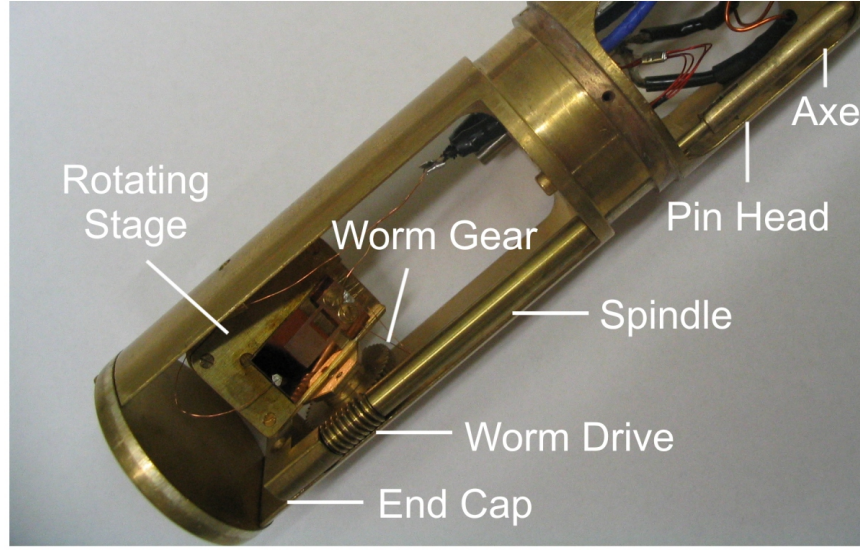


Figure 2.25: A schematic drawing of the various components of the rotator.

around a vertical axis. The worm drive in turn is coupled to the worm gear and causes both the gear and the rotating stage fixed to it to rotate around a horizontal axis. The gear has a feed-through to allow for the two shielded wires to be connected to the torque meter fitted on top of the rotating stage. The shielded wires are fixed to a CuBe spring which keeps the wires back-stretched and facilitates the rotation process back and forth. All the components of the rotator were made out of brass to ensure a homogenous thermal contraction of all the components at low temperatures.

The worm gear ratio is given by n_1/n_2 where n_1 is the number of teeth of the worm gear and n_2 is that of the worm gear drive ($n_2 = 1$ since the worm drive acts as a single toothed gear). The worm gear we used has 50 teeth, thus for one full rotation of the driving worm, one expects a rotation of the gear by $360/n_1 \approx 7.2^\circ$. This value may vary depending on the precision of the manufactured gear. To that end, we have calibrated the rotation of the stage by pointing a laser at mirror fixed on top of the stage. We have tracked the change of the laser reflection on a wall ~ 3 m away. Figure 2.26 shows a schematic diagram of the calibration setup. The incident laser beam is reflected on the mirror M and the reflected beam R_1 hits the wall at the point C. If the stepper motor is rotated by x steps, the stage/mirror will rotate by an angle θ , and consequently the reflected beam R_2 will hit the wall at the point D. Measuring the distances AB, BC, and CD enables us from calculating the corresponding θ value using the following equation,

$$\theta = \frac{\alpha_1 - \alpha_2}{2} = \frac{\tan^{-1}\left(\frac{BD}{AB}\right) - \tan^{-1}\left(\frac{BC}{AB}\right)}{2} \quad (2.37)$$

Rotating the driving worm by 360° gives us a value of $\theta \approx 7.17^\circ$ which is consistent with the predicted value of 7.2° . This process is not very reproducible though, and it

strongly depends on the laser/mirror alignment. We found that rotating the mirror by 360° and altering the number of steps to reproduce the position of the laser spot on the wall was more efficient. The number of steps to rotate the stage by 360° is approximately 20056 steps. This is equivalent to $\sim 0.07^\circ$ per step, thus defining the resolution of the rotation to be approximately 0.1° .

Computer control

All the instruments were controlled through home written Labview computer codes or virtual instruments (VIs) . Four independent VIs were developed to independently control the capacitance bridge, the temperature controller (Oxford ITC503), the stepper motor, and the magnet power supply (Oxford IPS500232). In addition these VIs were merged to create other main VIs to perform various tasks:

1- "CapVsAngle": A VI to control capacitance versus angle measurements with a certain step in degrees performed at a certain temperature and fixed magnetic field. The user sets an initial angle, a target angle, a step in degrees, and a fixed magnetic field value. The output data file contains the values of the angle, capacitance, loss, temperature, magnetic field, and the average time (AV) of the bridge at each data point.

2- "CapVsField": A VI to control capacitance versus field measurements with a certain step in tesla performed at a certain temperature and fixed angle. Here the user is prompted to set the initial field, target field, the step in tesla, and the angle. The output data file again contains the values of the magnetic field, capacitance, angle, loss, and temperature at each data point. The software in addition automatically gives the value of ΔC by subtracting the capacitance at each point from that recorded at

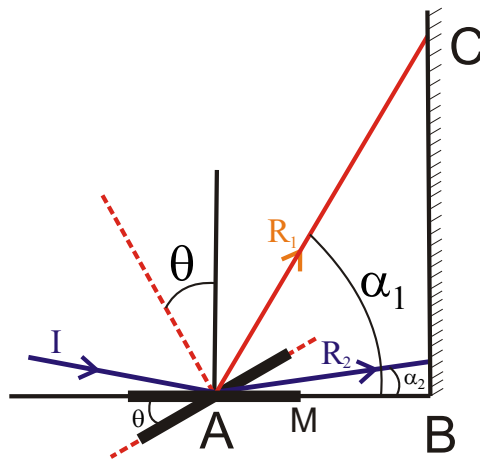


Figure 2.26: A schematic diagram showing the calibration setup of the rotator.

the initial field. In addition, this code generates a log file which has the same name as the data filename and includes the time and date at which the measurements were performed. The log file includes information inserted by the user such as the name of the sample, its mass, the orientation of the crystal, and user comments.

3- "CapVsTemperature": A VI to control capacitance versus temperature measurements. The user chooses the initial temperature T_i , final temperature T_f , a step t_s , the value of precision ϵ , and the number of loops to wait n_l (this is equivalent to a waiting time). The software then gives an order to the temperature controller to set the initial temperature T_i and wait for a number of loops n_l then measure the capacitance and proceed to the next temperature $T_f + t_s$. The number of loops is counted only if the current temperature T_c is within the precision limit (i.e. $|T_c - T_i| < \epsilon$). This option is installed to ensure the stability of the temperature before performing any measurement and proceeding to the next temperature. The output datafile contains the values of the magnetic field, temperature, capacitance, and loss.

2.5 Exploiting the experimental setup

In this section we show how an experimentalist can exploit his experimental setup to its maximum extent. We illustrate how do we exploit different features of the setup to get information about the orientation, temperature, and magnetic axes of the sample or even about extrinsic effects which are not directly related to the sample itself.

2.5.1 Crystal orientation

As already mentioned, the precise orientation of the crystal is crucial in torque measurements. With the aid of an optical microscope, one is able to align the sample with a precision of few degrees. Commercial systems that are enabled with rotating stages are usually equipped with a feedback loop in order to find the zero point position of the stage ($\theta=0$). In our system, we utilize the dependence of the capacitance on the cantilever and the crystal's weight in order to find the zero point position and precisely orient the crystal. Figure 2.27 shows the capacitance versus angle of a bare cantilever. The change in the capacitance is solely due to the weight of the lever itself. At 90° , the cantilever's weight pulls it towards the base plate thus decreasing the separation distance d and consequently maximizing the capacitance value. Similarly, we observe a minimum in the capacitance at 270° . The weight of the crystal on top of the cantilever enhances the the peak in the capacitance. This enables us to determine the 90° (or 270°) angle "in situ" with a precision of 0.2° . This is particularly important as one often loses the exact position of the rotating stage due to a failure in the stepper motor, rotating axis, or the controlling software.

2.5.2 Temperature calibration

Recording temperatures precisely is of the utmost importance in torque measurements, especially for determining the breaking field B_{Br} . The capacitance of a double plate

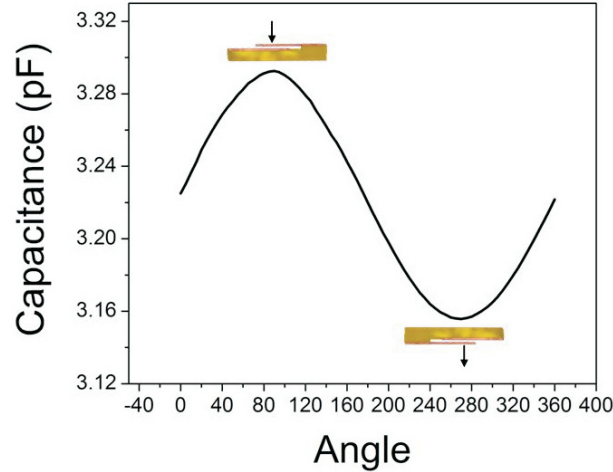


Figure 2.27: Capacitance of a bare cantilever. The insets show the corresponding cantilever orientation at 90° and 270°

capacitor depends on the dielectric constant of the dielectric separating both plates as shown in Equation 2.13. At temperatures below 4.2 K, liquid helium covers the cantilever and the temperature sensor. We allow the condensation of liquid helium by increasing the gas pressure in the sample chamber or increasing the needle valve throughput in the VTI. Having liquid Helium covering the torque meter is advantageous as it ensures a perfect thermal coupling and thus, provides a very high precision on the recorded temperatures. The presence of liquid Helium is detected by observing a sudden jump of the capacitance due to the change in the dielectric constant from that of vacuum, to the one of liquid helium. Figure 2.28 shows the sudden increase of the capacitance after having liquid Helium in between the capacitor plates.

Moreover, the dielectric of liquid helium is strongly temperature dependent between 1.5 and 4.2 K [56]. We have measured the dielectric constant by recording the capacitance with (C_{Liquid}) and without (C_{vacuum}) liquid helium.

$$\varepsilon_{He} = \frac{C_{\text{Liquid}}}{C_{\text{vacuum}}} \quad (2.38)$$

Figure 2.29 shows the temperature dependence of the dielectric constant of liquid Helium II. There is a good agreement with the reported experimental and theoretical values ([56][57]). In theory, by using this approach one can perform a precise calibration of the temperature sensor. The slight disagreement to the reported values, is probably due to the fact that the vacuum measurement is not performed at UHV. For the purpose of our experiment, the peak at 2.17 K was sufficient to check the validity of temperatures shown by the sensor. One important observation is the increase of the noise level above 2.17 K. Below 2.17 K, liquid Helium is a superfluid which does not boil. Between 2.17 and 4.2 K, the liquid behaves just as a normal fluid which boils thus releasing bubbles that in turn lead to a considerable noise level. To that end, most of the measurements performed above 2K were performed using exchange gas as thermal coupler and not liquid Helium.

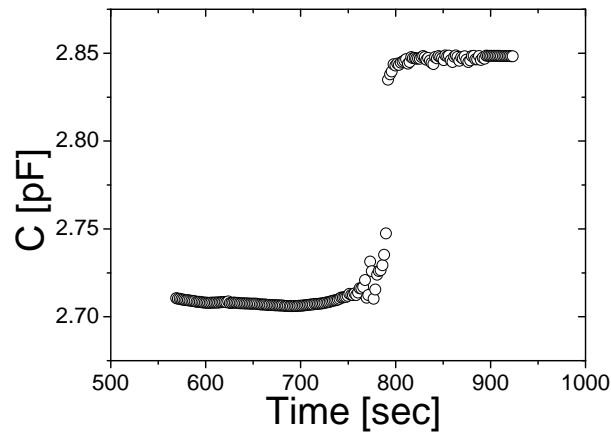


Figure 2.28: Observation of liquid Helium in between the plates of the capacitor. The capacitance jumps from 2.706 pF to 2.848 pF which corresponds to a change of the dielectric constant from 1 to 1.05 (the dielectric of liquid helium at 4.2K).

2.5.3 Remnant field

Another important aspect in magnetic measurements is the precision of the external magnetic field applied. Having absolute zero field is of particular importance for performing zero field cooled measurements. Superconducting magnets usually retain remnant magnetic fields due to trapped flux lines. The value of this remnant field depends on the history of the magnet. For example if the field was swept up to the maximum

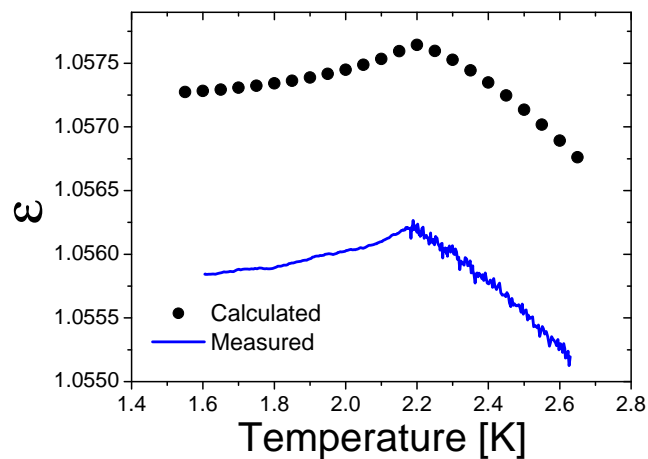


Figure 2.29: The measured and calculated (from [57]) dielectric constant of liquid Helium at saturated vapor pressure. The reference vacuum capacitance was measured at around 0.1 mbar.

field (10 Tesla in our case), the remnant field will be higher than that remaining after having a lower field. One can always insert a tesla-meter and place it precisely in the center of the field in order to measure the remnant field. This requires a special insert though, and it is not very practical to repeat this process prior to any measurement. Another rather simple way to determine the remnant field is to utilize the torque of the sample itself. The torque is directly proportional to the external magnetic field applied and therefore it should vanish at absolute zero applied field. Sweeping the field from $-B_o$ to $+B_o$ enables us to obtain the value of the remnant field. Figure 2.30 shows such a measurement where the torque was measured at 5K and the magnetic field being at 5° from the easy axis of a Mn_{12} acetate single crystal. The experiment can be performed practically at any temperature and angle where the torque has an appreciable value. The minimum in the torque signal in this case corresponds to zero torque value and the corresponding magnetic field is the remnant magnetic field. The remnant field determined in this measurement is 84 gauss, which is a typical value for these superconducting magnets.

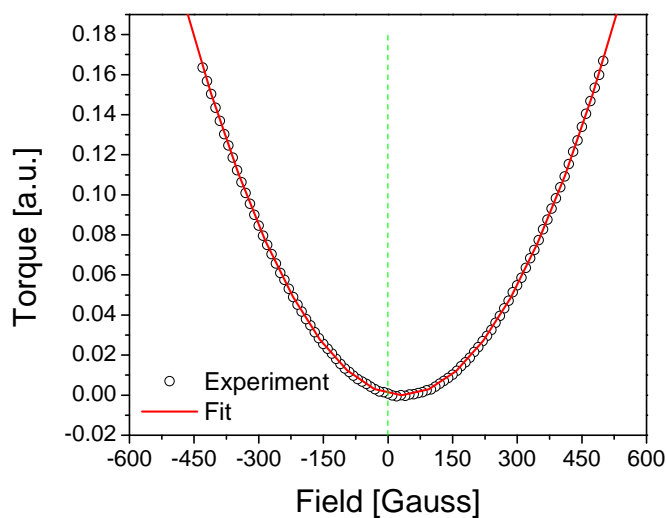


Figure 2.30: Torque signal of a Mn_{12} acetate single crystal between -500 and +500 Gauss. The remnant field is around 33 Gauss where the torque signal is minimum.

Chapter 3

Breakdown of the Giant Spin Model in Mn₆ SMM

3.1 Introduction

Increasing the energy barrier against the reversal of magnetization in single molecule magnets (SMMs) has been the focus of numerous studies in molecular magnetism. Despite the combined efforts of chemists and physicist to find suitable systems that could retain the magnetization for long time at high temperatures, Mn₁₂-acetate was the system with the highest blocking temperature and anisotropy barrier of 3.5 K and 74.4 K, respectively, until recently [58]. In general, the relaxation time in the classical regime can be modeled using the Arrhenius law given by [59],

$$\tau = \tau_0 \exp\left(\frac{U}{k_B T}\right) \quad (3.1)$$

Accordingly, there are two main factors that can affect the relaxation time τ . Firstly, the anisotropy barrier, given in a first approximation by $U \sim DS^2$ (D is the axial anisotropy parameter), has to be large enough to prevent the reversal of the magnetization via a classical thermally activated, multi-step Orbach process mediated by spin-phonon interactions. This can be achieved by the simultaneous increase of D and S , two variables that are intrinsically linked together [39]. Secondly, the pre-exponential factor τ_0 in the Arrhenius law, that is linked to the difference in energy between the upper states in the energy level diagram, has to be large [59]. In addition to the classical relaxation mechanism, the quantum tunnelling of the magnetization (QTM) that characterizes the very low temperature spin dynamics of SMMs, has to be minimized, since it provides a short path for the relaxation of the magnetization. In this chapter, we describe a class of Mn³⁺ based clusters that made a step forward in elevating the anisotropy barrier in SMMs. Furthermore, these systems have served as prototype models to study the different factors playing a role in the relaxation mechanism. The two compounds to be discussed belong to a family of hexanuclear Mn³⁺ clusters (from now on Mn₆) which, despite of their similar nuclear structure, display a rich variety of spin ground states and anisotropy energy barriers [60][58]. The six

Mn^{3+} ions are arranged in two triangles, with dominant ferromagnetic (FM) exchange interaction between, and within, the two triangles. It has been found that the nature of the intra-triangle exchange interaction can be switched from antiferromagnetic (AF) to FM by substituting the moiety bridging the Mn^{3+} ions, leading to a change of the ground state from a low spin ($S = 4$) to a high spin state ($S = 12$) [60]. Furthermore, deliberate structural distortions have been successfully used to tune the values of the exchange interactions [58]. The isotropic exchange interaction, and consequently the overall anisotropy barrier, has thus been found to be very sensitive to the structural details. It is therefore quite important to accurately determine the exchange interactions for different structures to deduce magneto-structural correlations. Eventually, this information can be used to engineer new clusters with selectively modified molecular structures that match the optimized conditions for the desired magnetic properties.

We investigated two members of a family of Mn_6 clusters, with chemical formulae, $[\text{Mn}_6\text{O}_2(\text{Et-sao})_6(\text{O}_2\text{CPh}(\text{Me})_2)_2(\text{EtOH})_6]$ (compound **(1)**), and $[\text{Mn}_6\text{O}_2(\text{Et-sao})_6(\text{O}_2\text{CPh})_2(\text{EtOH})_4(\text{H}_2\text{O})_2] \cdot 2\text{EtOH}$ (compound **(2)**) [58][60][61]. The two molecules display very similar structures consisting of six Mn^{3+} ions ($s = 2$), which are arranged in two staggered triangular units related by an inversion center (see Figure 3.1). The only structural difference between the two molecules resides in the organic ligand cages, in proximity of the transition metal ions. The coupling between the magnetic ions occurs via superexchange pathways involving oxygen and nitrogen ions. Since the exchange interactions are very weak (≈ 1 meV), the magnetic properties of the clusters are found to be extremely sensitive to intramolecular bond angles and distances. Even small structural distortions have tremendous impact on the spin relaxation dynamics of the system. Systematic synthesis and studies of various members of the Mn_6 family has evidenced that the nature of the coupling is extremely sensitive to the intra-triangular Mn-O-N-Mn torsion angles [62][63]. There is a critical value for the torsion angle of $\sim 31^\circ$, above which the pairwise exchange interaction switches from antiferromagnetic to ferromagnetic, while a further enhancement of the angle increases the strength of the FM interaction. Molecules (1) and (2) have the same spin ground state $S = 12$, but despite their very similar structures, the two molecules have different effective energy barriers ($U_{\text{eff}} \approx 86.4$ K for (1) and $U_{\text{eff}} \approx 53$ K for (2)).

In order to unveil the mystery behind the different anisotropy barriers in the two compounds, we performed frequency domain magnetic resonance spectroscopy (FDMRS) and inelastic neutron scattering (INS) measurements on both systems. This particularly enabled us to look at the low lying spin excitations and consequently map the energy spectra of the systems. The results show how the exchange interaction in these molecules plays a crucial role in determining the relaxation of the magnetization and how it affects the QTM in SMMs. The two techniques give complementary information that is not accessible by other techniques, enabling the accurate determination of the microscopic spin Hamiltonian parameters and the understanding of the spin dynamics. The FDMRS measurements show an unprecedentedly large number of spin excitations within the ground spin state multiplet. These transitions were observed in the INS as well but more importantly, the INS spectra show the transitions to other higher energy spin multiplets which enabled us to determine the energy separation between these different multiplets in both compounds. The accurate determination of the

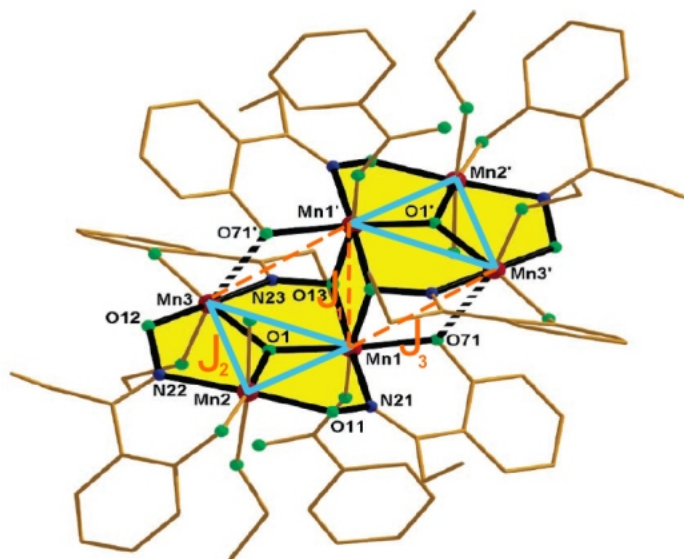


Figure 3.1: The molecular structure of $[\text{Mn}_6\text{O}_2(\text{Et-sao})_6(\text{O}_2\text{CPh})_2(\text{EtOH})_4(\text{H}_2\text{O})_2]\cdot 2\text{EtOH}$ (compound (2)) highlighting its core [Mil07a].

spin Hamiltonian parameters has provided a conclusive evidence to explain the different magnetic properties of the two molecules. The results give an insight into the effect of the low-lying spin excited states onto the relaxation dynamics of the magnetization.

3.2 Results and discussion

3.2.1 FDMRS

FDMRS measurements were performed by using a previously described spectrometer [18](See Chapter 1). The samples were all ground and pressed into polycrystalline powder pellets of 10 mm diameter. Figure 3.2 shows FDMR transmission spectra on a pellet of mass = 240.8 mg, and thickness = 3.05 mm of compound (1) (a), and a pellet of mass = 283.44 mg, and thickness = 2.78 mm of compound (2) (b). The spectra were recorded at various temperatures between 2 and 40 K using linearly polarized radiation in the frequency range 2-17.5 cm^{-1} (only the frequency range where the transitions are observed is shown). All spectra were recorded in the absence of an external magnetic field. A temperature independent oscillating baseline caused by the interference of the monochromatic radiation between the parallel surfaces of the sample was fitted over the spectrum measured at 40 K with the resulting value of a real ($\epsilon' = 3.59$) and complex ($\epsilon'' = 0.012$) components of the dielectric permittivity for compound (1) and $\epsilon' = 3.01$, $\epsilon'' = 0.049$ for compound (2). Figure 3.3 shows the spectra normalized (i.e. divided) by the 40 K spectrum. The normalized spectra allow us to precisely determine the resonance frequencies eliminating the effect of the oscillating baseline. We have used the giant spin Hamiltonian (GSH) in order to calculate the energy spectra of

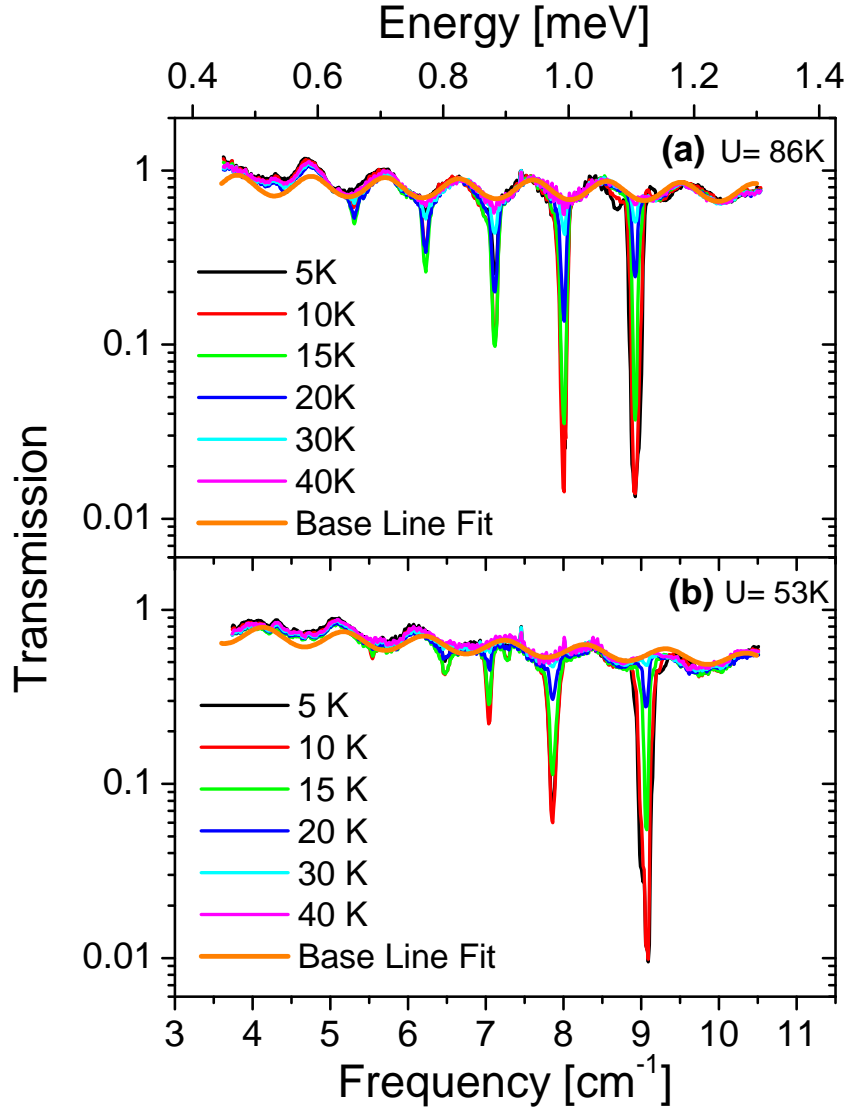


Figure 3.2: FDMR spectra of compound (1) and (2) are shown in (a) and (b), respectively, at various temperatures. The baseline fit describes the Fabry-Pérot like interferences between the parallel surfaces of the sample.

the two systems and consequently fit the GSH parameters to reproduce the observed intramultiplet transitions,

$$\hat{H} = D\hat{S}_z^2 + E(\hat{S}_x^2 - \hat{S}_y^2) + B_4^0\hat{O}_4^0 \quad (3.2)$$

Table 3.1 shows the experimental frequencies of the absorption lines and the calculated ones obtained using the best-fit parameters [$D = -0.362(1) \text{ cm}^{-1}$, $B_4^0 = -6.0(4) \times 10^{-6} \text{ cm}^{-1}$] for (1) and [$D = -0.372(1) \text{ cm}^{-1}$, $B_4^0 = -3.09(5) \times 10^{-6} \text{ cm}^{-1}$] for (2). Figure 3.4 shows the calculated spectra with the above ZFS parameters at 10 K. The experimental lines are much narrower ($11 \mu\text{eV}$ FWHM) than those observed for other SMMs,

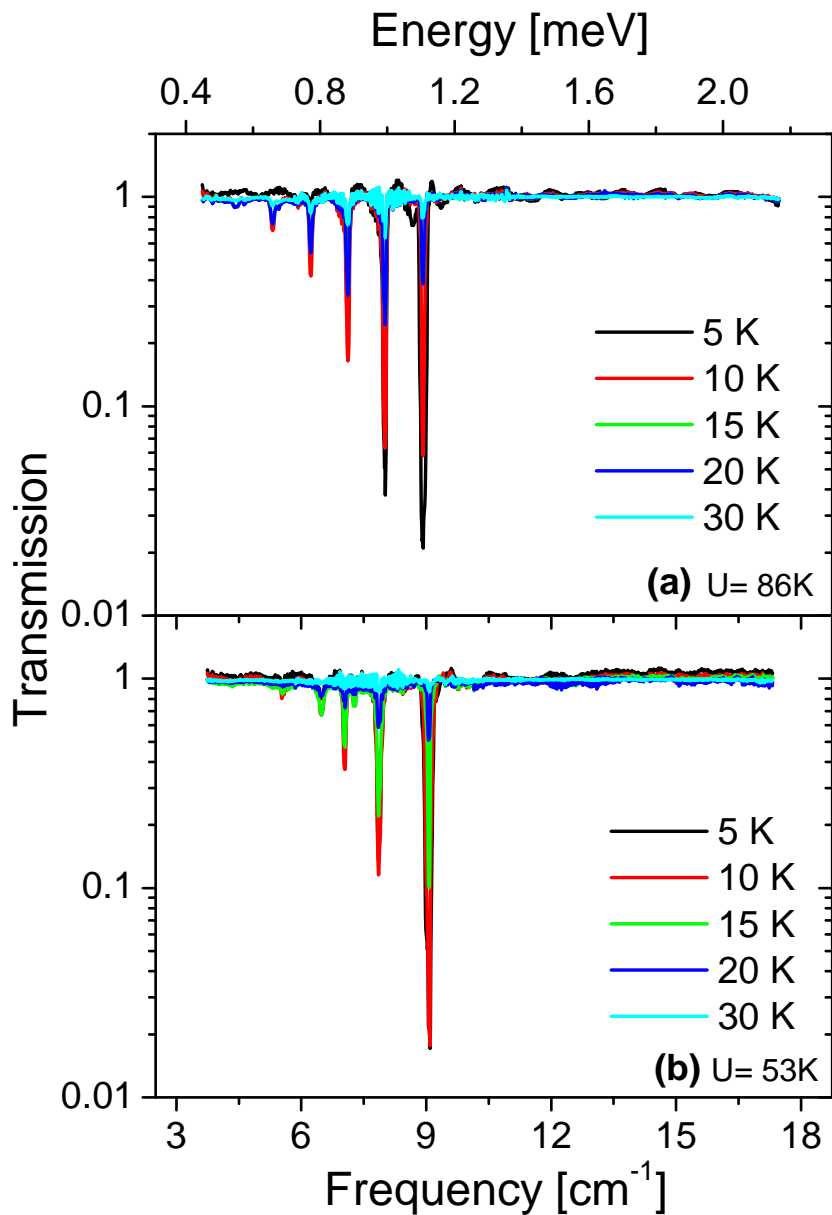


Figure 3.3: FDMR spectra of compound (1) and (2) are shown in (a) and (b), respectively, at various temperatures. The spectra are normalized by the 40 K spectrum.

e.g. $23 \mu\text{eV}$ FWHM for $\text{Mn}_{12}\text{acetate}$. The ZFS values are in themselves not remarkable, and close to those reported for other manganese clusters with similar ground state spins, e.g. $D_{S=10} = -0.457 \text{ cm}^{-1}$ for $\text{Mn}_{12}\text{acetate}$ [64], $D_{S=17/2} = -0.247 \text{ cm}^{-1}$ for Mn_9 [65]. Interestingly, the fourth order axial ZFS is an order of magnitude smaller than for Mn_{12}Ac . This type of ZFS is currently accepted to parameterize effects of mixing between spin multiplets (S-mixing) [66], which would mean that S-mixing is only limited, contrary to expectation. However, the fit (Figure 3.4) does not simulate the resonance line positions satisfactorily, which is in contrast to the situation for other molecular

Table 3.1: A list of the experimentally obtained and calculated resonance frequencies for compounds (1) and (2). All the frequencies are given in cm⁻¹.

	1	2	3	4	5	6
Compound (1)						
Experiment	8.92(1)	7.99(2)	7.11(1)	6.22(1)	5.32(2)	4.43(5)
Calculated	8.96	7.99	7.06	6.19	5.36	4.57
Compound (2)						
Experiment	9.05(1)	7.86(3)	7.04(1)	6.48(2)	5.54(3)	-
Calculated	8.88	8.01	7.16	6.34	5.54	4.76

nanomagnets that feature strong S-mixing, e.g. Ni₄ [67]. The agreement between the calculated and experimental values seems to be better for compound (1) than that of (2). The inclusion of transverse terms in the Hamiltonian did not improve the fit. The spectra as well as the extracted anisotropy parameters of both compounds are very similar. In fact, the calculated energy barrier based on the extracted parameters is even lower for compound (1) (75.17 K) than that of compound (2) (77.16 K) and lower than the experimentally observed barrier. Note that $U_{\text{exp}} < U_{\text{eff}}$ is often observed but not the contrary. This surprising result leaves us with the dilemma of having two different energy barriers for the two molecules which could not be explained based on fitting the observed FDMR spectra with the GSH.

3.2.2 Inelastic neutron scattering

Inelastic neutron scattering (INS) was used in order to gain better insight into the energy spectra of both compounds. Unlike FDMRS, INS is sensitive to inter- as well as intra-multiplet transitions. As mentioned earlier, the two techniques obey different selection rules ($\Delta S = 0$; $\Delta M_S = \pm 1$ for FDMRS and $\Delta S = 0, 1$; $\Delta M_S = 0, \pm 1$ for INS). This particularly allows us to probe the excited state levels with spin $S = 11$ using INS.

INS experiments were performed by Joris van Slageren, and Tatiana Guidi and coworkers using the time-of-flight spectrometers NEAT at the Hahn-Meitner Institut (Berlin) and IN5 at the Institute Laue-Langevin (Grenoble). Non-deuterated polycrystalline samples were used in all the measurements.

Figures 3.5 (a) and (b) show the high resolution INS experimental data for compounds (1) and (2), respectively, collected on IN5 with an incident wavelength of 6.7 Å. At the lowest temperature $T = 2$ K, only the ground state is populated, and the lowest energy excitation can be thus easily attributed to the intra-multiplet transition from the $|S = 12, M_S = \pm 12\rangle$ ground state to the $|S = 12, M_S = \pm 11\rangle$ first excited state. The position of this intra-multiplet excitation is found to be at about the same energy

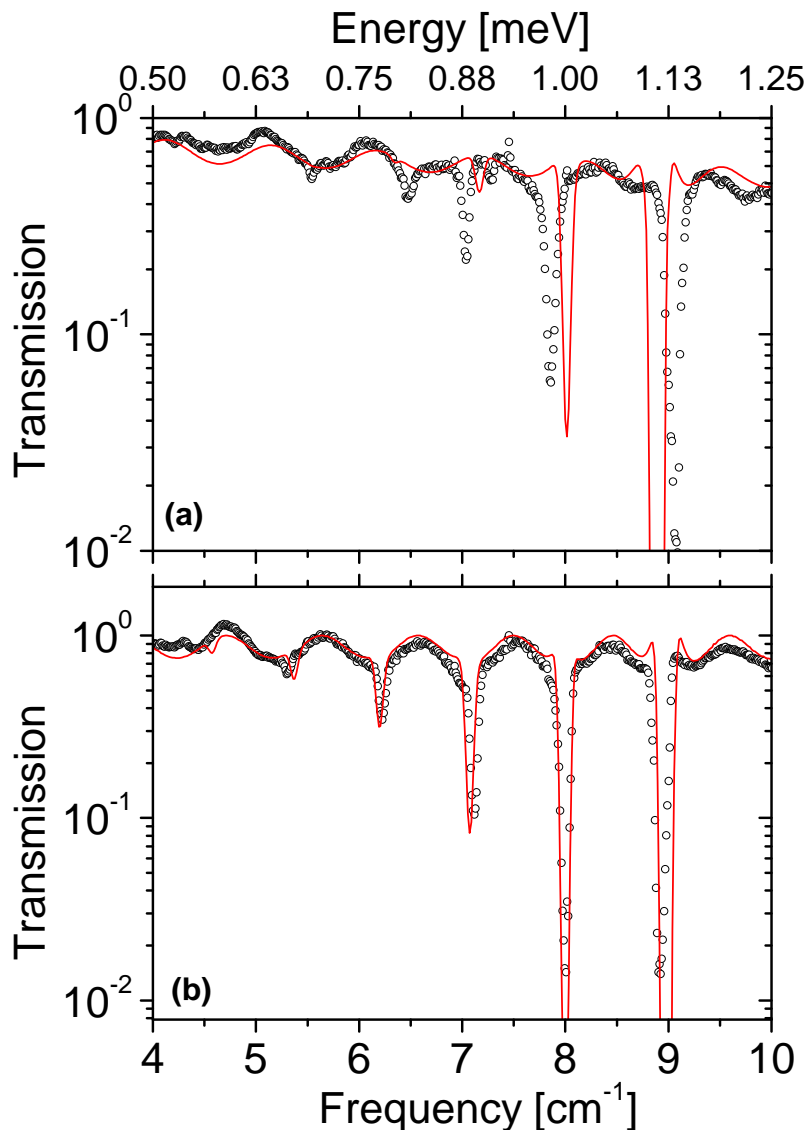


Figure 3.4: 10 K FDMR spectrum (symbols) and best fit (lines) using the GSH parameters indicated in the text for compound (2)(a) and compound (1)(b).

in both compounds, i.e. ~ 1.1 meV (ca. 8.9 cm^{-1} , Line 1 in the FDMR spectra; see Table 3.1). The low energy spectra (below 1.1 meV) of the two complexes do not display significant differences, again indicating only slight changes in the anisotropy of the system. On the contrary, the first inter-multiplet $S = 12 \rightarrow S = 11$ excitation is at about 1.41 meV in compound (2) while it is not visible in the spectra of compound (1) at 6.7 \AA . This can be understood by looking at the data at higher energy transfer, collected with an incident wavelength of 3.4 \AA (Figure 3.6 (a) and (b)). Indeed the first inter-multiplet excitation is considerably elevated in energy in compound (1) with respect to compound (2), from 1.41 meV to 1.865 meV. This gives direct evidence of an increase of the isotropic exchange parameters in (1), knowing that the anisotropy

parameters are approximately the same in both molecules. The INS spectra collected at a base temperature of 2 K, enabled us to directly access the whole set of intra-multiplet and inter-multiplet transitions allowed by the INS selection rules in both compounds. The magnetic origin of the observed excitations was evidenced by raising the temperature to 17 K; the intensity of the peaks decreases as the temperature is increased. A total of five inter-multiplet excitations to the ground state to the $S = 11$ excited state were detected.

The assignment of the observed excitations to intra- or inter-multiplet transitions was confirmed by comparison with the FDMRS measurements. The positions of the intramultiplet INS transitions are consistent with the FDMRS results. Due to the different selection rules of INS and FDMRS, we could conclude that the peaks above 1.2 meV energy transfer correspond to intermultiplet transitions, being absent in the FDMRS spectra (see Figure 3.3). The observation of numerous inter- and intra-multiplet transitions in these systems enabled us to use the microscopic Hamiltonian to interpret the experimental results. The fitting was performed by Stefano Carretta from the University of Parma. All the measurements (including the FDMRS results) can be reproduced by describing the system by the following Hamiltonian,

$$\begin{aligned} \hat{H} = & \sum_{i < j} J_{ij} \hat{\mathbf{s}}(i) \cdot \hat{\mathbf{s}}(j) + \sum_i d_i \hat{s}_z^2(i) + \sum_i e_i [\hat{s}_x^2(i) - \hat{s}_y^2(i)] \\ & + \sum_i b_{4i}^0 [\hat{s}_z^4(i) + [25 - 30s(s+1)] \hat{s}_z^2(i)] \end{aligned} \quad (3.3)$$

where $\mathbf{s}(i)$ is the spin operator of the i th Mn ion. The first term is the isotropic exchange, while the second, third, and fourth terms describe local crystal-fields (the z -axis is taken perpendicular to the plane of the triangles). The structure of Mn₆ fixes the minimal number of free parameters in the Hamiltonian (3.3): three different exchange constants J_1 , J_2 , J_3 (Figure 3.1) and two sets of zero-field splitting (ZFS) parameters d_1 , c_1 , e_1 and d_2 , c_2 , e_2 . In principle, we have 6 sets of ZFS parameters which correspond to the 6 Mn ions. However, sites 1 and 1', 2 and 2', 3 and 3' are related by an inversion center which reduces the number of ZFS sets to 3. The coordination geometry of sites 1 and 3 are rather similar, thus we assumed them to be equal ending up in only two sets of ZFS parameters. The dominant ZFS terms are the second-order axial ones. Since experimental information is insufficient to fix the four small b_4^0 and e parameters, we have chosen to constrain the ratios $b_{4_1}^0/b_{4_2}^0$ and e_1/e_2 to the ratio d_1/d_2 . The anisotropic terms break rotational invariance and in this case they lead to a large amount of mixing of different S multiplets ([66]). A simultaneous fit of the exchange and ZFS interactions was performed. The results are summarized in table 3.2. The exchange coupling is ferromagnetic and the strongest exchange interaction is the intertriangle one between the two central Mn ions. Non-axial contributions to the Hamiltonian appear to be $< 1\%$ of the axial ones and too small to be determined precisely by these measurements. Ferromagnetic exchange couplings have the same order of magnitude as the axial crystal field interactions. This makes Mn₆ unique, as several excited multiplets are partially nested within the ground $S = 12$ one (see Figure 3.7). For instance, a multiplet with easy-plane effective anisotropy is clearly visible around 5 meV, well below the anisotropy barrier of the $S = 12$ ground multiplet

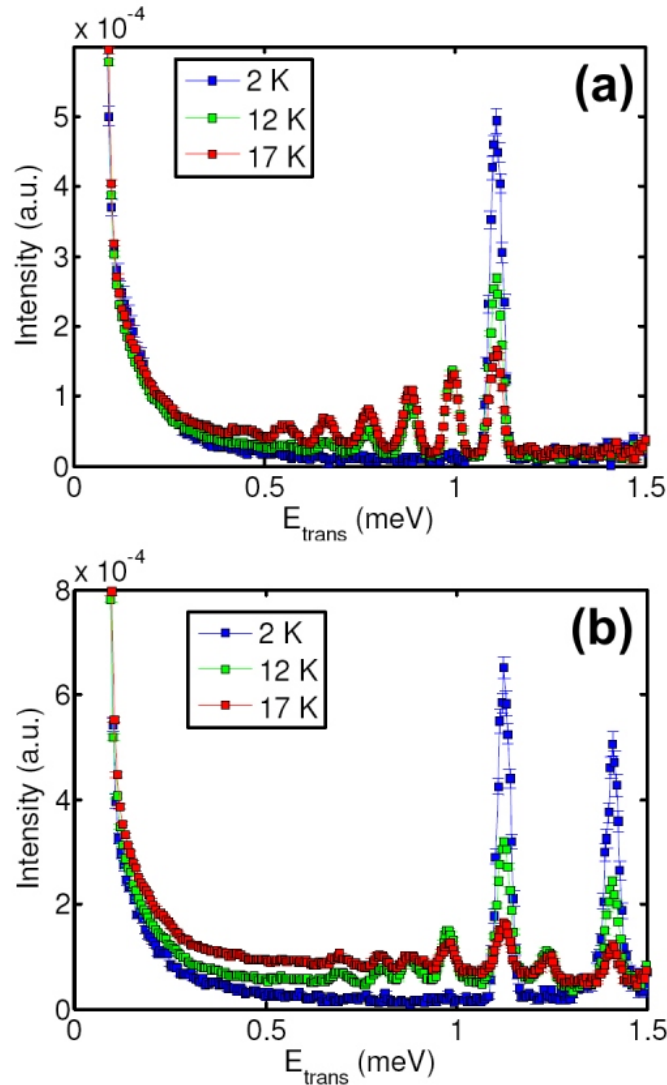


Figure 3.5: INS spectra collected with an incident wavelength of 6.7 \AA at 2, 12, and 17 K. (a) for compound (1) and (b) for compound (2).

($\sim 6.8 \text{ meV}$). This nesting leads to a very large degree of S mixing of the spin wave functions and strongly influences the relaxation behavior. The substantial decrease of isotropic exchange in compound (2) leads to an even larger degree of nesting of excited S multiplets within the ground one. This is evident in the calculated energy spectra (Figure 3.7). These results clearly demonstrate that the giant-spin mapping completely breaks down in these two molecules, not only for the large S-mixing in the wave functions, but much more fundamentally for failing to account for the number of states located below the barrier. Since the main difference between (1) and (2) is the position of the excited S manifolds, these systems provide the possibility to investigate the role of these manifolds in determining the relaxation dynamics. This gives a plausible explanation to the lower effective anisotropy barrier (U_{eff}) in the second compound since many different relaxation paths passing through excited multiplets can contribute to the decay of the magnetization.

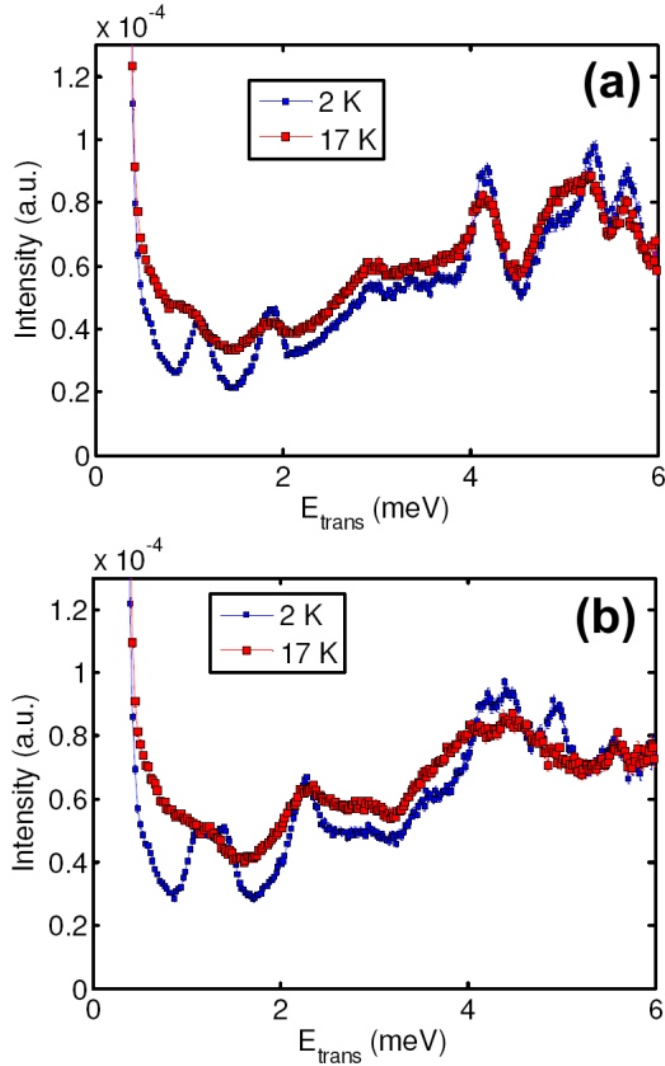


Figure 3.6: INS spectra collected with an incident wavelength of 3.4 \AA at 2 and 17 K. (a) for compound (1) and (b) for compound (2).

3.3 Conclusions

We have studied two different variants of Mn_6 which have very similar structures yet different magnetic properties. In particular, the two compounds have different anisotropy barriers of 86 K (a record barrier) and 53 K. We have shown that the giant spin model is inadequate for these systems and the implementation of the microscopic Hamiltonian is necessary. The different exchange and anisotropy parameters were obtained thanks to the numerous low excitation spectra observed in FDMRS and INS. Moreover, we demonstrated that the excited spin multiplets play a crucial role in the magnetization relaxation by mixing into the spin ground state. This admixing of the spin states provides new tunnel pathways that strongly affect the magnetization relaxation and reduce the effective anisotropy barriers.

Table 3.2: The spin Hamiltonian parameters obtained for both compounds by fitting the microscopic Hamiltonian to the INS and FDMRS spectra.

	$U_{eff}(K)$	J_1	J_2	J_3	d_1	d_2	$b_{4_1}^0$
(1)	86.4	-0.63	-0.31	0.07	-0.25	-1.0	-0.0005
(2)	53	-0.84	-0.59	0.007	-0.20	-0.76	-0.001

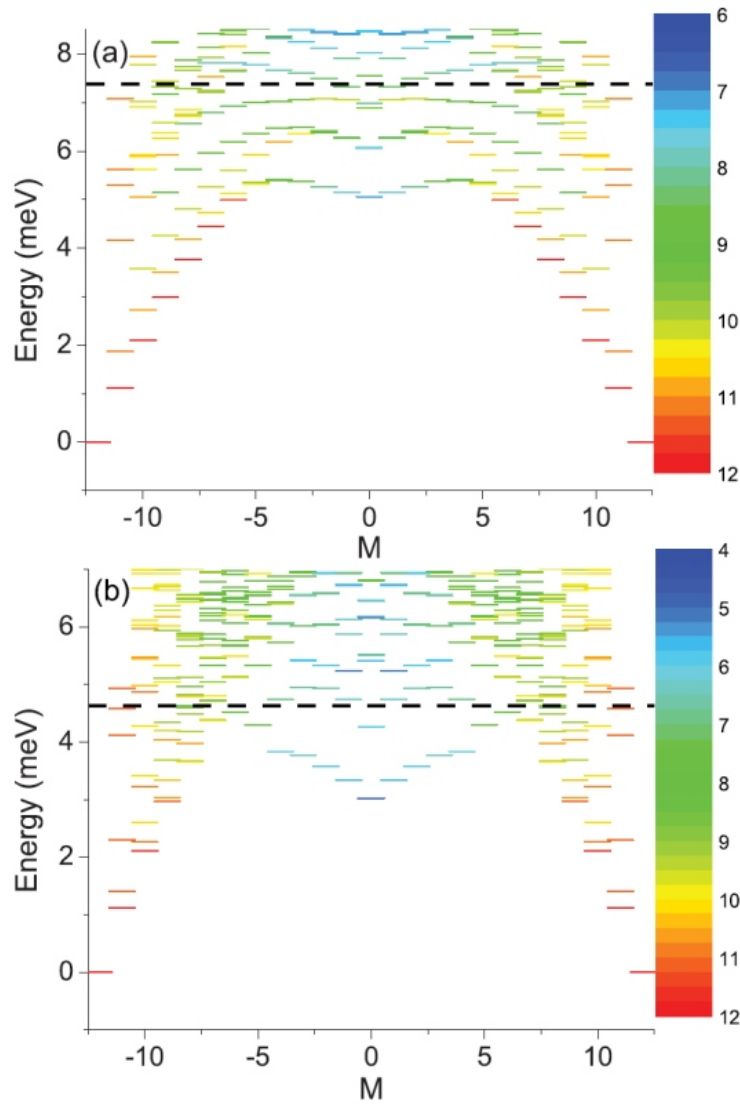


Figure 3.7: Energy levels as a function of the z-component of the total spin for (1) (a) and (2) (b). The color maps S_{eff} , where $\langle S^2 \rangle = S_{eff}(S_{eff} + 1)$. The black dashed lines correspond to the observed value of U_{eff} .

Chapter 4

Magnetic Anisotropy of a Photomagnetic Iron Dimer

4.1 Introduction

As we discussed in Chapter 1, one of the important properties of molecular magnets is the bistability of the magnetization, which makes these systems interesting in terms of data storage applications. From a technical point of view, in order for a material to be incorporated in a device it is often desirable to be able to switch (e.g. on and off) the properties of the material. In molecular magnetism, by far the best studied class of photo-switchable materials is that of spin-crossover complexes [68]. In these complexes, which are most often mononuclear Fe(II) complexes, the energies of the high-spin ($S = 2$) and low-spin ($S = 0$) states, which are delicately dependent on the ligand field strengths of the ligands, are relatively close. Because the high-spin (HS) state has larger (spin degeneracy and vibrational) entropy than the low-spin (LS) state, at high temperatures it is a thermodynamically favorable state. On cooling, at a certain temperature a transition to the LS state occurs. This transition can be gradual or abrupt, and can also show thermal hysteresis, due to cooperative lattice interactions [68]. A very important discovery was that irradiation at low temperature of the molecule in the low spin state can lead to population of the high-spin state which is metastable at those temperatures. This effect was named light-induced spin state trapping (LIESST) [68].

Up to now, the majority of known spin crossover complexes is mononuclear. A recent development in spin-crossover research has been the study of dinuclear and higher nuclearity complexes [69][70]. The binuclear spin-crossover complex is the simplest model compound to study the synergetic effect of intramolecular and intermolecular interactions. The spin-crossover phenomenon is molecular, but the magnetic behavior strongly depends on intermolecular interactions. In some of these studies weak intramolecular exchange interactions between the high-spin iron(II) ions were reported. The analyses in these studies were hindered by the fact that both exchange interactions and zero-field splitting (ZFS) lead to a decrease in the magnetic susceptibility at low

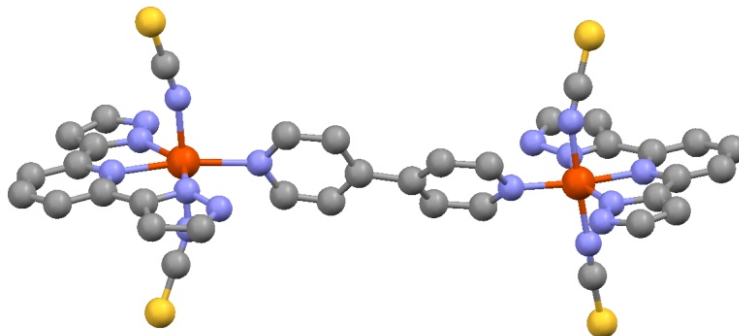


Figure 4.1: Structure of one of the molecules of Fe_2NCS in the unit cell at 100 K projected along the b axis. The HS iron(II) atom is on the left (blue ball), while the LS one is on the right.

temperatures and a separation between both effects is not easy. None of these studies addressed the magnetic anisotropy of the photoinduced HS state.

In the present investigations we have aimed at combining a large magnetic anisotropy and photoswitching of the spin states simultaneously in one system. The ultimate aim is to create photo-switchable single-molecule magnets. The system we have chosen is $[\text{Fe}(\text{bpp})(\text{NCS})_2]_2(4,4'\text{-bpy})$ (hereafter $\text{Fe}_2\text{-NCS}$), where bpp is 2,6-bis(3-pyrazolyl)pyridine and 4,4'-bpy is 4,4'-bipyridine. We show how diverse experimental techniques can complement each other to fully characterize the magnetism of the system.

4.2 Experimental

The magnetic susceptibility and magnetization measurements were performed on carefully selected single crystals with masses ranging from 100-500 μg , on a Quantum Design SQUID magnetometer. Most of the crystals grow as prisms with the long axis being the crystallographic b -axis. Crystal quality and cell parameters were checked, and satisfactory crystals were indexed to permit the single crystal orientation. In view of the various sources of error in orienting the crystals, we estimate the accuracy to be in the order of 10° . Photomagnetic experiments were performed at the University of Bordeaux with a Spectra-Physics Kr+ laser coupled through an optical fiber into the SQUID cavity. The angle dependent magnetization measurements were recorded at the University of Florence with a Cryogenics S600 SQUID magnetometer equipped with an automatic horizontal sample rotator. Torque magnetometric measurements were performed on the home built setup described in Chapter 2, and Frequency domain magnetic resonance spectroscopy (FDMRS) measurements were performed on a previously described spectrometer [18]. The FDMRS measurements were performed on a large single crystal at various temperatures in zero applied magnetic field. The crystal was mounted on the largest face with the crystallographic b -axis vertically aligned. The torque simulations were performed using a self written program (Section 1.6).

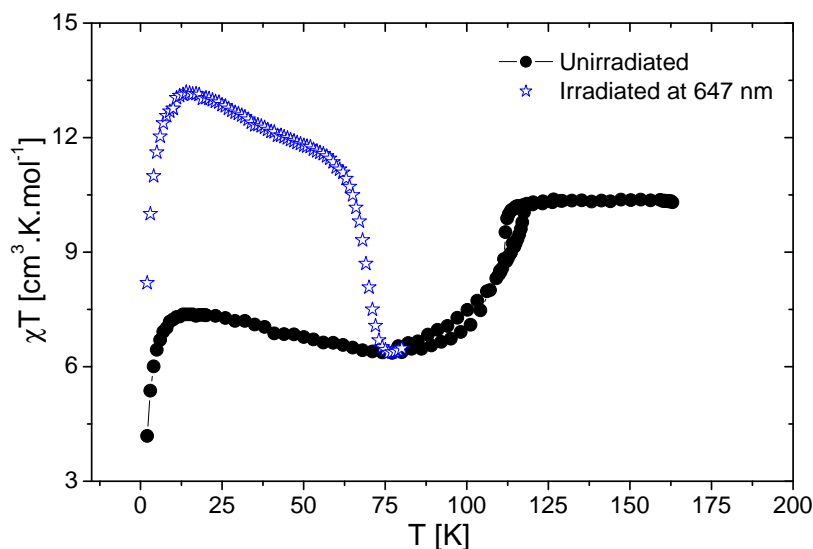


Figure 4.2: χT as a function of temperature for measurements performed on an Fe_2NCS single crystal along (001) direction (c^*) at 1000 G ($T < 20$ K) and 1 Tesla ($T > 20$ K).

4.3 Results and discussion

4.3.1 Crystal structure and photomagnetic measurements

The crystallographic and photomagnetic studies were performed at the University of Bordeaux by Dr. Patrick Rosa and his coworkers. Here we briefly comment on the structure of the compound and its photomagnetic properties. At room temperature, the system is monoclinic within the spacegroup $P2_1/n$. The asymmetric unit is one-half of the molecule, the other half being generated through an inversion center. There are two molecules in the unit cell, with differing orientations that are related by the glide plane of the space group $P2_1/n$. A first crystallographic phase transition at $T = 161$ K removes the inversion center, as well as the screw axes, but does not change the molecular orientations by much. A second phase transition occurs at around 115 K which this time is only associated with the spin transition of one of the two ions. This phase transition shows a hysteretic behavior of 4 K width. The symmetry is apparently still monoclinic C -centered, but it was only possible to solve and refine satisfactorily the structure in the corresponding primitive triclinic cell within spacegroup $P-1$. Figure 4.1 shows the molecular structure at 100 K. This phase transition does not alter the general orientation of the molecules much. A change in the bond lengths for only one of the iron(II) indicates that only that ion undergoes a spin state transition and adopts the low-spin state, i.e. all molecules are mixed HS-LS.

Figure 4.2 shows the results of the single crystal susceptibility measurements on a single crystal along the (001) direction, where χT is plotted versus temperature. At high temperatures, the susceptibility shows a paramagnetic behavior. On cooling,

there is a sudden drop in χT at ca. 115 K. The susceptibility shows a small thermal hysteresis at this transition. This hysteresis was also observed in crystal structure studies [71]. This drop in the χT value confirms the fact that one of the iron(II) ions in the molecule is in the LS configuration ($S = 0$). Light irradiation ($\lambda = 647$ nm, $P_{eff} = 3$ mW/cm²) causes an increase in the susceptibility, virtually saturating after 10 minutes. This LIESST effect changes the electronic configuration of the LS centers into the HS metastable state. The χT values indicate that conversion is complete [72]. On increasing the temperature after irradiation, the susceptibility increases rapidly up to a temperature of ca. 10 K and decreases smoothly similarly to the unirradiated crystal up to 60 K. Above 60 K, χT decreases rapidly as the thermal relaxation from the light-induced metastable state becomes faster than the measurement time.

4.3.2 FDMRS

In order to quantify the ZFS in this system, which is one of the main aims of this study, we have performed FDMRS measurements on a large single crystal (inset Figure 4.3), which was mounted on its largest face (presumably (101)). These are the first FDMRS measurements on one single crystal, with just measurements on mosaics having been reported before [73][74]. The magnetic field component of the microwave radiation (B_{ac}) was polarized parallel and perpendicular to the long axis of the crystal using wire grid polarizers, in two different sets of measurements. The measurements with B_{ac} parallel to the b crystallographic axis show a strong feature at 19.9 cm⁻¹ (Figure 4.3 (a)). The intensity of the absorption peak is temperature independent, hence it is attributed to a vibrational transition. Such an excitation couples to the electric field component of the radiation (which is perpendicular to b). Vibrational transitions have been found at similar energies before and were attributed to bending motions of aromatic rings [75]. With B_{ac} perpendicular to the long axis of the crystal, the vibrational transition is not observed. Instead a feature is observed at 9 cm⁻¹, the intensity of which decreases strongly with temperature. This indicates its origin is a magnetic resonance transition, because the intensity of the resonance lines that corresponds to such transitions is proportional to the population difference between initial and final states. A small but apparent splitting of the resonance line can be observed which may be either an artefact due to standing waves in the beam, or due to a small rhombic distortion [76]. The splitting of the $M_S = \pm 1$ states is equal to $6E$ for an $S = 2$ system, which would make E/D of the order of 0.01, if the observed splitting is attributed to a rhombic distortion. No photomagnetic effect was observed upon photo-irradiation ($\lambda = 632$ nm). Presumably the large crystal size prevented significant conversion, given that the high-spin state is not transparent at the irradiation wavelength. Polarizer angle dependent studies show that the maximum absorption intensity is obtained at $100 \pm 10^\circ$ (Figure 4.4), showing that the b direction is close to the unique axis, since the microwave magnetic field should be perpendicular to the ZFS unique axis in order to induce a magnetic resonance transition [13]. The magnetic field dependence could not be studied because the crystal exploded during preliminary in-field measurements due the torque forces created by the applied field and the present magnetic anisotropy. The temperature dependence of the observed line at 9 cm⁻¹ shows that the transition

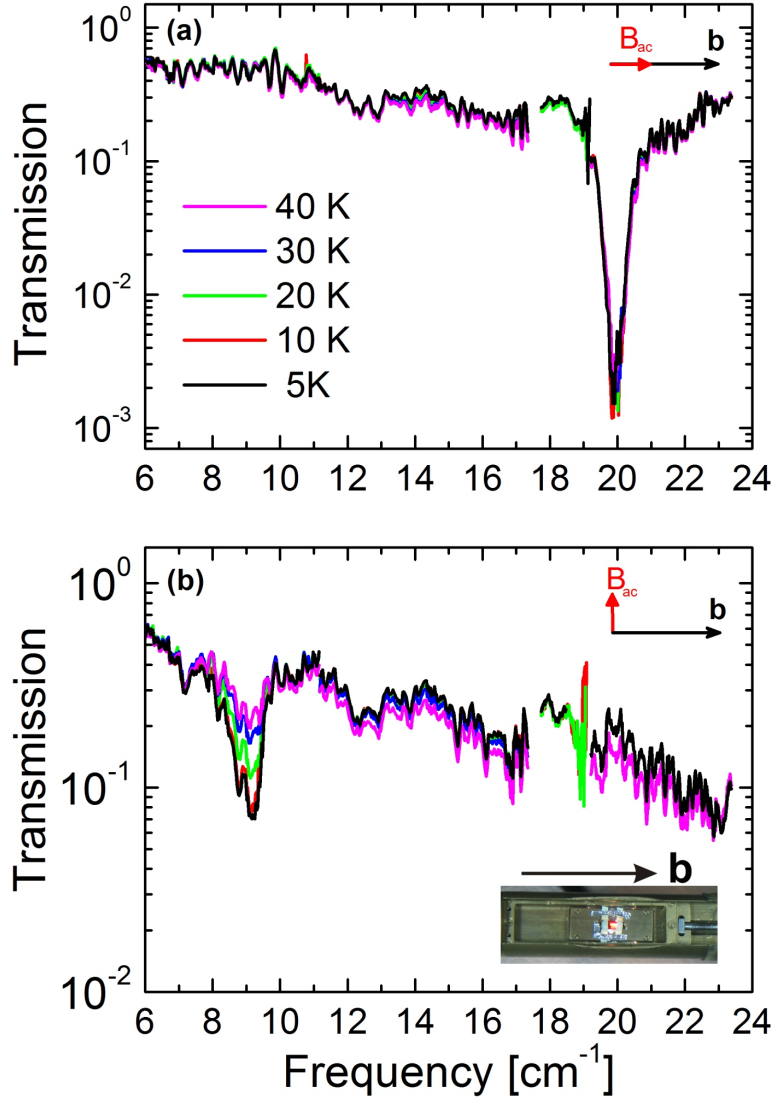


Figure 4.3: FDMR spectra on an Fe₂NCS single crystal (inset) with B_{ac} parallel (a) and perpendicular (b) to the b crystallographic axis.

originates from the ground state (the lowest M_S state). Here we introduce the two possible scenarios for the energy diagram of the Fe₂-NCS. From the photomagnetic data, we know that there is only one HS ion in each dimer. The spin ground state is therefore assumed to be $S = 2$ (this is confirmed by the magnetization data, see below). For an $S = 2$ spin ground state with hard axis anisotropy, the $M_S = 0$ is the ground state (Figure 4.5 (a)), and the observed transition is exactly equal to D (the splitting between $M_S = 0$ and $M_S = \pm 1$). However, in the case of easy axis anisotropy (Figure 4.5 (b)), the observed transition corresponds to that between the $M_S = \pm 2$ and $M_S = \pm 1$ which is given by $3D$, and thus $D = -3 \text{ cm}^{-1}$ (The negative sign indicating that we have an easy axis). The ambiguity of the energy scheme and the nature of the magnetic anisotropy is elucidated by the magnetization and torque measurements

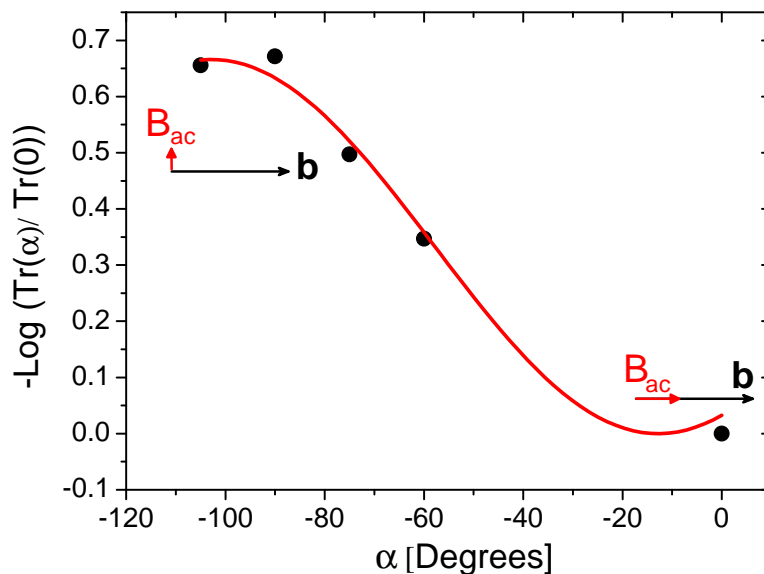


Figure 4.4: The normalized intensity of the resonance line at 9 cm^{-1} vs the angle between B_{ac} and b .

presented in the following sections.

4.3.3 Susceptibility and angle resolved magnetization measurements

Having restricted the axial ZFS parameter D to only two values, we performed angle resolved magnetization measurements in order to determine the direction of the easy axis, and eventually characterize the anisotropy in the system. Figure 4.6 shows the magnetization on a single crystal placed with the b axis parallel to the rotation axis.

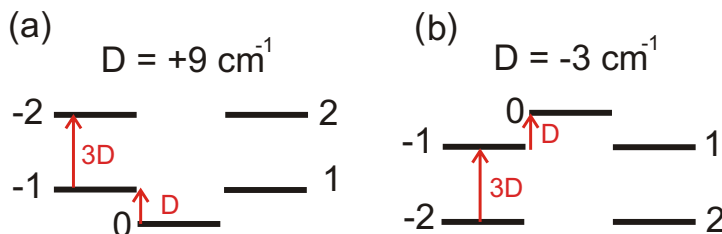


Figure 4.5: The energy diagram for an $S = 2$ spin system with a hard (a) and easy (b) axis anisotropy.

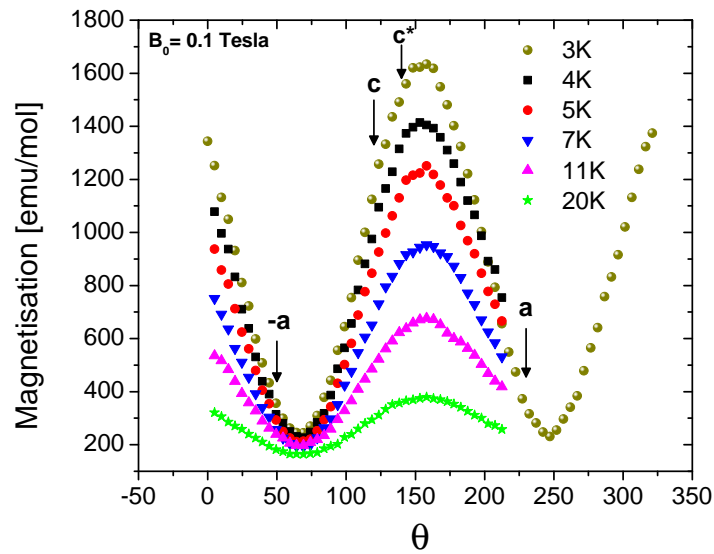


Figure 4.6: Magnetization measured in the ac plane at 0.1 Tesla and different temperatures. The arrows indicate the angles at which the various crystallographic axes are either parallel or antiparallel to the external field.

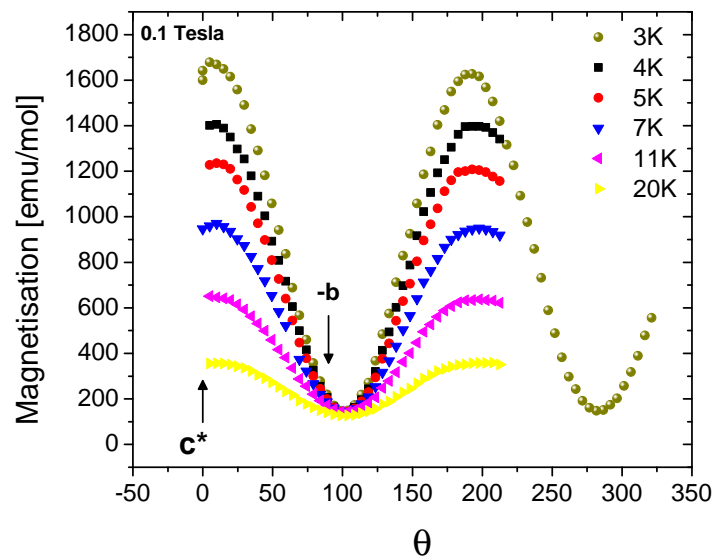


Figure 4.7: Magnetization measured in the bc^* plane at 0.1 Tesla and different temperatures. The arrows indicate the angles at which the various crystallographic axes are either parallel or antiparallel to the external field.

The magnetization is therefore recorded in the ac plane at 0.1 Tesla and different temperatures. Note that θ is an experimental angle of the rotator, and the angles at which the crystallographic axes is parallel to the field are indicated on the graph. The magnetization shows a local minimum and maximum at 66° and 155° , respectively. Measurements were also performed rotating around a , in the bc^* plane (Figure 4.7). The magnetization here shows a minimum which is 10° from b and a maximum at 10° from c^* .

In principle, the anisotropy axis in molecular magnetic systems is a molecular property and not a crystallographic one, and hence it does not have to be along one of the crystallographic axes or in any of the three crystallographic planes. In addition, we know that there are two molecules with different orientations per unit cell. In view of this, a connection between the molecular and the crystallographic structure was made in order to comprehend the angle resolved magnetization (keeping in mind that a unique axis is not necessarily aligned along a molecular axis either unless it is imposed by symmetry). While the indexing and orientation of the crystals used in the magnetization was done at room temperature, the magnetization was performed at low temperatures (lower than 30 K). A correlation between the room temperature and 30 K structure is therefore necessary. The 30 K triclinic cell was transformed into a metrically equivalent monoclinic cell similar to the room temperature cell. Superposition of the 293 K structure and the transformed 30 K monoclinic structure (Figure 4.8) shows that we have indeed similar packings and orientations of the molecules within the crystal. We can therefore assume the coincidence of crystallographic axes between room temperature and low temperature. More to the point, we have obtained the Cartesian coordinates of vectors corresponding to: i) crystallographic axes; ii) normals to rotation planes used for the magnetic measurements; iii) relevant molecular axes, obtained for each high spin Fe by the least line given by Fe and the two nitrogen atoms of similar ligands (pyrazole, pyridine, and thiocyanate), which for the two complexes of the asymmetric unit gives a total of 6 axes. The usual convention is followed, that is x along a , y along b and z along c^* . Those cartesian coordinates are reported in Table 4.1 below. Furthermore, in order to correlate the molecular geometry and the angle resolved magnetization, we have calculated the angles between the projections of the 6 molecular axes, in the ac (Table 4.2) and bc^* (Table 4.3) planes, and the different crystallographic axes. For example, a local maximum in the magnetization recorded in a crystallographic plane, may correspond to the direction where the field is either parallel to the projection of an easy axis or perpendicular to the projection of a hard axis in that particular plane. From Tables 4.2 and 4.3, a number of conclusions can be drawn:

In the ac plane:

- 1- The projections of (Fe1Py), (Fe4Py) are almost parallel to c^* . Thus the magnetization maximum and minimum correspond to the two axes being approximately respectively parallel and perpendicular to the applied field.
- 2- In the same manner, magnetization maximum at 156° and minimum at 66° correspond to axes (Fe4Pz, Fe1Pz), being approximately respectively perpendicular and parallel to the magnetic field.

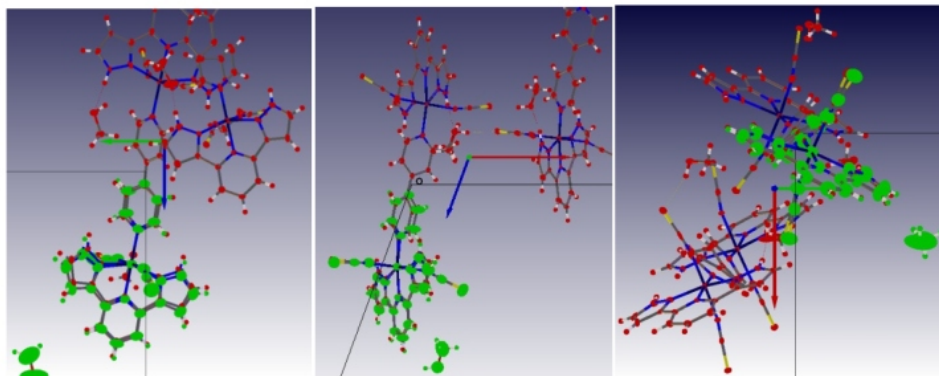


Figure 4.8: Superposition of the 293 K structure asymmetric unit (in green) and the 30 K monoclinic structure asymmetric unit (in red), as seen along (100), (010) and (001).

In the bc^* plane:

- 1- The magnetization maximum at 190° corresponds to the axis (Fe1Pz) perpendicular and (Fe1Py) parallel to the magnetic field, while (Fe4Pz) and (Fe4Py) are rotated by some 24° .
- 2- For magnetization minima at 101 and 281° , the situation is exactly reversed.

The magnetization angle dependence can be thus tentatively accounted for: either by a hard axis anisotropy with its axis lying close to the (Fe1Pz), (Fe4Pz) directions for each HS Fe(II); or by an easy axis anisotropy with its axis lying close to the (Fe1Py), (Fe4Py) directions for each HS Fe(II). Decision between both possibilities cannot be made based on the magnitude of the magnetization. Maxima and minima values of the magnetization are quite similar for both rotation measurements.

To put things together, the FDMRS data has given quantitative values for the axial anisotropy suggesting a hard or an easy axis scenario. The angle resolved magnetization did not raise this ambiguity, but rather assigned the hard or easy axes to two different possible molecular axes. Therefore, torque magnetometry measurements were necessary to elucidate the nature of the anisotropy.

4.3.4 Cantilever torque magnetometry

Identifying the nature of the anisotropy is a strong point of torque magnetometry (see Chapter 2). The problem is easily solved if the direction of the quantization axis is known (if it is imposed by symmetry, for example). In that case, one has to query whether the unique axis moves towards or away from the externally applied field, hence deduce respectively an easy or a hard axis anisotropy. In the $\text{Fe}_2\text{-NCS}$ system, the situation is more complicated. There are several limitations which hinder a straightforward

deduction of the sign of the anisotropy parameter, namely, the uncertainty in defining the direction of the unique axis, and the fact that there are two molecules per unit cell. In magnetization measurements, one typically measures the magnetization along the field direction. The other two components are not measured and they virtually do not influence the measured z component of M (z being the field direction). On the

Table 4.1: Cartesian coordinates of crystallographic axes, planes, and of molecular axes.

Name	m1,m2,m3	Atom symbols
a axis	1.0000 0.0000 0.0000	
a^* axis	0.9380 0.0000 0.3466	
b, b^* axis	0.0000 1.0000 0.0000	
c axis	-0.3466 0.0000 0.9380	
c^* axis	0.0000 0.0000 1.0000	
Plane (ac)	0.0000 1.0000 0.0000	
Plane (bc^*)	1.0000 0.0000 0.0000	
Axis [Fe1pz]	0.4459 -0.8737 -0.1944	N2a-Fe1-N3a
Axis [Fe4pz]	-0.3898 -0.8973 0.2070	N2d-Fe4-N3d
Axis [Fe1py]	0.0420 0.2001 -0.9789	N4a-Fe1-N1a
Axis [Fe4Py]	0.0509 -0.2119 -0.9760	N4d-Fe4-N1d
Axis [Fe1NCS]	0.9017 0.4012 0.1611	N6a-Fe1-N5a
Axis [Fe4NCS]	0.9221 -0.3483 0.1687	N6d-Fe4-N5d

Table 4.2: Signed angles of crystallographic axes to projections of molecular axes in the ac plane.

	a	a^*	b	b^*
[Fe1pz]	-23.56	-43.83	+49.27	+69.54
[Fe4pz]	-27.97	-48.25	+41.75	+62.03
[Fe1py]	-87.54	+72.18	-17.82	+2.45
[Fe4Py]	-87.02	+72.71	-17.29	+2.99
[Fe1NCS]	+10.13	-10.15	+79.85	-79.87
[Fe4NCS]	+10.37	-9.91	+80.09	-79.64

Table 4.3: Signed angles of crystallographic axes to projections of molecular axes in the bc^* plane.

	b	c^*
[Fe1pz]	-12.54	-77.46
[Fe4pz]	+12.99	+77.01
[Fe1py]	+78.45	-11.55
[Fe4Py]	-77.75	+12.25
[Fe1NCS]	-21.88	+68.12
[Fe4NCS]	+25.84	-64.16

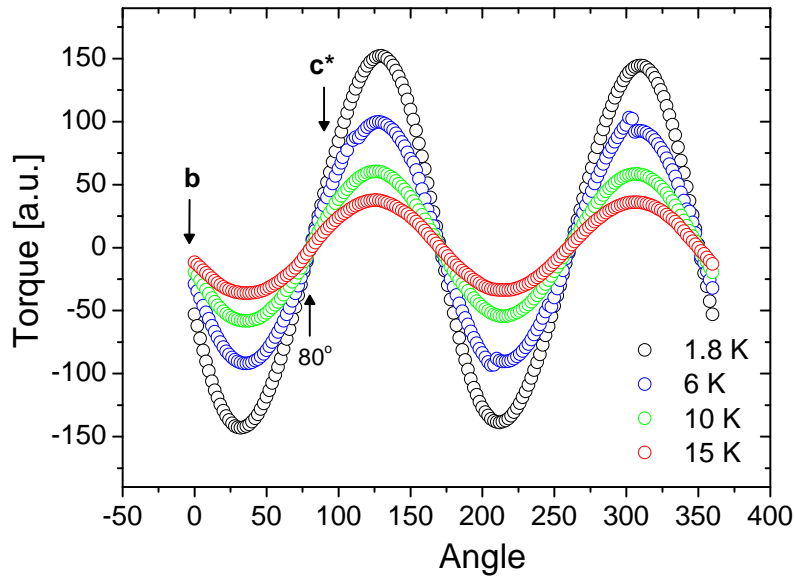


Figure 4.9: Angle-dependent torque signals, measured in the bc^* plane at 1 Tesla and different temperatures. The arrows indicate the angles at which the b and c^* crystallographic axes are parallel or antiparallel to the external field.

contrary, a cantilever torque measurement is not only sensitive to the transverse component of the torque (along the y direction), but in addition, the other two components of the torque (along z and x) may have an influence on the measured y component (see Chapter 2). For that reason, it is desirable to orient the crystal in such a way that only one torque component is present while the other two components are nil. This is practically not possible if there is more than one molecule in the unit cell with different angles with the external field. However, as explained in Chapter 2, owing to the careful design of the cantilevers we used, the torque along the x and z directions can be neglected for low torque signals. We have, therefore, measured the angle resolved torque at low magnetic fields, and the field dependent torque at very small angles to avoid having a large torque signal. Figure 4.9 shows the angle dependent torque signal in the bc^* plane at different temperatures and an external field of 1 Tesla. Note that there is a 90° difference in the initial position of the crystal compared to the magnetization measurement and the rotation is in the opposite sense (at $\theta = 0^\circ$, the field is parallel to b , and at $\theta = 90^\circ$ it is parallel to c^*). The results closely match the magnetization data. The sign of the torque with the particular geometry of the crystal/cantilever indicates that the crystal moves away from the b crystallographic axis towards the c^* axis. This indicates that we have a hard or an easy axis close to b or c^* , respectively. The torque vanishes at -10 and 80° , which again confirms the finding that the projection of the hard (or easy) axis in the bc^* is at approximately 10° from b (or c^*). We calculated the angle dependence of the torque considering a hard axis (Figure 4.10 (a)) at 10° from b or an easy axis at 10° from c^* . The simulated spectra show a better

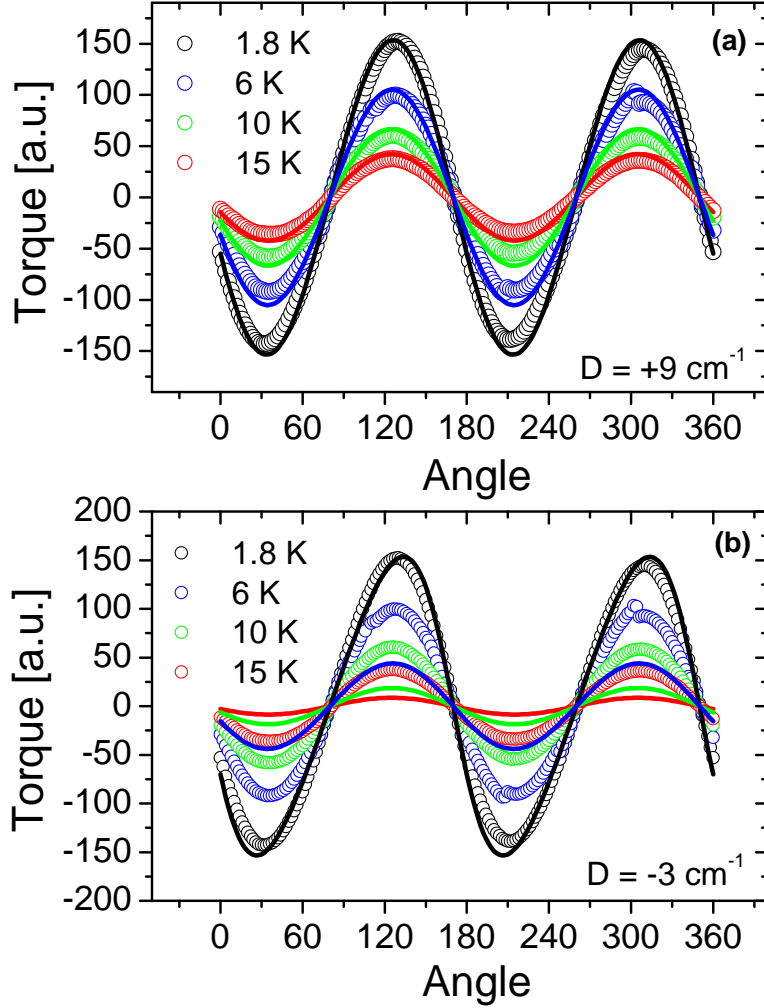


Figure 4.10: Angle dependent torque signals (circles), measured in the bc^* plane at 1 Tesla and at different temperatures. The lines show the calculated torque signals with $D = +9 \text{ cm}^{-1}$ (a) or -3 cm^{-1} (b) (see text).

agreement for $D = +9 \text{ cm}^{-1}$ at 10° from b . To illustrate that, we have performed a semi-quantitative comparison of the calculated and the measured values by using the conversion factor $(\tau_n = \tau_c(\theta, T) \cdot \tau_m(130^\circ, 1.8K) / \tau_c(130^\circ, 1.8K))$, where τ_n , τ_c , and τ_m are the normalized, calculated, and measured torque signals, respectively. In other words, we assumed a superposition of the calculated and measured values at 130° and 1.8 K (the strongest signal) to highlight the deviation of the signal at other angles and temperatures. Figure 4.10 clearly shows a much better agreement for a system with positive anisotropy (a), while the deviation of the higher temperature calculated curves from the measured ones is obvious in the case of an easy axis anisotropy (b).

One more piece of evidence confirming a hard axis anisotropy comes from the field dependent torque measurements for two different angles (170.25° and 260.25°).

Figure 4.11 (a) shows the torque signals at 170.25° . This angle is 0.25° from the projection of the hard axis (assuming a hard axis close to b) and 89.75° from the easy axis (assuming an easy axis close to c^*). The calculated torque signals for the two different scenarios are shown in Figure 4.11, (b) for $D = -3 \text{ cm}^{-1}$, and (c) for $D = +9 \text{ cm}^{-1}$. In the case of an easy axis, we have a transverse field (89.75° from c^*), and the torque shows a peak which is temperature dependent. For $D = -3 \text{ cm}^{-1}$, this peak is evident in the calculated signals around 4 Tesla at 1.8 K, but it is not observed in the experiment. In the case of a hard axis scenario (89.75° from c^*), the magnetic field is almost axial and we have a quadratic field dependence of the torque which decreases by increasing temperature in agreement with the experiment. The situation is inverted for the second measured angle at 260.25° . In an analogous manner, we can interpret the torque signals at 260.25° shown in Figure 4.12 (a). The calculated signals (Figure 4.12 (b) and (c)) further support a hard axis anisotropy of $+9 \text{ cm}^{-1}$ at around 10° from b . It is worth mentioning, that a peak in the measured signal at 1.8 K would be expected for an axial field with a hard axis, but for D of $+9 \text{ cm}^{-1}$ this peak would appear around 10 Tesla.

4.4 Conclusions

In conclusion, we have studied a photoswitchable $\text{Fe}_2\text{-NCS}$ system which has a phase transition at 113 K where one of the two iron centers undergoes a spin state transition from HS to LS state. The system is switched into a HS-HS state at low temperatures under the irradiation of 640 nm. We have studied the magnetic anisotropy of the LS-HS state at low temperatures. Collecting combined data from FDMRS, angle resolved magnetization, and torque magnetometry, we were able to prove that the system has a hard axis anisotropy of $D = +9.0(2) \text{ cm}^{-1}$ with the hard axis close to the Pz-Fe-Pz mean axis in the individual molecular frame. These studies contribute to a better insight into the magnetic anisotropy of spin crossover systems. Furthermore, we have demonstrated the necessity of having complementary techniques in studying the magnetic anisotropy in molecular magnets, where the information extracted from a single technique may in some cases lead not only to an incomplete, but rather to an erroneous picture. Our aim is to find a photoswitchable system with strong easy axis anisotropy, eventually leading to photoswitchable single molecule magnets.

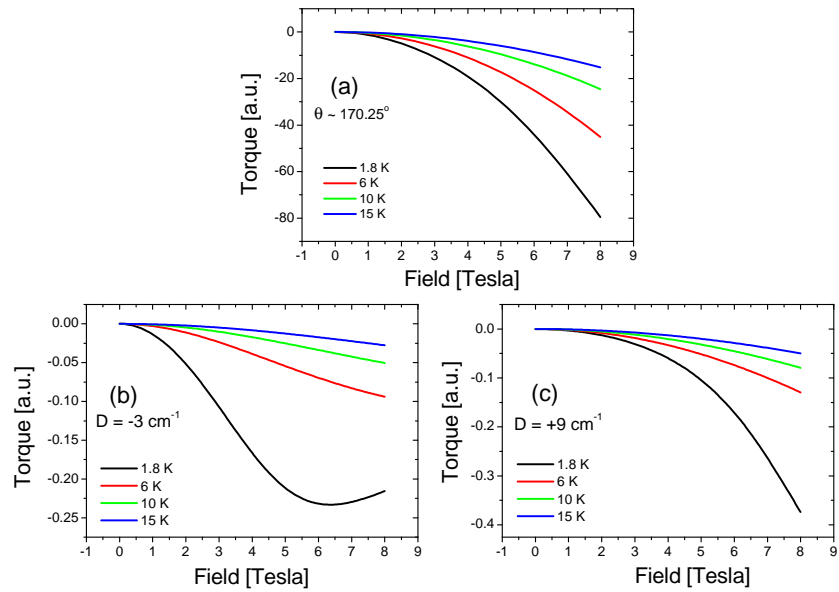


Figure 4.11: (a) Measured torque signals at 170.25° , and different temperatures. (b) and (c) show the calculated signals with $D = -3 \text{ cm}^{-1}$ and $+9 \text{ cm}^{-1}$, respectively (see text).

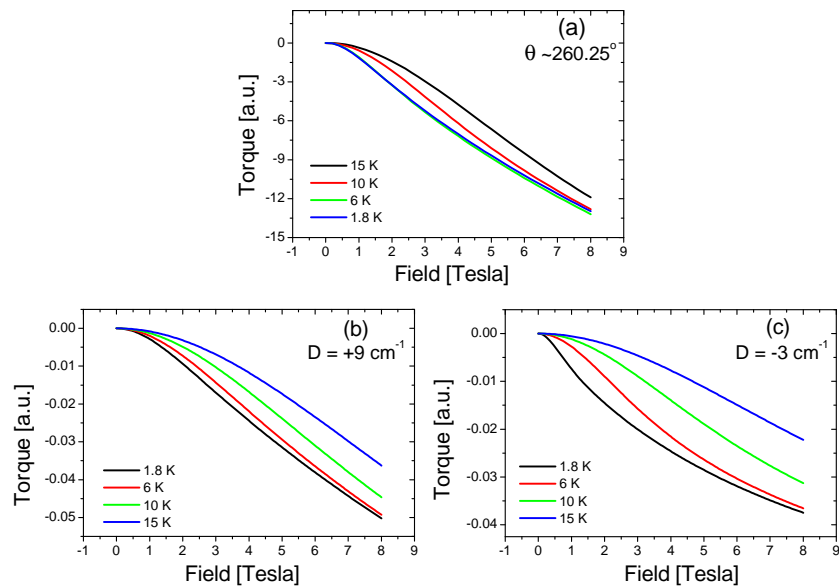


Figure 4.12: (a) Measured torque signals at 260.25° , and different temperatures. (b) and (c) show the calculated signals with $D = +9 \text{ cm}^{-1}$ and -3 cm^{-1} , respectively (see text).

Chapter 5

A Weakly Coupled Fe(II) dimer: A Workbench to Investigate Exotic Quantum Phenomena

5.1 Introduction

Molecular clusters with antiferromagnetic (AF) exchange interactions have attracted considerable interest due to their rich quantum magnetic properties. In particular, they are promising candidates to observe macroscopic quantum coherence reflected in the coherent tunnelling of the Néel vector [77][78]. A variety of AF systems with different number of spins and diverse topologies were reported in literature (cubanes [67], grids [36][79], and rings [35][80][81][33]). Most of the reported systems have relatively strong exchange coupling constants ($J > D$) which results in the typical picture of the energy spectrum for such an AF system, i.e. a system with a non-magnetic ground state ($S = 0$ for even number of equal spins) that successively changes its spin ground state into an $S = 1$, $S = 2$, etc... ground state, under the effect of an external magnetic field applied along the easy or the hard axis (see Section 2.2.3). The picture is rather different for a system with weak exchange coupling ($J < D$) where the spin microstates of the highest coupled spin S are lowered in energy with respect to the microstates of the other spin states ($S-1$, $S-2$, etc...). This leads to having a smaller number of field induced level crossings with the ground state and consequently, a smaller number of steps in the magnetization or torque curves. The number of steps or level crossings into the ground state depends on the relative strength of the interactions in the spin Hamiltonian. Few systems were reported in literature [82][83][84] where an easy axis type anisotropy is stronger than the exchange interaction. In [82] and [84], no full magnetic characterization was reported and the value (and sign) of the axial anisotropy parameter should be used with care. We have seen in the Mn_6 system (Chapter 3) how the deviation from the strong exchange limit leads to spin mixing and eventually the breakdown of the giant spin model. Here we look at the lower extreme in the coupling scheme series where the exchange is much weaker than the single ion anisotropy, or what is known as the weak exchange limit. We present an Fe(II) exchange coupled dimer and

we show how the magnetic properties arising from the competing interactions in the spin Hamiltonian are rendered in the weak exchange limit. Furthermore, the properties of the low lying energy states demonstrate that the system is a promising candidate to investigate exotic quantum phenomena.

5.2 Experimental

Powder X-ray diffraction data were recorded using a PANalytical X'Pert MPD diffractometer with Bragg-Brentano geometry, Cu $K\alpha$ radiation and a backscattering graphite 370 monochromator. The magnetic susceptibility up to 7 Tesla, and at low temperatures, were measured with a commercial SQUID magnetometer (Quantum Design). The high field magnetization measurements (up to 12 Tesla) were performed with a vibrating sample magnetometer (VSM), at the University of Florence. Low field torque magnetometric measurements were performed on the home built setup described in Chapter 2, and high-field (and low temperature) torque measurements were performed at the Grenoble High Magnetic Field Laboratory (GHMFL) on a copper beryllium cantilever inserted into magnet M9. The energy diagrams, torque, magnetization, and susceptibility were calculated using a self written program (See Section 1.6).

5.3 Results

5.3.1 Crystal structure

The complex $[\text{Fe}(\text{3-bpp})(\text{NCS})_2]_2(\text{4,4'-bipy})_2$ (where 3-bpp stands for 2,6-bis-(3-pyrazolyl)-pyridine and 4,4'-bipy for 4,4'-bipyridine) (hereafter Fe_2 -Penta) was synthesized at the University of Bordeaux by Dalila Fedaoui and Patrick Rosa. The compound can be obtained either as a yellow powder or as yellow crystalline needles or elongated prisms. Powder X-ray diffraction patterns were measured to ensure that powder and single crystals are identical. Structure was solved and refined satisfactorily at room temperature and 120 K (Figure 5.1 a) in triclinic settings, in the spacegroup P-1. The asymmetric unit consists of one metallic complex and one hydrogen-bonded bipyridine. No significant change outside thermal contraction was seen in the 120 K structure.

The Fe-N bond lengths, between 2.009(3) and 2.042(3) Å for the thiocyanate ligands, and 2.193(2) and 2.198(2) Å for the pyrazole moieties point clearly towards a high-spin state for Fe(II), as seen for the FeN_6 chromophore. Close contacts are found between the iron center and one sulphur end-point of another complex thiocyanate ligand: 3.755(1) Å (Figure 5.1 b). The two Fe(II) complexes are related by an inversion center, the corresponding dimer is stacked along the c axis. The corresponding Fe-Fe distance of 6.723(2) Å is close enough to account for a weak exchange interaction. The second closest Fe-Fe distance, at 8.763(2) Å, is already too long to reasonably account for a significant exchange interaction. Here, the contact is mediated through π -stacking interactions between the 3-bpp ligands of adjacent complexes along the a axis.

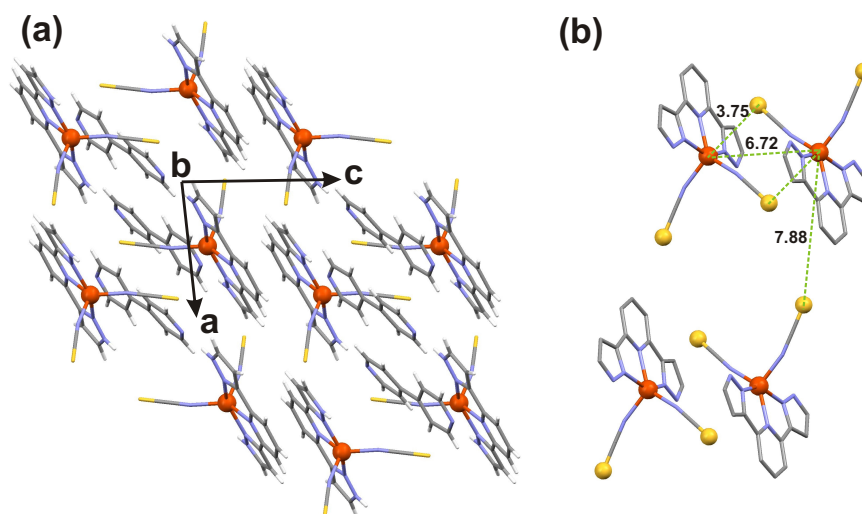


Figure 5.1: (a) Crystal structure at 120 K as seen along b with the a and c axes indicated. (b) Short contact lengths are indicated within and in between adjacent dimers.

A search of the Cambridge Structural Database (revision 5.30, November 2008) for compounds showing Fe-S intermolecular contacts in the 3.5-4 Å range yielded no relevant structures with Fe(II).

5.3.2 Magnetization and low field torque studies

To assess the strength and nature of the exchange interaction (if any), magnetic susceptibility measurements were performed on a 20.4 mg pressed powder sample of Fe₂-Penta. Figure 5.2 (a) shows χ and (b) shows χT versus temperature. The susceptibility shows a peak at around 15 K and χT drops at lower temperatures. Both curves (χ and χT) are therefore reminiscent of a system with AF exchange coupling. Moreover, magnetization curves shown in Figure 5.3 further support the hypothesis of having an AF ground state in zero field which crosses into a magnetic state at ~ 4.2 Tesla. The crossing is evident from the inflection point at 4.2 Tesla and the temperature dependence of the magnetization curves as well. In view of this result, one would expect evenly spaced crossing fields as it is well known for AF clusters ([30][33][85], see Chapter 2). It is important to point out that the absolute value of the magnetization after the crossing is higher than what is expected for an $S = 1$ Fe(II) dimer (assuming that we observe an $S = 0$ to $S = 1$ spin state transition which amounts to $2\mu_B$ for $g = 2$). To assess the origin of this crossing, we have performed magnetization measurements up to higher magnetic fields to observe whether another level crossing can be seen (Figure 5.4). Even up to 12 Tesla, no further crossing is observed and the magnetization continues to increase smoothly without reaching saturation. This unusual behavior is an indication that we are dealing with an unconventional AF system. In order to investigate the anisotropy of the system, we performed low field torque magnetometry up to 8 Tesla. The measurements were performed on an 88 μg single crystal. The shape of the crystal is very irregular with numerous small faces corresponding to different crys-

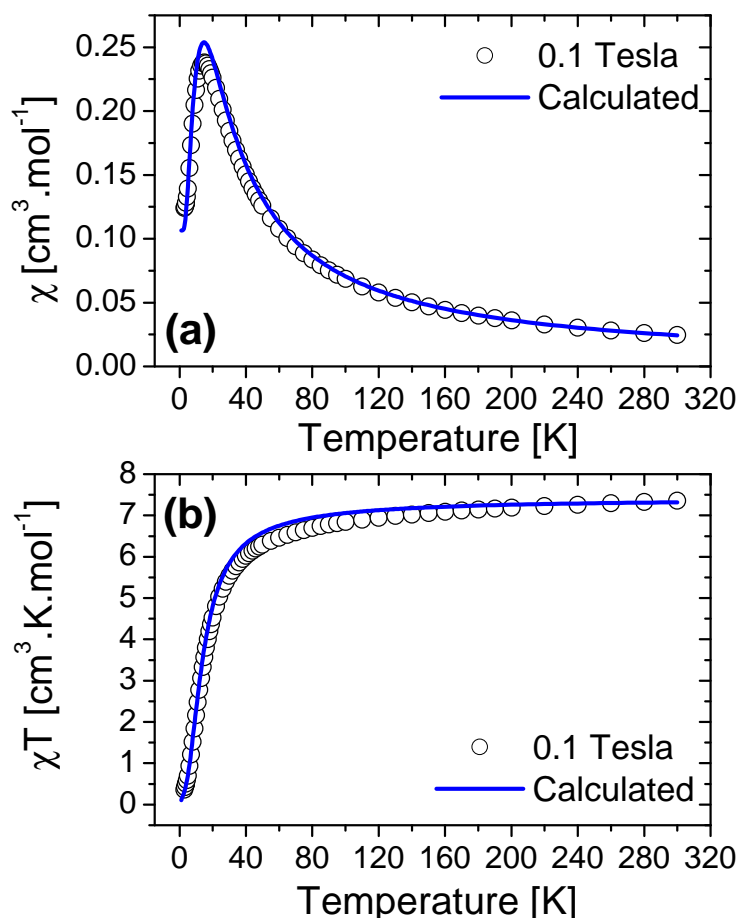


Figure 5.2: The measured and calculated χ (a) and χT (b) values versus temperature at 0.1 Tesla of a powder pellet of Fe₂-Penta.

tallographic planes. This made a precise orientation of the crystal on the cantilever extremely difficult. We therefore estimate the error in the orientation of the crystal in all single crystal measurements to be $\sim 10 - 15^\circ$. Figure 5.5 shows the angle resolved torque measurements in the ac and bc crystallographic planes at 1.8 K and in an external field of 8 Tesla. The crystal shows a very strong torque signal in the ac plane which is an indication that the system is strongly anisotropic. In the ac plane, the torque vanishes for the magnetic field being around 10° from a , while the signal is approximately 10 times smaller in the bc plane over the whole angular interval. This gives us a clear indication that the principal magnetic axis is close to the a crystallographic axis. Hence, the signal observed in the bc plane might be due to a small contribution of the principal axis which is not exactly along the rotation axis for the rotation in the bc plane. In addition, rhombic anisotropy may also lead to having a finite torque signal in the hard plane. Furthermore, we performed angle resolved measurements in the ac plane below and above the crossing point which was observed in the magnetization. Figure 5.6 shows the angle resolved torque at 1.8 and 15 K and an external field of

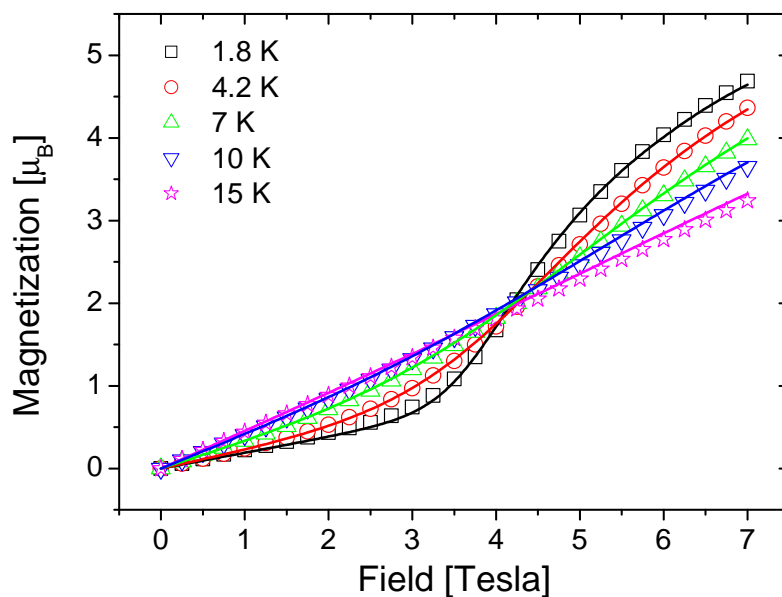


Figure 5.3: Powder magnetization measurements at various temperatures. The lines are fits with the spin Hamiltonian parameters discussed in the text.

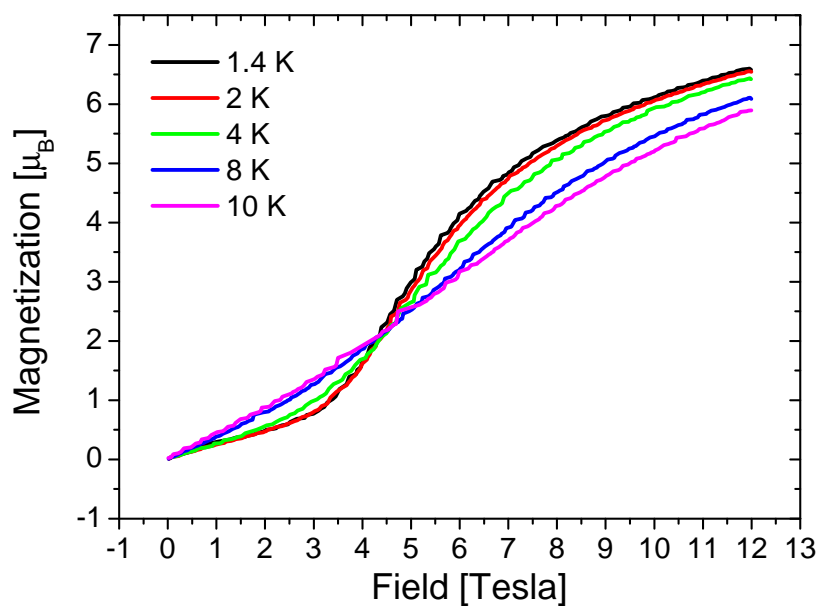


Figure 5.4: Powder magnetization measurements at various temperatures up to 12 Tesla.

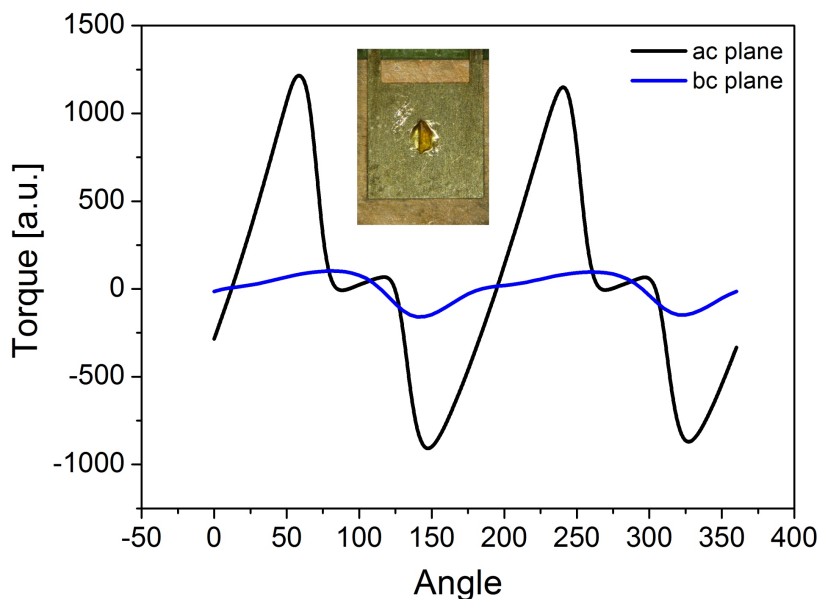


Figure 5.5: Angle resolved torque measurements for an 8 Tesla magnetic field rotated in the ac and bc planes at 1.8 K. The inset shows a picture of the single crystal placed on the cantilever.

2 Tesla. The results show a standard behavior of magnetically anisotropic clusters in the low field regime where the torque varies with $\cos\theta \sin\theta$ (chapter CTM). Interestingly, the torque signal switches sign going from 2 to 15 K which indicates that the ground and the excited states have opposite anisotropies. On the other hand, the 8 Tesla data (Figure 5.7) shows a rather more complicated picture, where a kink in the 2 K data is observed around 100° . In contrast to the 2 Tesla results, at 8 tesla, the torque has the same sign at both temperatures except in the range where the kink is observed.

5.3.3 High field torque magnetometry

The magnetization up to 12 Tesla showed neither a second inflection point nor saturation. To that end, we performed high field torque magnetometric measurements at 50 mK and up to 32 Tesla. Figure 5.8 shows the torque signal for the magnetic field applied at 1.6° , 3.6° , and 7.6° from the easy axis at 50 mK. The results confirm those of the magnetization and only a single step in the torque is observed up to 32 Tesla. The step occurs at a magnetic field which is lower than that observed in the magnetization measurements. This is not surprising since the crossing field is angle dependent. The magnetization was performed on a powder sample, and hence an average crossing field was observed. To that end, the torque was measured at different angles and the crossing field was extracted from the maximum of the numerical derivative $d\tau/dB$ (Figure 5.9). The crossing field again shows an unconventional behavior different from that previously observed in AF systems (where $B_c \propto (\cos^2\theta/2 - 1)$, θ is the angle between the field and the easy axis). Note that the high-field torque curves presented in Figure 5.8 were corrected by averaging the torque curves at $+\theta$ and $-\theta$ (see Chapter 2 for

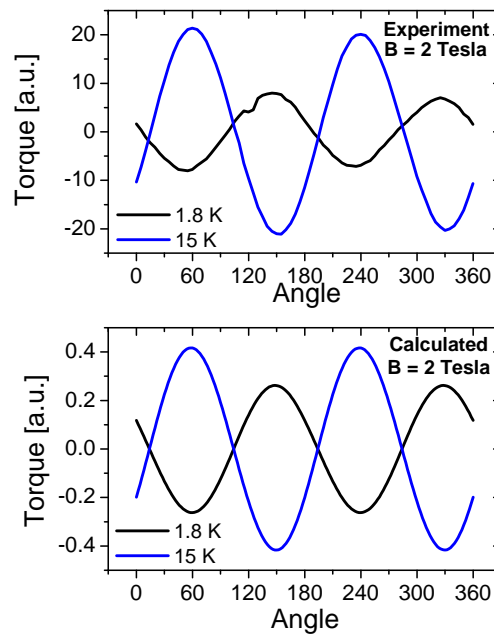


Figure 5.6: The measured(top) and calculated(bottom) angle resolved torque curves at 1.8 and 15 K at an external field of 2 Tesla in the ac plane.

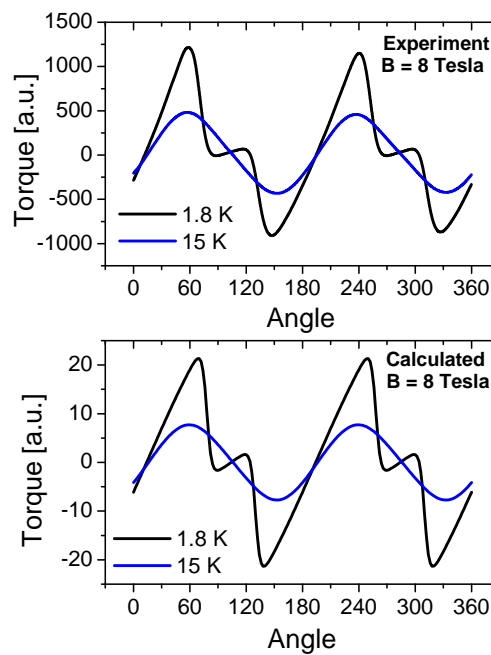


Figure 5.7: The measured(top) and calculated(bottom) angle resolved torque curves at 1.8 and 15 K at an external field of 8 Tesla in the ac plane.

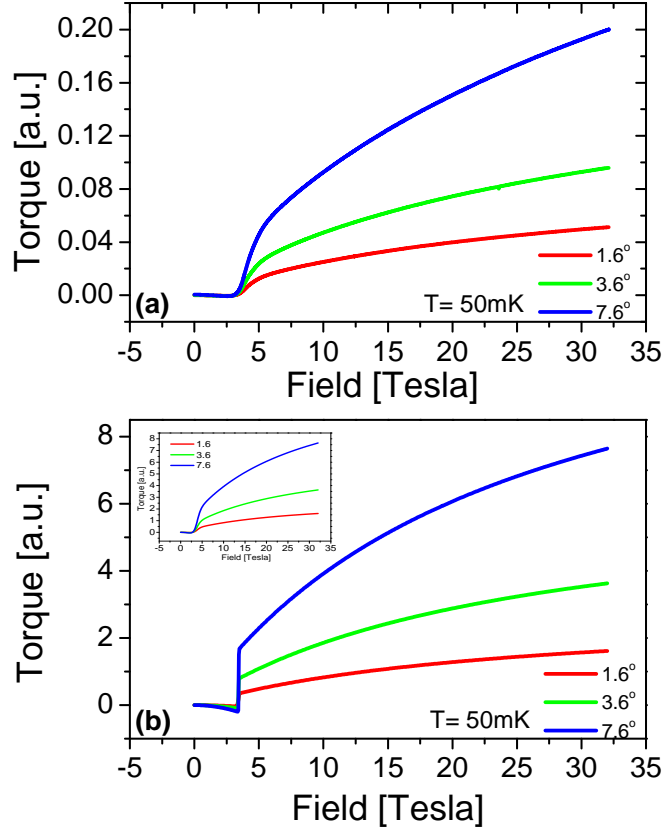


Figure 5.8: (a) Experimentally obtained torque signals at different angles at 50 mK (b) Calculated torque signals at 50 mK. The inset in (b) shows the calculated torque signals at T= 2.5 K.

details of the averaging process). The raw torque data and the averaged curves are shown in the supplementary information.

5.4 Analysis and discussion

We start by introducing the spin Hamiltonian used to describe the system,

$$\hat{H} = -J\hat{\mathbf{S}}_1 \cdot \hat{\mathbf{S}}_2 + D(\hat{S}_{1z}^2 + \hat{S}_{2z}^2) + g\mu_B\mathbf{B} \cdot (\hat{\mathbf{S}}_1 + \hat{\mathbf{S}}_2) \quad (5.1)$$

where the first term is the Heisenberg exchange term, the second term is the single ion anisotropy term, and the last term describes the Zeeman interaction. The two Fe(II) single ions within the dimer are related by an inversion center, hence both ions must have, collinear anisotropy tensor and the same anisotropy term D. The results obtained in various measurements enabled us to understand and describe the system with high accuracy. The non-magnetic ground state observed in the magnetization and torque

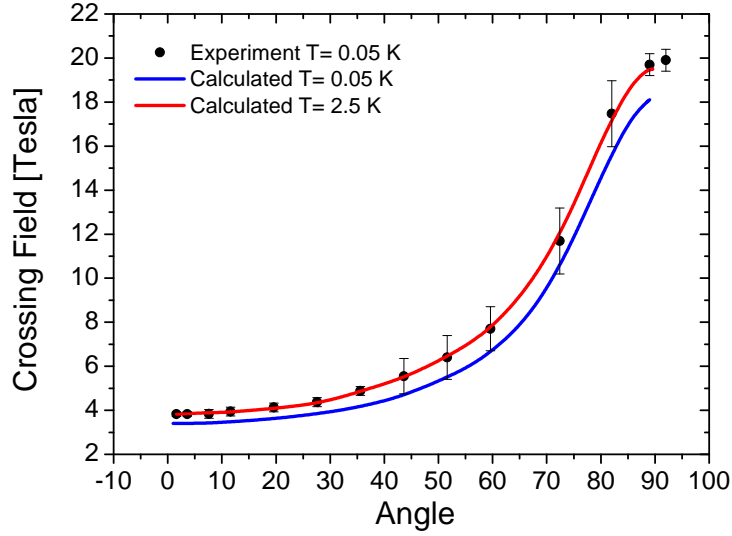


Figure 5.9: The crossing field as extracted from the inflection point of the torque curves at 50 mK. The calculated crossing fields were extracted similarly from calculated torque curves at $T = 0.05$ K and 2.5 K.

measurements, in addition to the maximum in the χ vs T data strongly point towards an AF ground state ($J < 0$). Furthermore, the observed value of the crossing (~ 4.2 Tesla) in the magnetization measurements indicates that the coupling constant is on the order of few Kelvin. At the same time, since Fe(II) single ions contain a small spin-orbit contribution to the magnetic moment (6 d electrons), we restricted the g value to $g \geq 2$. Moreover, the sign of the torque signals predicts a single ion anisotropy of the easy type, and therefore the axial anisotropy term was confined only to negative values ($D < 0$). As mentioned above, in the strong exchange limit, one would expect to observe 4 level crossings instead of one. The number of crossings successively decreases as we go to the weak exchange limit (as J/D decreases) until eventually only one crossing is observed for $D \gg J$. This points towards having the system in the weak-exchange limit.

Motivated by all these conclusions drawn from the various complementary results obtained, we performed extensive simulations in order to obtain the set of spin Hamiltonian parameters which describes our system best: $g = 2.23(5)$, $J = -1.74(6)$ cm^{-1} , and $D = -8.5(4)$ cm^{-1} . These values were obtained from the magnetization fits (Figure 5.3). Using the same set of parameters we obtained outstanding agreement between the various calculated and experimental data (all simulations shown above were performed with the same set of parameters). The results demonstrate that we have an antiferromagnetically coupled dimer with weak exchange coupling and a much stronger single ion anisotropy ($D \approx 5J$). Note that for $D = 0$ (or $D \ll J$), $[\hat{S}, \hat{H}] = 0$ where S , the total spin, remains conserved. However, if $D \gg J$, the spin states are strongly mixed, and S is no longer a good quantum number (see next section) whereas M_S remains a good quantum number in the absence of a transverse field. The energy spectrum of

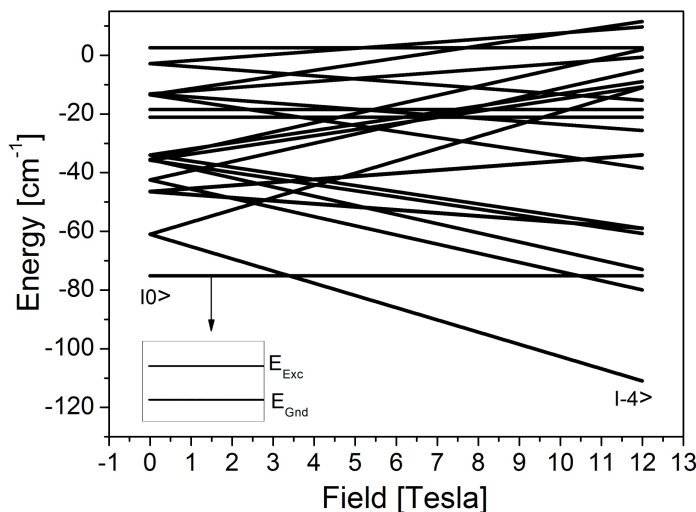


Figure 5.10: The energy spectrum of Fe₂-Penta for the easy axis parallel to the external applied field. The system undergoes a spin state crossing at ~ 3.4 Tesla. The inset shows the energies of the lowest two energy levels.

the system, calculated with the best-fit spin Hamiltonian parameters provided above, is shown in Figure 5.10. The nature of the ground state $|Gnd\rangle$ and the first excited state ($|Exc\rangle$) is discussed later, but at this point it is important to know that they are both non-magnetic ground states with $M_S = 0$. Above these two states, we have the $M_S = \pm 4$ doublet of the $S = 4$ spin state. Under the effect of an axial magnetic field, the system undergoes a spin state transition from the ground state to the $|4, -4\rangle$ state in one single step. This is reflected as a giant step in the magnetization which changes from zero (before the crossing) to $\sim 8.9 \mu_B$ (after the crossing). In a powder, the step is broadened due to the different orientations of the easy axes within the sample, but nevertheless we can see that we have one crossing centered around 4.2 Tesla and the magnetization value goes up to around $6.3 \mu_B$ at 12 Tesla. The calculated χ and χT curves versus temperature at 0.1 Tesla with the same set of parameters agree with the same picture and reproduce the experiments (Figure 5.2). χ was also measured and successfully reproduced at higher magnetic fields (shown in supplementary information).

The angle resolved torque measurements are very rich in information and in fact one can nicely explain their behavior based on the weak-exchange model. Figure 5.6 shows the angle resolved torque at 2 Tesla, the system is in the ground non-magnetic state for all angles between 0 and 360° at this field. At 1.8 K, only the ground and the first excited states ($|Gnd\rangle$ and $|Exc\rangle$) are populated. Despite the fact that both states have $M_S = 0$ and zero magnetization, they still have a finite torque signal which comes from the magnetic character induced by the mixing of the excited spin states¹. The anisotropy of the first spin excited state is positive (hard axis) and this is reflected in the torque signal (the torque is negative for angles between 10 and 100°). At higher

¹The $M_S=0$ state of a system with positive D value (hard axis) for instance, has zero magnetization but it has a torque contribution if $S \neq 0$.

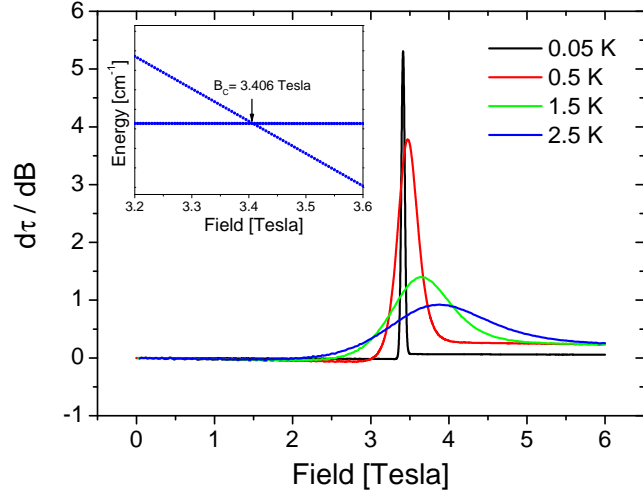


Figure 5.11: Calculated $d\tau/dB$ at different temperatures. The maximum of $d\tau/dB$ is temperature dependent. The inset shows the energy spectrum indicating the crossing field value.

temperatures (at 15K) the $M_S = -4$ state is populated and the torque switches sign as expected. Note that the ratio between the max (at 15K) and the min (at 1.8 K) of the torque signal at around 60° of the 15 and 1.8 K data can only be reproduced with the above parameters. The situation is more complicated at 8 Tesla. The system is in the $M_S = -4$ state for angles between c.a. 10 and 70° , but for higher angles, the ground state of the system remains the non-magnetic state. For angles where we have an $M_S = -4$ ground state, the torque signal has the same sign for $T = 1.8$ and 15 K where the signal is higher at the former temperature as expected. However, for the small interval in angle where the system is still in the non-magnetic state, we see that torque switches sign and behaves in analogy with the 2 Tesla data. The fact that 8 Tesla is neither high nor low enough field for the system to be either in the non-magnetic or the $M_S = -4$ state, respectively, leads to this unconventional angular dependence of the torque signal. In other words, the system switches spin state as a function of angle at a constant external field. This can be better understood by looking at the crossing field values versus angle in Figure 5.9. At around 60° , the level crossing is expected at 8 Tesla, and plainly for angles higher than 60° , one needs to apply a field higher than 8 Tesla to energetically favor the $M_S = -4$ state. Figure 5.9 shows the calculated crossing field versus angle at two different temperatures (0.05 and 2.5 K). While the experiments were performed at 0.05 K, the 2.5 K simulated data shows a better agreement with the experiment. The key to understanding this contradiction lies in the process of extracting the crossing field values from the torque measurements. The crossing field is extracted from a magnetization or torque signal by taking the derivative of the torque with respect to the field $d\tau/dB$. In other words, this shows the rate of the change of the torque which in principle should be maximum at the level crossing. Hence, it is common to assign the maximum of $d\tau/dB$ to the crossing field.

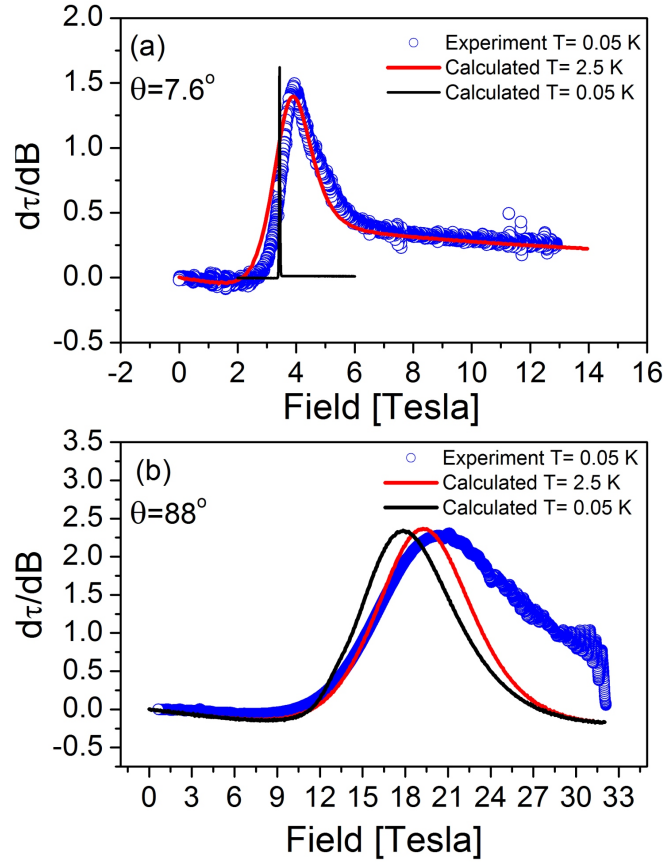


Figure 5.12: Experimentally obtained and calculated $d\tau/dB$ at 7.6° (a) and 88° (b) (see text).

Figure 5.11 shows the calculated $d\tau/dB$ values for different temperatures. The energy level diagram is temperature independent and equally is the level crossing. However, we can clearly see that the maximum of $d\tau/dB$ does depend on the temperature and more fundamentally on the width of the step. We have therefore compared the widths of the experimentally observed $d\tau/dB$ to the theoretically calculated ones (Figure 5.12) with effective temperatures higher than 0.05 K that mock the broad experimental signals keeping in mind the different underlying physics. The width of the simulated torque curves at 2.5 K is comparable to the experimentally observed one, and consequently the extracted level crossings show a much better agreement. The real reason behind the broadening of the torque signals can be threefold in our opinion: (i) a distribution in the spin Hamiltonian parameters (especially D) could lead to a distribution in the step position, and hence a broader step, (ii) a misorientation of the crystal where a τ_x component can be superimposed on the measured τ_y signal and/or the force component induced by the magnetic field inhomogeneity, and (iii) additional weak interactions in the spin Hamiltonian (such as Dzyaloshinski-Moriya) which could lead to an anti-crossing of the levels and thus broaden the step (see Chapter 2). This sort of non-thermal broadening was observed in several AF systems ([35][38][81]) but the effect is more pronounced in our case. Further research is needed to confidently attribute the

broadening to one or more of these scenarios.

One more piece of evidence to the validity of our model comes from the high-field torque magnetometry. Figure 5.8 shows the experimental torque signals at 1.6, 3.6, and 7.6° (a) at 50 mK, and the calculated signals (b) with the same set of parameters used to describe the other results ($g = 2.23(5)$, $J = -1.74(6) \text{ cm}^{-1}$, and $D = -8.5(4) \text{ cm}^{-1}$). Aside from the non-thermal broadening observed in the experiment, there is a very good qualitative agreement between the calculated and experimentally observed signals. The torque remains zero (with a small negative contribution) until the first and only crossing field where it shows a step and then it increases quadratically with B as expected up to 32 Tesla. The inset of 5.8 shows the calculated torque signals at 2.5 K which again as discussed above show a better agreement with the experimental data. The agreement between the calculations and the experiment is not as good for the 88° data shown in Figure 5.13. We were not able to measure the torque at angles larger than 92° because of the strong signal (the signal saturates after having a short contact between the cantilever and the lower plate due to strong torque signals). This hindered our ability in properly defining the position of the zero torque signal, and thus made the averaging of the torque around 90° an imprecise procedure. Another source of error that may be contributing to the discrepancy between the calculations and the experiment at 88° is the misalignment of the crystal which is more crucial for higher torque signals. Note that the relative strength of the torque at 88 and 1.6° (as shown in Figure 5.13) is also in favor of having an easy axis close to the crystallographic a axis where the expected signal is much stronger for transverse (88°) rather than axial fields (1.6°). Finally, the performed FDMRS measurements (shown in supplementary information) do not show any resonance line in the frequency range 4-17 cm^{-1} . This is in agreement with the calculated energy spectrum of the system (Figure 5.10). In this frequency range one would not expect any resonance line. The first line (between $M_S = -4$ and $M_S = -3$) would appear around 19 cm^{-1} . The $M_S = 0$ to the $M_S = -4$ transition is at 15 cm^{-1} , but this excitation is not allowed by selection rules. Further investigations including High-Field ESR may give additional information on the energy spectrum of the system.

5.5 Properties of low lying energy states

In this section, we focus on the physics of the two lowest energy eigenstates of the system. In an AF dimer, the classical ground spin-state configuration consists of two states labeled up and down which correspond to the two orientations of the Néel vector \mathbf{n} being along $\pm \mathbf{e}_z$ (where \mathbf{e}_z is a unit vector along the easy axis). However, quantum mechanically the two lowest states of a system in the weak-exchange limit are composed of the symmetric and antisymmetric combination of the up and down states and can be described as,

$$\begin{aligned} |Gnd\rangle &= \frac{|\uparrow\downarrow\rangle + |\downarrow\uparrow\rangle}{\sqrt{2}} \\ |Exc\rangle &= \frac{|\uparrow\downarrow\rangle - |\downarrow\uparrow\rangle}{\sqrt{2}} \end{aligned} \quad (5.2)$$

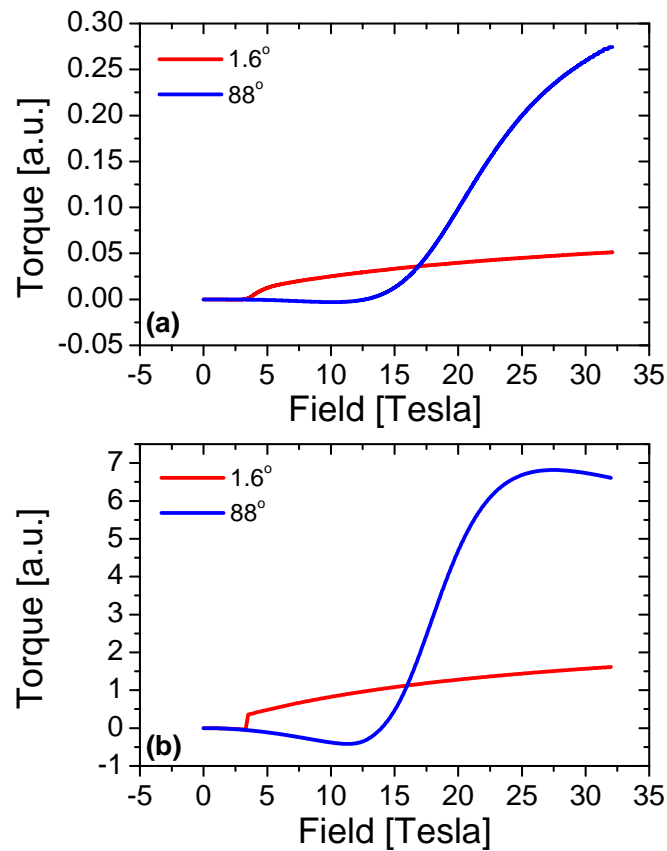


Figure 5.13: The measured (a) and calculated (b) torque signals at 1.6° and 88° at 50 mK.

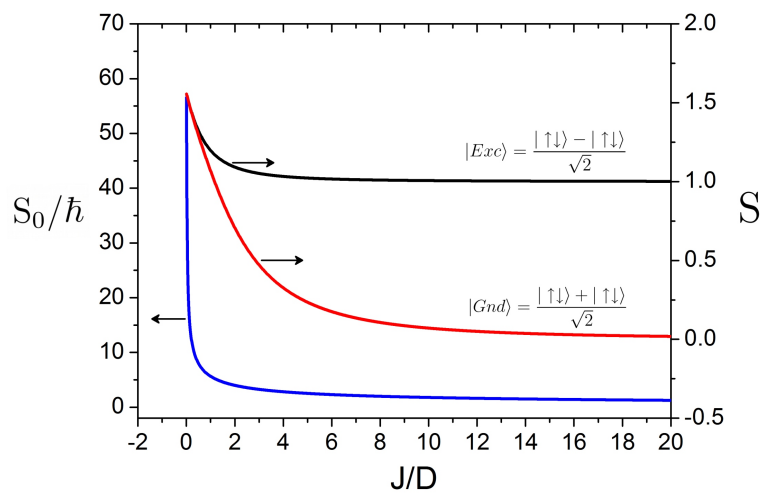


Figure 5.14: The calculated expectation value of S (right) for $|Gnd\rangle$ and $|Exc\rangle$ and the tunnel action (left) as they vary with J/D .

These two states are separated in energy by the tunnel splitting Δ . As mentioned earlier, in the weak-exchange limit the mixing of the spin states becomes important. Figure 5.14 (right axis) shows the spin S extracted from $\langle Gnd|\hat{S}^2|Gnd\rangle$ and $\langle Exc|\hat{S}^2|Exc\rangle$ for the $|Gnd\rangle$ and $|Exc\rangle$ states respectively versus J/D . For high J/D values (strong-exchange), the spin states are pure and we have an $S = 0$ and $S = 1$ for the $|Gnd\rangle$ and $|Exc\rangle$ states, respectively. As we approach the weak-exchange limit ($J < D$), the spin states become strongly mixed and eventually the two states have the same spin expectation value. The tunnel splitting between the two states for a transverse field B_x is given by a semiclassical approach to be [77],

$$\Delta = \Delta_0 \left| \sin\left(\pi \frac{Ng\mu_B B_x}{4|J|}\right) \right| \quad (5.3)$$

where $\Delta_0 \propto e^{-4s\sqrt{|D/J|}}$, is the tunnel splitting at zero field and N is the number of spins. This approach is quite useful for systems with a large number of spins N (like AF rings), since the Hamiltonian dimension in these systems is big. In our system, the dimension of the Hamiltonian is (625), hence we can calculate the tunnel splitting by diagonalizing the microscopic Hamiltonian. Figure 5.15 shows the energy difference between the lower two states (tunnel splitting) as a function of an external transverse field applied along x . The oscillation of the tunnel splitting demonstrates the constructive and destructive interferences predicted by the semi-classical Eq. (5.3). This periodic quenching of the tunnel splitting was already observed for ferromagnetic [86], and antiferromagnetic molecular nanomagnets [81]. Another parameter that is important to introduce is the tunnel action $S_0/\hbar = Ns\sqrt{2|D/J|}$, which is a crucial parameter defining the condition for the Néel vector tunnelling to occur ($S_0/\hbar > 2$). On the one hand, the tunnelling action in the Fe_2 dimer, $S_0/\hbar \approx 12.5$ is much larger than that observed in AF rings (Table 5.1). On the other hand, the tunnel splitting at zero field is around 83 MHz (as extracted from the energy spectrum), which is large enough to be accessible by several experimental techniques, especially NMR. In fact, these numbers show that the Fe_2 -Penta dimer is an optimized system with high tunnelling action (unlike AF rings) and moderate tunnel splitting (unlike ferromagnetic clusters) which makes it a very good candidate to study macroscopic quantum coherence such as tunnelling of the Néel vector. Several NMR spectrometers operate in frequency ranges close to 100 MHz. This gives us the opportunity to directly access the tunnel splitting by observing the microwave induced transition. Another way is to study the proton nuclear spin-lattice relaxation rate as a function of transverse field. We expect an enhancement in the relaxation rate at a magnetic field where the cross-relaxation effect between the nuclear Zeeman reservoir and the reservoir of the two split lower states takes place.

5.6 Conclusions

In conclusion, we have studied a unique antiferromagnetically coupled $Fe(II)$ dimer. The full characterization of the system shows that the exchange coupling is much weaker than the strong single ion anisotropy. This leads to an energy diagram different than that observed for the strongly coupled systems. The interplay between exchange

Table 5.1: S_0/\hbar of different AF systems reported in literature, and of the Fe₂-Penta studied in this work.

	S_0/\hbar
Fe ₁₀	3.32
CsFe ₈	3.91
NaFe ₆	2.47
LiFe ₆	1.54
Fe ₁₈	5.9
Fe ₂ -Penta	12.5

and single ion anisotropy leads to this unique picture of the spin state crossings where only a single transition occurs from a non-magnetic ground state to an $M_S = -4$ state. This is reflected in a giant step in the magnetization, analogous to the spin flip seen in antiferromagnets with long range order. Furthermore, the system exhibits a tunnelling action S_0/\hbar of 12.5, and a tunnel splitting of ~ 83 MHz. Motivated by these numbers, we propose this system as a potential candidate to observe coherent tunnelling of the Néel vector.

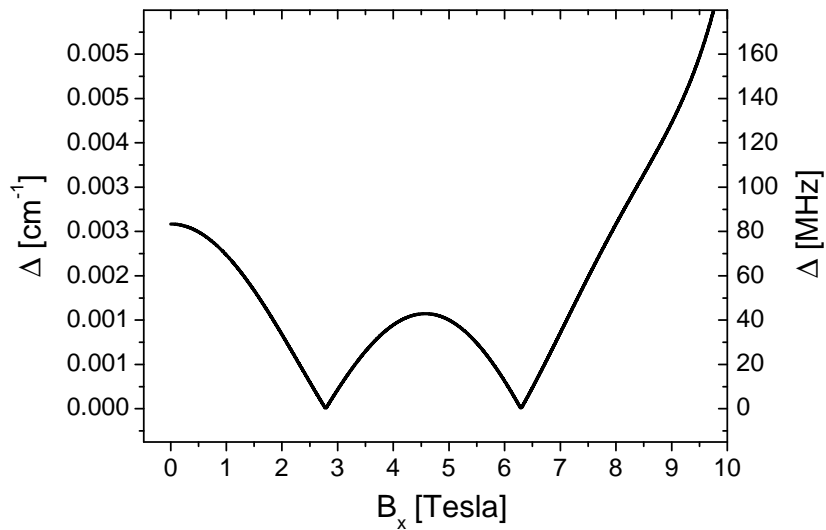


Figure 5.15: The energy gap between the lowest two quantum states versus a transverse field as simulated with Eq. (5.1).

5.7 Supplementary Information

This section includes the supplementary figures discussed in the preceding sections.

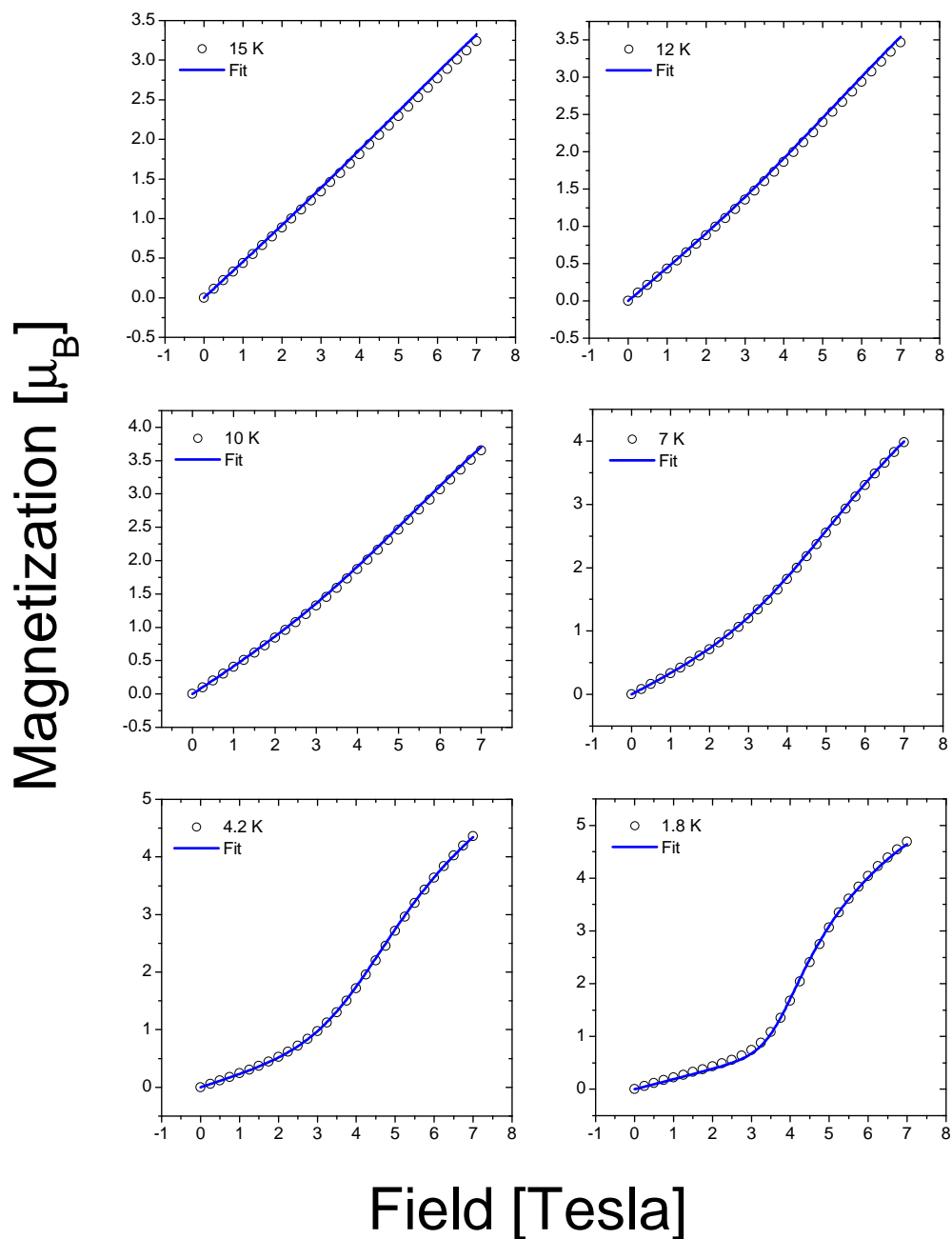


Figure 5.16: Powder magnetization measurements at various temperatures. The lines are fits with $g = 2.23(5)$, $J = -1.74(6) \text{ cm}^{-1}$, and $D = -8.5(4) \text{ cm}^{-1}$.

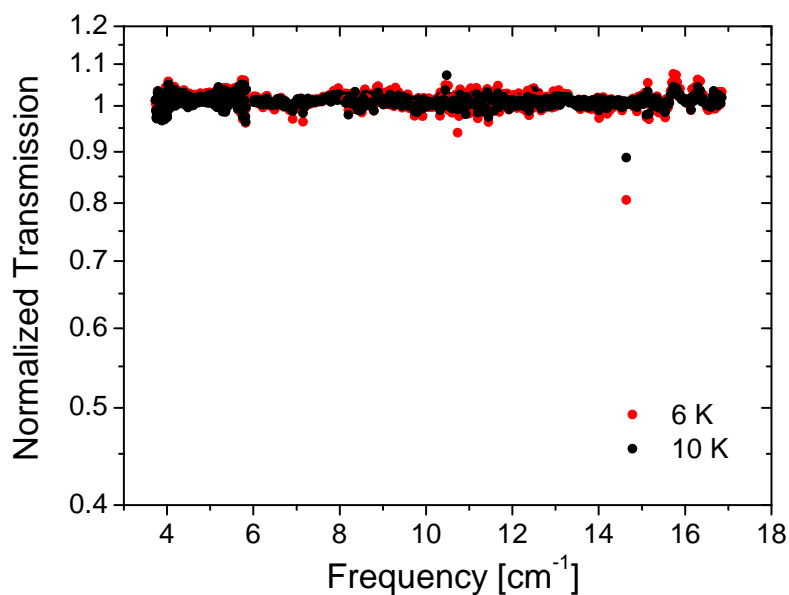


Figure 5.17: FDMR normalized spectra at 6 and 10 K. The transmission spectra at both temperatures were divided by the 19 K spectrum. No resonance lines are observed in whole frequency range.

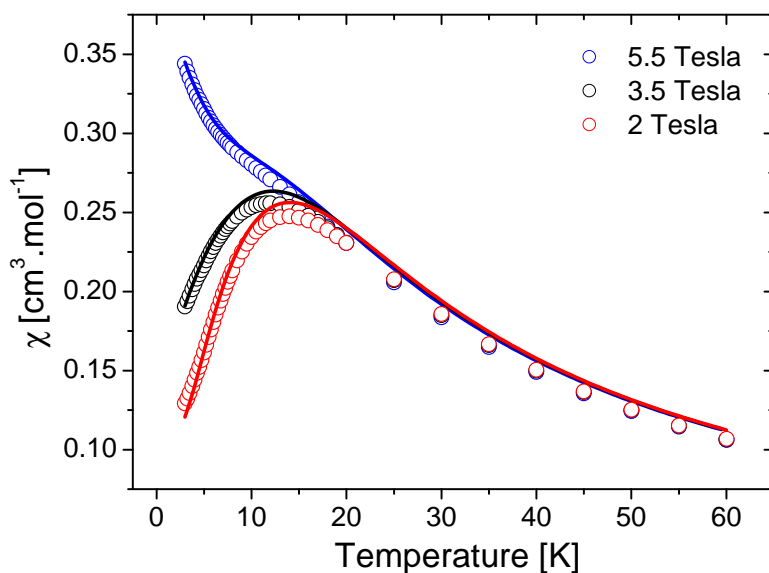


Figure 5.18: The measured χ values at 3 different fields vs temperature. The lines are calculated with the spin Hamiltonian parameters: $g = 2.23(5)$, $J = -1.74(6)$ cm⁻¹, and $D = -8.5(4)$ cm⁻¹.

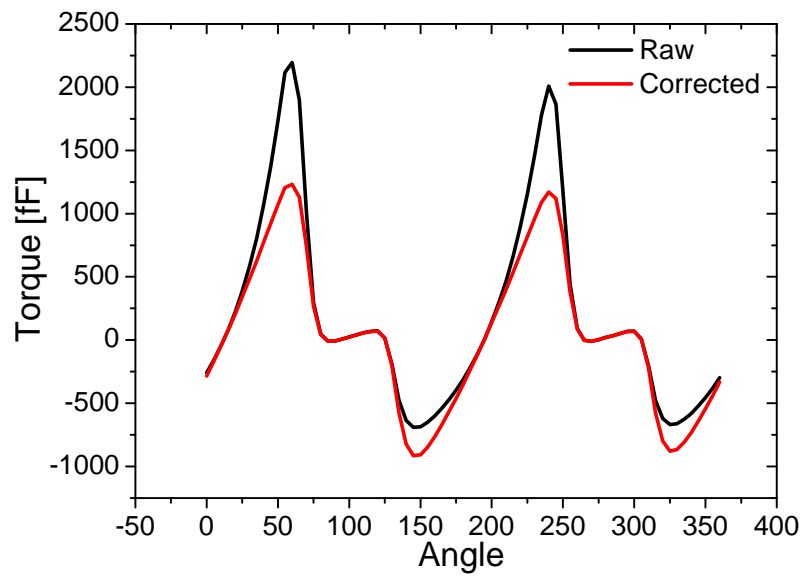


Figure 5.19: The raw torque data and the corrected values for the non-linear response of the cantilever.

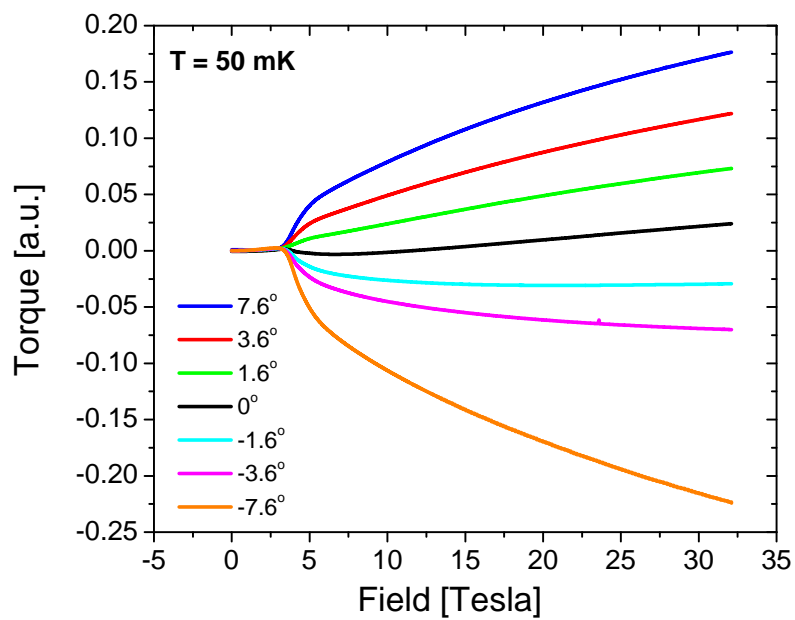


Figure 5.20: Raw torque curves for the magnetic field applied at different angles close to 0° from the easy axis.

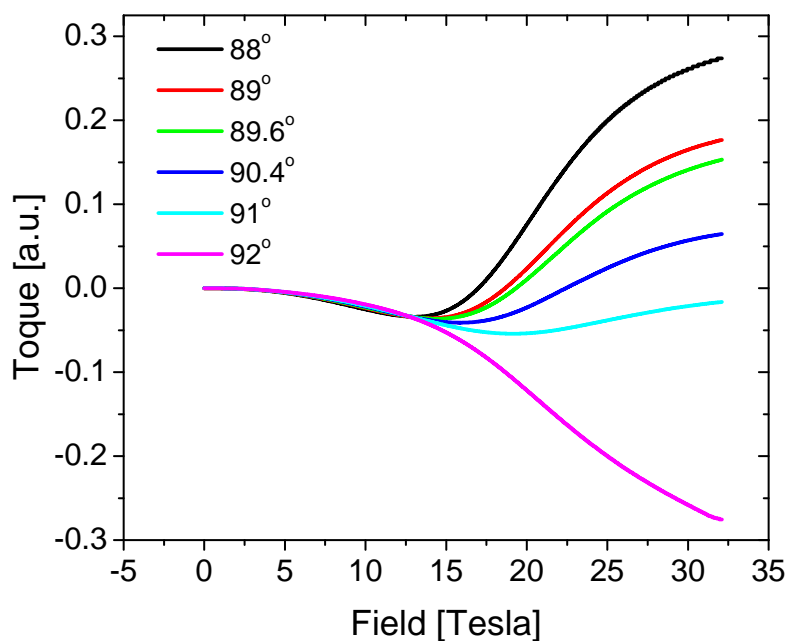


Figure 5.21: Raw torque curves for the magnetic field applied at different angles close to 90° from the easy axis.

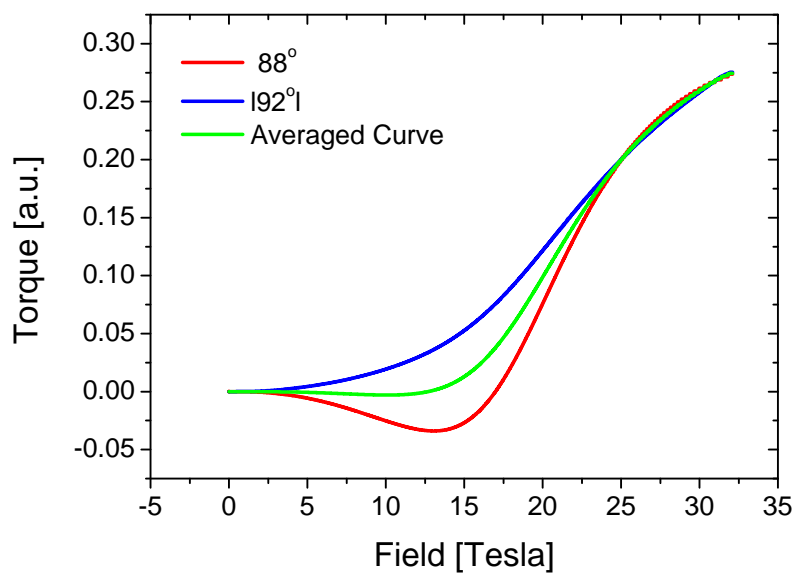


Figure 5.22: The raw torque data at 88° and the absolute value of the torque signal at 92° . The average curve is $(\tau(88^\circ) - \tau(92^\circ))/2$.

Chapter 6

High Field Torque Magnetometry on a Molecular Dysprosium Triangle

6.1 Introduction

Lanthanides are fundamentally different from transition metals, having their valence electrons in the 4f rather than the 3d orbitals. As a consequence, lanthanides have weaker ligand fields than the transition metal coordinated ions. However, they possess large magnetic moments and quite often large magnetic anisotropy due to the strong spin-orbit coupling, which makes them interesting building blocks for single molecule magnets (SMMs). The fact that the unpaired electrons in the 4f orbitals are effectively shielded, leads to weak exchange interactions, which makes coupling between single ions rather a difficult task. On the other hand, mononuclear complexes of 4f ions have shown slow relaxation of the magnetization at very high temperatures [87] compared to those observed in transition metals. Despite the out of phase ac signal observed above 40 K, hysteresis curves were observed only at very low temperatures [88]. On cooling, deviations from the Arrhenius law predicted for SMM behavior become more important, which indicates that tunneling plays a crucial role in the relaxation of the magnetization. In fact the high probability of tunneling, and consequently under-barrier relaxations, cancel any remnant magnetization. It is therefore of crucial importance to obtain information on the low lying sublevels of the 4f electronic systems, in order to understand the magnetism, and especially the relaxation mechanisms of these compounds.

Few reports had appeared on polynuclear lanthanide-based systems [89][90]. Recently, Luzon and coworkers have reported an elegant study on a molecular Dysprosium triangle, which has unusual magnetic properties [91], namely, showing slow relaxation of the magnetization, yet having a non-magnetic ground state. The compound is a trinuclear Dy^{3+} with the chemical formula, $[\text{Dy}_3(\mu_3\text{-OH})_2\text{L}_3\text{Cl}(\text{H}_2\text{O})_5]\text{Cl}_3$, hereafter called Dy_3 (where L is the anion of ortho-vanillin) [92]. The structure is shown in Figure 6.1, the three lanthanide ions are held together by multiple bridges comprised by five oxygen atoms, two belonging to the OH^- ions lying above and below the plane of the triangle and the other three belong to the phenolato group of the *o*-vanillin

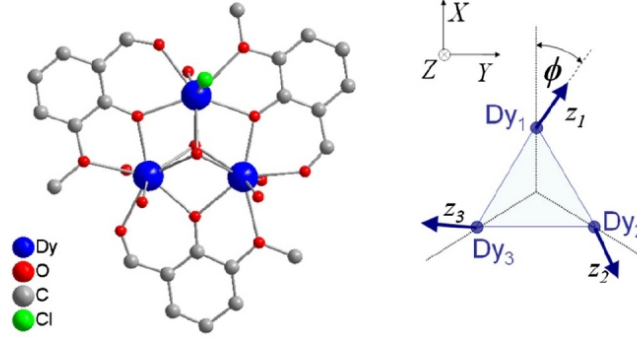


Figure 6.1: Left: View of the molecular structure of Dy_3 cluster where the hydrogen atoms, the chloride counteranions and the solvent molecules of crystallization have been omitted. Right: Schematic view of the spin structure of the Dy_3 triangular cluster and of the local easy axes orientation in respect of the laboratory XYZ reference frame [91].

ligands [92]. The molecule has almost an idealized trigonal symmetry (C_3), if not for the chloride atom connected to only one of the Dy^{3+} ions. Typically, triangles with half integer spins which are antiferromagnetically coupled to each other, are frustrated magnetic systems with a magnetic ground state. In this compound, the coexistence of the C_3 symmetry, the single-ion Ising-like strong magnetic anisotropy, and the antiferromagnetic (AF) interaction between the single ions, results in a non-magnetic ground state. The C_3 symmetry causes the easy axes of the single ions, which are located in the plane of the triangle, to be at 120° one from each other. Furthermore, the magnetic moments of the individual Dy^{3+} ions are pinned to the easy axis direction due to the large single ion anisotropy. Eventually, the AF interaction in between the single ions couples these three magnetic moments which cancel each other leading to a non-magnetic ground state. This is confirmed by the low temperature magnetization for an axial field (Figure 6.2 (a)), which remains practically zero for low fields with a sudden jump to the saturation value of $20 \mu_B$ around 8 kOe [91]. The authors used the spin Hamiltonian approach to model the system, considering an effective spin $1/2$ for each Dy^{3+} with a large easy axis anisotropy, i.e. an Ising spin, in a first approximation. As a further improvement for the model, the ground ($|J = 15/2, m_J = \pm 15/2\rangle$) and the first excited ($|J = 15/2, m_J = \pm 13/2\rangle$) doublets, were considered to describe the energy levels of the single ion. The expression of the Hamiltonian used to describe the system is,

$$\hat{H} = -j(\hat{\mathbf{S}}_1 \cdot \hat{\mathbf{S}}_2 + \hat{\mathbf{S}}_2 \cdot \hat{\mathbf{S}}_3 + \hat{\mathbf{S}}_3 \cdot \hat{\mathbf{S}}_1) - g\mu_B \sum_{i=1,3} \mathbf{B} \cdot \hat{\mathbf{S}}_i + \frac{\delta_o}{14} \sum_{i=1,3} \left(\left(\frac{15}{2} \right)^2 - \hat{S}_{z_i}^2 \right) \quad (6.1)$$

The first term is the isotropic (Heisenberg) exchange between the Dy^{3+} ions, the second is the Zeeman term, and the last term describes the single-ion anisotropy and δ_o is the zero field splitting between $|J = 15/2, m_J = \pm 15/2\rangle$ and $|J = 15/2, m_J = \pm 13/2\rangle$

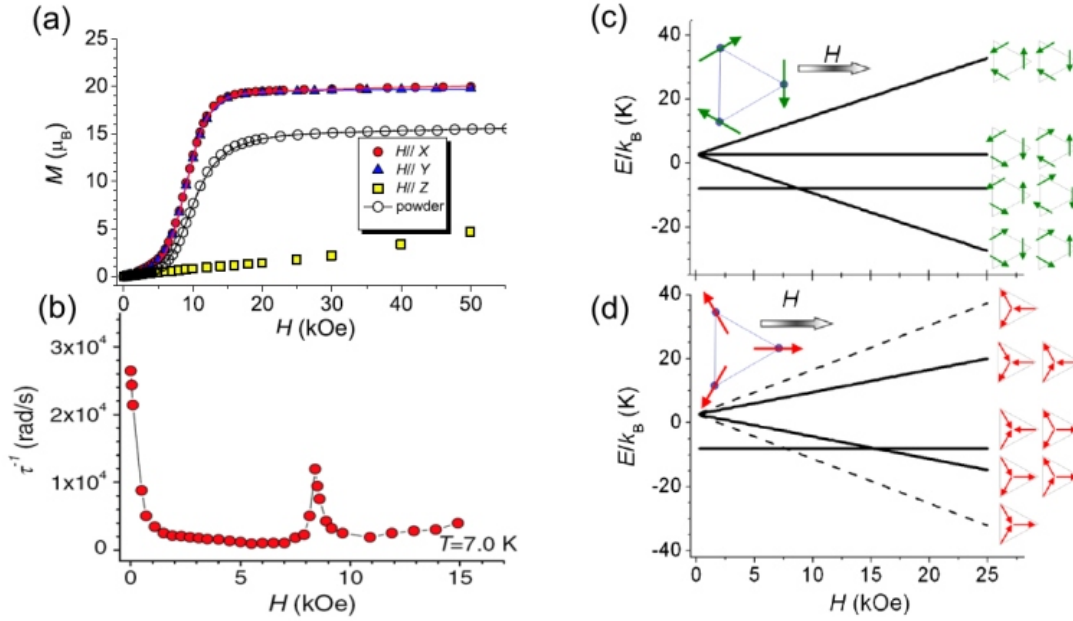


Figure 6.2: (a) Field dependence of the magnetization measured along the X, Y, and Z axes at 1.9 K. The solid lines represent the calculated values with equation (x) and the best-fit parameters (b) Field dependence of the relaxation rate measured at 7 K with the field applied along Y. The Zeeman splitting of the levels due to the application of the field along the X axis (bisector) are shown in (c) for $\phi = 90^\circ$, and (d) for $\phi = 0^\circ$. The spin structure for each state is schematized by the arrows. The nondegenerate states are highlighted by dashed lines. Modified from [91].

states of each Dy^{3+} ion. Figure 6.2 shows the calculated energy spectrum for the coupled Dy_3 using (6.1), with the best-fit parameters $j = 0.092$ K, $g = 1.35$, and $\delta = 102.5$ K obtained by fitting the powder magnetization data for $\phi = 90^\circ$ (c), and $\phi = 0^\circ$ (d). ϕ is the angle that defines the direction of the easy axes in the triangle (Figure 6.1). The energy spectra for both extremes (0 and 90°) in ϕ are very similar, the only difference is the splitting of the excited states, where in the case of $\phi = 0$, a second crossing with the non-magnetic state is expected at around 15 kOe. Dy_3 is also characterized by a very rich and unique magnetization dynamics. Despite the non magnetic ground state, the relaxation rate decreases on lowering the temperature following an Arrhenius law $\tau = \tau_0 \exp(U/k_B T)$, as predicted for SMM behavior. Figure 6.2 (b), shows the relaxation rate of the magnetization versus an externally applied field in the plane of the triangle at 7 K [91]. At zero field, the relaxation of the magnetization seems to occur due to the reversal of one spin inside the triangle, and quantum tunneling of the magnetization enhances the relaxation rate. Far from any level crossings, the relaxation seems to occur through an Orbach process, and at 3 kOe the barrier U is around 120 K. This value is extracted from the ac susceptibility measurements, and therefore it is an effective barrier which is affected by the under barrier processes. At c.a. 8 kOe (first level crossing), the relaxation rate is again enhanced. Note that the

two conditions (at 0 and 8 kOe), where an enhancement is observed, are fundamentally different. The former corresponds to flipping of the magnetic moment of one of the Dy ions due to the resonance between the $15/2$ and $-15/2$ levels. The situation is rather different at the first level crossing, where the tunneling is supposed to occur between two eigenstates of the coupled spin system. On the other hand, ab initio calculations [93], based on the complete active space self-consistent-field (CASSCF) method, have shown that each Dy^{3+} in the triangle has a ground state doublet mainly described as $|J = 15/2, m_J = \pm 15/2\rangle$. The first excited doublet is separated by c.a. 200-300 K, depending on which of the three non-equivalent sites is considered.

The determination of the sublevel structure of lanthanides in general is a difficult task, both experimentally and theoretically. As δ_o plays a crucial role in the relaxation mechanism, it is therefore important to determine its value independently in order to better explain the unconventional dynamics of the system. Standard magnetometry is not very sensitive to the value of δ_o . To that end, we have performed high-field torque magnetometry to quantify the crystal field splitting in the system. In addition, we performed low temperature (mK range) torque measurements to investigate the nature of the level crossing, and hence explain the enhancement in the relaxation rate at the crossing.

6.2 Experimental

Dy_3 single crystals were synthesized as described in [92]. Low field torque magnetometric measurements were partly performed on the home built setup described in Chapter 2, and partly on a commercial Oxford silicon CTM at the University of Florence. High-field (and low temperature) torque measurements were performed at the Grenoble High Magnetic Field Laboratory (GHMFL) on a copper beryllium cantilever inserted into magnet M9. Some of the measurements were performed at the National High Magnetic Field Laboratory (NHMFL) in Tallahassee. The energy diagrams, and torque signals were calculated using a self written program (See Modeling techniques).

6.3 Results and discussion

6.3.1 Spin Hamiltonian model

We have used the same approach as Luzon et al to calculate the energy of the lowest lying levels in Dy_3 , and consequently describe the magnetic properties of the system. The same Hamiltonian described in (6.1) was used with the exception that the spin operators used were different. Instead of using the $|15/2, \pm 15/2\rangle$ and $|15/2, \pm 13/2\rangle$ as basis, we have used the former in addition to $|15/2, \pm 5/2\rangle$ in order to simplify our calculations. In fact, we have used a $3/2$ spin operator which normalized by a factor of 5 to employ the same spin Hamiltonian parameters used in [91]. This assumption is valid, since in Lanthanides, the m_J sublevels of the J ground state are not necessarily arranged in a decreasing order of m_J as in transition metals, and could be irregularly

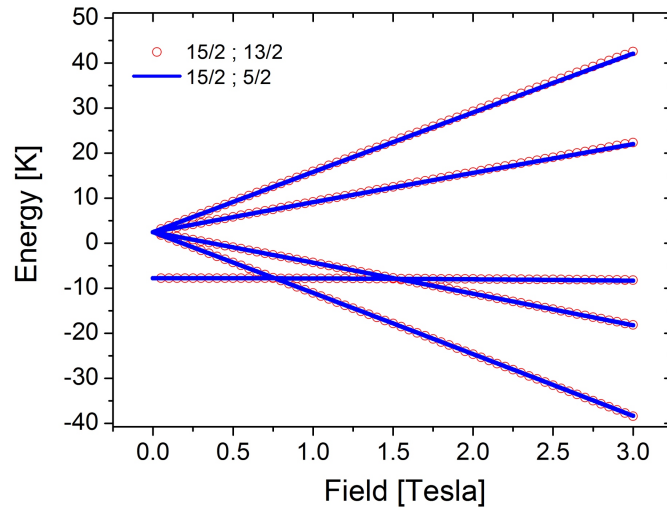


Figure 6.3: The energy levels of the Dy_3 calculated with $j = 0.092$ K, $g = 1.35$, and $\delta = 102.5$ K for both models discussed in the text.

placed in the energy level scheme. Quantum mechanically, the \hat{S}_+ operator of an $3/2$ spin system, connects the $-1/2$ and $+1/2$ states, while the two $13/2$ states are not connected in the original basis used by Luzon et al, at least not in the first order. Broadly speaking, the assumption of implementing the spin Hamiltonian is in itself a simplification to model the Dy_3 energy diagram. Figure 6.3 demonstrates the agreement between the calculated energy diagrams with our model and that from Luzon et al.

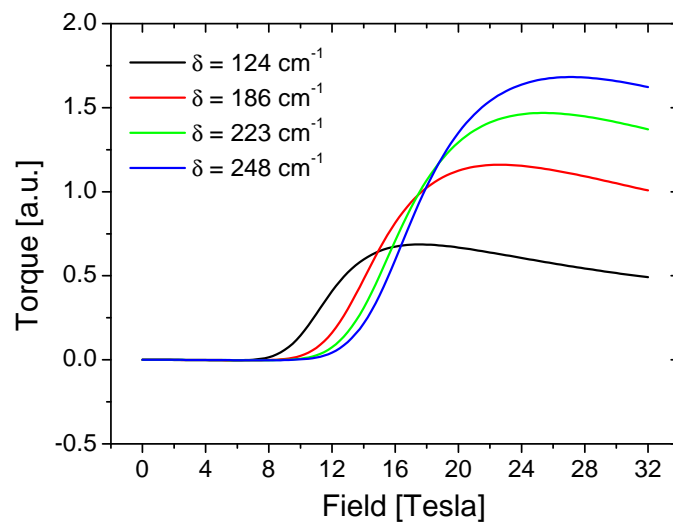


Figure 6.4: Torque signals calculated for different δ values at 50 mK and $\theta = 88^\circ$. The peak shifts to higher fields with increasing δ .

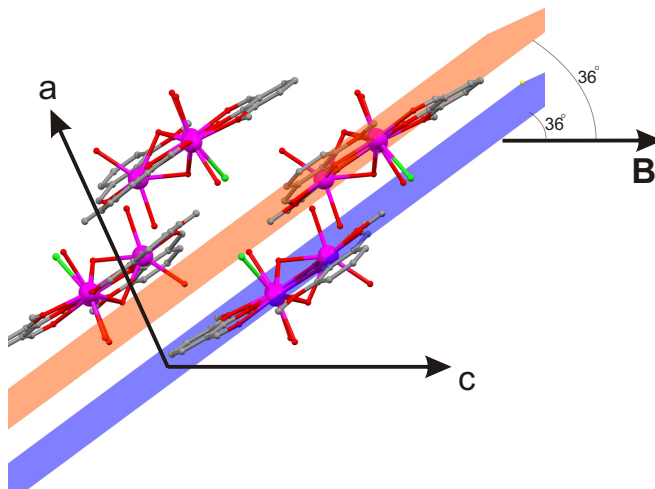


Figure 6.5: Crystal structure of the Dy_3 as seen in the ac plane. The b axis goes into the sheet and is aligned along the rotation axis of the torque meter. b bisects the planes of the two independent triangles (highlighted), which make an angle of 5.2° with each other. Both planes make the same angle with the external field.

Here we define a new parameter for the anisotropy δ which is the separation in energy between the $15/2$ and the $5/2$ rather than the $13/2$ state. δ is given in terms of δ_o as,

$$\delta = \frac{\left(\frac{15}{2}\right)^2 - \left(\frac{5}{2}\right)^2}{\left(\frac{15}{2}\right)^2 - \left(\frac{13}{2}\right)^2} \cdot \delta_o = \frac{50}{14} \cdot \delta_o \quad (6.2)$$

The inclusion of the first excited doublet has a subtle effect on the calculated torque signal as we will see below. For an Ising spin, i.e. considering only the lowest spin doublet ($\pm 15/2$), the torque signal increases quadratically with the magnetic field (up to infinity). On the other hand, the inclusion of a finite anisotropy by considering the excited doublet at an energy δ above the ground state, results in a different torque signal. In particular, the torque value drastically changes above the breaking field beyond which the quantization axis switches from the single ion easy axis to that of the external field. Figure 6.4 demonstrates the dependence of the torque signal on the value of δ for a transverse external field.

6.3.2 Low field torque magnetometry

The ab initio expectations of δ [93], and the value expected by Luzon et al., suggest that the peak in the torque signal for transverse fields is only observed at high fields. We have performed preliminary low field torque measurements to ensure that. The crystal was placed on its 100 face with the b crystallographic axis parallel to the rotation axis (Figure 6.5). Consequently, the field was rotated in the ac plane. The unit cell of Dy_3 contains two magnetically independent molecules. The two symmetry related triangles have their edges and bisectors almost parallel, forming an angle of only 5.2° . We have chosen b to be along the rotation axis, in order to have the magnetic field at the same

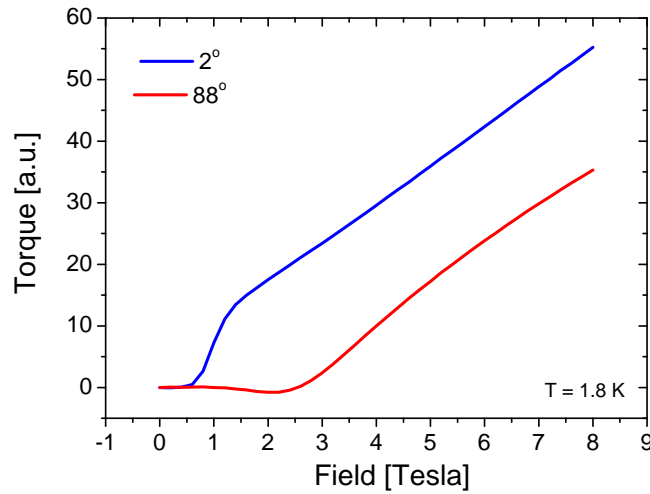


Figure 6.6: Low field torque signals measured at 1.8 K for an axial ($\theta = 2^\circ$) and a transverse ($\theta = 88^\circ$) field.

angle from both triangles. The drawback of this is that the field is never entirely in or perpendicular to the planes of the triangles, which makes the measurements of torque signals at small angles (or angles close to 90°) a difficult task. In addition, the fact that the triangles (which include the easy axis of the single-ions) are not solely lying in one plane with the external field, leads to having a torque component not only along the y direction which bends the cantilever up or down, but also along the other two directions, x and z (see Chapter 2).

Figure 6.6 shows the torque signal up to 8 Tesla measured at 1.8 K for an axial ($\theta \sim 2^\circ$) and a transverse ($\theta \sim 88^\circ$) field. The torque at 2° is practically zero until the system crosses into a magnetic state at around 0.8 Tesla, and the torque increases quadratically up to 8 Tesla as expected. At 88° , the situation is quite different, the torque starts to increase at around 3 Tesla and continues to increase quadratically up to 8 Tesla. The result demonstrates the need of a higher magnetic field in order to observe the drop of the torque signal which would aid in quantifying δ .

6.3.3 High field torque magnetometry

Magnetic anisotropy

A Dy_3 single crystal was placed on the cantilever in the same orientation as described in the preceding section. The angle dependent torque measurement showed that the torque signal vanishes after a rotation of 36° as expected from the crystal structure (Figure 6.5). Rotating the cantilever further by 90° , we end up by having the magnetic field almost perpendicular to the planes of the triangles. Figure 6.7 shows the raw torque data at different angles close to 90° . In fact, the choice of the 90° signal was

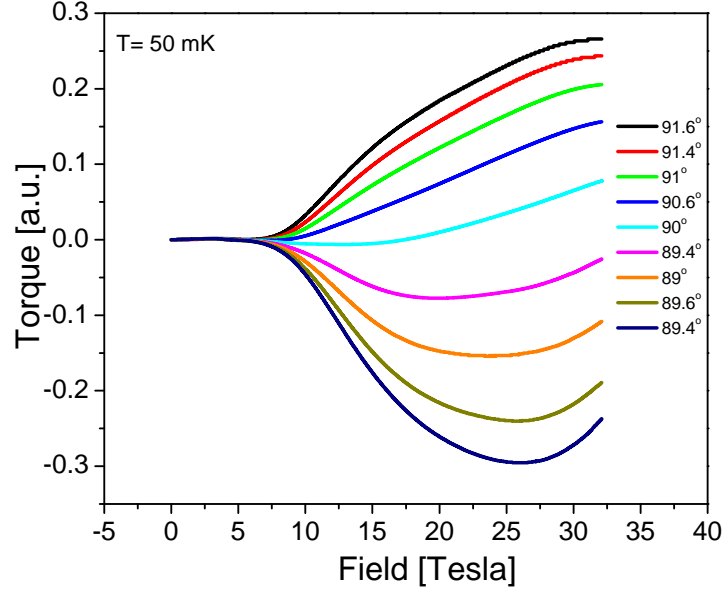


Figure 6.7: The torque signals measured at different angles close to 90° at 50 mK.

chosen from these torque signals. At 90° , the torque signal should go to zero, but as discussed above, the field is not 100% perpendicular to the triangles. In addition, the inhomogeneity of the magnetic field and the transverse torque components (τ_x, τ_z) can contribute to the measured torque signals. An inhomogeneous field induces a Faraday force which has a quadratic dependence on the external field (see Chapter 2), and it is directed along the external field gradient. The measured torque signal (τ_m) is therefore given as a combination of τ_y (the value of interest which is perpendicular to the arm of the cantilever), and another term which has a quadratic field dependence,

$$\tau_m(\theta) = \tau_y(\theta) \pm \alpha B^2 \quad (6.3)$$

where α parameterizes the strength of the quadratic contribution. We assume that the quadratic term dependence on the angle is negligible for small changes in θ . The process of eliminating the quadratic term was discussed in details in Chapter 2. Figure 6.7 shows $\tau(\theta)$ and $\tau(180 - \theta)$ signals at different angles close to 90° measured at 50 mK. The Faraday force which is directed along the external field as depicted in Figure 6.8 leads to increasing the capacitance (i.e. the torque signal) at these angles, and consequently the quadratic term is added to the torque signal. Knowing that $\tau_y(180 - \theta) = -\tau_y(\theta)$, the average torque signal was therefore obtained by eliminating the quadratic contribution,

$$\tau_{av}(\theta) = \frac{\tau_m(180 - \theta) - \tau_m(\theta)}{2} = \frac{\tau_y(180 - \theta) + \alpha B^2 - \tau_y(\theta) - \alpha B^2}{2} \quad (6.4)$$

Figure 6.9 (a) shows the different averaged curves at different angles. A peak in the torque signal is evident at around 28 Tesla which shifts to slightly higher fields at

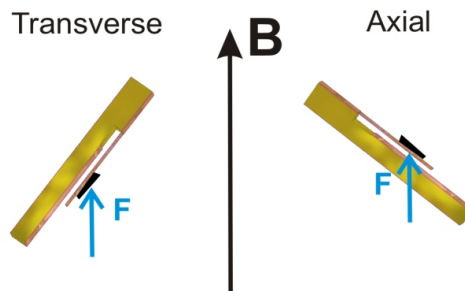


Figure 6.8: The actual orientation of the torque meter for the axial and transverse field torque measurements. The Faraday force bends the cantilever away from the lower electrode for the former case, while it bends it towards the electrodes for the measurements performed with transverse fields.

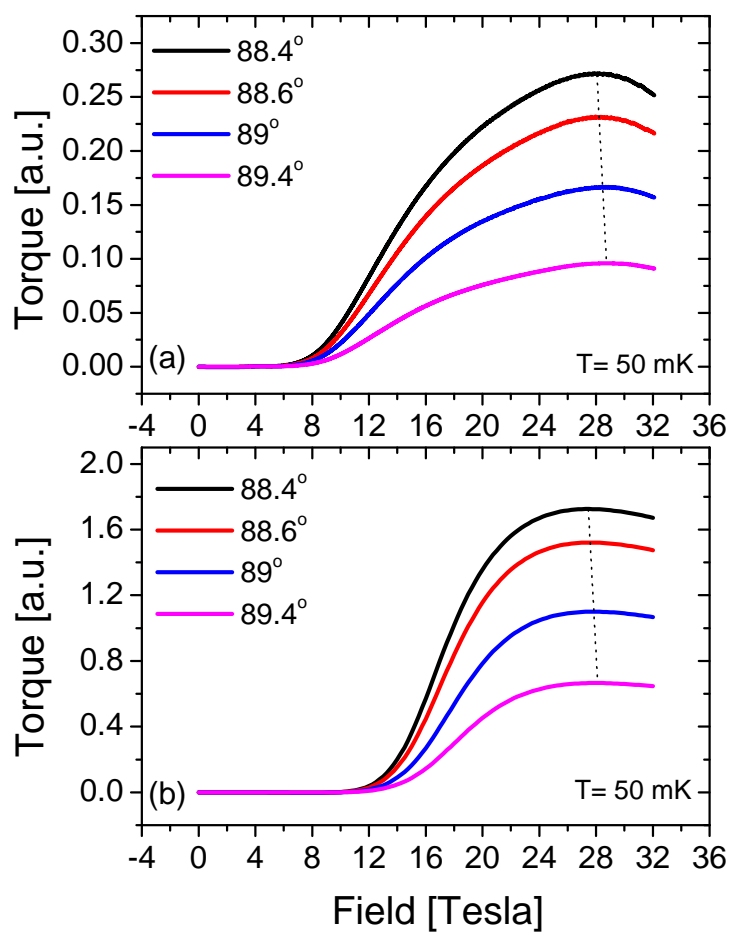


Figure 6.9: (a) The averaged torque signals at different angles close to 90° at 50 mK. (b) Similar calculated curves with the best fit parameters discussed in text.

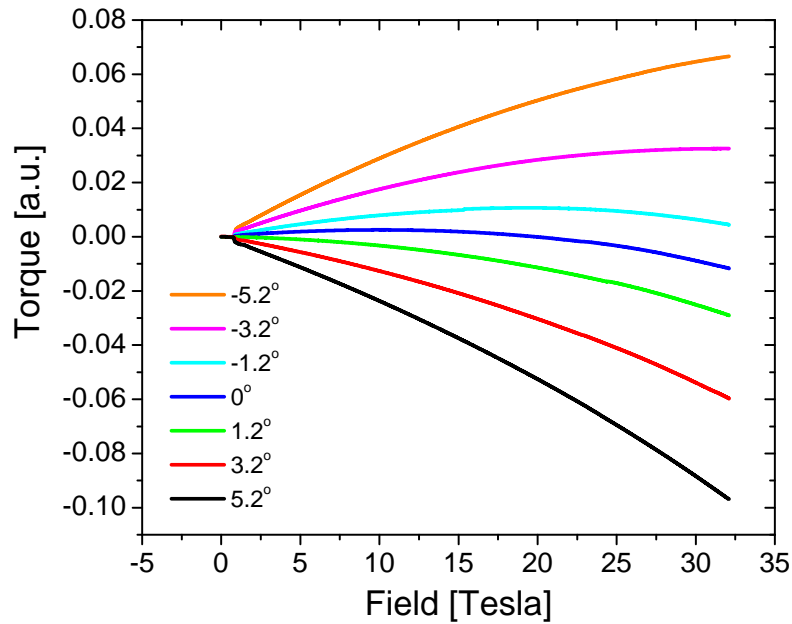


Figure 6.10: Torque signals measured at different angles close to 0° at 50 mK.

higher angles. Figure 6.9 (b) shows the calculated torque signals for $\delta = 250 \text{ cm}^{-1}$, $j = 0.064 \text{ cm}^{-1}$, and $g = 1.35$ at 50 mK, which reproduce fairly well the experimentally observed curves. The calculated curves also show a peak around 28 Tesla which exhibits the same tendency when going to higher angles. The value of δ was varied to best fit the experimentally observed torque signals. The slight (but apparent) difference between the calculated and the measured curves is due to the limited precision of the correction procedure by averaging the data, and due to the non optimized orientation of the crystal. In addition, the model that we assumed to describe the system may be oversimplified, hence the slight disagreement is not surprising. The extracted value for δ of $250 \pm 10 \text{ cm}^{-1}$ is close to that expected by ab initio calculations [93]. It is worth noting that this value quantifies the anisotropy in the system. Care must be taken in assigning this value of δ to the actual energy separation between the two quantized states of $m_J = \pm 15/2$ and $m_J = \pm 5/2$ with the simple model that we considered. Nevertheless, this value of 250 cm^{-1} is a valid estimate of the anisotropy in the system independent of the model used. In principle, the same value should be obtained if the excited doublets are taken as $\pm 13/2$ rather than $\pm 5/2$.

A confirmation to the validity of the above arguments and correction procedure comes from the axial field (field close to being in the plane of the triangles) data. For axial fields, a sharp step in the torque signal at around 0.8 Tesla is expected. The torque then increases quadratically with the external field up to high field values without any peak. Figure 6.10 shows the raw torque signals measured at different angles close to 0° , and at $T = 50 \text{ mK}$. For this orientation of the torque meter, the expected effect of the Faraday force on the torque signal is inverted due to the different

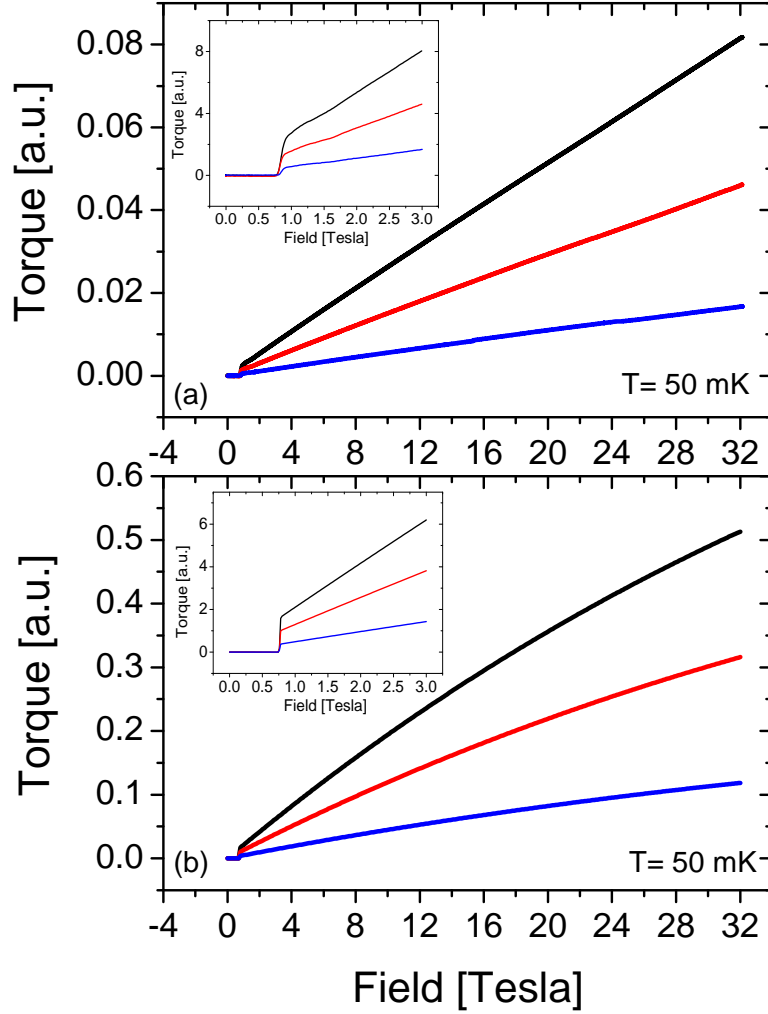


Figure 6.11: (a) The averaged torque signals at different angles close to 0° at 50 mK. (b) Similar calculated curves with the best fit parameters discussed in text. The insets zoom onto the steps observed at around 0.8 Tesla in both graphs.

orientation of the cantilever (Figure 6.8). In this case, the force causes the cantilever to move away from the base plate, thus reducing the measured capacitance value, and consequently decreasing the extracted torque signal. In this case, the measured torque is expressed as,

$$\tau_m = \tau_y - \alpha B^2 \quad (6.5)$$

Hence, Eq. (6.4) was also used to eliminate the quadratic term. The averaged torque signals (Figure 6.11 (a)) are in good agreement with those calculated (Figure 6.11 (b)) with the best fit parameters ($\delta = 250 \text{ cm}^{-1}$; $j = 0.064 \text{ cm}^{-1}$; $g = 1.35$). The insets in Figure 6.11 show a narrower field region where the steps at ~ 0.8 Tesla are evident.

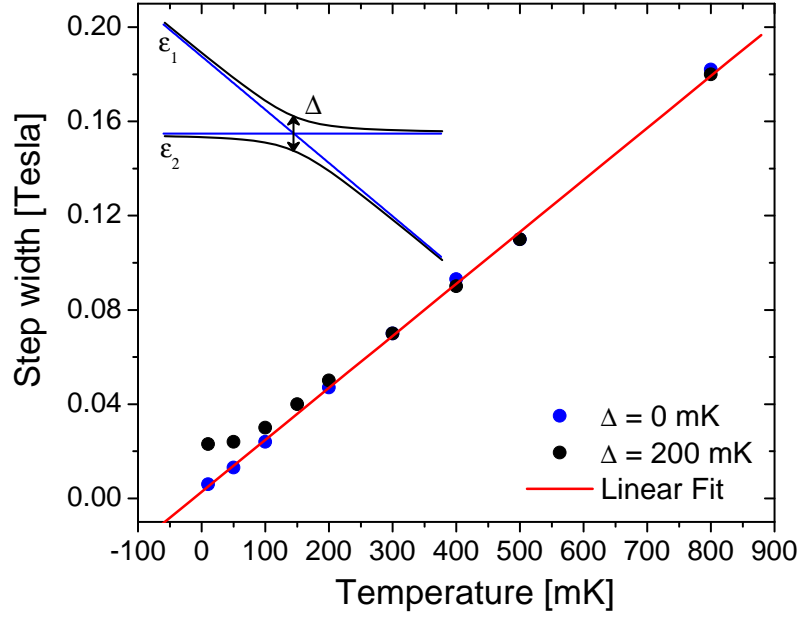


Figure 6.12: The step width extracted from the calculated torque signals of an arbitrary two level system (inset) with a real crossing ($\Delta = 0^\circ$) and an avoided crossing ($\Delta = 200$ mK). The line demonstrates the linear dependence of the $\Delta = 0$ data points.

Level crossing

In this section, we focus on the step observed in the torque curves for axial fields. In principle, studying the step width vs temperature can give valuable information about the nature of the crossing. In particular, it enables us to estimate the value of the level mixing in the case of an avoided level crossing. At low temperatures, only the lowest two energy states are populated, and the system can be described by a two level Hamiltonian [39],

$$\hat{H} = \begin{pmatrix} \epsilon_1 & \frac{\Delta}{2} \\ \frac{\Delta}{2} & \epsilon_2 \end{pmatrix} \quad (6.6)$$

where ϵ_1 and ϵ_2 are the energies of the two individual levels, and Δ quantifies the mixing between these two levels ($\Delta = \epsilon_1 - \epsilon_2$ at the crossing). The width of the step induced in the torque (or magnetization) curve at the level crossing depends on the temperature, as well as on the level mixing (also called tunnel splitting) Δ . For a real crossing ($\Delta = 0$), the step width has a linear dependence on the temperature, while for a nonzero Δ value, the step width deviates from the linear behavior, and it becomes temperature independent for $T \ll \Delta$. This is depicted in Figure 6.12 for an arbitrary two level system for $\Delta = 0$ and 200 mK. For $\Delta = 200$ mK, the width deviates from the linear dependence below 200 mK, and becomes temperature independent below c.a. 100 mK. We have measured the temperature dependence of the torque signal at 5.2° between 50 and 800 mK (Figure 6.13). The width of the

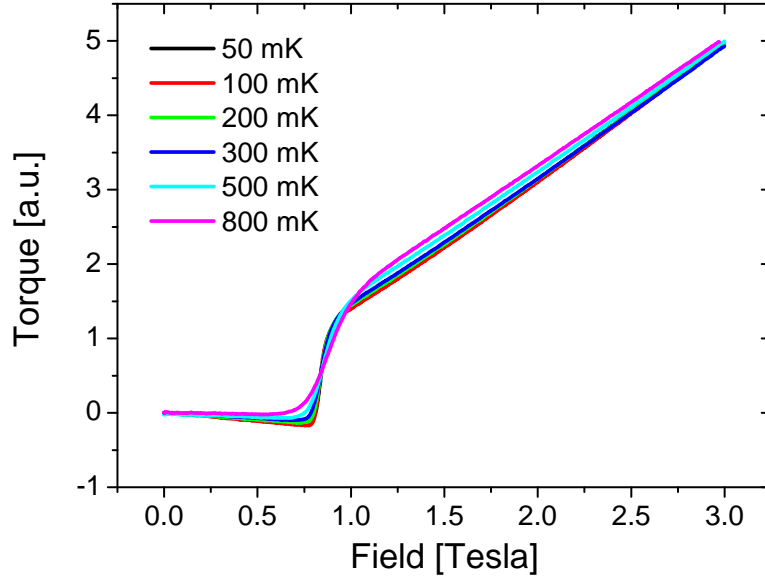


Figure 6.13: Temperature dependence of the torque signals angle $\theta = 5.2^\circ$.

step at different temperatures is extracted by fitting the first derivative of the torque ($d\tau/dB$) to a Gaussian function. Figure 6.14 shows the extracted step width plotted vs temperature. A deviation from the linear dependence is evident for $T < 200$ mK. It is worth noting that the error of the step width is less than 20 gauss as obtained from the Gaussian fit. The step width extracted from the calculated torque signals is obviously smaller than the experimentally obtained values (Figure 6.14). In addition, the calculated width does not level off but rather decreases linearly down to 50 mK. However, in our model, the Hamiltonian (6.3) does not include any terms that mix the levels at the level crossing (neglecting the small transverse field at 5.2°). The observed temperature independent step width, points towards level mixing at the level crossing of an order 100-200 mK. This can be considered as a plausible explanation for the enhanced relaxation rate of the magnetization at the level crossing which was observed by Luzon and coworkers.

An eye-catching feature in the curves recorded at different temperatures (Figure 6.13), is the behavior above the level crossing. For a two level crossing, one inflection point is typically observed in the torque curves at different temperatures. We have measured the temperature dependence of the torque at a different angle to certify the observed behavior. Figure 6.15 shows the measured temperature dependence of the torque at 3.2° . There are two apparent inflection points at 0.82 Tesla (B_{C1}) and 1.00 Tesla (B_{C2}). One possible explanation for this could be accounted for by the second excited state level crossing in the energy diagram. The different calculated torque signals shown above were calculated for $\phi = 0$, i.e. for the easy axes perpendicular to the edges of the triangle (see Figure 6.1). The energy level diagram depicted in Figure 6.16 shows the dependence of the first ground state crossing and the second excited state

crossing on the value of ϕ . The first crossing shifts to higher fields, while the second crossing shifts to lower fields with increasing ϕ . For $\phi = 20$, and at $\theta = 3.2^\circ$, B_{C1} and B_{C2} are also equal to 0.82 and 1.00 Tesla as extracted from the calculated energy level diagram. In this case, the expected temperature dependence is different from that of a two level crossing. Below B_{C1} , state 1 is the ground state, while states 2 and 3 are the second and third excited states, respectively. Between B_{C1} and B_{C2} , state 2 is the ground state while states 1 and 3 are the second and third excited states, respectively. Finally, state 3 crosses state 1 at B_{C2} while state 2 remains the ground state of the system. This leads to having three regions where we expect different temperature dependence of the torque signals, which is in agreement with the experiment (Figure 6.15). This observed temperature dependence enable us to determine a value for ϕ of 20° , and hence get a better insight into the spin structure within the Dy_3 triangle. The inset in Figure 6.15 shows that the torque curves converge to the same value at 3 Tesla, which confirms that the different behavior at the level crossing is not simply due to an absolute shift of the curves over the whole field range. Note that we have taken the position of the second crossing as that which occurs between the 50 and the 800 mK curve since it is an excited state crossing and it is more likely to be observed at the higher temperatures. On the other hand, the calculated torque signals with $\phi = 20^\circ$ (Figure 6.17) do not reproduce the temperature dependence observed in the experiment. One reason for that might be again the absence of an interaction in the Hamiltonian which can mix the states especially at the level crossing leading to a different magnetic character for the three states. It is worth noting that the torque

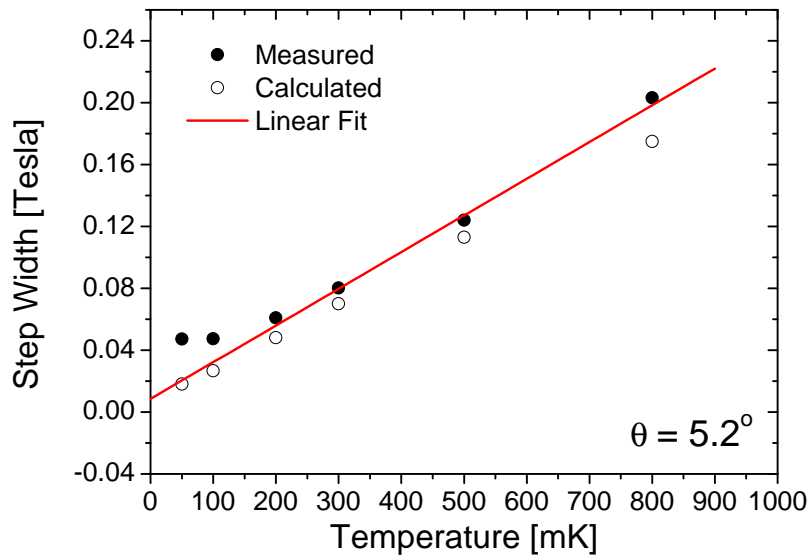


Figure 6.14: The step width extracted by taking the derivative of the torque signals in Figure 6.13 at different temperatures. The circles are similarly extracted from the calculated torque signals with the best fit parameters. A deviation from the linear dependence is evident for the experimentally obtained values below 200 mK.

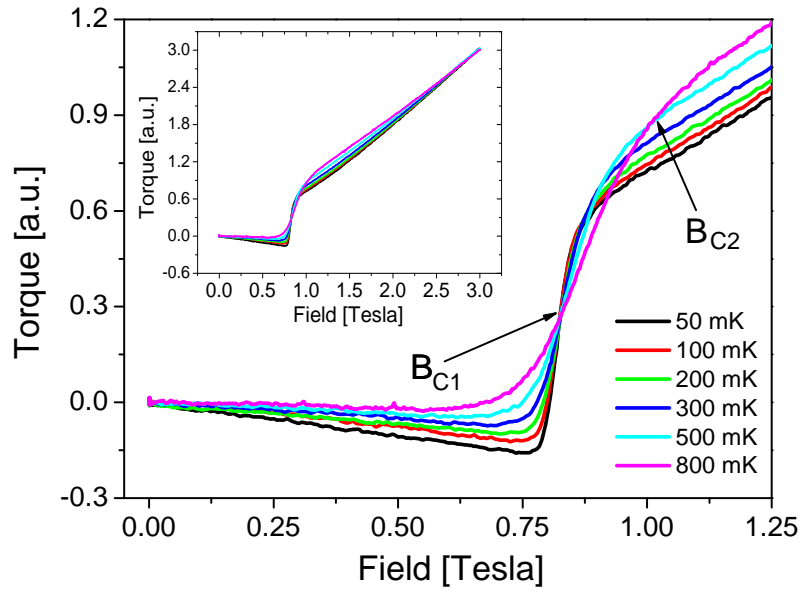


Figure 6.15: Temperature dependence of the torque signals at an angle $\theta = 3.2^\circ$. Two inflection points are evident at B_{C1} and B_{C2} . The inset shows the same curves up to 3 Tesla.

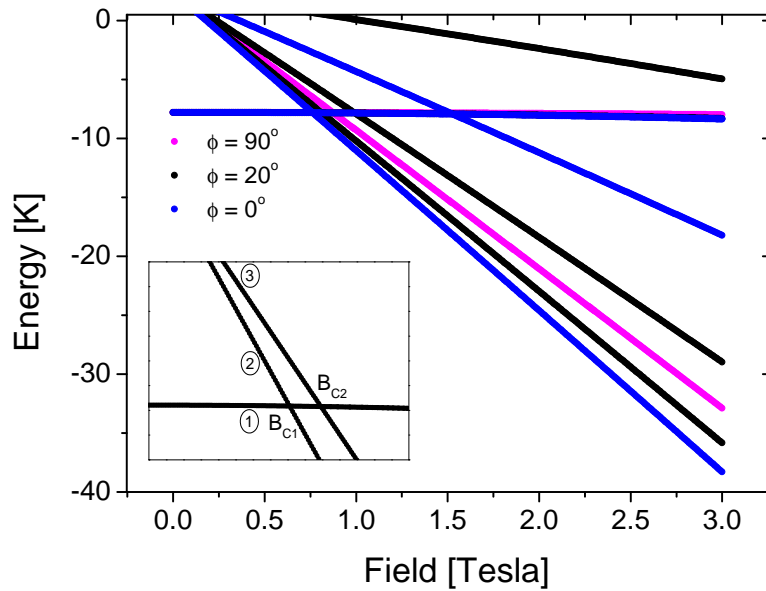


Figure 6.16: The energy diagrams calculated for different ϕ values. The crossing fields depend on ϕ . The inset illustrates the three regions where the temperature dependence of the torque varies: i- $B < B_{C1}$, ii- $B_{C1} < B < B_{C2}$, and iii- $B > B_{C1}$ (see text).

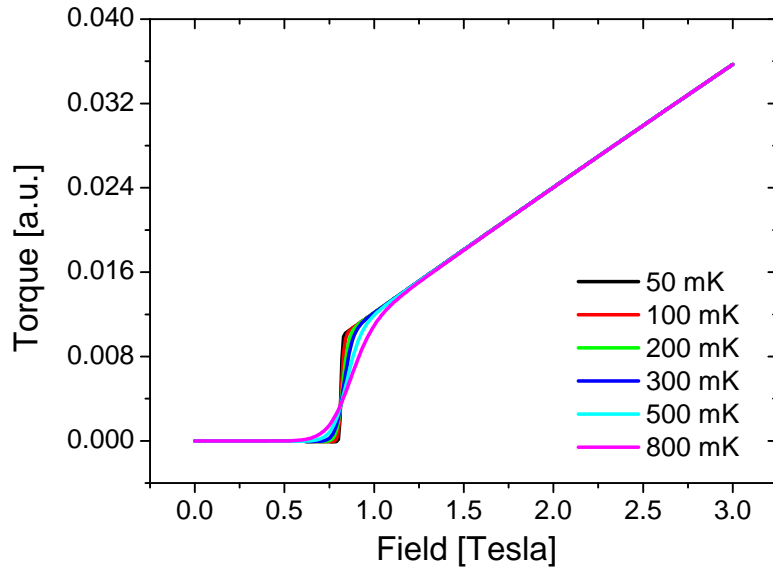


Figure 6.17: The torque signals calculated with (6.1) at different temperatures for $\delta = 250 \text{ cm}^{-1}$; $j = 0.064 \text{ cm}^{-1}$; $g = 1.35$; $\theta = 3.2^\circ$ and $\phi = 20^\circ$.

signals for transverse fields are almost independent of ϕ , and hence the extracted value of δ is also independent of ϕ . This can be understood as for θ values close to 90° , the magnetic field is perpendicular to the plane of the triangle, and the orientation of the spins within the triangle has therefore a minor effect on the torque signal.

6.4 Conclusions

To conclude, the performed high field torque magnetometric studies enabled us to quantify the anisotropy in the molecular Dy_3 triangle. The observed peak in the torque signal at around 28 Tesla for transverse magnetic fields indicates that $\delta = 250 \pm 10 \text{ cm}^{-1}$, which is close to the values expected from previously performed ab initio calculations. In addition, temperature dependent investigation of the step observed in the torque signal at the level crossing in the mK range points toward a level mixing of the order of 100-200 mK. This value, which is not accounted for in the simple spin effective model that is used to describe the system, can give a plausible explanation to the enhancement in the magnetization relaxation rate observed at the level crossing in previous studies. Furthermore, two different inflection points were observed in the torque signal which may be assigned to the ground and the excited state crossing in the energy diagram. From the positions of these inflection points, an estimate of $\phi = 20^\circ$ is obtained which shed light on the spin structure within the Dy_3 triangle. More research is needed to develop new models which can give a more precise explanation of the magnetism of the system. This study was performed on an intricate system with complicated crystal structure. In a more general picture, this study has contributed

to a better understanding of lanthanide based systems. In particular, we have proven that high field torque magnetometry is a strong tool to investigate the anisotropy in these systems, especially in mononuclear lanthanide SMMs.

Chapter 7

Torque Detected Electron Spin Resonance

7.1 Introduction

We have seen in the previous chapters how spectroscopic and magnetometric techniques were successfully used to study the magnetic anisotropy in various single-molecule magnets (SMMs). Spectroscopy remains to date the most powerful method to investigate anisotropy in such systems. Most spectroscopic measurements are based on standard electron spin resonance (ESR) techniques. Conventional ESR spectrometers, which use microwave (MW) cavities to detect magnetic resonance transitions are hindered by their limited discrete frequencies. Commercial spectrometers are typically available at 10, 30, and 90 GHz. Above 90 GHz, the dimensions of the cavity to be used become too small, and almost impossible to be implemented. However, high-frequency ESR setups, which employ the cavity perturbation technique, can go up to frequencies of 700 GHz, but again they are limited to discrete frequencies or very narrow frequency ranges [94]. On the other hand, broad band methods, such as frequency domain magnetic resonance spectroscopy (FDMRS) or inelastic neutron scattering (INS), suffer from their low sensitivity. Measurements performed on single crystals of SMMs using FDMRS or INS are very rare, and two studies are known where mosaics were used instead [75][74]. In fact, the first single crystal study in FDMRS is reported in this Thesis, where an exceptionally large single crystal was used (Chapter 4). The increasing number of SMMs with their zero field splittings values varying in a wide frequency range, demand a highly sensitive magnetic resonance method covering a broad frequency range. To that end, we have exploited our experience in FDMRS and CTM in order to combine both techniques, thus developing a novel torque detected ESR (TDESR) method, to study very small single crystals of SMMs in a broad frequency range.

Detecting magnetic resonance transitions via measuring the change in the magnetization was introduced more than 40 years ago [95]. Since then, different magnetic sensors, such as SQUIDS [96], micro-SQUIDS [42], and Hall probes [97][98] were used to detect the change of the magnetization under the effect of microwave radiation off and on resonance. SQUIDS and micro-SQUIDS are highly sensitive but they have an

upper limit of the external magnetic field applied (8 Tesla for SQUID and much less for a micro SQUID). In addition, they have a slow response time. On the contrary, Hall bars which are also highly sensitive, have a fast response time, but they have shown subtle heating effect under microwave irradiation [98]. In most of the reported measurements, wave-guides were used to couple the MW radiation emitted from the MW sources (mainly Gunn diodes) to the samples. The setups were limited to either single frequencies or very narrow frequency ranges.

All of the above approaches have used magnetic sensors which measure the magnetization. We have used cantilever torque magnetometry (CTM) instead. CTM is highly sensitive (see Chapter 2), has a fast response time compared to commercial SQUIDS, and can be operated up to high magnetic fields. In addition, the CuBe cantilevers used show virtually no effect of the MW radiation on the measured torque values off resonance. Furthermore, the conventional torque measurements performed in advance on the crystal of interest "in situ", provide an initial estimate of the magnitude and orientation of the axial anisotropy. We have used BWO tunable frequency sources to generate coherent, linearly (or circularly) polarized MW radiation in the THz range. The crystal can be easily rotated in an external magnetic field to perform angle dependent ESR measurements. In the following sections, we present the novel method developed with full capabilities of varying different experimental parameters (frequency, field, temperature, angle, and MW polarization). This flexibility makes the information extracted from the measurements invaluable in magnetic resonance methods especially to study magnetic anisotropy in SMMs. We also present extensive results on an Fe₄ SMM to demonstrate the strength of this method in determining the anisotropy parameters with very high precision.

7.2 Basic principle

In conventional ESR methods or in FDMRS, the transmitted MW radiation is detected. Hence, the sensitivity of these techniques strongly depends on the sensitivity of the MW detectors, and on the number of photons absorbed at resonance. Torque (or magnetization) detected ESR, measures the effect that a magnetic resonance transition induces in the magnetic properties of the sample. These techniques exploit the high sensitivity of magnetic sensors in order to detect very small changes in the magnetic moment of the sample. Let us consider an $S = 5$ high spin cluster, with an easy axis anisotropy, for the sake of illustration. The system is described by the Hamiltonian $\hat{H} = D\hat{S}_z^2 + g\mu_B\mathbf{B}\cdot\hat{\mathbf{S}}$, and consequently the energy of the different m states is described as: $E(m) = Dm^2 + g\mu_B mB$. The torque of an ensemble of spins (containing all the molecules in a crystal), depends on the population of the different spin states. This is given by the Boltzmann distribution, and the total torque of the system can be expressed as,

$$\tau = \sum_m \tau_m \cdot \frac{e^{-\beta E_m}}{Z(B, T)} \quad (7.1)$$

where τ_m is the torque of an individual spin in the m state ($m = -5, -4, \dots, 0, \dots, +4, +5$). $Z(B, T)$ is the partition function, and $e^{-\beta E_m}$ describes the weight of each τ_m at a

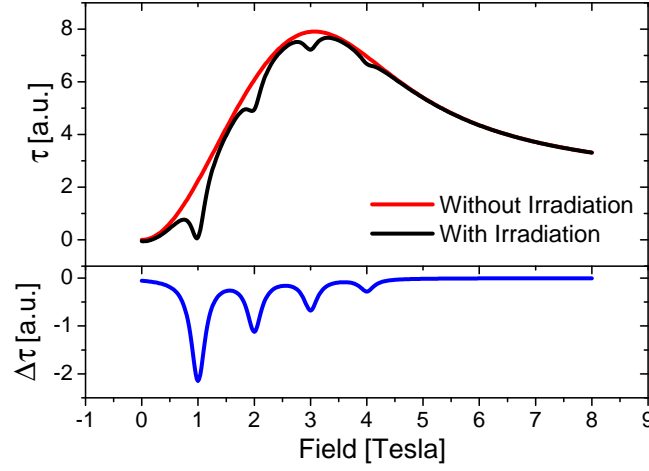


Figure 7.1: A simulation depicting the torque signals of an irradiated and non-irradiated crystal (top). An ESR-like line-shape is the resultant of subtracting both torque signals (bottom).

temperature T ($\beta = 1/k_B T$). The population of the states is modified as the temperature changes, and consequently, the torque values change at different temperatures. Besides temperature, MW induced magnetic resonance transitions can modulate the population of the individual states. Only the populations of the two particular states, between which the transition is induced, are modified at resonance. In order to focus on the ground state transition between the $m = -5$ and the $m = -4$ states, let us rewrite (7.1) as,

$$\tau_u = \frac{(e^{-\beta E_{-4}})\tau_{-4} + (e^{-\beta E_{-5}})\tau_{-5}}{Z(B, T)} + \tau_r \quad (7.2)$$

where τ_u is the non-irradiated total torque value, and the first two terms on the r.h.s. are the torque values of the -5 and -4 states, and τ_r is the torque of the remaining m states. A MW radiation of energy $h\nu_0 = E_{-5} - E_{-4}$ will induce a transition from the $m = -5$ to the $m = -4$ state, thus increasing the population of the latter, and decreasing that of the former. As a consequence, the total torque value is changed on resonance, and the degree of change is governed by the instantaneous population of the -4 and -5 states,

$$\tau_{irr} = \frac{((1 - \alpha)e^{-\beta E_{-4}} + \alpha e^{-\beta E_{-5}})\tau_{-4} + ((1 - \alpha)e^{-\beta E_{-5}} + \alpha e^{-\beta E_{-4}})\tau_{-5}}{Z(B, T)} + \tau_r \quad (7.3)$$

where α is a fraction of the population difference between the -5 and -4 states off resonance, which depends on the MW power. The maximum value of α is 0.5, corresponding to equal populations of the -5 and the -4 states (saturation). Note that τ_r is not affected upon the irradiation by $h\nu_0$, since the population of other m states is not directly altered. Practically speaking, if the torque is therefore measured with (τ_{irr}) and without (τ_u) MW irradiation, the difference between the two signals ($\tau_{irr} - \tau_u$) gives

an ESR-like line-shape (Figure 7.1). From this measurement, one can extract the same information obtained by conventional ESR methods.

7.3 Experimental setup

The experimental setup used to perform TDESr measurements consists of two main parts (Figure 7.2). The first is the optical part which deals with the generation, and focusing of the microwave radiation onto the crystal. The second is the torque magnetometer which measures the torque signal under an external magnetic field. The quasi-optical setup is in fact the same one used to perform FDMRS (Chapter 1). The MW is generated by a set of tunable frequency sources that cover the range 30-1440 GHz ($1\text{-}48\text{ cm}^{-1}$), known as backward wave oscillators (BWOs). The whole frequency range is covered by about a dozen BWO sources. The frequency can be swept with a resolution of 0.1 MHz, or set to a certain fixed value. The output power of BWOs varies from several hundreds of mW for the long-wavelength sources (providing radiation at frequencies around 100 GHz) to 1 mW for the short-wavelength side (up to 1.5 THz). Figure 7.3 shows the MW output power for the various BWO sources. The radiation generated by BWOs is coherent, highly monochromatic, and linearly polarized to a high degree (99.99%). The emitted MW beam is focused on the sample in the cryostat using several lenses, and the intensity of the MW is measured with a Golyay cell detector. The MW detection is essential to align the beam, and the intensities are measured to compare the output power at different frequencies. The lenses are made of Quartz or Teflon, and have a typical diameter of 5 to 10 cm with a focal length of 5 to 20 cm. Free-standing wire grids, consisting of an array (diameter 10 cm) of parallel tungsten wires (10 to 15 μm thick) with a spacing of some tens of micrometers, are used to change the polarization of the radiation. The crystal which is oriented on the cantilever, is inserted into an Oxford Instruments Spectromag 4000 (Temperature range: 1.7 to 300 K; Field: 0 to 8 Tesla). The cryostat has a split-coil superconducting magnet with enlarged optical Mylar windows. Both Voigt

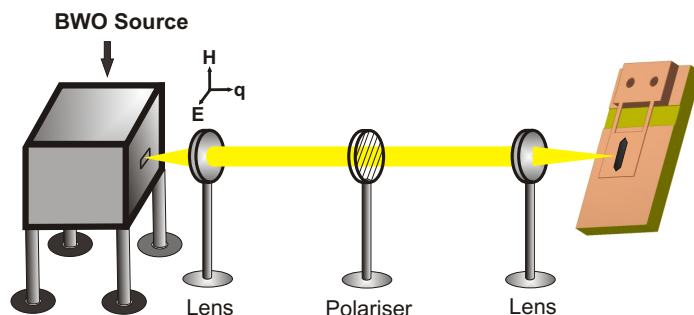


Figure 7.2: A schematic drawing of the quasi-optical setup to illustrate how the beam is focused onto the single crystal located inside the cryostat (not shown). The depicted size of the cantilever is relatively enlarged for clarity.

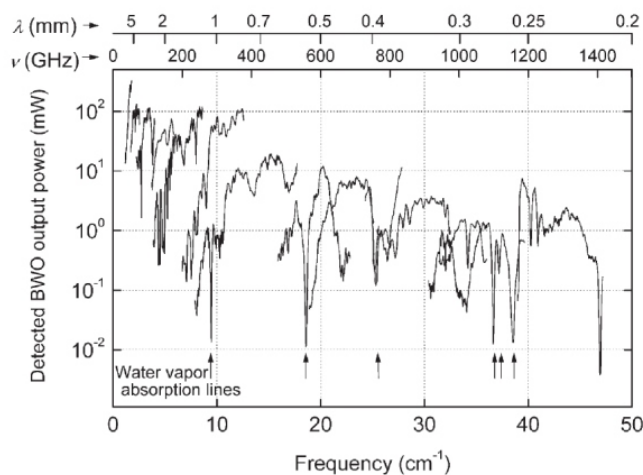


Figure 7.3: Output power patterns for various BWOs spanning the 30 GHz to 1440 GHz frequency range [18].

(wavevector of the electromagnetic radiation perpendicular to the external magnetic field) and Faraday configurations (wavevector parallel to the external magnetic field) can be used. A special sample holder was designed to perform torque magnetometric measurements under MW irradiation. The insert is fitted with two coaxial cables to measure the capacitance of the torque meter at low temperatures. Two heaters, and a Cernox temperature sensor are added to control and measure the temperature. The lower part of the insert is shown in Figure 7.4. This piston-like shaped holder was carefully designed to allow the rotation of the torque meter, and consequently the crystal, with respect to the external field. At the same time, the design enables the vertical movement of the torque meter to be substituted by an aperture which permits the MW beam to reach the detector. In practice, this would allow the user to place the aperture at the middle of the cryostat windows, and align the MW beam and the cryostat, such that the beam passes through the middle of the aperture. The piston can be then moved back into the middle of the windows, thus placing the crystal at the center of the MW beam. At this stage, the piston can be rotated against the external horizontal field with the aid of a stepper motor, with steps of $< 1^\circ$. Owing to the 4 windowed cryostat, the crystal can be rotated between 0 and 180° while irradiated. The details of the torque meters and the detection procedure are presented in (Chapter 2). For the measurements presented in this chapter, we have used CuBe cantilevers of $25 \mu\text{m}$ thickness. An Andeen-Hagerling 1 kHz capacitance bridge was used to measure the capacitance between the cantilever and the lower copper plate which is proportional to the torque induced by the crystal (see Chapter 2).

7.4 Results and discussion

In order to conduct a proof of concept study, we have chosen an $[\text{Fe}_4(\text{L})_2(\text{dpm})_6]$ complex (Hdpm = 2,2,6,6-tetramethylheptane-3,5-dione), $\text{H}_3\text{L} = \text{S-H}_3\text{CCH}_2\text{CH}(\text{CH})_3\text{CH}_2\text{O-}$

$\text{CH}_2\text{C}(\text{CH}_2\text{OH})_3$ hereafter referred to as $\text{Fe}_4\text{-rac}$. The system consists of 4 Fe^{3+} ions that are antiferromagnetically coupled to give a total ground spin state of $S = 5$. The spin Hamiltonian parameters (SHPs) determined from high-frequency ESR measurements performed on powder are reported as $\{D = -0.449 \text{ cm}^{-1}, E = 0.03 \text{ cm}^{-1}, B_4^0 = 2.4 \text{ cm}^{-1}\}$ [99]. The duality of our technique enables us to pre-investigate the system with the conventional torque magnetometry, and subsequently perform TDESr. The two measurements are performed on the same mounted crystal "in situ". In the following section, we present the data obtained by performing the conventional CTM measurements, where a rough estimate of the axial anisotropy and the direction of the easy axis are determined. The last section shows the TDESr results.

7.4.1 Cantilever torque magnetometric measurements

Figure 7.5 shows a polar plot of the measured torque of a $\sim 100 \mu\text{g}$ $\text{Fe}_4\text{-rac}$ single crystal. The crystal was placed on its $10\bar{1}$ plane with the b axis parallel to the rotation axis. The magnetic field is consequently rotated in the ac plane. The corresponding crystal structure is shown on top of the torque signal. $\theta = 0^\circ$ corresponds to the magnetic field (green arrow) parallel to the cantilever arms, i.e. at 30° from the easy axis (the normal (dashed line) to the plane containing the 4 Fe^{3+} ions (orange balls) as imposed by the symmetry of the molecule). After a 30° rotation, the magnetic field is aligned with the easy axis, and consequently, the torque signal drops to zero. The agreement between the experimentally observed and the expected angles based on the crystal structures is evident. Rotating further by 90° , the magnetic field ends up in being in the plane of the 4 iron ions and the torque drops again to zero. The torque thus vanishes for the magnetic field parallel or perpendicular to the easy axis, as expected for a magnetically anisotropic paramagnet. The angle resolved measurement provides a precise information on the orientation of the easy axis, a crucial information to carry out single crystal ESR measurements. In order to determine the axial anisotropy, we have performed field dependent torque measurements for transverse magnetic fields, at different temperatures. The field at which a peak is observed (the

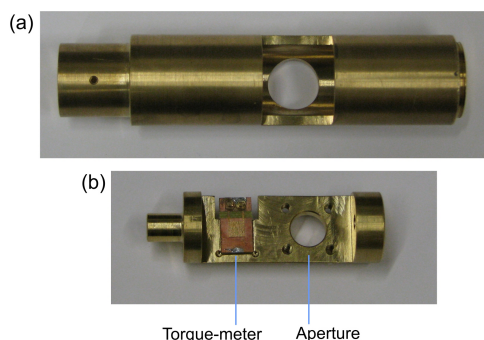


Figure 7.4: The lower part of the insert dedicated to perform TDESr measurements. The part shown in (b) goes into the cylinder shown in (a) to form the piston-like piece discussed in the text.

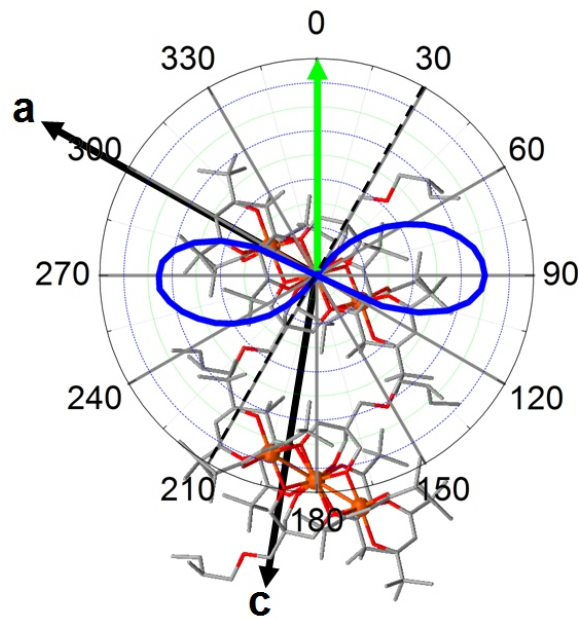


Figure 7.5: Polar plot of the torque signal (blue line) at $B=0.5$ Tesla and $T=1.65$ K for the field (green arrow) being rotated in the ac crystallographic plane. The crystal structure is superimposed on the polar plot (see text). The negative part of the torque is omitted for clarity.

breaking field, as discussed in Chapter 2) in the torque signal is temperature dependent, but it is also directly linked to the anisotropy in the system. Figure 7.6 shows the measured torque signal at different angles close to 90° , at 1.63 K. The solid lines are the calculated torque curves with the best fit parameters $\{D = -0.40(2) \text{ cm}^{-1}, E = 0 \text{ cm}^{-1}$,

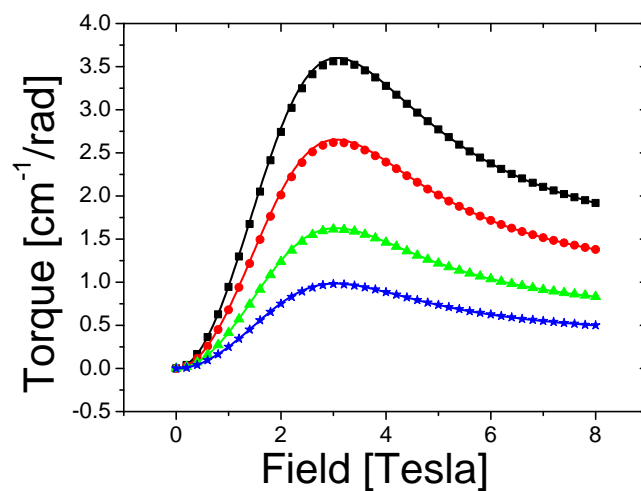


Figure 7.6: Measured torque signal at 86.5° (squares), 87.5° (bullets), 88.5° (triangles), and 89.1° (stars) at $T=1.63$ K. The solid lines are the fits for $g=1.98$ and $D=-0.4 \text{ cm}^{-1}$.

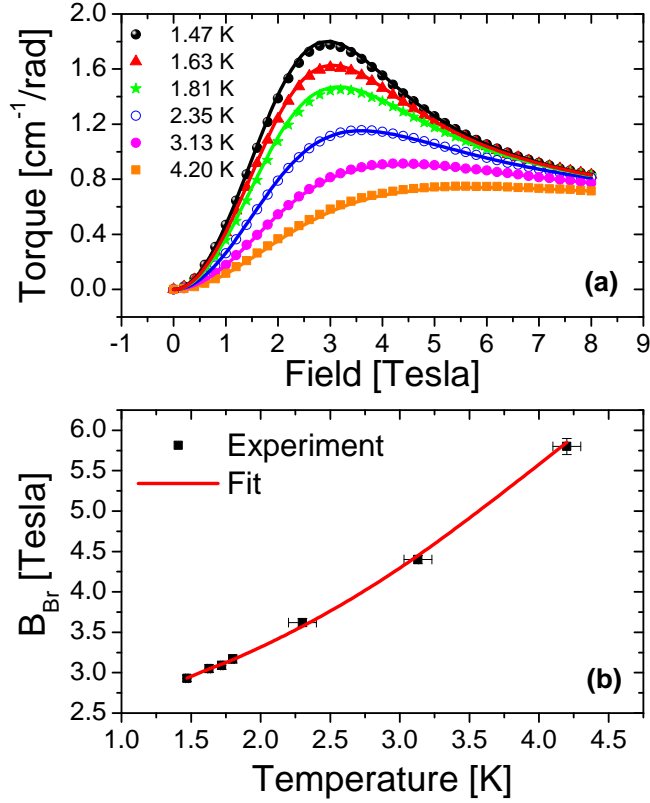


Figure 7.7: (a) The measured field dependence of the torque at 88.5° for different temperatures. The solid lines are the fits for the spin Hamiltonian parameters discussed in the text. (b) Breaking field extracted from the maxima of the plots in (a) versus temperature.

$B_4^0 = 0 \text{ cm}^{-1}$, and $g = 1.98$ }. The absolute values of the torque were determined by using a scaling factor α , obtained from the torque value at 8 Tesla for each curve ($\tau[\text{cm}^{-1}/\text{rad}] = \alpha \cdot \tau[\text{fF}]$ at 8 Tesla). A confirmation of the axial anisotropy obtained from torque magnetometry is given by the temperature dependent curves (Figure 7.7(a)). The position of the peak is plotted versus temperature in Figure 7.7(b), with the best fit calculated using the parameters given above. The measurements enable us to determine an approximate value of $D = -0.4 \text{ cm}^{-1}$, which is close to that obtained by high-frequency ESR. However, we have found that the technique is not sensitive enough, to accurately determine the transverse anisotropy or higher order parameters, especially without any prior knowledge of any other spin Hamiltonian parameters.

7.4.2 Torque detected electron spin resonance

We have used the same single crystal to perform the TDESr measurements. The ac magnetic field component of the MW radiation was oriented perpendicular to both, the externally applied field, and the easy axis (Figure 7.8). This ensures that the ac magnetic field is always perpendicular to the quantization axis (whether it is the

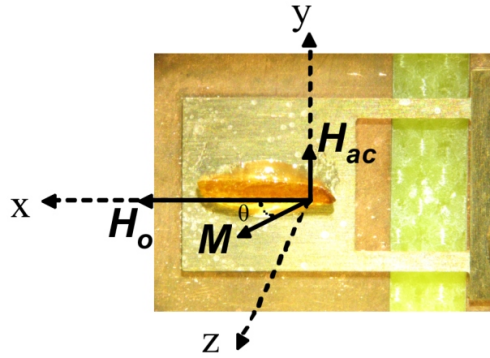


Figure 7.8: A picture of the single crystal with the orientation of the external field (\mathbf{H}_o), the microwave field (\mathbf{H}_{ac}), and the easy axis along which the magnetization (\mathbf{M}) is oriented at zero field and low temperature, is depicted.

external field or the easy axis). θ is the angle between the external field and the easy axis ($\theta = 0$ is defined as the angle at which the external field is parallel to the easy axis. This position is obtained from the angle resolved measurements shown in the previous section (Figure 7.5)).

Frequency swept TDES

One major advantage of our technique to conventional ESR method, is the broad band MW frequency that is accessible. This particularly enables us to study diverse

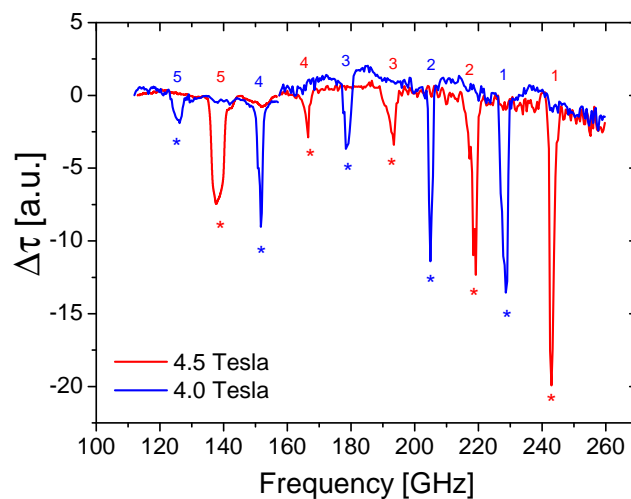


Figure 7.9: TDES spectra at 20 K, and two different magnetic fields (4 and 4.5 Tesla), applied at 5° from the easy axis. The asterisks designate the positions of the calculated frequencies with the SHPs discussed in the text.

magnetic systems with varying ZFS amplitudes. In the frequency swept measurements, an external magnetic field is applied to induce a torque signal which is measured by the torque meter. The MW frequency is then swept in the presence of a constant external field, thus inducing ESR transitions between the different spin multiplets at the resonance frequencies. This is reflected as a change in the torque signal as explained above, and the change ($\Delta\tau$) is detected by the torque meter. Figure 7.9 shows $\Delta\tau$ at 20 K recorded in the MW frequency range 100-250 GHz, with an external field of 4, and 4.5 Tesla. The magnetic field was applied at 5° from the easy axis. Such a TDESR spectrum, requires less than 1 minute to be acquired, which is much less than the time needed to record a conventional ESR spectrum. In total, five resonance lines are observed at 4 tesla in this frequency range, corresponding to the fine structure of the $S = 5$ spin ground state (1: $M_S = -5$ to -4 ; 2: $M_S = -4$ to -3 ; 3: $M_S = -3$ to -2 ; 4: $M_S = -2$ to -1 ; 5: $M_S = -1$ to 0). The lines shift to higher frequencies as the magnetic field is increased to 4.5 Tesla, thus indicating that the lines are of magnetic resonance origin. In fact, if the field is further increased to 4.8 Tesla, a sixth resonance line is observed corresponding to the $M_S = 0$ to $M_S = +1$ transition (Figure 7.10). This is a resounding proof of the very high sensitivity of the technique. Especially if compared to FDMRS, TDESR is several orders of magnitude more sensitive. The number of observed lines in ESR in general is important for a precise determination of the spin Hamiltonian parameters. If one line is observed, one may only predict an approximate value for the axial zero field splitting parameter. However, with an increasing number of resonance lines, the higher order parameters and/or transverse parameters can be obtained with high precision. We have used the following spin Hamiltonian to fit the observed spectra,

$$\hat{H} = D\hat{S}_z^2 + E(\hat{S}_x^2 - \hat{S}_y^2) + B_4^0(\hat{S}_z^4 + (25 - 30S(S+1))\hat{S}_z^2) + g\mu_B\hat{S}\cdot\mathbf{B} \quad (7.4)$$

where D is the axial ZFS parameter, and E parameterizes the transverse anisotropy that is permitted by the non-axial crystallographic symmetry of the molecule. The line-to-line separation between the observed resonances increases smoothly for the excited state transitions, thus pointing to the presence of fourth-order axial anisotropy term (B_4^0) of opposite sign with respect to the D term. The best-fit parameters obtained by fitting the various spectra presented in this chapter are given by: $\{D = -0.448(2) \text{ cm}^{-1}$, $E = 0.03(1) \text{ cm}^{-1}$, $B_4^0 = 1.8(3) \times 10^{-5} \text{ cm}^{-1}$, and $g = 1.985(4)\}$. The parameters are basically identical to those reported by high-frequency ESR [99] within the experimental error. The broad frequency range which we can access allows us to span the whole energy spectrum of the system. Figure 7.11 shows the calculated energy spectrum with the above spin Hamiltonian parameters, and the experimentally observed resonance lines at different magnetic fields. There is an outstanding agreement for all the observed resonances. The data basically demonstrate how we can tune our experimental parameters to probe any excitation in this spectral window.

The intensities of the resonance lines in Figure 7.9 are not normalized by the different MW output power at different frequencies. Besides the population difference and the transition probability between the states, the MW power and the absolute torque value affect the intensity of the observed resonance lines in TDESR. As mentioned earlier, the MW power is frequency dependent, and consequently the intensity of the

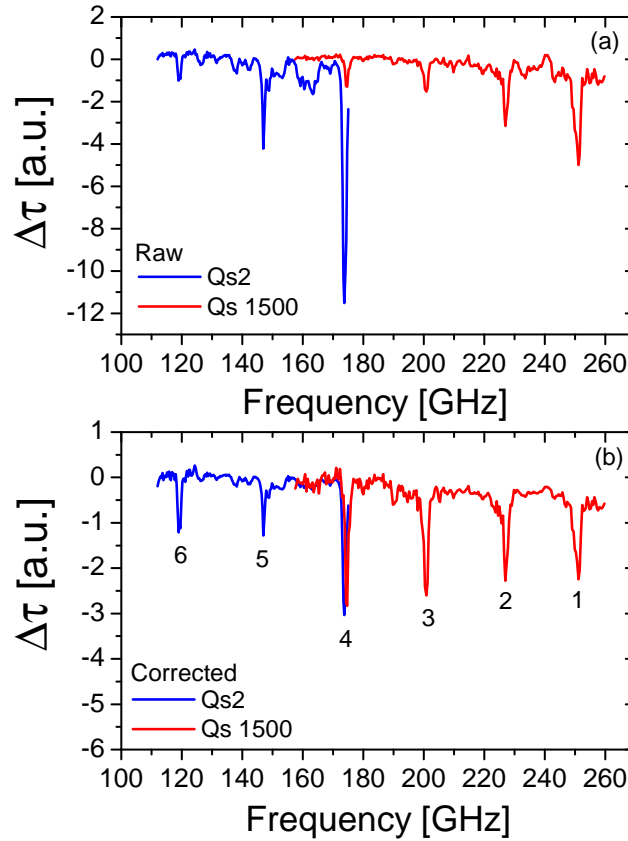


Figure 7.10: TDESr spectra at 20 K recorded with two different MW sources. The external field is 4.8 Tesla applied at 5° from the easy axis. (a) shows the raw data, while (b) shows the data corrected for the output power of the MW sources.

resonance lines is also frequency dependent. Therefore, in the frequency swept measurements, the $\Delta\tau$ values have to be divided by the output power to correct for that. Figure 7.10 shows the $\Delta\tau$ at 20 K recorded for the MW frequency range 100-250 GHz at 4.8 Tesla. The spectra were recorded using two MW sources to cover this frequency range, namely the QS2 and the QS1500. The two sources overlap between 157 and 175 GHz, while the output power of the former is much higher in this frequency range. The effect of the higher power is clearly seen in the higher intensity of line 4 in the raw data (Figure 7.10(a)). After correcting for the different MW power of the two sources, the two lines recorded with the two sources are roughly of equal intensity. Note that we compare the intensity of the lines throughout this chapter as the line-widths of all the resonance lines are very similar.

When sweeping the frequency, one practically changes the high voltage of the BWO source. In FDMRS, this high dc voltage is modulated by an ac voltage between 0 and 50 volts to eliminate frequency dependent artifacts. High modulation voltages strongly affect the low frequency intensities. Figure 7.12 shows the resonance between the -5 and -4 states at around 138 GHz, with an external field of 2 tesla ($T = 16$ K, $\theta = 4^\circ$).

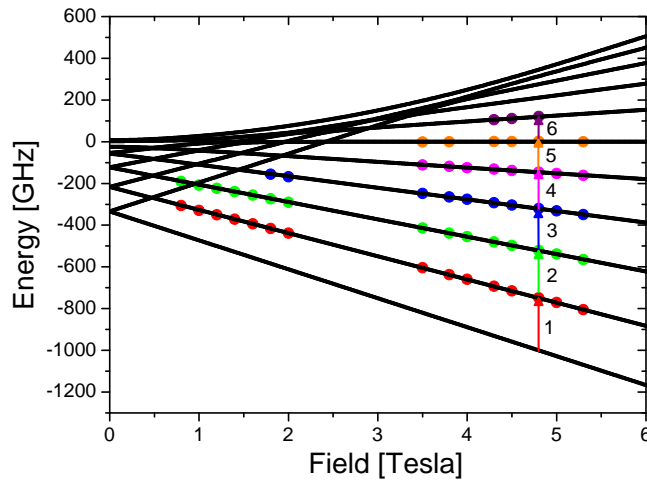


Figure 7.11: The calculated energy spectra with $D = -0.448(2) \text{ cm}^{-1}$, $E = 0.03(1) \text{ cm}^{-1}$, $B_4^0 = 1.8(3) \times 10^{-5} \text{ cm}^{-1}$, and $g = 1.985(4)$ (lines). The circles designate the resonance frequencies of the different resonance lines extracted from the TDESRS spectra at different fields and/or frequencies.

The resonance line is broadened by increasing the modulation voltage, and the intensity is strongly cut off. The frequency of 138 GHz corresponds to a high voltage of around 800 volts. A modulation of 50 volts (p-p) corresponds to a width of 6 GHz around 138 GHz as observed in the experiment. Below 15 volts, decreasing the modulation voltage has virtually no effect. Note that the zero volt modulation voltage has the same quality (signal to noise ratio) as the 50 volt spectrum. Therefore, in TDESRS the modulation voltage does not improve the quality of the spectra as in FDMRS, since the MW radiation is not detected. To that end, it is advantageous to perform TDESRS at zero modulation voltage. All the measurements reported in this chapter are performed with 0V modulation voltage, unless stated otherwise.

It is worth noting that, phonon absorptions which are sometimes observed in FDMRS (see Chapter 4) are not expected to be of importance in TDESRS, the technique is only sensitive to magnetic resonance transitions which lead to a change in the torque signal.

Field swept TDESRS

An alternative to the frequency swept measurements, is the field swept mode of operation. Instead of sweeping the frequency, the field is swept at a fixed MW frequency. The ESR transitions are induced at the resonance fields, i.e. the fields that satisfy the resonance condition. In this mode, the torque signal is measured with and without irradiation, the difference between the two signals results in an ESR-like line shape.

Figure 7.13 (a) shows the torque signals of the non-irradiated and irradiated crystal at 143 GHz and 20 K. The torque signal of the irradiated crystal shows characteristic

dips at the resonance fields indicating the occurrence of the ESR transition. $\Delta\tau$ is shown in 7.13 (b), where the $M_S = -5$ to -4 , -4 to -3 , and -3 to -2 transitions are observed at 0.91, 1.78, and 2.71 Tesla, respectively. The asterisks indicate the positions of the resonance fields calculated with the best-fit SHP provided above. The advantage of the field swept to the frequency swept mode is that the MW frequency, and consequently the MW power is kept constant. Hence, the different resonance lines are not altered by the MW power. On the other hand, the resonance lines occur at different fields, i.e. at different absolute torque signals. The non-linear response of the torque meter leads to increasing the signal at higher fields (for positive torque signals). As a consequence, the change in the torque signal $\Delta\tau$ is modified by the non-linear response, and resonances at higher fields are more intense. However, the torque values can be corrected for the non-linearity as explained in Chapter 2. Figure 7.13 (b) shows the raw, and the corrected $\Delta\tau$ values. The low field resonance line is not affected by the non-linear response, but the high field lines are clearly modified by that. Interestingly, the non-linear response can be exploited in this method to observe very weak resonance lines. A very small change in the torque will induce a relatively large capacitance change if we are in the non-linear regime. Hence, for weak resonance lines to be detected, the absolute torque value should be increased by either increasing the field, the angle θ , or decreasing the temperature. This is perhaps the only application in capacitance based torque magnetometry, where the non-linear response of the torque meter is considered to be advantageous.

Other experimental variables

In addition to the ability to simultaneously control the field and the MW frequency, other experimental parameters such as the temperature, and the angle θ can be con-

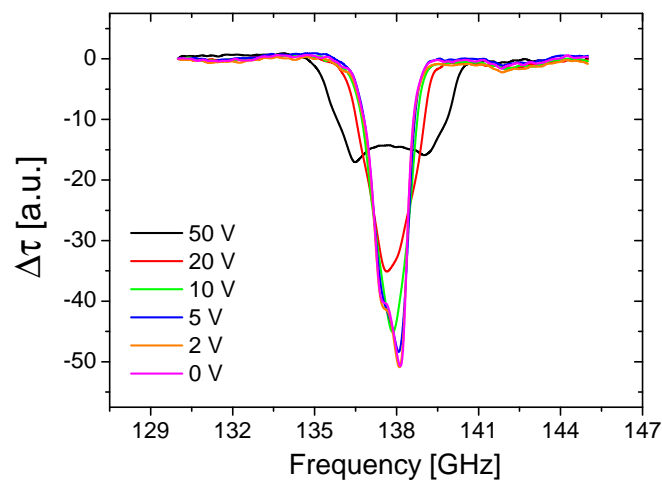


Figure 7.12: TDES R spectra of the -5 to -4 transition at 2 Tesla ($\theta = 4^\circ$, $T = 16$ K) recorded at different modulation voltages.

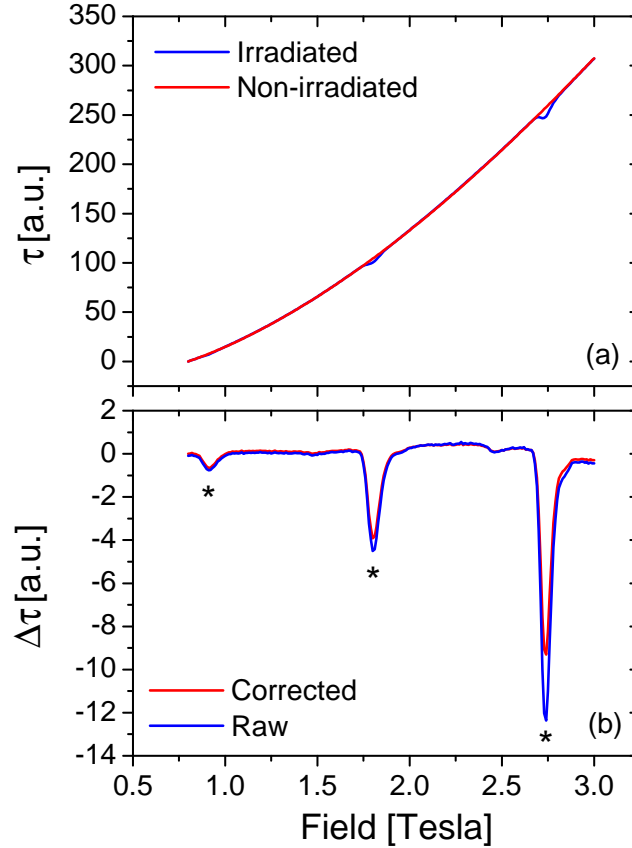


Figure 7.13: (a) Torque signals of the irradiated and non-irradiated single crystal at 143 GHz ($\theta = 5^\circ$, $T = 20$ K). (b) The difference of the two torque signals in (a) is plotted. The asterisks indicate the position of the calculated resonance fields with the SHPs discussed in the text.

trolled as well. Temperature dependent ESR measurements in SMMs are typically useful to determine the sign of the axial ZFS parameter. This is done by monitoring the intensity of the resonance lines with temperature. Consequently, the ground state transition can be assigned to either the low frequency (high field), or high frequency (low field) resonance line, therefore deducing a positive, or a negative D value, respectively. In TDESr, the sign of D is readily extracted from the sign of the torque signal as explained in Chapter 2. However, if the intensity of the resonance lines versus temperature is to be monitored, the $\Delta\tau$ values must be corrected. The absolute torque values are temperature dependent, thus $\Delta\tau$ is modified by the non-linear response of the cantilever as in the case of the field swept TDESr. Figure 7.14 shows frequency swept spectra at 12 and 25 K, with an external field of 4.3 Tesla applied at 5° from the easy axis. The asterisks show the calculated 12 K intensities relative to the 25 K intensities. A large disagreement is apparent between the experimentally obtained and the calculated intensities. The $\Delta\tau$ values of the 12 K spectrum are artificially enhanced due to the non-linear response of the torque meter. A comparison to the relative cal-

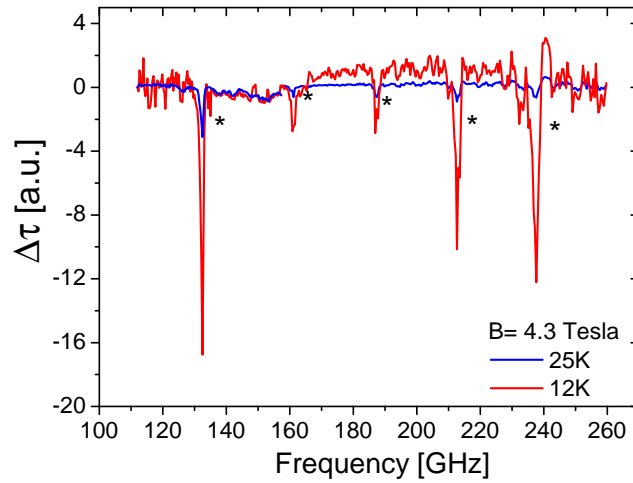


Figure 7.14: TDESER spectra at 12 and 25 K. The asterisks show the relative calculated intensities of the 12 K (see text).

culated intensities shows that the corrected intensities are yet not sufficient to explain this discrepancy. This is attributed to the limitation of the correction procedure.

One more particularly important feature of the setup is, the ability to perform angle dependent ESR measurements. Angle dependent ESR measurements are important to study the transverse anisotropy, and the degree of symmetry breaking, which strongly affect the quantum tunnelling rates. In the current setup, we are able to perform angle dependent TDESER measurements with an angular resolution of $< 1^\circ$. In addition the polarization of the microwave field can be changed between $0-90^\circ$, i.e. parallel or perpendicular to the external field. This particularly allows us to induce transition between strongly mixed states, which are either mixed by the transverse anisotropy or by a transverse field. Figure 7.15 (a) shows the TDESER spectra at 5, 10, and 15° . The resonance lines shift to lower frequencies with increasing angle, as expected. Figure 7.15 (b) shows the resonance frequencies of the -5 to -4 transition extracted from the TDESER spectra by fitting the resonance absorption lines with a Gaussian fit. The solid line shows the calculated resonance frequencies with the best fit parameters.

Another important aspect, is the heat induced by the MW radiation. Magnetization detected ESR techniques using Hall-bars as magnetic sensors reported a strong effect of the MW radiation on the measured magnetization values off resonance [98]. This could be attributed to the heating of the sample or the Hall-bar itself, induced by MW radiation. In order to investigate the effect of the MW radiation on our measurements, we have measured the torque signal off resonance with and without radiation at 16 K. The MW frequency was set to 162.5 GHz, where the MW power of the BWO source (QS2) is maximum. An external field of 4.8 Tesla was applied at 5° from the easy axis, such that the magnetic resonance condition is not satisfied. Figure 7.16 (a) shows jumps in the torque signal upon turning the MW radiation On and Off. The signal changes by around 13 fF under irradiation. Measuring the change in the

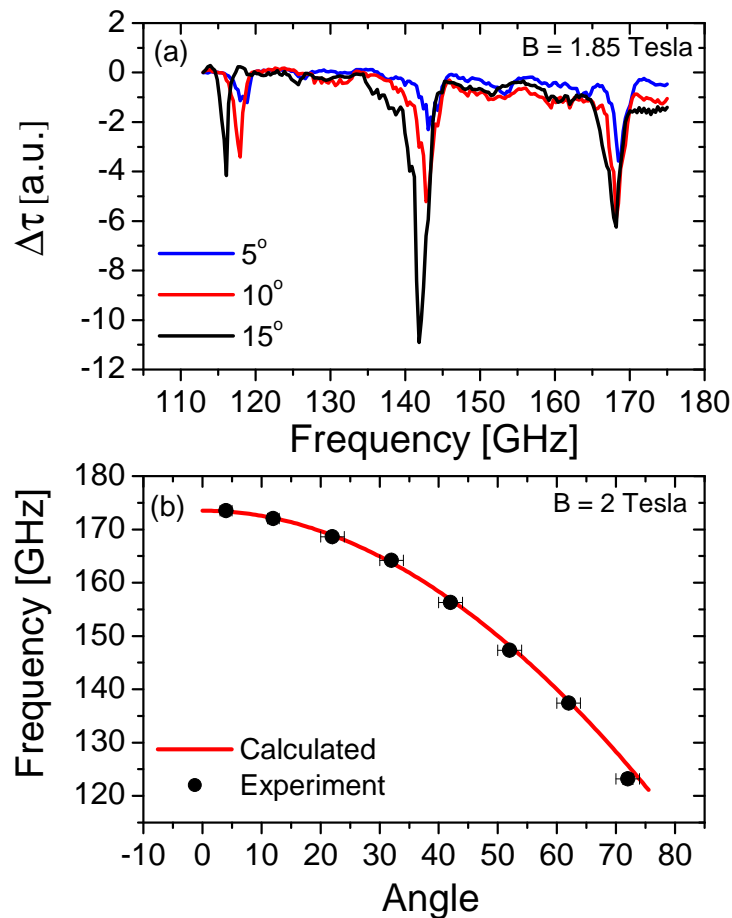


Figure 7.15: (a) TDESIR spectra recorded for three different angles at 1.85 Tesla and 20 K. (b) Resonance frequencies for the -5 to -4 transition vs angle θ between the external field (2 Tesla) and easy axis (circles). The line is the calculated resonance frequencies with the SHPs discussed in the text.

torque with temperature shows that a change of 13 fF corresponds to an increase in the temperature of around 120 mK above 16 K (Figure 7.16 (b)). The measurements were repeated several times to ensure reproducibility. This result shows that the effect of the MW radiation on the spin temperature of the sample is negligible. In other words, this clearly demonstrates that apart from inducing magnetic resonance transitions, the MW radiation has a minor effect on the recorded spectra. This is presumably owed to the good thermal coupling between the crystal/cantilever and the phonon bath, and the fact that the capacitance measurement itself is rather independent of small temperature fluctuations. It is worth noting that the technique is not limited to anisotropic material. In principle, one could use the same setup to detect magnetic resonance transitions in isotropic systems as well. In that case, the torque meter should be placed in an inhomogeneous magnetic field to detect the magnetization of the sample rather than the torque (which is absent in that case).

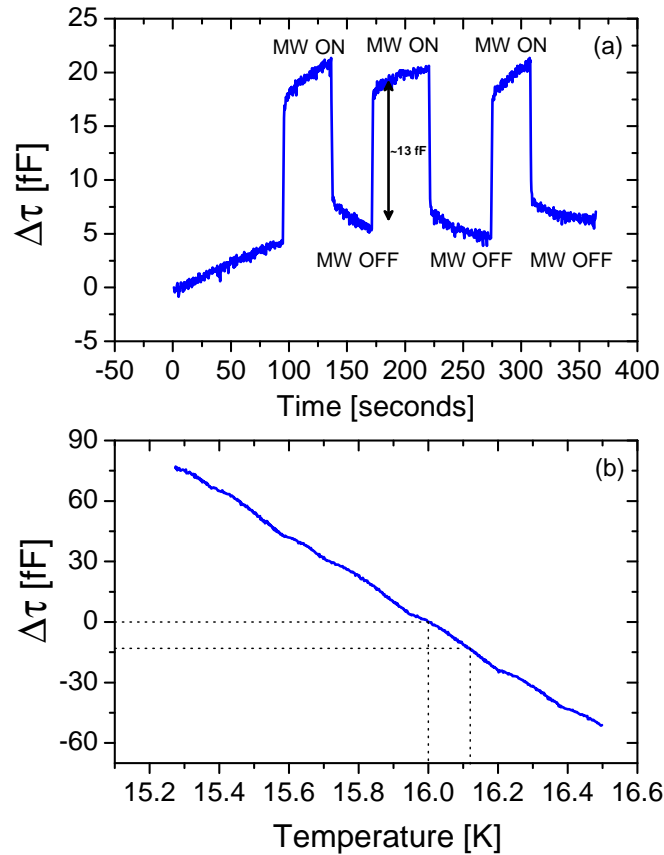


Figure 7.16: (a) Oscillations in the recorded torque signal at 16 K for an external field of 4.8 Tesla ($\theta = 5^\circ$) upon turning the MW radiation of 162.5 GHz On and Off. (b) The change in the torque signal vs temperature around 16 K.

Line width and line shape studies

As we have seen in the preceding sections, the non-linear response and the microwave power play an important role in determining the intensity (or line width of the resonance lines). This makes an accurate study of the line width vs. temperature, field or angle, a difficult task with the current setup. One possibility to avoid the error induced by the non-linear response of the torque meter, is by operating the torque meter in the constant separation distance mode. This is envisaged through introducing a feedback loop which keeps the capacitance value constant by applying a dc voltage that induces an electrostatic force compensating for the magnetic force of the sample. By performing proper calibration for the torque meter, the magnetic torque can be then related to the externally applied dc voltage. This mode of operation, not only allows the elimination of the non-linearity in the signal, but it also enables the measurement of larger single crystals, and consequently higher TDESr signals. Further development of the current setup is needed to realize this mode of operation.

On the other hand, line shapes obtained by the current method can be as infor-

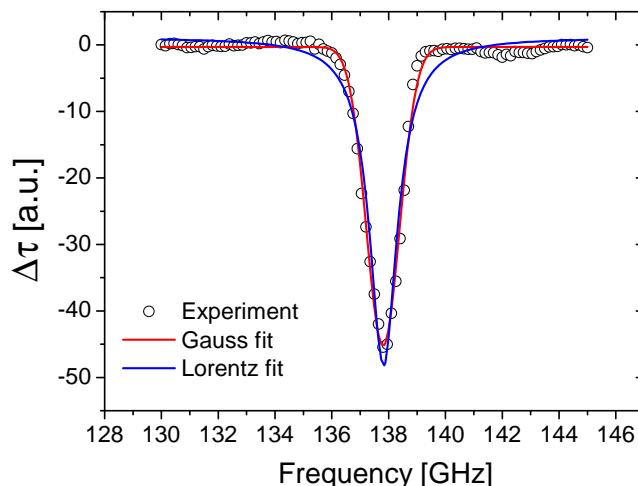


Figure 7.17: Resonance line between the $M_S = -5$ and -4 state recorded at an external field of 3.5 Tesla ($\theta = 4^\circ$, $T = 16$ K) fitted with a Lorentz and a Gauss function.

mative as those recorded in conventional ESR. Field swept mode is more suitable to perform line shape studies in case the resonance signal is strong enough. The stability of the MW power in this mode leads to a better signal to noise ratio than in the frequency swept mode. Nevertheless, the frequency swept mode can be used to study line shapes by tuning the resonance line of interest into a frequency range where the MW power is relatively stable. Figure 7.17 shows the resonance line at around 138 GHz (External field : 3.5 Tesla, $\theta = 4^\circ$, $T = 16$ K). The fit procedure shows that the line is inhomogeneously broadened and is described best with a Gaussian fit rather than a Lorentzian, suggesting a distribution in the ZFS parameters. The FWHM of 1.24 GHz, or 0.04 cm^{-1} , is much narrower than previously reported line widths for other SMMs (0.12 cm^{-1} for Fe_8 [100] and 0.18 cm^{-1} for Mn_{12} [73]). The broad frequency range enabling frequency/field dependent line shape studies, as well as angle dependent line shape studies, would allow us to characterize the nature of the broadening mechanisms (g , D , or E strain) in different SMMs.

7.5 Conclusions

We have developed a novel torque detected broad band ESR method to study small single crystals of single molecule magnets. The combination of torque and magnetic resonance detection renders this technique a very strong method to study anisotropy in these systems. The measurements can be done in the frequency swept mode covering the frequency range of 30 GHz - 1.5 THz at a fixed external field, or in the field swept mode (0-8 Tesla) at a fixed microwave frequency. In addition, angle dependent ESR measurements can be easily performed with a rotation capability between 0 and 180° . The diversity of the experimental parameters that could be controlled (magnetic

field, microwave frequency, angle, polarization, and temperature) would enable us to span the full energy diagram of a variety of systems. However, the drawback of the current setup lies in the effect of the non-linear response of the torque meter on the observed intensities. To avoid this problem, we propose employing a feedback loop, which enables the operation of the torque meter in the constant capacitance mode. Moreover, we demonstrated the strength of our new setup by studying an Fe₄-rac complex, and we were able to successfully determine the spin Hamiltonian parameters with a very high precision, which were found to be in excellent agreement with those obtained from high-frequency ESR performed on powder.

Chapter 8

Summary

Magnetic anisotropy lies at the heart of the molecular magnetism field of research. It is the magnetic anisotropy which leads to slow relaxing magnetic moments in single-molecule magnets (SMMs). The anisotropy also plays a vital role in the process of macroscopic quantum tunneling of the magnetization (QTM). Axial terms in the spin Hamiltonian, together with the spin ground state, define the magnitude of the energy barrier against the reversal of the magnetization ($U = DS^2 + B_4^0 S^4$). On the other hand, the transverse terms create superpositions of quantum spin states, thus enabling the tunneling of the spin through the barrier. As a consequence, the relaxation rates of the magnetization are enhanced, and the energy barrier U is replaced by an effective barrier (U_{eff}), which accounts for the tunneling induced relaxation besides the thermal one. It is therefore of utmost importance, to be able to determine the anisotropy parameters with high precision in these systems. Consequently, the understanding of the magnetic anisotropy in molecular magnetic clusters can lead to a better understanding of the underlying physics of the magnetic and quantum behavior of SMMs.

In this Thesis, we have aimed at studying the magnetic anisotropy in diverse molecular magnetic systems. For that purpose, we have used several experimental resonant and non-resonant techniques. Spectroscopy remains to date the most powerful method to investigate anisotropy in such systems. We have used frequency domain magnetic resonance to spectroscopically probe the spin fine structure of the ground state in molecular nanomagnets. However, not all systems are spectroscopically active, and spectroscopy may fail in systems with unfavorable spin-lattice relaxation times, large zero field splittings (ZFS), or excessive dipolar broadening. Therefore, we have also used magnetometry to either complement or replace spectroscopy in some systems. Finally, we combined both methods, thus creating a torque detected ESR technique.

Cantilever torque magnetometry (CTM) is the technique which takes the largest part in this Thesis. We have developed a capacitance based CTM method to carry out experiments on single crystals of molecular nanomagnets. In a SMM, the spin of the individual molecule is preferentially oriented along the easy axis of the molecule. The non-collinearity of the easy axis and the externally applied magnetic field, induces a magnetic torque which tends to align the easy axis with the latter. This magnetic torque bends the cantilever which forms a parallel-plate capacitor together with a

copper plate which lies at 30-100 μm below the cantilever. We have used the capacitive method to detect the degree of bending of the cantilever under an external torque. The bending of the lever leads to a change of its distance to the lower plate, and consequently to a change in the capacitance which is detected by an external capacitance bridge. We have used non-magnetic CuBe cantilevers of 25 and 80 μm thickness to assemble a set of torque meters covering the sensitivity range of 10^{-6} to 10^{-11} Nm. A special sample holder with a horizontal rotating stage was developed, and the measurement procedure was automated with the aid of several Labview codes. In magnetically anisotropic paramagnets, the torque induced by a magnetic field applied in the (xz) plane at an angle θ from the easy axis which also lies in the same plane is given by,

$$\tau_y = B^2 \left(\frac{M_z}{B_z} - \frac{M_x}{B_x} \right) \cos \theta \sin \theta \quad (8.1)$$

The term in brackets is the magnetic anisotropy of the system, and therefore, the torque is a direct probe for it. In addition, angle resolved torque measurements are particularly important to determine the sign of the anisotropy in the system. Magnetic torque measurements are not only useful to characterize the anisotropy of paramagnetic centers, but it can also provide information on the exchange interaction in the system, especially in antiferromagnetic clusters. We have successfully used CTM to study the magnetic anisotropy, as well as exchange interactions in the various systems.

Increasing the energy barrier against the reversal of magnetization in SMMs has been the focus of numerous studies in molecular magnetism. Despite the combined efforts of chemists and physicist to find suitable systems that could retain the magnetization for long time at high temperatures, Mn_{12} -acetate was the system with the highest blocking temperature and anisotropy barrier of 3.5 K and 74.4 K, respectively, until recently. We have studied two different variants of Mn_6 of spin ground state $S = 12$, and where one of them has a record barrier of 86 K (compound 1). Surprisingly, despite the very similar structure of the second compound, it has a smaller anisotropy barrier of 53 K (compound 2). In order to elucidate the reason for the different anisotropy barriers in the two compounds, we performed FDMRS and inelastic neutron scattering (INS) measurements on both systems. This enabled us to look at the low lying spin excitations and consequently map the energy spectra of the systems. The FDMR spectra show six sharp resonance lines between 5 and 9 cm^{-1} , which are very similar for both compounds. Interestingly, the resonance frequencies are not reproduced with the giant spin model (GSM). However, the model fits better to compound (1) than it fits to compound (2). Inelastic neutron scattering (INS) was used in order to gain better insight into the energy spectra of both compounds. Unlike FDMRS, INS is sensitive to inter- as well as intra-multiplet transitions. This particularly enabled us to probe the $S = 12$ to $S = 11$ transitions. The INS spectra demonstrate that the $S = 11$ is closer to the $S = 12$ spin state in compound (2). As a consequence, the spin states are strongly mixed providing new tunnel pathways that strongly affect the magnetization relaxation and reduce the effective anisotropy barriers. Moreover, this study has shown that the GSM is inadequate for these systems and the implementation of the microscopic Hamiltonian is necessary. In addition, we have seen how small structural distortions can have a tremendous effect on the anisotropy barrier.

One particularly interesting branch of molecular magnetism is that of photomagnetic clusters. These systems, which are quite often mononuclear Fe(II) complexes can undergo a spin crossover from a low spin (LS) state to a high spin (HS) state under the effect of temperature, pressure, or irradiation. In the present investigations we have aimed at combining large magnetic anisotropy and photoswitching of the spin states simultaneously in one system. The ultimate aim is to create photo-switchable single-molecule magnets. The system we have chosen is $[\text{Fe}(\text{bpp})(\text{NCS})_2]_2(4,4'\text{-bpy})$. We show how diverse experimental techniques can complement each other to fully characterize the magnetism of the system. The photomagnetic studies were performed at the University of Bordeaux by Dr. Patrick Rosa and his coworkers. At high temperatures, the susceptibility shows a paramagnetic behavior. On cooling, there is a sudden drop in χT at ca. 115 K. The susceptibility shows a small thermal hysteresis at this transition. This hysteresis was also observed in crystal structure studies. The drop in the χT value confirms the fact that one of the iron(II) ions in the molecule is in the LS configuration ($S = 0$). Light irradiation ($\lambda = 647 \text{ nm}$, $P_{\text{eff}} = 3 \text{ mW/cm}^2$) causes an increase in the susceptibility, virtually saturating after 10 minutes. This LIESST effect changes the electronic configuration of the LS centers into the HS metastable state. We have studied the magnetic anisotropy of the LS-HS state, which has an $S = 2$ spin ground state at low temperatures, using FDMRS, angle resolved magnetization, and CTM. FDMR spectra show a single magnetic resonance transition at around 9 cm^{-1} . The temperature dependence shows that the observed transition is a ground state transition. The absence of the excited state transition leaves the question of the type of the anisotropy in the system open. For an easy axis type anisotropy, the observed transition would give a D value of -3 cm^{-1} , while a D of $+9 \text{ cm}^{-1}$ is rather expected in the case of hard axis anisotropy. To raise this ambiguity, angle resolved magnetization measurements were performed in two different crystallographic planes. The absolute values of the magnetization maxima and minima in both planes were very similar which made the assignment of the easy (or hard) axis to a certain crystallographic axis impossible. Since we have two molecules per unit cell, a connection between the molecular axes and the crystallographic ones was made in order to comprehend the angle resolved magnetization data. This resulted in a valuable piece of information, restricting the anisotropy axis to either a hard axis lying close to the (Fe-Pyrazole-Fe) mean axis, or an easy axis close to the (Fe-Pyridine-Fe) mean axis. A strong proof for the nature of the anisotropy came from CTM measurements. Angle-resolved, as well as field dependent torque measurements demonstrate that the system possesses a hard axis anisotropy with a D value of $+9 \text{ cm}^{-1}$, and directed along the (Fe-Pyrazole-Fe) mean axis. These studies contribute to a better insight into the magnetic anisotropy of spin crossover systems. We have therefore demonstrated the necessity of having complementary techniques in studying the magnetic anisotropy in molecular magnets, where the information extracted from a single technique may in some cases lead not only to an incomplete, but rather to an erroneous picture. Our ultimate aim is to find a photoswitchable system with strong easy axis anisotropy, eventually leading to photoswitchable SMMs.

Molecular clusters with antiferromagnetic (AF) exchange interactions have attracted considerable interest due to their rich quantum magnetic properties. In particular, they are promising candidates to observe macroscopic quantum coherence reflected in the

coherent tunneling of the Néel vector. Most of the reported systems have relatively strong exchange coupling constants ($J > D$) which results in the typical picture of the energy spectrum for such an AF system, i.e. a system with a non-magnetic ground state ($S = 0$ for even number of equal spins) that successively changes into an $S = 1$, $S = 2$, etc... ground state, under the effect of an external magnetic field applied along the easy or the hard axis. We have studied a unique antiferromagnetically coupled Fe(II) dimer (Fe₂-Penta). Unlike what is commonly observed in strongly coupled systems, the magnetization shows only one level crossing around 4.2 Tesla, and continues to increase smoothly up to 12 Tesla. The model that we proposed based on the full characterization of the system, assumes that the exchange coupling is much weaker than the strong single ion anisotropy of the Fe(II). The magnitudes of the exchange interaction and the g value, were determined from the susceptibility and the magnetization measurements. On the other hand, the sign and magnitude of the single ion anisotropy D were extracted from the low- and high-field torque magnetometric measurements. The combination of these data allowed a precise determination of the spin Hamiltonian parameters to be, $g = 2.23(5)$, $J = -1.74(6) \text{ cm}^{-1}$, and $D = -8.5(4) \text{ cm}^{-1}$. The consequences of a weak exchange on the magnetic and quantum properties of the system are vital. For $D = 0$ (or $D \ll J$), $[\hat{S}, \hat{H}] = 0$ where S , the total spin, remains conserved. However, if $D \gg J$, the spin states are strongly mixed, and S is no longer a good quantum number whereas M_S remains a good quantum number in the absence of a transverse field. The energies of the different spins are therefore rearranged in the weak limit, and in our case, we observe that the $M_S = -4$ state lies closest to the ground non-magnetic doublet. As a consequence, instead of having a gradual increase of the magnetization, a giant magnetic step is observed in the magnetization directly at the first level crossing which magnetically correspond to a crossover from an $M_S = 0$ to an $M_S = -4$ state. This step is analogous to the spin flip seen in antiferromagnets with long range order. On the other hand, the energy and the composition of the ground doublet, that correspond to the two states with different orientations of the the Néel vector, are also strongly affected by the J/D ratio. The tunnel splitting which separates these two states in energy is estimated from the Hamiltonian to be around 83 MHz. Furthermore, the tunneling action S_0/\hbar , which is a measure of the probability for the Néel vector to tunnel, is estimated to be 12.5, which is two times the highest reported value in the Fe₁₈ antiferromagnetic ring. Motivated by these values of Δ and S_0/\hbar , we propose this system as a candidate to observe coherent tunneling of the Néel vector.

Lanthanides are fundamentally different from transition metals, having their valence electrons in the 4f rather than the 3d orbitals. As a consequence, lanthanides have weaker ligand fields than the transition metal coordinated ions. However, they possess large magnetic moments and quite often large magnetic anisotropy due to the strong spin-orbit coupling, which makes them interesting building blocks for SMMs. Mononuclear 4f complexes have shown slow relaxation of the magnetization at very high temperatures compared to those observed in transition metals. Despite the out of phase ac signal observed above 40 K, hysteresis curves were observed only at very low temperatures (mK range). There is a widespread agreement that fast tunneling in these systems is behind the absence of the hysteresis curves. It is therefore of crucial importance to obtain information on the low lying sublevels of the 4f electronic

systems, in order to understand the magnetism, and especially the relaxation mechanisms in these compounds. We have chosen a Dy_3 triangle with peculiar magnetic properties, namely, the system shows a slow relaxation of the magnetization despite the nonmagnetic ground state. Using the spin effective model to describe the system, we devised a spin Hamiltonian that considers that for each Dy^{3+} , the ground state doublet is $|15/2, \pm 15/2\rangle$, and the excited state doublets $|15/2, \pm 5/2\rangle$ at energy δ from the ground state. Knowing that the torque signal strongly depends on the anisotropy, we calculated torque signals for transverse fields which predict a peak at high magnetic fields depending on the value of δ . To that end, we have performed high field torque magnetometric measurements at large scale facilities in Grenoble and Tallahassee. The results confirmed our expectations showing a peak in the torque signal at around 28 Tesla, which enabled us to quantify the anisotropy $\delta = 250 \pm 10 \text{ cm}^{-1}$. In addition, temperature dependent investigation of the step observed in the torque signal at the level crossing in the mK range points toward a level mixing of the order of 100-200 mK. This value, which is not accounted for in the simple spin effective model that is used to describe the system, can give a plausible explanation to the enhancement in the magnetization relaxation rate observed at the level crossing in previous studies. Furthermore, two different inflection points were observed in the torque signal which may be assigned to the ground and the excited state crossing in the energy diagram. From the positions of these inflection points, an estimate of $\phi = 20^\circ$ is obtained which shed light on the spin structure within the Dy_3 triangle. More research is needed to develop new models which can give a more precise explanation of the magnetism of the system. This study was performed on an intricate system with complicated crystal structure. In a more general picture, this study has contributed to a better understanding of lanthanide based systems. In particular, we have proven that high field torque magnetometry is a strong tool to investigate the anisotropy in these systems, especially in mononuclear lanthanide SMMs.

Having successfully used spectroscopy and CTM to study the magnetic anisotropy in various SMMs, we exploited our experience in both techniques, thus combining them to develop a novel torque detected ESR (TDESR) method to study very small single crystals of SMMs in a broad frequency range. Conventional ESR spectrometers are highly sensitive, but they are hindered by their limited discrete frequencies, while broad band techniques such as FDMRS or INS suffer from their low sensitivity. TDESR combines both features together, i.e. high sensitivity and broad band spectroscopy. TDESR measures the effect that a magnetic resonance transition induces in the magnetic torque of the sample. On resonance, the microwaves induce a spin rotation, and consequently the value of the torque changes for an ensemble of spins. This change of the torque is detected by the highly sensitive torque magnetometer. The experimental setup used to perform TDESR measurements consists of two main parts. The first is the optical part which deals with the generation, and focusing of the microwave radiation onto the crystal. The second is the torque magnetometer which measures the torque signal under an external magnetic field. A special sample holder was designed to perform torque magnetometric measurements under microwave irradiation. The measurements can be done in the frequency swept mode covering the frequency range of 30 GHz - 1.5 THz at a fixed external field, or in the field swept mode (0-8 Tesla) at a fixed microwave frequency. In addition, angle dependent ESR

measurements can be easily performed with a rotation capability between 0 and 180°. In order to conduct a proof of concept study, we have chosen an Fe₄-rac compound with an $S = 5$ spin ground state. The duality of our technique enables us to pre-investigate the system with the conventional torque magnetometry, and subsequently perform TDESR. The two measurements are performed on the same mounted crystal "in situ". Conventional torque measurements provided an estimate of the axial anisotropy in the system ($D = -0.4 \text{ cm}^{-1}$), and enabled us to determine a precise orientation of the easy axis. TDESR measurements were performed in the frequency swept mode, as well as in the field swept mode, at different temperatures and angles. The spin Hamiltonian parameters [$D = -0.448(2) \text{ cm}^{-1}$, $E = 0.03(1) \text{ cm}^{-1}$, $B_4^0 = 1.8(3) \times 10^{-5} \text{ cm}^{-1}$, and $g = 1.985(4)$] were found to be in excellent agreement with those obtained from high-frequency ESR performed on powder. The obtained spectra clearly demonstrated the high sensitivity of the technique. The drawback of the current setup lies in the effect of the non-linear response of the torque meter on the observed intensities. To avoid this problem, we propose employing a feedback loop, which enables the operation of the torque meter in the constant capacitance mode. Furthermore, we have demonstrated that the diversity of the experimental parameters that could be controlled (magnetic field, microwave frequency, angle, polarization, and temperature), would enable us to span the full energy diagram of a variety of systems.

In conclusion, we have investigated the magnetic anisotropy in several molecular nanomagnets with diverse magnetic properties. In particular, we have seen how the interplay between the exchange and the single ion anisotropy can affect the anisotropy barrier (as in the Mn₆ systems), as well as the energy level scheme and the magnetic properties (as in the Fe₂-Penta system). Furthermore, our study on Dy₃, has contributed to the understanding of magnetic anisotropy in lanthanide-based molecular magnets, which may lead to the development of improved SMMs. In addition, we have demonstrated the necessity of employing complementary techniques in studying the magnetic anisotropy in molecular magnets, where the information extracted from a single technique may in some cases lead not only to an incomplete, but rather to an erroneous picture. Finally, we have developed a novel torque detected ESR method, which is a promising technique to study magnetic anisotropy in molecular nanomagnets.

Bibliography

- [1] www.electronics.ca/presscenter/articles/983/1/Magnetic-Materials-Market-is-Projected-to-Reach-285-Billion-by-2012 (July, 2009)
- [2] M. Mannini, F. Pineider, P. Saintavitt, C. Danieli, E. Otero, C. Sciancalepore, A. M. Talarico, M. A. Arrio, A. Cornia, D. Gatteschi, and R. Sessoli: *Nat. Mater.* **8** (2009) 194
- [3] L. Bogani, and W. Wernsdorfer: *Nat. Mater.* **7** (2008) 179
- [4] S. Hill, R. S. Edwards, N. Aliaga-Alcalde, and G. Christou: *Science* **203** (2003) 1015
- [5] F. E. Hallak, J. van Slageren, J. Gómez-Segura, D. Ruiz-Molina, and M. Dressel: *Phys. Rev. B* **75** (2007) 104403
- [6] J. R. Friedman, M. P. Sarachik, J. Tejada, and R. Ziolo: *Phys. Rev. Lett.* **76** (1996) 3830
- [7] L. Thomas, F. Lioni, R. Ballou, D. Gatteschi, R. Sessoli, and B. Barbara: *Nature* **383** (1996) 145
- [8] S. J. Blundell: *Contemp. Phys.* **48** (2007) 275
- [9] G. Bihlmayer: *Magnetism goes nano, Schriften des Forschungszentrums Juelich* **26** (2005)
- [10] J. J. Sakurai: *Modern Quantum Mechanics*: Addison-Wesley, second edn. (1994)
- [11] H. Haken, and H. C. Wolf: *The Physics of Atoms and Quanta*: Springer-Verlag, third edn. (1993)
- [12] D. Gatteschi, R. Sessoli, and J. Villain: *Molecular Nanomagnets*: Oxford University Press (2006)
- [13] A. Abragam, and B. Bleaney: *Electron Paramagnetic Resonance of Transition Metal Ions*: Dover (1986)
- [14] A. Bencini, and D. Gatteschi: *EPR of Exchange Coupled Systems*: Springer Verlag (1990)
- [15] E. del Barco, A. D. Kent, S. Hill, J. M. North, N. S. Dalal, E. M. Rumberger, D. N. Hendrickson, N. Chakov, and G. Christou: *J. Low Temp. Phys.* **140** (2005) 119
- [16] J. Clarke: *SQUIDS: Principles, noise, and applications*: Academic press (1990)
- [17] R. R. Joyce, and P. L. Richards: *Phys. Rev.* **179** (1969) 375
- [18] J. van Slageren, S. Vongtragool, B. Gorshunov, A. Mukhin, N. Karl, J. Krzystek, J. Telser, A. Mueller, C. Sangregorio, D. Gatteschi, and M. Dressel: *Phys. Chem. Chem. Phys.* **5** (2003) 3837
- [19] R. Basler, C. Boskovic, G. Chaboussant, H. Guedel, M. Murrie, S. T. Ochsenbein, and A. Sieber: *Chem. Phys. Chem.* **4** (2003) 920
- [20] R. Boča: *Coord. Chem. Rev.* **248** (2004) 757
- [21] J. Schnack: *cond-mat/0501625, X5.1-X5.36* (2005)
- [22] S. Blundell: *Magnetism in Condensed Matter*: Oxford University Press (2004)

- [23] S. E. Sebastian, N. Harrison, E. Palm, T. P. Murphy, C. H. Mielke, R. Liang, D. A. Bonn, W. N. Hardy, and G. G. Lonzarich: *Nature* **454** (2008) 200
- [24] C. Rossel, P. Bauer, D. Zech, J. Hofer, M. Willemin, and H. Keller: *J. Appl. Phys.* **79** (1996) 8166
- [25] D. E. Farrell, C. M. Williams, S. A. Wolf, N. P. Bansal, and V. G. Kogan: *Phys. Rev. Lett.* **61** (1988) 2805
- [26] A. S. van Steenbergen, J. A. A. J. Perenboom, S. A. J. Wiegers, and J. C. Maan: *Physica B* **246-247** (1998) 164
- [27] R. F. Penoyer: *Rev. Sci. Instrum.* **30** (1959) 711
- [28] D. E. Farrell, J. P. Rice, and D. M. Ginsberg: *Phys. Rev. Lett.* **67** (1991) 1165
- [29] R. Berger, C. Gerber, H. P. Lang, and J. K. Gimzewski: *Microelectron. Eng.* **35** (1997) 373
- [30] A. Cornia, D. Gatteschi, and R. Sessoli: *Coord. Chem. Rev.* (2001) 573
- [31] R. D. Heyding, J. B. Taylor, and M. L. Hair: *Rev. Sci. Instrum.* **32** (1961) 161
- [32] J. S. Brooks, M. J. Naughton, Y. P. Ma, P. M. Chaikin, and R. V. Chamberlin: *Rev. Sci. Instrum.* **58** (1987) 117
- [33] J. van Slageren, R. Sessoli, D. Gatteschi, A. A. Smith, M. Helliwell, R. E. P. Winpenny, A. Cornia, A. L. Barra, A. G. M. Jansen, E. Rentschler, and G. A. Timco: *Chem. Eur. J.* **8** (2002) 277
- [34] A. Cornia, M. Affronte, A. G. Jansen, D. Gatteschi, A. Caneschi, and R. Sessoli: *Chem. Phys. Lett.* **322** (2000) 477
- [35] M. Affronte, A. Cornia, A. Lascialfari, F. Borsa, D. Gatteschi, J. Hinderer, M. Horvatić, A. G. M. Jansen, and M. H. Julien: *Phys. Rev. Lett.* **88** (2002) 167201
- [36] O. Waldmann, L. Zhao, and L. K. Thompson: *Phys. Rev. Lett.* **88** (2002) 066401
- [37] R. Boča: *Theoretical Foundations of Molecular Magnetism*: Elsevier (1999)
- [38] O. Waldmann, S. Carretta, P. Santini, R. Koch, A. G. M. Jansen, G. Amoretti, R. Caciuffo, L. Zhao, and L. K. Thompson: *Phys. Rev. Lett.* **92** (2004) 096403
- [39] O. Waldmann: *Phys. Rev. B* **75** (2007) 174440
- [40] S. Carretta, P. Santini, G. Amoretti, M. Affronte, A. Ghirri, I. Sheikin, S. Piligkos, G. Timco, and R. E. P. Winpenny: *Phys. Rev. B* **72** (2005) 060403
- [41] O. Waldmann, C. Dobe, H. U. Guedel, and H. Mutka: *Phys. Rev. B* **74** (2006) 054429
- [42] W. Wernsdorfer, A. Mueller, D. Mailly, and B. Barbara: *Europhys. Lett.* **66** (2004) 861
- [43] G. Meyer, and N. M. Amer: *Appl. Phys. Lett.* **53** (1998) 1045
- [44] S. Alexander, L. Hellemans, O. Marti, J. Schneir, V. Elings, P. K. Hansma, M. Longmire, and J. Gurley: *J. Appl. Phys.* **65** (1989) 164
- [45] F. J. Giessibl, and B. M. Traftas: *Rev. Sci. Instrum.* **65** (1994) 1923
- [46] C. Lee, T. Itoh, and T. Suga: *Sens. Actuators A* **A72** (1999) 179
- [47] R. Griessen: *Cryog.* **13** (1973) 375
- [48] M. Qvarford, K. Heeck, J. G. Lensink, R. J. Wijngaarden, and R. Griessen: *Rev. Sci. Instrum.* **63** (1992) 5726
- [49] M. Weber, R. Koch, and K. H. Rieder: *Phys. Rev. Lett.* **73** (1994) 1166
- [50] www.goodfellow.com (July, 2009)
- [51] L. B. Hunt: *J. Sci. Instrum.* **21** (1944) 97

- [52] O. Waldmann: *Phys. Rev. B* **65** (2001) 024424
- [53] C. Rossel, M. Willemin, A. Gasser, H. Bothuizen, G. I. Meijer, and H. Keller: *Rev. Sci. Instrum.* **69** (1998) 3199
- [54] M. P. Schwarz, D. Grundler, I. Meinel, C. Heyn, and D. Heitmann: *Appl. Phys. Lett.* **76** (2000) 3564
- [55] C. R. Hibbeler: *Mechanics of Materials*: Springer-Verlag, sixth edn. (2004)
- [56] J. Andelin: *Phys. Rev. Lett.* **18** (1967) 483
- [57] M. Chan, M. Ryschkewitsch, and H. Meyer: *J. Low. Temp. Phys.* **26** (1977) 211
- [58] C. J. Milios, A. Vinslava, W. Wernsdorfer, S. Moggach, S. Parsons, S. P. Perlepes, G. Christou, and E. K. Brechin: *J. Am. Chem. Soc.* (2007)
- [59] J. Villain, F. Hartmanboutron, R. Sessoli, and A. Rettori: *Euro. Phys. Lett.* **27** (1994) 159
- [60] C. J. Milios, A. Vinslava, P. A. Wood, S. Parsons, W. Wernsdorfer, G. Christou, S. P. Perlepes, and E. K. Brechin: *J. Am. Chem. Soc.* **129** (2007) 8
- [61] C. J. Milios, C. P. Raptopoulou, A. Terzis, F. Lloret, R. Vicente, S. P. Perlepes, and A. Escuer: *Angew. Chem.* **43** (2004) 210
- [62] C. J. Milios, S. Piligkos, and E. K. Brechin: *Dalton Trans.* (2008) 1809
- [63] R. Inglis, L. F. Jones, C. Milios, S. Datta, A. Collins, S. Parsons, W. Wernsdorfer, S. Hill, S. P. Perlepes, S. Piligkos, and E. K. Brechin: *Dalton Trans.* (2009) 3403
- [64] I. Mirebeau, M. Hennion, H. Casalta, H. Andres, H. U. Guedel, A. V. Irodova, and A. Caneschi: *Phys. Rev. Lett.* **83** (1999) 628
- [65] S. Piligkos, G. Rajaraman, M. Soler, N. Kirchner, J. van Slageren, R. Bircher, S. Parsons, H. U. Guedel, J. Kortus, W. Wernsdorfer, G. Christou, and E. K. Brechin: *J. Am. Chem. Soc.* **127** (2005) 5572
- [66] S. Carretta, E. Livioti, N. Magnani, P. Santini, and G. Amoretti: *Phys. Rev. Lett.* **92** (2004) 207205
- [67] N. Kirchner, J. van Slageren, B. Tsukerblat, O. Waldmann, and M. Dressel: *Phys. Rev. B* **78** (2008) 094426
- [68] P. Guetlich, and H. A. Goodwin: *Spin Crossover in Transition Metal Compounds I*: Pearson Prentice Hall (2005)
- [69] G. Chastanet, C. Carbonera, C. Mingotaud, and J. Létard: *J. Mater. Chem.* **14** (2004) 3516
- [70] N. O. Moussa, G. Molnár, S. Bonhommeau, A. Zwick, S. Mouri, K. Tanaka, J. A. Real, and A. Bousseksou: *Phys. Rev. Lett.* **94** (2005) 107205
- [71] P. Rosa: *To be published*
- [72] D. Fedaoui, Y. Bouhadja, A. Kaiba, P. Guionneau, J. F. Létard, and Patrick Rosa: *Eur. J. Inorg. Chem.* (2008) 1022
- [73] S. Vongtragool, A. Mukhin, B. Gorshunov, and M. Dressel: *Phys. Rev. B* **69** (2004) 104410
- [74] J. van Slageren, S. Vongtragool, B. Gorshunov, M. Mukhin, and M. Dressel: *Euro. Phys. Lett.* **79** (2009) 224406
- [75] S. Vongtragool, B. Gorshunov, M. Dressel, J. Krzystek, D. M. Eichhorn, and J. Telsler: *Inorg. Chem.* **42** (2003) 1788
- [76] J. Telsler, J. van Slageren, S. Vongtragool, M. Dressel, W. M. Reiff, S. A. Zvyagin, A. Ozarowski, and J. Krzystek: *Magn. Reson. Chem.* **43** (2005) S130
- [77] F. Meier, and D. Loss: *Phys. Rev. Lett.* **86** (2001) 5373

- [78] A. Chiolero, and D. Loss: *Phys. Rev. Lett.* **80** (1998) 196
- [79] O. Waldmann, J. Hassmann, P. Mueller, G. S. Hanan, D. Volkmer, U. S. Schubert, and J. M. Lehn: *Phys. Rev. Lett.* **78** (1997) 3390
- [80] R. Caciuffo, T. Guidi, G. Amoretti, S. Carretta, E. Liviotti, P. Santini, C. Mondelli, G. Timco, C. A. Muryn, and R. E. P. Winpenny: *Phys. Rev. B* **71** (2005) 174407
- [81] O. Waldmann, T. C. Stamatatos, G. Christou, H. U. Guedel, I. Sheikin, and H. Mutka: *Phys. Rev. Lett.* **102** (2009) 157202
- [82] J. S. Sun, H. Zhao, X. Ouyang, R. Clérac, J. A. Smith, J. M. Clemente-Juan, C. Gómez-García, E. Coronado, and K. R. Dunbar: *Inorg. Chem.* **38** (1999) 5841
- [83] O. Waldmann, M. Ruben, U. Ziener, P. Mueller, and J. M. Lehn: *Inorg. Chem.* **45** (2006) 6535
- [84] D. M. Duggan, E. K. Barefield, and D. N. Hendrickson: *Inorg. Chem.* **12** (1973) 985
- [85] Y. Shapira, M. T. Liu, S. Foner, R. J. Howard, and W. H. Armstrong: *Phys. Rev. B* **63** (2001) 094422.
- [86] W. Wernsdorfer, R. Sessoli: *Science* **284** (1999) 133
- [87] N. Ishikawa, M. Sugita, T. Ishikawa, S. ya Koshihara, and Y. Kaizu: *J. Am. Chem. Soc.* **125** (2003) 8694
- [88] N. Ishikawa, M. Sugita, and W. Wernsdorfer: *Angew. Chem.* **117** (2005) 2991
- [89] L. G. Westin, M. Kritikosb, and A. Caneschi: *Chem. Commun.* (2003) 1012
- [90] M. T. Gamer, Y. Lan, P. W. Roesky, A. K. Powell, and R. Clérac: *Inorg. Chem.* **47** (2008) 6581
- [91] J. Luzon, K. Bernot, I. J. Hewitt, C. E. Anson, A. K. Powell, and R. Sessoli: *Phys. Rev. Lett.* **100** (2008) 247205
- [92] J. Tang, I. Hewitt, N. T. Madhu, G. Chastanet, W. Wernsdorfer, C. E. Anson, C. Benelli, R. Sessoli, and A. K. Powell: *Angew. Chem. Int. Ed.* **45** (2006) 1729
- [93] L. F. Chibotaru, L. Ungur, and A. Soncini: *Angew. Chem. Int. Ed.* **47** (2008) 4126
- [94] S. Takahashi, and S. Hilla: *Rev. Sci. Instrum.* **76** (2005) 023114
- [95] G. A. Candela: *J. Chem. Phys.* **42** (1965) 113
- [96] B. Cagea, S. E. Russek, D. Zipse, and N. S. Dalal: *J. Appl. Phys.* **97** (2005) 10M507
- [97] E. del Barco, A. D. Kent, E. C. Yang, and D. N. Hendrickson: *Phys. Rev. Lett.* **93** (2004) 157202
- [98] K. Petukhov, S. Bahr, W. Wernsdorfer, A. L. Barra, and V. Mosser: *Phys. Rev. B* **75** (2007) 064408
- [99] L. Gregoli, C. Danieli, A. L. Barra, P. Neugebauer, G. Pellegrino, G. Poneti, R. Sessoli, and A. Cornia: *Chem. Eur. J* **15** (2009) 6456
- [100] S. Hill, S. Maccagnano, K. Park, R. M. Achey, J. M. North, and N. S. Dalal: *Phys. Rev. B* **65** (2002) 224410

Acknowledgements

Although the list of individuals I would like to thank extends beyond the limits of the following three pages, I would like to acknowledge here my gratitude for many people who contributed either directly or indirectly to this work.

I am sincerely grateful to my direct supervisor Dr. Joris van Slageren. From Joris, I gained a great deal of experience in the field of molecular magnetism throughout the years. With him, I have learned how to be an independent researcher, but also how to cooperate with him and with other collaborators. I am deeply grateful for all the time that he has dedicated to me and for his patience, support, and friendship. I am also thankful for his meticulous correction of my Thesis, which considerably improved my writing skills.

I would like to express my gratitude to my supervisor Prof. Martin Dressel who supported and encouraged me during my whole stay at Pi1. I am especially grateful for his confidence in me and the freedom that he has given me to pursue different projects of my own. I am also thankful to him for proofreading this Thesis.

I thank Prof. Jörg Wrachtrup who kindly accepted to co-referee my Thesis.

Thanks are also due to Christoph Schlegel with whom I shared the Labs during my PhD and had many fruitful discussions. He was always there for a helping hand. Lapo Bogani who joined our institute in the last couple of months of my PhD was of great help to me. I am grateful especially for his courage and dedication to go to Tallahassee instead of me.

Many thanks to all the former and current members of Pi1, especially, Dr. Bruno Gompf, Shadi Yasin, Eva Rose, Stefan Kaiser, Natalia Drichko, Judith Bach, Martin Hövel, Neven Barisic, Matthias Fischer, Stephan Martens, Michael Dumm, Katrin Steinberg, Marc Scheffler, and Christian Stehle. Many thanks to Mrs. Gabriele Untereiner for her continuous technical support. I would also like to thank Frank Teufel who made sure that the cryostat was always full of Helium during the last year of my PhD.

I would like to thank the members of the mechanical workshop for their outstanding work which I highly appreciate. I doubt that I will be able to work with such a highly skilled team in the future. I also want to thank the members of the low temperature department for their kindness, and for the smile they had on their face every time I was there to pick up another can of Helium. I am also thankful to the members of the electronic workshop who did a fine and elegant wiring of some parts of the setup.

They have all contributed to my knowledge of the German language which I am also grateful for.

I am deeply grateful to Mrs. Agnieszka Cienkowska-Schmidt for her great efforts in handling the administrative issues throughout my stay at Pi1. She was always of great help and support to me. I am also thankful to Mrs. Carril who was always so kind to me and helped me maintain a relatively organized office.

During my PhD, I have spent three months in Florence, at the Laboratory of Molecular Magnetism under the supervision of Prof. Roberta Sessoli. This stay has brought me luck, success, and allowed me to make good friends and initiate new projects. I am indebted to Roberta for the invaluable time that she has spent with me, which helped me in having a profound understanding of many aspects in the field of molecular magnetism. I am also grateful for her detailed comments on parts of this Thesis. It was Kevin Bernot who showed me that one has to handle a crystal in the same way he handles his own child. From Kevin, I learned all about indexing and orienting of crystals. Mael Etienne who was Kevin's successor joined me in Grenoble to measure the Dy₃ compound. I was also glad to have him and Lapo Gorini here in Stuttgart, where we tried to put molecular magnets on gold plated cantilevers. I am thankful for them for the good time we spent together and for teaching me how to deposit the molecules on surfaces. In Florence, I also had the pleasure to work with Javier Luzon on the modeling of the Dy₃ system. Javier has given me a lot of input and useful hints on the calculations that I have performed to model the system. I am also grateful to Prof. Andrea Caneschi who was the one to make sure that everything was running smoothly during my stay over there. Further thanks to all the members of the group in Florence with whom I had a very good time and I made good friendships.

I had a long fruitful and successful collaboration with Dr. Patrick Rosa from Bordeaux. I was very happy to work with him over the past three years. Patrick was the one who synthesized the beautiful Fe₂ compounds that I have studied. His knowledge and understanding of the chemistry of the systems was of great importance to our study.

I would like to thank Pedro Vidal for his continuous assistance on the theoretical problems that I had to tackle. Pedro has strongly contributed to all the modeling and theoretical calculations that I have made. I am especially grateful to his knowledge in mathematica which assisted me in developing the program to perform all the calculations.

I was glad to meet Prof. Andrea Cornia couple of times and discuss with him some fine details of torque magnetometry. I am thankful for the input that I got from him, and also for the Fe₄ crystals that he sent to me to perform the TDESr measurements. Further thanks are due to Prof. Annie Powell and Dr. Chris Anson for the Dy₃ crystals that they have sent to me.

All the INS measurements and analysis were performed by Dr. Joris van Slageren, Dr. Tatiana Guidi, Dr. Bella Lake, Olivier Pieper, Dr. Hannu Mutka, Dr. Michael Marek Koza; Dr. Stefano Carretta, Dr. Paolo Santini, and Prof. Giuseppe Amoretti. I am glad that they managed to do such a beautiful work.

I met Christoph Busche in Portugal at the ECMM. There we have initiated a nice collaboration through which I have studied some of Christoph's compounds.

Many thanks to Augusta Bianca Ene, Ora Bukoshi, Christoph Schlegel, and Katrin Steinberg for their collaborative efforts to translate the summary of this Thesis into German.

I am grateful for the financial support of the German science foundation resembled by the Graduate College of Magnetic Resonance. Thanks are also due to all the professors who contributed to the educational programme in the graduate college. Their lectures have broadened my knowledge in the magnetic resonance field of research. In particular, I would like to thank Prof. Emil Roduner for the all the time and concern that he has dedicated to the graduate college students. Further thanks to all the graduate college members with whom I enjoyed taking part in several workshops and classes.

I am grateful to the Grenoble High Magnetic Field Laboratory, and especially to Ilya Sheikin for his support in performing the high field torque measurements. I am also thankful to the National High Magnetic Field Laboratory, and especially to Dr. Eric Palm and Prof. Stephen Hill for giving us the opportunity to perform high field measurements in Tallahassee.

Of course I can not forget my wonderful friends that I met here in Stuttgart, Pegor Aynejian, Jules Mikhael, Pedro Vidal, Erhan Arac, and Serkan Ates with whom I shared my happy and sad moments. I am grateful that I got to know them all. I also thank the "Lebanese Team", especially, Talal Arnaout, Sami Tanios, and Bachar Zeiter with whom I enjoyed lovely moments of good Lebanese nights and food. Many thanks to my friends abroad Ziad Shaaban, Wissam Faraj, and Omar Yassine for their support and friendship.

Finally, I would love to thank my lovely mother, my sister, and my two brothers for their love and prayers. I especially want to thank my uncle Emil Forzali for being in my life. Katka, thank you for your patience, love, and support. I dedicate this Thesis to the memory of my father, whose dream has motivated and encouraged me to make it till the end.